

Advances in Optics and Photonics

Photomechanical materials and applications: a tutorial

MARK G. KUZYK^{1,*}  AND NATHAN J. DAWSON^{1,2} 

¹*Department of Physics and Astronomy, Washington State University, Pullman, Washington 99164-2814, USA*

²*Department of Natural Sciences, Hawaii Pacific University, Kaneohe, Hawaii 96744, USA*

*Corresponding author: kuz@wsu.edu

Received January 3, 2020; revised September 18, 2020; accepted September 27, 2020;
published November 30, 2020 (Doc. ID 387366)

The transistor has revolutionized civilization. The photon will enable the next revolution provided that photomechanical materials, which convert light energy into mechanical work, can be made substantially more efficient. This tutorial develops a unified picture of the photomechanical response from its microscopic origins to the bulk response. A statistical model of the relationship between the photomorphon, the smallest photomechanical material unit, and the bulk response provides the context for understanding the various mechanisms that can contribute. We then present experimental details of how the photomechanical response is measured and used to deduce the underlying mechanisms. A figure of merit for the photomechanical efficiency is defined and materials are reviewed. Finally, we describe the photomechanical optical device (POD) and how PODs can be combined to form highly intelligent materials. This tutorial spans the multidisciplinary topics needed to (1) understand the fundamental physics of the response, (2) design and process materials to control the response, and (3) build new devices and integrated photomechanical systems. © 2020 Optical Society of America

<https://doi.org/10.1364/AOP.387366>

1. History	850
2. Photomechanical Effects and Nonlinear Optics	854
2.1. Optical Path Length	854
2.2. Response Functions	858
2.3. Body Forces	864
2.3a. Thin Infinite Rod	864
2.3b. Finite Charged Rod	870
2.4. Optical Response Function	874
2.4a. Monochromatic Optical Field	875
2.4b. Two Monochromatic Optical Fields	877
2.4c. Narrow Linewidth Laser Excitation	878
2.4d. Mechanical Excitation in the Quantum Realm	880
3. Microscopic Comparison between Optics and Mechanics	881

4.	Relationship between Microscopic and Bulk Mechanical Properties	882
4.1.	Body Forces and the Linear Response Function	885
4.2.	Examples of Light-Induced Body Force	887
4.2a.	Charged Rod in an Electric Field	887
4.2b.	Optical Field in a Dielectric Rod—Instantaneous and Local Response	890
4.3.	Other Factors	893
4.4.	Quantum Origins of the Photomechanical Response	893
4.5.	Photomechanical Unit	898
4.6.	Photomorphon	899
5.	Statistical Model	901
5.1.	Force and Length Change	902
5.2.	Population Dynamics	903
5.3.	Length Dynamics	907
5.4.	Force Dynamics	909
6.	Mechanisms	911
6.1.	Fast Responses	916
6.1a.	Electronic Cloud Deformation	916
6.1b.	Molecular Reorientation	916
6.2.	Electrostriction and Photostriction	917
6.2a.	Electrostriction	917
6.2b.	Photostriction	917
6.2c.	Field Gradients	918
6.2d.	Experimental Observations	918
6.3.	Photothermal Heating	919
6.3a.	Radiative Heat Transfer	919
6.3b.	Conductive and Convective Heat Transfer	920
6.3c.	Diffusion of Heat through a Material	921
6.3d.	Boundary and Initial Conditions	923
6.4.	Heat Sources/Sinks and Photothermal Heating	924
6.4a.	Thermal Expansion	927
6.4b.	Photomechanical Effect via Photothermal Heating	928
6.5.	Photochemical Changes in Structure	929
6.5a.	Isomers	929
6.5b.	Photoisomerization	930
6.5c.	Examples of Photochromic Molecules	933
6.6.	Ordered Materials	934
6.6a.	Anisotropic Materials	934
6.6b.	Crystals and Translational Symmetry	935
6.6c.	Polymers	935
6.6d.	Liquid Crystals	935
6.6e.	Orientalional Order Parameter of Nematic Liquid Crystals	936
6.6f.	Landau–De Gennes Theory	937
6.6g.	Maier–Saupe Theory	938
6.6h.	Maier–Saupe Model of Photochromic and Non-Photochromic Mesogens with Similar Interaction Potentials	940
6.6i.	Liquid Crystal Polymers and Elastomers	943
6.7.	Leveraging Molecular Orientation	944
6.7a.	Ordered Material	944
6.7b.	Isotropic Material	945
7.	Measuring Photomechanical Response Functions	948
7.1.	Experimental Techniques	948
7.1a.	Clamped Sample–Side Illumination	948
7.1b.	Clamped Material–Waveguide Geometry	956
7.1c.	Bending	957

7.1d. Uniaxial Strain	959
7.2. Sign Conventions	961
7.3. Applications to Studies of Materials	962
7.3a. Bending	962
7.3b. Uniaxial Photomechanical Stress	963
7.3c. Uniaxial Length Change	965
7.3d. Mixed Orientational Hole Burning and Photothermal Heating	966
8. Efficiency and Figure of Merit	970
8.1. PM Unit Efficiency	970
8.2. Photomorphon Efficiency	970
9. Overview of Photomechanical Materials	971
9.1. “Photophone”	971
9.2. Bilayer Materials	972
9.3. Crystals of Small Molecules	973
9.3a. Irreversible Photomechanical Effects in Molecular Crystals	973
9.3b. Reversible Photomechanical Effects in Molecular Crystals	973
9.4. Amorphous Photochromic Polymers	974
9.5. Polymers	975
9.6. Liquid Crystal Elastomers/Polymers	976
9.7. Biological Photomechanical Materials	977
10. Devices	977
10.1. Bulk Photomechanical Optical Device	978
10.2. Miniaturized POD	982
10.3. Integrating Photomechanical Devices	985
10.3a. Cascading Devices	985
10.3b. Integrating PODs	986
10.4. Photomechanical Energy Harvesters	988
11. Conclusion	989
Appendix A: Material Tabulations	990
Abbreviations for Tabulated Materials	990
Appendix B: Strain Tensor	990
Appendix C: Stress	994
Appendix D: Poisson’s Ratio	995
Funding	996
Disclosures	996
References and Note	996

Photomechanical materials and applications: a tutorial

MARK G. KUZYK AND NATHAN J. DAWSON

1. HISTORY

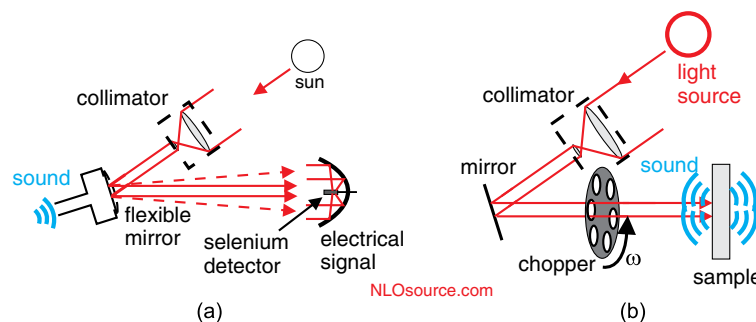
A light-induced change in a material's shape is called the photomechanical effect. Photomechanical effects surround us and have been operating on Earth since the birth of our planet. Sunlight, when absorbed by an object such as a rock, is converted to heat. The resulting temperature change leads to thermal expansion. This photothermal mechanism is the most ubiquitous and pronounced in nature.

The first-known deliberate investigations of the photomechanical effect were reported by Alexander Graham Bell in the 19th century [1]. His goal was to build what he called a photophone, which is shown in Fig. 1(a). The transmitter is made of a flexible mirror that oscillates in response to sound and deflects the collimated sunlight. Light modulated by sound at the transmitter is directed to a receiver made with a selenium photocell that converts light to an electrical signal that drives a speaker. Bell reported clearly hearing his assistant's voice at the receiver 213 meters away from the transmitter saying, "Mr. Bell, if you hear what I say, come to the window and wave your hat."

Lacking means of direct communications between the researchers, experiments over such large distances were impractical. Over shorter distances between transmitter and receiver, the voice of the individual at the transmitter overwhelmed the sound produced by the speaker, making measurements of the photocell's efficiency impossible. To circumvent this problem, Bell recognized that the critical requirement for measuring transmission efficiency was a well-defined modulated beam as a standard, so he replaced the membrane with a spinning perforated disk that converted the beam to a periodic train of pulses. This method produced well-defined tones at the speaker end without introducing direct sound from the transmitter end.

One idea spawns many others, and in this case, the spinning perforated wheel gave Bell the idea of investigating the direct conversion of light to sound. He exposed a variety of materials to pulsed light and found that most materials produce sound, an effect he called photophonics. By trial and error, he found that thin plates gave

Figure 1



(a) Bell's photophone; (b) his demonstration of light to sound conversion. Reproduced with permission from NLOsource.com [2].

louder tones than bulk samples and, as a consequence, postulated that the sound was generated at the surface. He made thin sheets of many materials and found that hard rubber produced the loudest sound, followed by antimony and zinc. Paper and mica were found to give the weakest sounds.

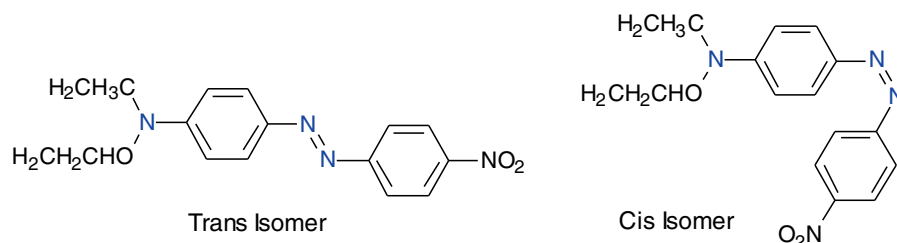
Shortly after Bell's first paper on the photophone, Moser studied the relative importance of electromotive forces and photothermal heating in selenium [3]. As excitement over the photophone waned, so too did the study of the mechanisms of the underlying physical processes.

In addition to the absorption of particle-like photons that cause photomechanical deformations, light is also wave-like. The classical description of light as an electromagnetic wave forces one to pause and ask if lower frequency electromagnetic waves or even static electric (or magnetic) fields can cause material deformations. The answer is yes, though the reverse process of mechanical deformations causing a potential difference across a material was discovered first. A piezoelectric material develops a potential difference between its ends when stressed. The piezoelectric effect was postulated to exist by Jacques and Pierre Curie and experimentally demonstrated in crystals of tourmaline, quartz, topaz, cane sugar, and sodium potassium tartrate tetrahydrate [4]. Quartz and sodium potassium tartrate tetrahydrate were found to have the largest piezoelectric effect, that is, the largest ratio of electric potential difference induced divided by the applied stress.

Gabriel Lippmann predicted in 1881 that a strain can be induced in a piezoelectric material by an applied voltage [5]. The Curies experimentally confirmed this inverse effect [6] and showed that it was reversible. The piezoelectric effect yields a deformation in proportion to the electric field, so light with zero average field is not expected to directly induce a strain. Lagowski and Gatos found that the piezoelectric effect is a critical part of the large photomechanical response of certain crystalline materials [7], which we discuss in more detail below. The modern era of photomechanics was reborn in the early 1970s with the serendipitous discovery by Agolini and Gay that a polymer doped with azo dyes is stressed by light [8]. In their experimental protocol, thin films were typically mounted on a stage. When heated, all other films measured would expand, then become taught when cooled. In contrast, the azo dye samples expanded first upon heating, then contracted over longer time scales, making the film taught at higher temperatures. Light exposure also caused the films to shrink.

Because the molecules are preferentially aligned in the plane of the film, Agolini and Gay argued that contraction originated from trans to cis isomerization, a process in which the shape of the molecule changes in a way that reduces its length along the original long axis of the trans form of the molecule by about 3.5 Å [9]. Azo dyes were known to change their conformation when either heated or excited with light, explaining their observations. Figure 2 shows as an example the azo dye disperse red 1 (DR1) in its two isomeric forms.

Figure 2



Example of the trans and cis isomer in azo dye DR1.

Lagowski and Gatos discovered the photomechanical effect in cadmium sulfide (CdS) semiconductors [7]. They used a xenon lamp, tunable double prism monochromator, and chopper tuned to around 100 Hz—the mechanical resonance frequency of the planar sample in a cantilever geometry. The amplitude of oscillation was determined from the reflected beam of a continuous wave He–Ne laser. The surface voltage was measured from the contact potential difference at 100 Hz using a gold reference electrode.

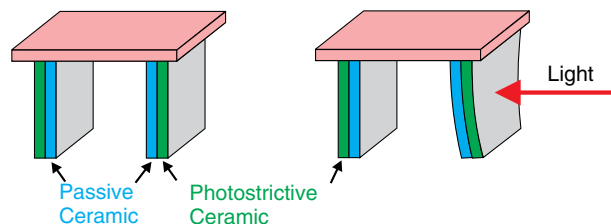
CdS was known to be a piezoelectric semiconductor [10], in which an electric field induces a strain. Lagowski and Gatos argued that the mechanism of the photomechanical effect was tied to the piezoelectric effect in a two-step process. First, the light excites the material and produces a surface photovoltage; then, the field from the surface charge causes a strain through the piezoelectric effect. This mechanism of light-induced electrostriction is called photostriction.

To test their hypothesis, Lagowski and Gatos measured the amplitude of the light-induced vibration as a function of the wavelength of excitation and found that it tracked with the surface photovoltage, confirming the prediction. The amplitude of oscillation was too large to be caused by radiation pressure, and thermal effects were ruled out by the observation that the vibration amplitude changed with pump wavelength when keeping the absorbed energy constant. They correctly predicted that any non-centrosymmetric material—i.e., a material in which no coordinate origin exists that leaves the material unchanged with all coordinates \mathbf{r} are changed to $-\mathbf{r}$ —had the potential for having a large photostrictive effect.

Uchino used the photostrictive mechanism in ceramics to make a walking device as shown in Fig. 3 [11–13]. A photostrictive ceramic and a passive ceramic are fused to enhance the bending effect through differential strain when the active side is illuminated. By pulsing the light source periodically to control the legs' motion, Uchino demonstrated that his device could walk across a planar surface. This was an early demonstration of the photomechanical effect being used in applications where actuators are controlled from a distance using light, circumventing the need to make physical contact with the walker. Additionally, this exercise demonstrated that a device could be powered using a remote light source without inducing electromagnetic interference.

All devices are made from the five canonical device classes as summarized in Fig. 4. Each electronic device class has a photonic counterpart. Fiber optic telecommunications, for example, is a mature technology that has replaced electrical wire in high-speed long distance transmission applications. Fiber optic devices are powered by lasers, another well-developed technology. By virtue of their exquisite sensitivity, light-based sensors built from interferometers [14–17] are the platform of choice,

Figure 3



Uchino Walker is made by fusing an active photostrictive ceramic and a passive ceramic to enhance photomechanical bending. Reproduced with permission from NLOsource.com [2].

especially in explosive environments where electrical sparks cannot be tolerated. Though not a mature technology, all-optical switching systems were demonstrated over two decades ago [18,19].

The conversion of light into mechanical motion is the optical counterpart of the electric motor or piezoelectric positioner, completing the list of canonical device classes. The development of a photomechanical technology would unleash the full power of optics.

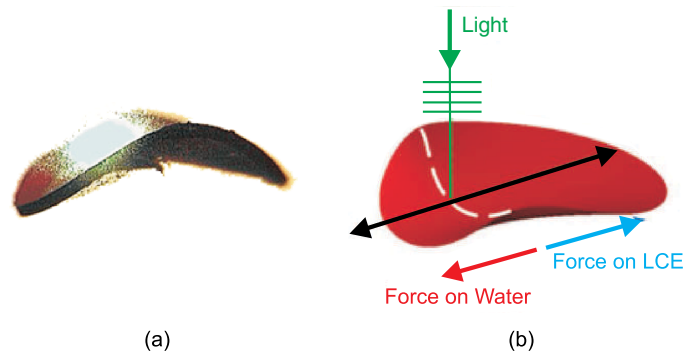
Welker and Kuzyk were the first to demonstrate an all-optical device that embodies all five device classes [21]. This interferometer-based fiber device was shown to actively stabilize the position of a 9 g mass suspended at the end of a 30 cm long photomechanical polymer fiber to within a tolerance of 3 nm even while applying large mechanical impulses to the system. The same device was miniaturized into a 5 mm length fiber with all canonical device classes being simultaneously performed in the same spatial volume, excluding the external laser source [22]. A more detailed description of PODs starts in Subsection 10.1.

Figure 4

	Optics	Electronics
Transmission	Optical Fiber Optical Interconnects	Wires Printed Wire Boards
Sensing	Fiber Interferometer Fluorescent Dyes	Thermistor Transducer
Switching and Logic	Electrooptic Materials Intensity Dependent n	Transistor
Actuation	Photostriction and Photomechanical Effects	Motor Piezoelectrics
Power	Laser	Battery/Power Supply

All devices are made from five device classes. For each electrical device, an optical counterpart has been demonstrated making it possible to construct all-optical devices that can perform any function that an electronics device can perform.

Figure 5



(a) Photograph of the potato-chip-shaped liquid crystal elastomer that swims away from light; (b) the shape is designed for a swimming motion when illuminated with pulsed light from above. Reprinted by permission from Macmillan Publishers Ltd.: M. Camacho-Lopez *et al.*, *Nat. Mater.* **3**, 307–310 (2004) [20]. Copyright 2004.

Camacho-Lopez and coworkers demonstrated the large photomechanical response of a liquid crystal elastomer (LCE) by making a potato-chip-shaped disk that swims away from pulsed light [20]. Figure 5(a) shows a photograph of the swimmer, and Fig. 5(b) shows how the shape results in a swimming motion when exposed to pulsing light from above.

This brings us to the present, when new materials are being developed to enhance the photomechanical response and novel devices are being fabricated to take advantage of these materials, such as the demonstration of a motor powered directly with light [23]. This tutorial and review begins with a description of the mechanisms of the photomechanical effect. It also discusses devices that have already been demonstrated, novel materials that are being deliberately engineered for large light-induced shape changes, and exciting future technologies, such as ultra-smart morphing materials, which will be enabled by photomechanical materials.

2. PHOTOMECHANICAL EFFECTS AND NONLINEAR OPTICS

In this section, we show that there is an intimate relationship between photomechanical phenomena and nonlinear optics. Such a relationship has important implications on the origin of these effects and gives the researcher insights into the design of materials and devices. Since nonlinear optics is a much more mature field, this analogy allows this vast body of literature to be applied photomechanics, so a familiarity of the underlying basis for nonlinear optics provides the reader with a useful tool.

Subsection 2.1 starts by defining the optical path length, then shows how it is symmetric in the refractive index and the length of the material. So a change in one of these properties is analogous to a change in the other one. Subsection 2.2 then defines the response function, which relates the applied stimulus—such as an electric field or light pulse, to the response—such as a change in the dipole moment, refractive index, or length. At this point in the derivation, the form of the response function is left unspecified. To get one requires a specific model of the material. Subsection 2.3 defines the body force, which is typically ignored in many applications of the theory of elasticity. To give the reader insights of how body forces can arise, we treat a uniformly charged material throughout its bulk (imagine charges mixed into an elastic material). We then use this model of a material to show how the response function can be calculated. We stress in Subsection 2.3 that the photomechanical force is a much more complex phenomena to model than the uniformly charged material, and emphasize that we are using this only for illustration and that typical photomechanical materials do not have a uniform charge density. The reader must wait until Section 4 to get a more rigorous derivation of how body forces can arise.

2.1. Optical Path Length

The optical path length is of fundamental importance to optics because its *extremum* determines the path taken by a ray of light between two points [24]. Known as Fermat's principle, it determines the angle of refraction in Snell's law and can be used to determine the focal point of a lens.

The optical path length, L , is defined by

$$L = \int_C n(\vec{r}) dr, \quad (1)$$

where $n(\vec{r})$ is the refractive index at position \vec{r} and C is the path of the ray, which need not be the actual path taken by the light beam. The actual path is determined by the *extremum* of Eq. (1), which is proportional to the transit time along the curve, with

the speed of light in vacuum as the constant of proportionality. The key phenomenon in a photomechanical material is a deformation in response to light. Because both the refractive index and the shape of a material change in response to light, the induced change in optical path length is the general phenomena that encompasses photomechanics via the length change and nonlinear optics via the change in the refractive index. To understand the change in optical path length, a brief diversion is required to explain the characterization of material deformation, and how physical deformations affect the refractive index.

For simplicity, consider a slab of material that is stretched along one of its axes, as shown in Fig. 6(a). If the material is inhomogeneous (its properties vary throughout the bulk like lumpy oatmeal), the strain at a point in the material depends on its location. If two points within a material near point \vec{r} are originally separated by a distance $dz(\vec{r})$ and the same two points are separated by $dz'(\vec{r})$ after deformation, the strain u is defined by

$$u(\vec{r}) = \frac{dz'(\vec{r}) - dz(\vec{r})}{dz(\vec{r})}. \quad (2)$$

The strain is thus the change in length per unit length. If the material is homogeneous, the strain is uniform and given by $u = \Delta\ell/\ell$.

The elasticity, or spring constant k , of a material is defined as the change in length per unit of force applied, or

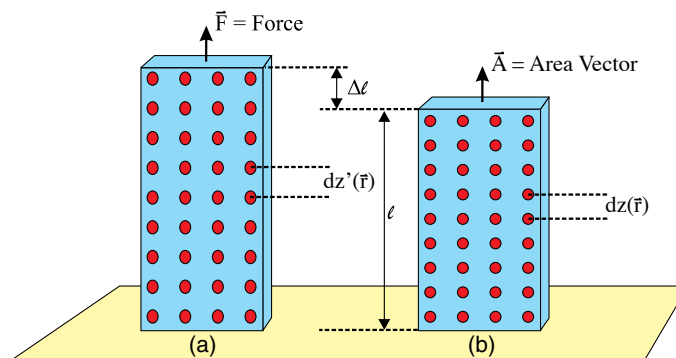
$$F = -k\Delta\ell. \quad (3)$$

The spring constant k , however, is not a fundamental material property because it also depends on the material's shape; for a fixed force, a long strand of material stretches more than a short thick cylinder. Young's modulus E , though, is a material property defined by

$$\sigma = -Eu, \quad (4)$$

where σ is the normal stress, defined as the force per unit of area applied to the material's surface, or $\vec{\sigma} = \vec{F}/A$. Equations (2)–(4) can be used to relate Young's modulus to the spring constant and shape parameters of the sample. For the homogeneous slab shown in Fig. 6, the two are related by

Figure 6



(a) Material stretches when a force is applied at one end. (b) The same material prior to stretching.

$$E = \frac{k\ell}{A}. \quad (5)$$

A measure of the lengths of the three orthogonal edges of the slab and the slab's spring constant yields Young's modulus using Eq. (5). For polymers such as PMMA, $E \approx 3 \text{ GPa} = 3 \times 10^9 \text{ N/m}^2$.

Next, consider the effect of the length change on the refractive index. If the material is of a type that when compressed, its cross-sectional area remains fixed, then the molecules must come closer together in the direction of the strain. If all other parameters remain the same, the higher molecular density will generally result in a higher refractive index, or

$$\frac{\Delta n}{n} = \frac{\Delta \rho}{\rho} = -\frac{\Delta \ell}{\ell}, \quad (6)$$

where ρ is the molecular number density. Using Eq. (4), Eq. (6) becomes

$$\frac{\Delta n}{n} = \frac{\sigma}{E}. \quad (7)$$

Now we are ready to determine the change in the optical path length for a stressed homogenous medium of refractive index n and length ℓ , where the optical path length is given by $L = n\ell$. The change in the optical path length due to stress is then given by

$$\frac{\partial L}{\partial \sigma} = \ell \frac{\partial n}{\partial \sigma} + n \frac{\partial \ell}{\partial \sigma}. \quad (8)$$

Dividing the far left-hand and right-hand sides of Eq. (6) by $\Delta \sigma$ and taking the limit of $\Delta \sigma \rightarrow 0$ yields

$$\ell \frac{\partial n}{\partial \sigma} = -n \frac{\partial \ell}{\partial \sigma}, \quad (9)$$

which when substituted into Eq. (8) yields $\frac{\partial L}{\partial \sigma} = 0$. This should not be surprising since the fractional increase (decrease) in the sample length is the same as the fractional decrease (increase) in refractive index. When a material is compressed, in addition to the density change, the molecular properties also change. Also, materials compressed along one axis can be strained in orthogonal directions. Thus, the two terms will not in general cancel [25,26]. However, even when the refractive index change opposes the length change to yield a fixed optical path length through the sample, such a sample inside one arm of an interferometer will lead to a change in the interferometer output, as follows.

If the interferometer is made of two equal arms of length d in vacuum, the optical path difference between the two is given by

$$\Delta = [(d - \ell) + n\ell] - [d] = (n - 1)\ell, \quad (10)$$

where $(d - \ell)$ is the distance that the light travels in vacuum within the arm that contains the material and the brackets surround the path lengths of the two arms. If the material is stressed, the change in the path difference is

$$\frac{\partial \Delta}{\partial \sigma} = \frac{\partial(n\ell)}{\partial \sigma} - \frac{\partial \ell}{\partial \sigma} = -\frac{\partial \ell}{\partial \sigma}, \quad (11)$$

where the last equality arises from the use of Eq. (9). The net result is that there is a change in the path length difference due to the fact that an increase of the sample length decreases the distance that the light travels in the vacuum by an amount $-\delta\ell$.

The refractive index change can be described with a simple phenomenological model, which in the scalar approximation is given by

$$\Delta n = C\sigma, \quad (12)$$

where C is the stress-optic coefficient and σ the stress. Equation (12) is the simple statement of the fact that when one stresses a material by squeezing on it, the refractive index changes in proportion to the stress and C is a property of the material.

In real materials, the squeezing on a material in one direction can change the refractive index that the light experiences for a polarization in a different direction. In this case, Eq. (12) takes the form

$$\Delta n_i = C_{ij}\sigma_j, \quad (13)$$

where C is the stress-optic tensor, σ_j is the stress from a force applied along direction j , and Δn_i is the change in the refractive index along direction i . Note that we are using summation convention, where the repeated index (j in this case) is summed over the Cartesian components of the second index of the tensor C . We use summation convention throughout this paper, where the summation spans the variable's domain.

In real life, the stress is a second rank tensor, as is the refractive index. The tensor properties of the stress are formally described in Appendix C. For now, the important phenomena that the reader should understand is that the refractive index of a material changes when a force is applied to it. For completeness, we state the most general form of the photoelastic effect, which is of the form

$$\Delta n_{ij} = C_{ijkl}\sigma_{kl}. \quad (14)$$

If the stress in a material is anisotropic, as it is in the vicinity of a stress point (for example, at a sharp tip pressing the surface of an object), the refractive index too will become anisotropic. As a result, the polarization of a light beam will be rotated in the material in proportion to the path length and the birefringence. Brewster discovered this phenomena in 1815 [27,28], which is called the photoelastic effect. The rotation of the polarization vector, $\delta\Phi$, is given by

$$\delta\Phi = \frac{2\pi}{\lambda}\ell C\delta\sigma, \quad (15)$$

where $\delta\sigma$ is the difference in stress between the two orthogonal polarizations, ℓ is the sample thickness, C is the stress-optic coefficient, and λ is the wavelength. The difference in optical path length of the two orthogonal polarizations follows as $\Delta L = \ell C\delta\sigma$.

The photoelastic effect is used to determine the stress distribution in a material. Figure 7 shows a white light photograph taken through crossed polarizers of utensils made with biodegradable materials. The color patterns can be used to map the stress distribution within the material, in this case, caused by the manufacturing process.

Equation (6) brings up an interesting point with regards to the relationship between the optical and mechanical properties of a material. Each underlying mechanism that alters the refractive index will also affect the local strain, and in aggregate, the bulk dimensions. Note that the delicate balance implied by Eq. (6) will in general not hold,

but light-induced changes of refractive index and length change are still related, albeit in a more complex way.

The relationship between length change and refractive index change is a material property. In ray optics, the fundamental principal that governs the optical path length also depends symmetrically on refractive index and length change. As such, length change and refractive index change are intimately related quantities. We can use this relationship to more deeply understand the mechanisms.

The light-induced change of the refractive index of a material is the subject of nonlinear optics, a field that in its modern incarnation spans several decades of intense research. This large body of knowledge can be applied to photomechanics. The microscopic origin of fast linear and nonlinear-optical phenomena is in the induced dipole moment in response to an electric field. Recall that a dipole moment is a product of the charge and displacement, so it changes with the redistribution of charge or in their relative positions. The fact that the dipole moment is the source of the refractive index implicitly makes it dependent on a length scale. As such, the relationship between refractive index and length persists to nanoscopic scales.

2.2. Response Functions

The bulk nonlinear-optical properties of a material are determined from the induced dipole moment per unit volume—called the polarization, \vec{P} , which for small applied fields, can be expanded in a series of the form

$$P_i(t) = P_i^{(0)} + \sum_{n=1}^{\infty} P_i^{(n)}(t), \quad (16)$$

where n is the order of the nonlinearity. The n^{th} -order polarization is of the form

$$P_i^{(n)}(t) = \int_{-\infty}^{+\infty} d\tau_1 \int_{-\infty}^{+\infty} d\tau_2 \dots \int_{-\infty}^{+\infty} d\tau_n R_{ijk\dots}^{(n)}(t; \tau_1, \tau_2, \dots, \tau_n) E_j(\tau_1) E_k(\tau_2) \dots, \quad (17)$$

Figure 7



White light photograph of biodegradable plastic utensils through crossed polarizers. The color patterns trace the stress in the material, which is imparted in the molding process [29].

and it is proportional to the product of n electric fields and the response function $R^{(n)}$, which is an $(n + 1)$ th-rank tensor.

The response function depends on the properties of the material. This section investigates its general properties. Models of the response function are left for latter sections. Subsection 2.3b illustrates how such models are built for body forces induced by an electric field on a material embedded with a uniform charge density as a pedagogical tool. The more complex calculations of the mechanical response of matter to light starts in Subsection 4.1.

Equation (17) states that the induced polarization at a given time is related to all applied electric fields at all previous times. The source of this nonlocality in time is in the response of the material, and it is most pronounced when the electric fields change rapidly compared with the response time of the material. For an instantaneous material response, the response function takes the form of a Dirac delta function, making the induced dipole at any particular time coincident with the applied field at that time. The tensor nature of the response function leads to induced dipoles aligned in a direction that is not collinear with the applied fields. The nonlinear terms imply that several fields acting in different directions can together give a response in a particular direction depending on the response tensor of the material.

Equation (17) ignores a response at one point in a material that depends on the fields at other points in the material. Such a spatially nonlocal response can be handled by augmenting the response function and electric fields with spatial coordinates in addition to time, and integrating over each spatial coordinate. In many nonlinear processes, such as harmonic generation, most common materials respond locally in space.

Similarly, the change in length of a material can be expressed as a series in the electric field. The length of a material along a single direction is given by

$$\ell(t) = \ell^{(0)} + \sum_{n=1}^{\infty} \ell^{(n)}(t), \quad (18)$$

where n is the order of the length change.

A mechanical system is inherently nonlocal in time. For example, an impulse applied to a bell results in a tone with decaying volume long after the impulse is gone. Similarly, a pulse of light applied to one point within the material can cause it to “ring” long after the light is gone, and the disturbance can affect parts of the material that were never illuminated. As such, the photomechanical response of the material will be nonlocal in time and space.

In analogy to Eq. (17), the n th-order strain in the i th direction at time t and at point \vec{r} in a material is related to the electric field according to

$$u_i^{(n)}(t, \vec{r}) = \frac{\Delta \ell_i^{(n)}}{\ell_i^{(n)}}(t, \vec{r}) = \int_{-\infty}^{+\infty} d\tau_1 \dots \int_{-\infty}^{+\infty} d\tau_n \int_{-\infty}^{+\infty} d^3\vec{r}_1 \dots \int_{-\infty}^{+\infty} d^3\vec{r}_n R_{ijk\dots}^{(n)}(t; \vec{r}; \tau_1, \dots, \tau_n; \vec{r}_1, \dots, \vec{r}_n) E_j(\tau_1, \vec{r}_1) E_k(\tau_2, \vec{r}_2) \dots, \quad (19)$$

where $R^{(n)}$ is the n th-order response function that has nonlocality built into it.

Equation (19) is a daunting expression, especially if one’s goal is an understanding of how an electric field leads to a strain. Working out some simple examples in limiting cases of Eq. (19) serves as a good pedagogical tool.

First, let us consider the tensor nature of the response function. Simply stated, $R_{ijk\dots}$ describes the magnitude of the strain for electric fields applied in the i, j, k, \dots directions. For example, Fig. 8 shows an electric field applied in the y direction that induces strains along $x, y,$ and z . The strain along the x axis, u_x , due to a field component along the y axis, E_y , is proportional to $R_{xy\dots}E_y \dots$

The order of the response function, n , describes the process when a number of fields must interact together to lead to a strain. For example, the strain along the x axis, u_x , due to a field component along the y axis, E_y , for a third-order response function is proportional to $R_{xyyy}^{(3)}E_y^3$. Since it is possible for fields of orthogonal polarizations to lead to a strain in any direction, terms such as $R_{xyzx}^{(3)}E_yE_zE_x$ describe the strain along x due to three fields along the x axis, y axis, and z axis acting together. All orders of nonlinearity are possible, leading to terms such as $R_{xyyzxxx}^{(6)}E_y^2E_zE_x^3$.

More often than not, researchers are interested in the linear response characterized by $R^{(1)}$, and experiments are designed to measure the strain along or perpendicular to the applied electric field E_z , so only $R_{zz}^{(1)}$ and $R_{xz}^{(1)}$ may be of interest. In such special cases, the theory can be formulated more simply in terms of scalar quantities.

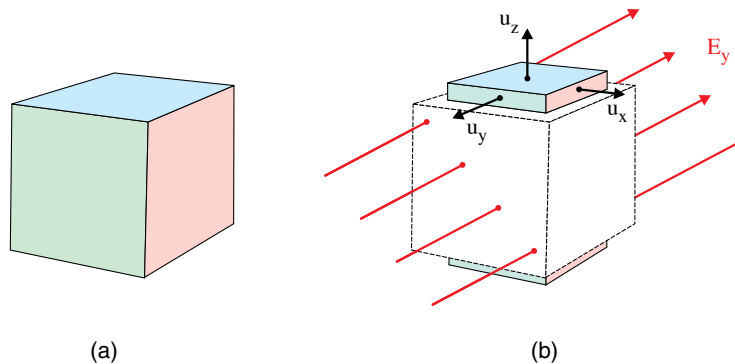
Nature obeys causality, meaning that cause precedes effect. As such, a material cannot deform before an electric field or stress is applied. Furthermore, the effect should always be the same for a fixed time after the cause. Applying these conditions to the response function requires that it depend only on differences between the time at which the field is applied and the response time, or rather, when it is of the form $R_{ijk\dots}^{(n)}(t - \tau_1, \dots, t - \tau_n)$. The response function vanishes when causality is violated—i.e., when at least one of its arguments is negative.

Next, let us consider an infinitesimal piece of material, where there is no surrounding material with which it can interact. Then, spatial nonlocality can be ignored. Under this assumption, and demanding causality, Eq. (19) becomes

$$u_i^{(n)}(t) = \int_{-\infty}^t d\tau_1 \dots \int_{-\infty}^t d\tau_n R_{ijk\dots}^{(n)}(t - \tau_1, \dots, t - \tau_n) E_j(\tau_1) E_k(\tau_2) \dots, \quad (20)$$

where the limits of integration are over a range of times that obey causality. Equation (20) allows us to focus on the time response. Spatially nonlocality can be similarly separated from the response time by assuming the material response to be instantaneous.

Figure 8



(a) Original volume element and (b) the same element when deformed by an electric field. The white box shows the original element for comparison.

Consider as an example a material with only a linear response function, $R^{(1)}(t)$, where the tensor properties can be ignored if the strain is always aligned with the electric field direction. If the electric field E_0 is applied as a short burst that remains for a time Δt and centered at $\tau = 0$, the strain will be given by

$$u^{(1)}(t) = \int_{-\infty}^t d\tau R^{(1)}(t - \tau) E(\tau) \approx R^{(1)}(t) E_0 \Delta t, \quad (21)$$

where we have assumed that Δt is of very short duration. Note that $E_0 \Delta t$ is analogous to an impulse, which is given by $F \Delta t$, where F is the force. Note that because $F = qE$, where q is the charge of the infinitesimal section of material, $E_0 \Delta t$ is proportional to the impulse. Equation (21) shows that the response function is the strain per unit electric field impulse as a function of time after the impulse has been applied. As such, a material's response function can be characterized by applying an impulse that is much shorter than any characteristic response time of the material and observing the time evolution of the strain.

We can recast an impulse in the form of a Dirac delta function by recognizing that the result would be the same if we chose the electric field impulse to be given by $E(t) = E_0 \Delta t \delta(t)$. From this point on, an electric field impulse of duration Δt will be expressed in this delta function form. Note that the Dirac delta function has dimensions that are the reciprocal of the argument's dimensions, e.g., $\delta(t)$ has dimensions of inverse time. The formulation of the response function up to this point is in the time domain and applicable to experiments where the time evolution of the strain is measured in response to a time-dependent electric field. For the specific case of sinusoidal varying electric fields, the frequency domain is more convenient. Considering again the linear strain in scalar form, the frequency domain response can be determined by Fourier transform, according to

$$\begin{aligned} \tilde{u}^{(1)}(\omega) &= \frac{1}{2\pi} \int_{-\infty}^{+\infty} dt \exp[-i\omega t] u^{(1)}(t) \\ &= \frac{1}{2\pi} \int_{-\infty}^{+\infty} dt \exp[-i\omega t] \int_{-\infty}^{+\infty} d\tau R^{(1)}(t - \tau) E(\tau). \end{aligned} \quad (22)$$

Regrouping terms in Eq. (22) so that the τ integral is done last, we get

$$\tilde{u}^{(1)}(\omega) = \frac{1}{2\pi} \int_{-\infty}^{+\infty} d\tau E(\tau) \exp[-i\omega\tau] \int_{-\infty}^{+\infty} dt \exp[-i\omega(t - \tau)] R^{(1)}(t - \tau). \quad (23)$$

Defining

$$\tilde{R}^{(1)}(\omega) = \int_{-\infty}^{+\infty} d(t - \tau) \exp[-i(t - \tau)] R^{(1)}(t - \tau), \quad (24)$$

Eq. (23) becomes

$$\tilde{u}^{(1)}(\omega) = \tilde{R}^{(1)}(\omega) \frac{1}{2\pi} \int_{-\infty}^{+\infty} d\tau \exp[-i\omega\tau] E(\tau) = \tilde{R}^{(1)}(\omega) \tilde{E}(\omega), \quad (25)$$

or

$$\tilde{u}^{(1)}(\omega) = \tilde{R}^{(1)}(\omega) \tilde{E}(\omega). \quad (26)$$

We note here that the Fourier transform of the electric field $\tilde{E}(\omega)$ has dimensions of electric field impulse, the Fourier transform of the strain, $\tilde{u}^{(1)}(\omega)$, has dimensions of strain multiplied by time, and the Fourier transform of the response function $\tilde{R}^{(1)}(\omega)$ has dimensions of the response function in the time domain multiplied by time.

A monochromatic electric field of the form

$$E(t) = \frac{1}{2}(E^{\omega_1} e^{-i\omega_1 t} + E^{-\omega_1} e^{+i\omega_1 t}), \quad (27)$$

where E^{ω_1} is the complex field amplitude with complex conjugate $E^{\omega_1*} = E^{-\omega_1}$, has Fourier transform

$$\tilde{E}(\omega) = \frac{1}{2\pi} \int_{-\infty}^{+\infty} dt E(t) e^{-i\omega t} = \frac{1}{2}(E^{\omega_1} \delta(\omega - \omega_1) + E^{-\omega_1} \delta(\omega + \omega_1)). \quad (28)$$

The Fourier transform $\tilde{E}_j(\omega)$ in Eq. (28) is thus a function of ω that peaks at $\pm\omega_1$ and has units of electric field multiplied by time. The strain can be transformed in the same way, yielding

$$\tilde{u}(\omega) = \frac{1}{2\pi} \int_{-\infty}^{+\infty} dt u(t) e^{-i\omega t} = \frac{1}{2}(u^{\omega_1} \delta(\omega - \omega_1) + u^{-\omega_1} \delta(\omega + \omega_1)). \quad (29)$$

Substituting Eqs. (29) and (28) into Eq. (30) yields

$$u^{(1)\pm\omega_1} = R^{(1)}(\pm\omega_1) E^{\pm\omega_1}. \quad (30)$$

Thus, the field amplitude is related to the strain amplitude in the same way as in Eq. (30), but here $E^{\pm\omega_1}$ is the field amplitude and has dimensions of electric field. In contrast, $\tilde{E}(\omega)$ is the Fourier transform of the electric field with dimensions of electric field multiplied by time.

We have arbitrarily defined the response function to relate the applied electric field to the strain. An equally good choice would have been to define a response function that relates the electric field to the stress. We thus have the freedom of choosing the most convenient response function for the task at hand.

Next we consider the second-order response function in scalar form. For an electric field given in the form of a delta function impulse at $t = 0$, or $E(t) = E_0 \Delta t \delta(t)$, Eq. (20) becomes

$$u^{(2)}(t) = \int_{-\infty}^t d\tau_1 \int_{-\infty}^{\tau_1} d\tau_2 R^{(2)}(t - \tau_1, t - \tau_2) E_0^2 (\Delta t)^2 \delta(\tau_1) \delta(\tau_2) = R^{(2)}(t, t) (\Delta t)^2 E_0^2. \quad (31)$$

Thus, $R^{(2)}(t, t)$ describes the strain as a function of time after an electric field impulse is applied at $t = 0$. $R^{(2)}(t, t)$ has dimensions of strain divided by the square of the applied electric field impulse.

The second-order material response quantifies the strain induced by two fields that act together. To get a better sense of its meaning, consider a response function of the form

$$R^{(2)}(t - \tau_1, t - \tau_2) = R_0^{(2)} \exp[-\alpha(t - \tau_1)] \exp[-\alpha(t - \tau_2)], \quad (32)$$

which simply states that the material response decays at a rate α after the field is turned off. For an electric field made of two pulses separated in time by δt ,

$$E(t) = E_1 \Delta t \delta(t) + E_2 \Delta t \delta(t - \delta t), \quad (33)$$

Eq. (20) becomes

$$\begin{aligned} u^{(2)}(t) = & \int_{-\infty}^t d\tau_1 \int_{-\infty}^t d\tau_2 R_0^{(2)} \exp[-\alpha(t - \tau_1)] \cdot \exp[-\alpha(t - \tau_2)] \\ & \times (E_1 \delta(\tau_1) + E_2 \delta(\tau_1 - \delta t)) \cdot (E_1 \delta(\tau_2) + E_2 \delta(\tau_2 - \delta t)), \end{aligned} \quad (34)$$

which yields

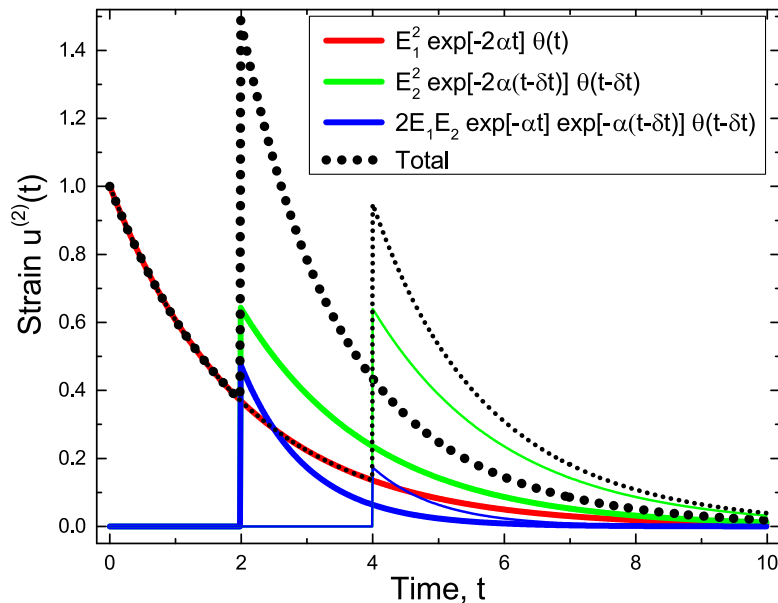
$$\begin{aligned} \frac{u^{(2)}(t)}{R_0^{(2)}} = & E_1^2 \exp[-2\alpha t] \theta(t) + E_2^2 \exp[-2\alpha(t - \delta t)] \theta(t - \delta t) \\ & + 2E_1 E_2 \exp[-\alpha t] \exp[-\alpha(t - \delta t)] \theta(t) \theta(t - \delta t), \end{aligned} \quad (35)$$

where the step function $\theta(t)$ reminds us of causality.

The first two terms on the right-hand side of Eq. (35) are the contributions to $u^{(2)}(t)$ from each of the two pulses individually, as given by Eq. (31). As such, it is the sum of two decaying exponentials, one that starts after the first pulse arrives and one that starts after the second pulse arrives. The cross term is a product of the two pulses, and therefore vanishes if one pulse or the other is not present.

Figure 9 illustrates the contributions to the response function for $\delta t = 2$ (thick curves) and $\delta t = 4$ (thin curves). Note that the curve for $E_1^2 \exp[-2\alpha t] \theta(t)$ (red) is the same in both cases. The contributions from each of the individual pulses is of the same amplitude and time constant in both cases. However, the amplitude of the cross term is lower when the two pulses are further apart—scaling in proportion to the exponent of the time difference $\exp[-\alpha \delta t]$.

Figure 9



Contributions to the response function (black dots) from each pulse (red and green curves) and from the cross term between pulses (blue). The thick curves are for $\delta t = 2$ and the thin curves for $\delta t = 4$.

One can imagine in the case of a third-order response function that the strain has contributions from three individual pulses, pairs of pulses, and products of all three pulses. The n^{th} -order response function is thus best understood by considering the mixing of n pulses.

We can also take the Fourier transform of Eq. (20) to get the frequency response. Defining

$$\tilde{R}_{ijk}^{(2)}(\omega_1 \pm \omega_2; \omega_1, \omega_2) = \int_{-\infty}^{+\infty} d\tau_1 \int_{-\infty}^{+\infty} d\tau_2 \exp[-i\tau_1] \exp[-i\tau_2] R_{ijk}^{(2)}(\tau_1, \tau_2), \quad (36)$$

the Fourier transform of Eq. (20) yields

$$\tilde{u}_i^{(2)}(\omega_1 \pm \omega_2) = \sum_{jk} \tilde{R}^{(2)}(\omega_1 \pm \omega_2; \omega_1, \omega_2) \tilde{E}_j(\omega_1) \tilde{E}_k(\omega_2). \quad (37)$$

The frequency domain response function $\tilde{R}_{ijk}^{(2)}(\omega_1 \pm \omega_2; \omega_1, \omega_2)$ shows that the strain will oscillate at sum and difference frequencies of the applied electric fields. As such, $\tilde{R}_{ijk}^{(2)}(\omega_1 \pm \omega_2; \omega_1, \omega_2)$ can be measured by applying sinusoidal fields at two frequencies and measuring the strain response at the sum or difference frequencies. Higher-order response functions can also lead to sum and difference frequency strain response, so the second-order response function can be isolated at low field amplitude where the strain amplitude $u_i^{(2)\omega_1 \pm \omega_2}$ is proportional to the product of the two field amplitudes, $E_j^{\omega_1} E_k^{\omega_2}$. A field at the single frequency ω will produce a strain at 2ω (sum frequency) or a static strain (difference frequency).

Equations (36) and (37), which include the tensor nature of the response, can be easily generalized to higher-order response functions by inspection. Note that we have assumed $\omega_1 > \omega_2$.

2.3. Body Forces

In this section, we consider the influence of body forces and how they contribute to the response function. We start with a simple pedagogical model that ignores complications such as nonlinearity and orthogonality between the applied electric field and the induced strain, then treat more complex examples that are relevant to geometries typical in experiments.

2.3a. Thin Infinite Rod

Consider an infinitely long but thin rod made of a homogenous material in which longitudinal mechanical waves are described by the wave equation

$$\frac{1}{c^2} \frac{\partial^2 u}{\partial t^2} = \frac{\partial^2 u}{\partial y^2}, \quad (38)$$

where y is the coordinate along the length of the rod, u is the strain along y , and c is the speed of the mechanical wave. Since all of the action is along the y direction, all of the parameters are represented in scalar form.

The speed of the mechanical wave is proportional to Young's modulus; but, for the purposes of this calculation, c will be considered a given value. We also assume a dispersion relationship $\omega = ck$ so that Eq. (38) already presupposes that the speed of the wave is independent of the frequency. As such, any function of the form

$$u(y, t) = f(y \pm ct) \quad (39)$$

is the most general solution of Eq. (38), where $f(x)$ is an arbitrary function. Therefore, a mechanical pulse of arbitrary shape will retain its shape as it propagates down the rod. $\pm c$ corresponds to the two independent solutions: a wave traveling to the left and a wave traveling to the right.

The most general solution is a superposition of two waves of arbitrary shape traveling in opposite directions,

$$u(y, t) = f(y - ct) + g(y + ct). \quad (40)$$

The velocity is then given by

$$\dot{u} \equiv \frac{\partial u(y, t)}{\partial t} = c(-f'(y - ct) + g'(y + ct)), \quad (41)$$

where $f'(x) \equiv \partial f(x)/\partial x$. If the cylinder is stressed and then quickly released so that it starts from rest at $t = 0$ such that $\dot{u}(y, 0) = 0$, then clearly $-f'(y) + g'(y) = 0$, and the general solution is then given by

$$u(y, t) = \frac{1}{2}(f(y - ct) + f(y + ct)), \quad (42)$$

where $f(y, 0)$ is the strain as a function of x at $t = 0$.

Now we are ready to use the above results to study how Eq. (19) is used by applying it to the infinite rod. It is worth repeating the fact that the response function describes how a material reacts to an electric field impulse, so we start by expressing the field as a delta function in space and time,

$$E = E_0 \Delta y \Delta t \delta(t' - t_0) \delta(y' - y_0), \quad (43)$$

where the pulse is applied at position y_0 at time t_0 . Note that the electric field is along y , so all vectors are in the same direction, making all quantities scalars.

Using the electric field given by Eq. (43), Eq. (19) becomes

$$u(y, t) = \Delta y \Delta t \int_{-\infty}^t dt' \int_{-\infty}^{+\infty} dy' R^{(1)}(y - y', t - t') E_0 \delta(t' - t_0) \delta(y' - y_0), \quad (44)$$

where causality demands that $t' \leq t$; hence, the upper limit of the integral cuts off at time t . Evaluating Eq. (44), the strain is

$$u(y, t) = E_0 \Delta y \Delta t R^{(1)}(y - y_0, t - t_0). \quad (45)$$

If the electric field impulse given by Eq. (43) induces a strain at $t = 0$ of the form

$$u(y, 0) = E_0 \Delta y \Delta t R_0 \delta(y - y_0), \quad (46)$$

where R_0 is the strength of the photomechanical response, Eq. (42) gives the time evolution of the strain as

$$u(y, t) = \frac{1}{2} E_0 \Delta y \Delta t R_0 (\delta[y - y_0 - c(t - t_0)] + \delta[y - y_0 + c(t - t_0)]). \quad (47)$$

Comparing Eqs. (45) and (47), the response function is given by

$$R^{(1)}(y - y_0, t - t_0) = \frac{1}{2} R_0 (\delta[y - y_0 - c(t - t_0)] + \delta[y - y_0 + c(t - t_0)]). \quad (48)$$

The strain induced in a long thin rod by an electric field of arbitrary time dependence and spatial variation along the rod to first order in the field is determined from the first term in Eq. (19), or

$$u(y, t) = \int_{-\infty}^{+\infty} dt' \theta(t-t') \int_{-\infty}^{+\infty} dy' R^{(1)}(y-y', t-t') E(y', t'), \quad (49)$$

where for convenience, we enforce causality using $\int_{-\infty}^t dt' \rightarrow \int_{-\infty}^{+\infty} dt' \theta(t-t')$. Substituting Eq. (48) into Eq. (49) yields

$$u(y, t) = \frac{R_0}{2} \int_{-\infty}^{+\infty} dt' \theta(t-t') [E(y-c(t-t'), t') + E(y+c(t-t'), t')], \quad (50)$$

where the delta function eliminates the integration with respect to position.

Below are examples for two different applied field profiles to illustrate how the response function is used to determine the strain in an infinite, dispersionless rod. Another example shows how clamped boundary conditions are treated using d'Alembert's method. Finally, the Fourier transform method is described as an approach for treating a rod with dispersion.

Electric field impulse

Consider an impulse applied at $t = 0$ to the interval $0 < y < a$, represented by

$$E = E_0 \Delta t \delta(t) \theta(y) \theta(a-y), \quad (51)$$

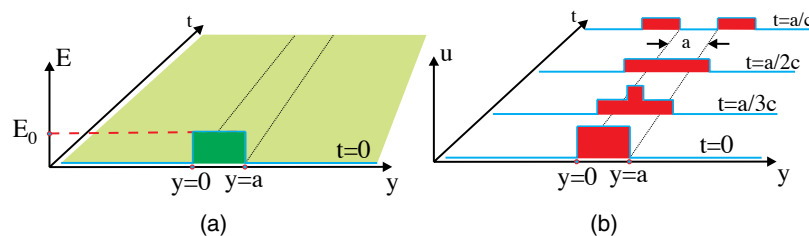
where $\theta(t)$ is the Heaviside step function. Figure 10(a) shows the electric field impulse in the (y, t) plane.

Substituting Eq. (51) into Eq. (50) gives

$$\begin{aligned} u(y, t) &= \frac{E_0 \Delta t R_0}{2} \int_{-\infty}^{+\infty} dt' \theta(t-t') \delta(t') [\theta(y-c(t-t')) \theta(a-\{y-c(t-t')\}) \\ &\quad + \theta(y+c(t-t')) \theta(a-\{y+c(t-t')\})] \\ &= \frac{E_0 \Delta t R_0}{2} \theta(t) [\theta(y-ct) \theta(a-\{y-ct\}) + \theta(y+ct) \theta(a-\{y+ct\})]. \end{aligned} \quad (52)$$

Figure 10(b) shows a plot of Eq. (52), which corresponds to two rectangular pulses that overlap at $t = 0$ and travel in opposite directions at velocity c . This is the form required by Eq. (42).

Figure 10



(a) Electric field impulse and (b) the strain as a function of position and time.

Step electric field

Consider an electric field that is turned on at time $t = 0$ and is applied to the point $y = 0$, or

$$E = E_0 \Delta y \delta(y) \theta(t). \tag{53}$$

Substituting Eq. (53) into Eq. (50) gives

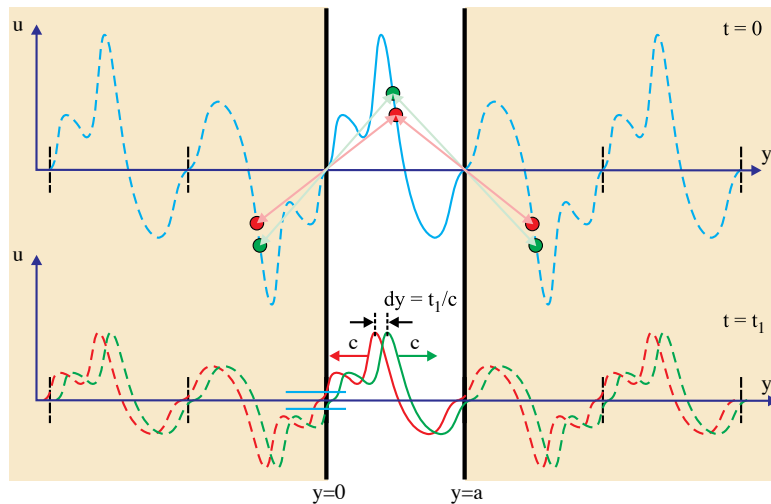
$$u(y, t) = \frac{E_0 \Delta y R_0}{2} \left[\theta\left(\frac{y}{c}\right) \theta\left(t - \frac{y}{c}\right) + \theta\left(-\frac{y}{c}\right) \theta\left(t + \frac{y}{c}\right) \right]. \tag{54}$$

The first step function in each term of Eq. (54) comes from the causality step function. It restricts the first term to the half-space $y > 0$ —where the wave is traveling to the right, and the second term to the half-space $y < 0$ —where the wave is traveling to the left. In each case, the strain jumps to $E_0 \Delta y R_0 / 2$ at coordinates $\pm |y|$ at time $t > |y|/c$, the time it takes the wave to reach that point from the origin, where the field is applied.

Rod with clamped ends

In the previous examples, the rod was assumed infinite. For a finite rod, reflections from the ends will propagate back into the rod. This case can be treated using a simple trick where the finite rod can be viewed as a finite piece of an infinite rod that meets the required boundary conditions.

Figure 11



Top, plot of the strain as a function of position for a rod clamped at its ends at $y = 0$ and $y = a$. The solid blue curve shows the strain, and the dashed blue curve shows the extension of the plot using the criteria that the continuation be centrosymmetric about the boundaries. The light red arrows indicate two points between the walls and their centrosymmetric counterparts outside. Bottom, the blue curve is split into two equal amplitude waveforms that propagate in opposite directions. The sum of the two curves (green and red) gives the time dependence of the strain. Note that the boundary conditions are preserved because the sum of the two curves vanishes at the boundary at all times.

If the rod is clamped at both ends, the strain vanishes there. For illustration, consider a photomechanical impulse that leads to the waveform as shown in Fig. 11. The white region with the blue waveform on the top plot is the initial strain profile.

D'Alembert's solution is used to solve for the time dependence of the strain by finding a solution for an infinite rod that matches the boundary conditions imposed by the finite rod. Because this solution obeys the wave equation and the boundary conditions, it is the unique solution to the problem.

The first step is to make the waveform periodic by extending it using the criterion that the curve be centrosymmetric with respect to the wall; that is, for every point on the curve between the walls (solid blue curve), draw a line from that point to the wall, and extend it the same length to the other side of the wall, going through the rod's contact point with the wall. This line should lie on the extended curve (dashed blue lines). The light red arrows show where the red dots within the rod are mapped into two points, one on each side the rod. The green points and arrows show another part of the curve. The same process is repeated at each new virtual boundary to generate an infinite waveform. Note that a simple way to visualize the process is to imagine two mirror reflections at the boundary. First determine the mirror image of the waveform about the vertical boundary (u axis), then get the mirror image about the y axis.

Next, express the solution as a sum of left- and right-going waveforms, each with half the amplitude of the original extended waveform, as shown at a later time t_1 by the red and green curves on the bottom portion of Fig. 11. Note as the waveforms propagate, the sum of the two always vanishes at the boundary. This feature is built into the procedure by the requirement of a center of inversion at each boundary.

The final step requires us to apply the above periodic boundary conditions to generalize the response function given by Eq. (48). Recall that the response function describes the result of a delta function impulse and Eq. (48) shows that two counter-propagating delta functions are emitted from the point where the field interacts with the rod. For the clamped case, we see that a series of alternating inverted waveforms must be added in the extended space. For the case of delta functions, then, each interval will contain a delta function that is inverted relative to its two neighbors. As such, Eq. (48) becomes

$$R^{(1)}(y - y_0, t - t_0) = \frac{1}{2} R_0 \sum_{n=-\infty}^{\infty} (-1)^n \times [(\delta[y - y_0 + na - c(t - t_0)]) + \delta[y - y_0 + na + c(t - t_0)]], \quad (55)$$

where a is the interval size and $n = 0$ in the sum corresponds to the interval containing the rod.

Rod with dispersion

The speed of a mechanical wave might depend on its frequency, a property called dispersion. Dispersion can be represented by a relationship between the wave vector k and the angular frequency ω . For example,

$$\omega = c(\omega)k \quad (56)$$

is a dispersion relationship, where $c(\omega)$ is the speed of a wave of frequency ω . Equation (56) makes intuitive sense because $k = 2\pi/\lambda$ and the frequency corresponds to the number of times a peak of the sinusoidal wave passes a reference point. Since the peaks are separated by a wavelength, the speed of the wave is given by $c(\omega) = \omega/k$, which is just Eq. (56).

In these cases, it is more convenient to work in the frequency domain of the response function, given by Eq. (30). Equation (30) can be generalized to allow for both nonlocality and delayed response, and takes the form

$$\tilde{u}^{(1)}(\omega, k) = \tilde{R}^{(1)}(\omega, k) \tilde{E}(\omega, k). \quad (57)$$

For the case of a single monochromatic wave, Eq. (56) can be expressed in analogy with Eq. (30) as

$$u^{(1)(\pm\omega, \pm k)} = R^{(1)}(\omega, k) E^{(\pm\omega, \pm k)}. \quad (58)$$

Experimental determination of the response function requires that an electric field of only a single wavelength and frequency be applied. The amplitude $E^{(\pm\omega, \pm k)}$ results in an amplitude of the strain response $u^{(1)(\pm\omega, \pm k)}$. The ratio of the two, according to Eq. (58), yields the response function at that frequency and wavelength. To determine the response function in the space-time domain, this measurement must be repeated for all frequencies and then reverse Fourier transformed.

The techniques described above use special cases to illustrate how the strain response to an electric field is calculated through a response function. In the next section, we consider a material model that shows an example of the mechanisms of a length change and how body forces play a role.

Before moving on, we first need to take a small detour to discuss two equivalent views of nonlocal body forces that can be treated in two very different but equivalent ways. The choice of method used is typically made based on which approach is simpler.

Consider two distinct points within a photomechanical material labeled a and b . When an applied electric field encompasses both points, each part of the material will be strained in proportion to the strength of the field. The local contribution to the response function at point a is simply the strain at point a divided by the electric field at point a . However, the electric field at point b can induce a dipole moment there, which results in an electric field that can act back on point a .

The above scenario can be treated in two ways. The first and more common approach is to define the applied electric field at point a to be the *local* electric field. This is the field measured at point a due to all sources. In our example, the local field is given by the sum of the applied field and the dipole field due to point b . Both fields are proportional to the externally applied electric field so the local field will be given by the applied field times a factor that depends on the distance between points a and b , and the polarizability of the material—i.e., the magnitude of the induced dipole moment per unit applied field. Since light travels so much faster than a mechanical wave, we can ignore the time delay of the field at a due to b . However, the phase difference between the externally applied field and the induced dipole field can lead to interference effects that need to be taken into account if the distance between points a and b is comparable to or larger than the wavelength of the applied optical field. Usually, the dipole fields die down substantially over a wavelength, avoiding interference effects.

The problem is complicated by the fact the contributions of all other points in the material need to be included. In addition, the field from point a can induce a dipole at point b , which then induces a dipole at point a , and so on ad infinitum. Posed this way, the problem may appear to be messy, but miraculously, it is often easy to treat using self-consistent local field models [30]. In the case of induced dipoles in a rod for a field applied along the rod's axis, the sum total field in the material from all the dipoles is uniform and is proportional to the applied field. The constant of proportionality depends on the dielectric constant of the material.

To summarize the first approach, the local electric field at a point in the material is determined from a local field model that depends on the material's dielectric properties and its shape. The electric field used in the response function integral is understood to be the local field, which includes contributions from surrounding induced dipoles. The examples treated above are amenable to this approach.

In the second approach, the electric field used in the response function integrals is the applied electric field. In this case, the effective local field factors f are embedded in the response function. The two approaches are obviously equivalent since $R(fE) = (fR)E$.

Another complication that is usually ignored because its effects are small is the interplay between the electric field and the strain. If the strain in one part of the material is transmitted to another part via a mechanical wave, and if the mechanical wave induces a change in the electric field, the coupling between the field and the strain can lead to complex behavior that is difficult to model. While such effects are often higher-order corrections, if one is studying a nonlinear process such as the deformation due to the action of two fields through the second-order response function $R^{(2)}$, it is possible that coupling between a mechanical wave and the field in a first-order process can contribute to the second-order one.

Suffice it to say that local field models are complex and each specific system needs to be treated with great care to make certain that everything is taken into account. In this paper, we stick to the simplest cases and concentrate on the fundamental ideas.

2.3b. *Finite Charged Rod*

Physics textbooks are filled with simple illustrations of fundamental principles using physical systems that might be difficult to construct. The uniformly charged sphere or infinite-long cylinder, which contain a uniform charge density throughout, are used to illustrate Gauss's law in systems with spherical and cylindrical symmetry. In this section, we use a similar approach to bring insights into body forces imagining an elastic material that is filled with a uniform distribution of electric charge. One might imagine clever ways of making such a material, but we stress that such materials are not common. We contrive such a system not to model a particular material class, but rather to illustrate the fundamental principles of how body forces act. The mathematics of our analysis parallels that of the interaction of the gravitational field with all parts of a material, but gravitational fields cannot be easily turned off and on as the electric field.

As an example of a mechanism of the length change induced by a body force, we use Newton's laws to treat the case of a uniformly charged rod that is immersed in an electric field. We emphasize that the purpose of the calculations that follow is to provide a simple concrete illustration of a phenomenon that is simpler to visualize than those leading to a photomechanical force in real materials. As a result, this should give the reader insights into how body forces lead to response functions with spatial nonlocality. We will ignore the time dependence by focusing on the static solutions.

Subsection 4.1 develops a more general and elegant technique that is applicable to real materials.

As we will show below in one dimension for illustration, body forces result in non-uniform strain along the length of a homogeneous material. The length and change in length of a cylinder, as shown in Fig. 12, can be measured with a ruler and give the average strain \bar{u} ,

$$\bar{u} = \Delta L / L. \tag{59}$$

To measure deformation, we define a coordinate grid fixed to the body that stretches with the body as it is deformed. Figure 12 shows three representative grid lines in red on the surface of the cylinder. Only strain along the axis is considered, so vertical grid lines are not shown. The series of lines define N sections, labeled from bottom to top as 1 to N , and $N + 1$ “interfaces,” labeled 0 to N . The average strain on section i is thus given by

$$\bar{u}_i = \Delta \ell_i / \ell_i. \tag{60}$$

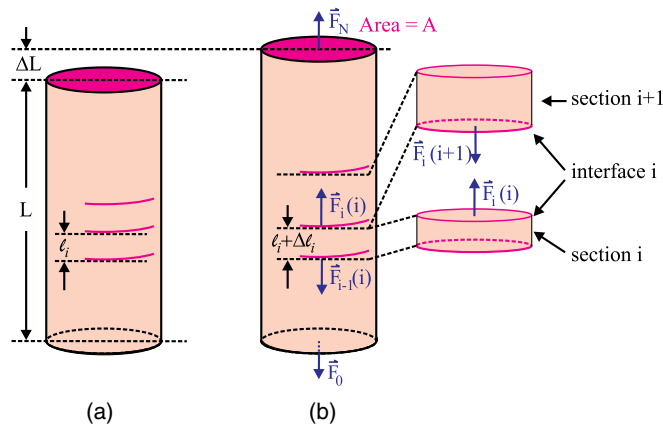
Equation (60) holds even when body forces act within the material.

Newton’s third law demands that action and reaction forces at a common interface between sections be of equal magnitude and opposite direction, or

$$\vec{F}_i(i) = -\vec{F}_i(i + 1), \tag{61}$$

where $\vec{F}_i(j)$ is the force on section j at interface i due to contact forces with the adjacent surface. The right portion of Fig. 12(b) shows two adjacent sections and the action/reaction forces on the shared interface. In the absence of body forces, the magnitude of the stress in the compressed cylinder is constant throughout the cylinder, or $|\vec{F}_0(1)|/A = |\vec{F}_1(1)|/A = |\vec{F}_1(2)|/A = \dots = |\vec{F}_N(N)|/A$. When body forces are present, the magnitude of the forces on the two ends of a segment are unequal, or $\vec{F}_i(i) \neq -\vec{F}_{i-1}(i)$.

Figure 12



(a) Unstressed and (b) uniaxially stressed cylinder. The strain on section i inside of a material is given by the change in length per unit length of that section when the material is stretched. The two sections shown to the right share a common interface, so action/reaction demands that $\vec{F}_i(i) = -\vec{F}_i(i + 1)$.

The total length of the cylinder is given by

$$L = \sum_{i=1}^N \ell_i, \quad (62)$$

the change in length is given by

$$\Delta L = \sum_{i=1}^N \Delta \ell_i, \quad (63)$$

and the average strain is

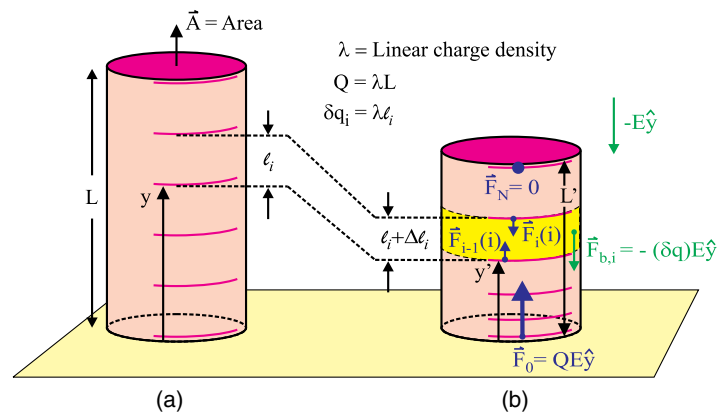
$$\bar{u} = \frac{\Delta L}{L} = \frac{\sum_{i=1}^N \Delta \ell_i}{\sum_{i=1}^N \ell_i}. \quad (64)$$

The average strain will equal the strain in each section when body forces are absent.

Consider now a uniformly charged cylinder with linear charge density λ sitting on a table as shown in Fig. 13(a) when gravity and repulsive forces between charges are negligible compared with the force on the charge from the applied electric field. Also assume that the charges are attached to the elastic material from which the cylinder is made. The $N + 1$ equally spaced red markings on the surface define the interfaces between the N sections. The top and bottom markings are slightly displaced from the end faces, where they belong, only to make them visible.

When an electric field E is applied to section i of length ℓ_i , the body force on that section will be given by $\lambda \ell_i$. The strain on section i will be induced by the stresses applied to each surface, which are determined by applying Newton's laws to each section and then solving the resulting system of equations. This example shows how a body force results in nonlocality, where the strain on each section of the material depends on all other parts of the material. Figure 13(b) shows the cylinder under the action of the applied electric field. Each slice of material will be acted on by the body force due to the applied electric field and the contact forces from above and below, which results in greater strain at the base than at the top surface.

Figure 13



(a) A uniformly charged cylinder sits on a table in the absence of body forces (assuming gravity and repulsive forces between the charges are negligible); (b) the same cylinder strained by a uniform electric field.

The bottom of the cylinder bears the full force, so the reaction force due to the table on the cylinder is $\vec{F}_0 = QE\hat{y}$. Since the top surface is unimpeded, and no contact force is applied from above, it experiences no force, so $\vec{F}_N = 0$. For a static cylinder, the \hat{y} component of the total force acting on the highlighted section, i , must vanish, yielding

$$F_{i-1}(i) - F_i(i) - F_{b,i} = 0, \quad (65)$$

where the body force due to the electric field is given by $\vec{F}_{b,i} = -\delta q \cdot E\hat{y}$ and $\delta q = \lambda\ell_i$ is the charge of slice i .

Equation (65) can be applied iteratively to calculate the magnitude of the contact force on any surface using the fact that $F_{b,i} = \delta q \cdot E$ is the same on each and the boundary conditions $F_0 = QE$ and $F_N = 0$ with $Q = N \cdot \delta q$. In particular, since $F_{N-1}(N) = E\delta q$ and $F_N(N) = 0$, then $F_{N-2}(N) = 2E\delta q$, etc., which yields

$$F_i(i) = (N - i)E\delta q = QE - i\delta q \cdot E. \quad (66)$$

The stress on segment i is then given by the average over the two interfaces,

$$\sigma_i = \frac{1}{2} \frac{F_{i-1}(i) + F_i(i)}{A} = \frac{QE}{A} - \frac{i\delta q \cdot E}{A} - \frac{\delta q \cdot E}{2A}, \quad (67)$$

where the segment is assumed to be thin enough so that the stress varies linearly with position.

If each segment before deformation is of the same height, $\ell_i = dy$, then $\delta q = Q \cdot dy/L$, and Eq. (66) becomes

$$\lim_{dy \rightarrow 0} \sigma_i = \sigma(y) = \frac{QE}{A} \left(1 - \frac{y}{L}\right) \equiv \sigma_0 \left(1 - \frac{y}{L}\right), \quad (68)$$

where we have used $y = idy$ and σ_0 is the stress on the bottom surface. The strain is then given by

$$u(y) = -\frac{\sigma(y)}{E'} = -\frac{\sigma_0}{E'} \left(1 - \frac{y}{L}\right), \quad (69)$$

where E' is Young's modulus, which should not be confused with the electric field amplitude.

Recall that the variable y represents the position in the stress-free cylinder. Any point within the deformed material, y' , is related to the point in the stress-free material according to

$$y' = y + \int_0^y u(y)dy = y - \frac{\sigma_0}{E'} \left(y - \frac{y^2}{2L}\right). \quad (70)$$

The length of the cylinder is calculated using Eq. (69) with $y = L$, yielding

$$L' = L \left(1 - \frac{\sigma_0}{2E'}\right). \quad (71)$$

The lesson here is that the deformation of a given slice of material depends on body forces being applied to other parts of the material. Light-induced strain also results from analogous body forces, so a nonlocal response will also contribute.

Note that the derivation above is the general approach for calculating the strain in the presence of body forces. Since the body forces here are uniform, Eq. (68) could have been derived in a much simpler way by recognizing that the force on the upper surface of segment i is simply the sum of all the forces above that segment, or $F_i = (N - i)dq \cdot E$. But $N - i = (L - y)/dy$, which trivially leads to Eq. (68) using the fact that $dq/dy = Q/L$.

Next we determine the response function for the static uniformly charged rod. As such, we are interested in only the spatial part of the response function. In this case, the strain will be related to the applied electric field according to

$$u(y) = \int_{-\infty}^{+\infty} d\xi R(y - \xi) E(\xi). \quad (72)$$

To get the response function requires that the strain response to an electric field impulse applied to one point in the material be determined. As we saw in Subsection 2.3a, a delta function impulse at position y_0 can be represented in the spatial domain as

$$E(y) = E_0 \Delta y \delta(y - y_0). \quad (73)$$

Substituting Eq. (73) into Eq. (72) and evaluating the integral yields

$$u(y) = R(y - y_0) \Delta y E_0. \quad (74)$$

To determine the response function, we need to determine $u(y)$. If the electric field is applied at point y_0 , the strain above that point ($y > y_0$) vanishes, and the strain below that point is uniform and given by

$$u(y) = -\frac{\lambda \Delta y \cdot E_0}{E' A} \quad \text{for } 0 < y < y_0, \quad (75)$$

where E' is Young's modulus and $\lambda \Delta y$ is the charge on the segment of width Δy . Note that since the rod ends on the table at $y = 0$, $u(y)$ is undefined for $y < 0$. Comparing Eqs. (75) and (74) yields the response function

$$R(y - y_0) = -\frac{\lambda}{E' A} \theta(y_0 - y) \theta(y). \quad (76)$$

We can check this response function for the case of the uniform electric field $E = E_0$. Substituting Eq. (76) into Eq. (72) yields

$$u(y) = -\frac{\lambda}{E' E_0 A} \int_0^L d\xi \theta(\xi - y) = -\frac{\lambda}{E' E_0 A} (L - y) = -\frac{\sigma_0}{E'} \left(1 - \frac{y}{L}\right), \quad (77)$$

the result we got in Eq. (69).

2.4. Optical Response Function

Up to this point, we have formulated the response function in terms of the electric field, which is the most general approach. Next, we consider the special case of an optical field, which is characterized by a high-frequency oscillation at ω with a period $2\pi/\omega$ that is much shorter than the response time of the material, and an amplitude $E_0(t)$ that varies much more slowly than the optical field. For the discussion that follows, we focus on the time dependence only.

First we consider the special case of a single monochromatic optical field, which is of interest to many experiments used in characterizing materials. Then, we consider the case of two monochromatic optical fields and show how beat frequencies can be used to excite the material.

2.4a. Monochromatic Optical Field

For monochromatic light, the electric field can then be expressed as

$$E(t) = E_0(t) \cos(\omega t). \quad (78)$$

Since we will be varying the light intensity on time scales that are long compared with an optical cycle, the so-called slowly varying envelope approximation will be used, or

$$\frac{dE_0(t)}{dt} \ll \omega E_0(t). \quad (79)$$

The strain response in the time domain is then given by

$$u(t) = \int_{-\infty}^{\infty} d\tau R^{(1)}(t - \tau) E_0(\tau) \cos(\omega \tau), \quad (80)$$

where the fact that the response function varies slowly over an optical cycle implies that $u(t) \approx u(t + 2\pi/\omega)$ and

$$R^{(1)}(t) \approx R^{(1)}\left(t + \frac{2\pi}{\omega}\right). \quad (81)$$

We can subdivide the integral in Eq. (79) into a sum over small time slices in the form

$$\int_{-\infty}^{\infty} d\tau = \sum_{k=-\infty}^{+\infty} \int_{k\Delta t}^{(k+1)\Delta t} d\tau, \quad (82)$$

where $\Delta t \equiv 2\pi/\omega$, yielding

$$u(t) = \sum_{k=-\infty}^{+\infty} R^{(1)}(t - k\Delta t) E_0(k\Delta t) \int_{k\Delta t}^{(k+1)\Delta t} d\tau \cos(\omega \tau). \quad (83)$$

The term $R^{(1)}(t - k\Delta t) E_0(k\Delta t)$ can be removed from the τ integral because it is approximately constant and the integral is evaluated by summing over the contributions of the response function over each interval Δt .

Since the integral of $\cos(\omega t)$ over a period vanishes, so does the strain. As such, there is no strain to first order in the electric field. We must therefore evaluate the response function to second order.

The strain response to second order in the electric field is given by

$$u(t) = \int_{-\infty}^{\infty} d\tau_1 \int_{-\infty}^{\infty} d\tau_2 R^{(2)}(t - \tau_1, t - \tau_2) E_0(\tau_1) E_0(\tau_2) \cos(\omega \tau_1) \cos(\omega \tau_2). \quad (84)$$

As in the linear case, we will assume that the response function varies slowly on times scales given by an optical cycle. However, in the nonlinear case, there is another time scale that needs to be considered, which originates at the microscopic level. Though the mechanical response will most certainly be slow, there are fast processes

that involve the mixing of two photons that can act together to excite an electron in the material on femtosecond time scales. The excitation may be fast, but subsequent relaxations that eventually lead to a mechanical response will be slow.

To account for the fast excitation process and the slow relaxation process that leads to a mechanical deformation, we need to incorporate into the response function two criteria. First, since the fast process is so much faster than the mechanical response, we can assume for all practical purposes that the two photons are required to interact with the material simultaneously. Second, time invariance requires that the response function depend on time differences. Taking these two criteria into account, we guess that the response function takes the form

$$R^{(2)}(t - \tau_1, t - \tau_2) = R(t - \tau_1, t - \tau_2)\delta(\tau_1 - \tau_2), \quad (85)$$

where $\delta(\tau_1 - \tau_2) = \delta((t - \tau_2) - (t - \tau_1))$ accounts for the simultaneity of the actions of the two fields, and $R(t - \tau_1, t - \tau_2)$ is the slowly varying part of the response function that describes the mechanical response.

Substituting Eq. (85) into Eq. (84) yields

$$u(t) = \int_{-\infty}^{\infty} d\tau_1 R'(t - \tau_1) E_0^2(\tau_1) \cos^2(\omega\tau_1), \quad (86)$$

where $R'(t - \tau_1) \equiv R(t - \tau_1, t - \tau_1)$. Equation (86) is in the form of a first-order response function that we evaluate by slicing the integral into time slices corresponding to an optical period using Eq. (83) with $E_0(\tau) \cos(\omega\tau) \rightarrow E_0^2(\tau) \cos^2(\omega\tau)$, which yields

$$\begin{aligned} u(t) &= \sum_{k=-\infty}^{+\infty} R'(t - k\Delta t) E_0^2(k\Delta t) \int_{k\Delta t}^{(k+1)\Delta t} d\tau \cos^2(\omega\tau) \\ &= \sum_{k=-\infty}^{+\infty} \frac{\Delta t}{2} R'(t - k\Delta t) E_0^2(k\Delta t), \end{aligned} \quad (87)$$

where we have used the fact that the integral of $\cos^2 \theta$ over one period is π .

Since Δt is small, the sum in Eq. (87) can be converted back into an integral, yielding

$$u(t) = \frac{1}{2} \int_{-\infty}^{+\infty} d\tau R'(t - \tau) E_0^2(\tau). \quad (88)$$

It is useful to step back and ponder the meaning of Eq. (88). Since an optical cycle is much shorter than the mechanical response time of the material, the strain responds only to the time-averaged optical field. To first order, the strain response vanishes since the time-averaged electric field vanishes. The second-order strain responds in proportion to the square of the field, which has a non-vanishing time average. The time dependence of the strain will thus follow the envelope function if it varies on time scales comparable to the mechanical response time of the material.

The intensity of the light beam is proportional to the square of the electric field amplitude, $I(t) \propto E_0^2(t)$, so Eq. (88) can be expressed in terms of the intensity,

$$u^{(1)}(t) = \int_{-\infty}^{+\infty} d\tau R^{(1)}(t - \tau) I(\tau), \quad (89)$$

where $R^{(1)}(t - \tau) \propto R'(t - \tau)$, and incorporates the 1/2 factor and the constants of proportionality between the square of the field and the intensity. Now, the order of the strain response is linear in the intensity, so we call the response function $R^{(1)}(t - \tau)$.

Note that all response functions that are odd-order in the electric field vanish, so the second-order electric field response function is related to the first-order intensity response function, the fourth-order electric field response function is related to the second-order intensity response function, and so on.

2.4b. Two Monochromatic Optical Fields

In this section, we consider two monochromatic fields. Again, we assume that the response function varies slowly compared with the period of each optical field, which takes the form

$$E_\alpha(t) = E_0^\alpha(t) \cos(\omega_\alpha t), \quad (90)$$

where $E_\alpha(t)$, ω_α , and $E_0^\alpha(t)$ are the electric field, the angular frequency, and amplitude of beam # α , respectively. The reader should beware that the subscript of the field IS NOT the polarization since we continue to use only scalar equations. The total electric field is then given by

$$E(t) = E_1(t) + E_2(t). \quad (91)$$

The total field $E(t)$ is the one used in determining the strain response. In analogy to the single-frequency approach that leads to Eq. (86), we get

$$u(t) = \int_{-\infty}^{\infty} d\tau_1 R'(t - \tau_1) E^2(\tau_1), \quad (92)$$

where using Eq. (91),

$$E^2(t) = (E_0^{[1]}(t))^2 \cos^2(\omega_1 t) + (E_0^{[2]}(t))^2 \cos^2(\omega_2 t) + 2E_0^{[1]}(t)E_0^{[2]}(t) \cos(\omega_1 t) \cos(\omega_2 t). \quad (93)$$

The strain response is the sum of contributions from the three terms in Eq. (92), where the first two terms are the individual contributions from the two monochromatic beams, as calculated in Subsection 2.4a. The third describes how the interaction between the two beams contributes to the strain.

We can use trigonometric identities to re-express the product of cosines in the last term of Eq. (93) to get

$$2E_0^{[1]}(t)E_0^{[2]}(t) \cos(\omega_1 t) \cos(\omega_2 t) = E_0^{[1]}(t)E_0^{[2]}(t) \{ \cos[(\omega_1 + \omega_2)t] + \cos[(\omega_1 - \omega_2)t] \}. \quad (94)$$

This cross term contains three time scales: (1) the slow envelope function, (2) the fast sum frequency $\omega_1 + \omega_2$, and (3) the difference frequency $\omega_1 - \omega_2$ —which can oscillate quickly or slowly depending on the values of ω_1 and ω_2 . Figure 14 shows these three time scales.

The approach here will be the same as in the monochromatic case, where the integral will be converted to a sum over time slices that are short compared with the strain response. Because the material does not respond mechanically at frequency $\omega_1 + \omega_2$, the response function is constant over this time scale, and therefore, the time average of $\cos[(\omega_1 + \omega_2)t]$ vanishes. The same will be true for the term oscillating at $\Omega = \omega_1 - \omega_2$ unless $1/\Omega$ is on a time scale equal to or smaller than the mechanical

strain response time. In this case, two beams of constant intensity will excite a sinusoidal time response of the material at the beat frequency Ω . If the beat frequency matches a mechanical resonance, large amplitude oscillations will be excited.

Putting it all together, the strain response due to the beating term is given by

$$u(t) = \int_{-\infty}^{\infty} d\tau_1 R(t - \tau_1) \sqrt{I_1(\tau_1) I_2(\tau_1)} \cos[(\omega_1 - \omega_2)\tau_1]. \quad (95)$$

If the response function is instantaneous on the time scale of the intensity variations and the oscillations at $\omega_1 - \omega_2$, so that it takes the form $R(t - \tau_1) = R_0 \Delta t \delta(t - \tau_1)$, the time dependence of the strain takes the form

$$u(t) = R_0 \sqrt{I_1(t) I_2(t)} \cos[(\omega_1 - \omega_2)t]. \quad (96)$$

If the intensities of the two beams are constant, i.e., $I_1(t) = I^{\omega_1}$ and $I_2(t) = I^{\omega_2}$, the strain response oscillates at the difference frequency.

In the most general case with more than two monochromatic beams incident on a material, difference frequencies between pairs of monochromatic waves can excite the material. This behavior is straightforward to show from the fact that if the total field can be expressed as a sum of monochromatic fields $E(t) = \sum_{\alpha} E_0^{\alpha} \cos(\omega_{\alpha} t)$, where ω_{α} is the frequency of the α^{th} field, the square of the electric field in Eq. (92) will be of the form

$$E^2(t) = \sum_{\alpha} \sum_{\beta} \sqrt{I^{\omega_{\alpha}} I^{\omega_{\beta}}} \cos(\omega_{\alpha} t) \cos(\omega_{\beta} t), \quad (97)$$

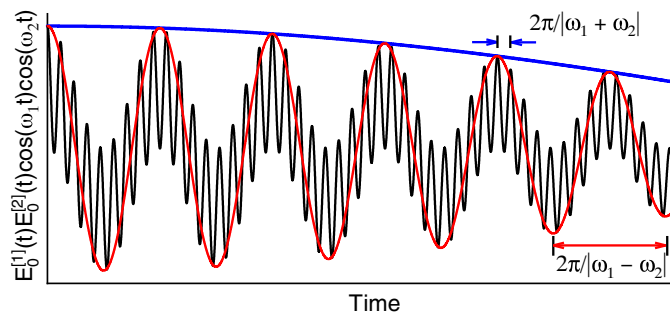
which contains only pairs of fields. As such, the material will oscillate in a superposition of all possible sum, difference, and first harmonic frequencies; but, only the difference frequencies will lead to slow-enough time variations if the frequencies are comparable, thus exciting strain oscillations. Note that Eq. (92) is equivalent to Eq. (96) for the special case of two monochromatic fields.

2.4c. Narrow Linewidth Laser Excitation

Even the best lasers are not monochromatic, but contain a spread of wavelengths that are characterized by a parameter called the linewidth, Γ . This can be used to excite mechanical modes in a material.

The intensity I^{ω} of the “monochromatic” field at frequency ω is a peaked function that can be approximated by a Gaussian of the form

Figure 14



$\cos(\omega_1 t) \cos(\omega_2 t)$ as a function of time (black), difference frequency oscillation (red), and envelope function $E_0^{[1]}(t) E_0^{[2]}(t)$ (blue).

$$I^\omega = I_0 e^{-(\omega - \omega_0)^2 / \Gamma^2}, \tag{98}$$

where ω_0 is the peak frequency. The solid red function plotted in Fig. 15 shows I^ω as a function of ω . Any two monochromatic waves within this spectrum can interact to excite a strain response when the difference between the optical frequencies $|\omega_1 - \omega_2|$ matches the material's resonance frequency ω' . The two colored vertical dashed lines in Fig. 15 label two frequencies ω_1 and ω_2 that are separated by ω' . Many such pairs are possible. The intensity of light at frequency ω_1 and ω_2 is given by I^{ω_1} and I^{ω_2} from Eq. (97). The strength of the driving term given by Eq. (96) is thus $\sqrt{I^{\omega_1} I^{\omega_2}}$. The strain response will therefore be maximum at a frequency where the product of the two intensities is maximum.

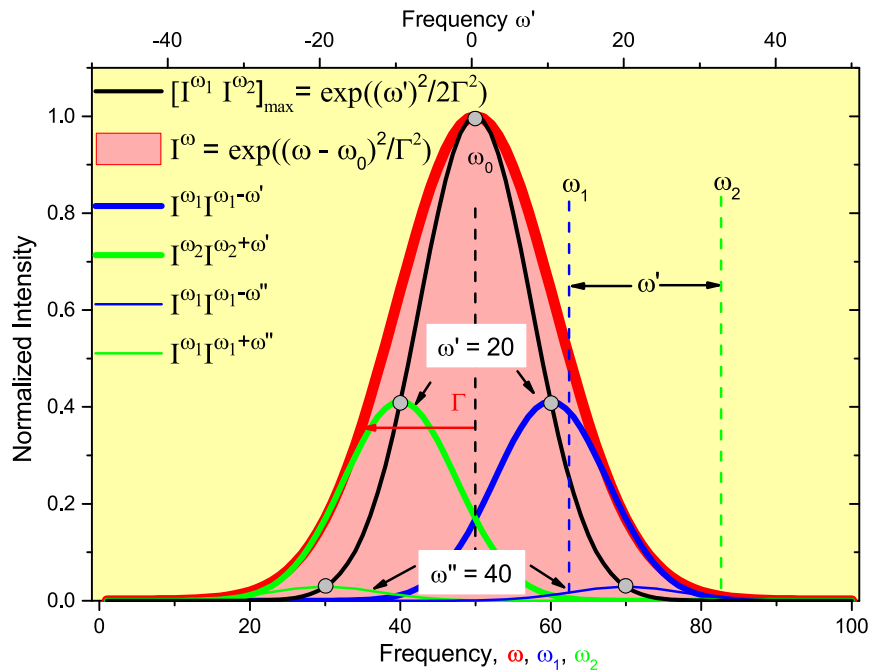
With $\omega_2 = \omega_1 + \omega'$, Eq. (97) gives

$$I^{\omega_1} I^{\omega_2} = I_0^2 e^{-(\omega_1 - \omega_0)^2 / \Gamma^2} e^{-(\omega_1 + \omega' - \omega_0)^2 / \Gamma^2}, \tag{99}$$

which can be shown by differentiation of Eq. (98) to be maximum when $\omega_1 = \omega_0 - \omega' / 2$ and $\omega_2 = \omega_0 + \omega' / 2$. Thus, the mechanical excitation is the strongest for the two monochromatic waves whose frequencies straddle the peak frequency and are separated by ω' , which yields

$$[I^{\omega_1} I^{\omega_2}]_{\max} = I_0^2 e^{-\frac{1}{2}(\omega')^2 / \Gamma^2}. \tag{100}$$

Figure 15



The red curve shows a Gaussian linewidth of a typical laser spectrum and represents the intensity of each monochromatic component as a function of frequency ω . The vertical black dashed line shows the center frequency ω_0 , and the two colored dashed lines show two wavelengths separated by the material resonance frequency ω' . The smaller blue and green curves show $I_{\omega_1} I_{\omega_1 - \omega'}$ as a function of ω_1 and $I_{\omega_2} I_{\omega_1 + \omega'}$ as a function of ω_2 for two different material resonance frequencies, ω' and ω'' . The smaller ω' is driven more strongly.

The solid black curve in Fig. 15 is a plot of $[I^{\omega_1} I^{\omega_2}]_{\max}$ as a function of ω' using Eq. (99). Thus, the condition for the strongest excitation of the mechanical response is $\omega' / \Gamma \ll 1$.

It is instructive to fix ω' , which is a material parameter, and vary ω_1 or ω_2 to assess when the response is maximum for a given laser source. The green and blue curves show the dependence of $I^{\omega_1} I^{\omega_2}$ on ω_1 or ω_2 for $\omega' = 20$ (larger peaks) and $\omega' = 40$ (smaller peaks). Note that when ω_1 and ω_2 straddle the peak symmetrically, $I^{\omega_1} I^{\omega_2}$ is maximized, as can be seen from the fact that the peaks (gray circles) fall on the black curves.

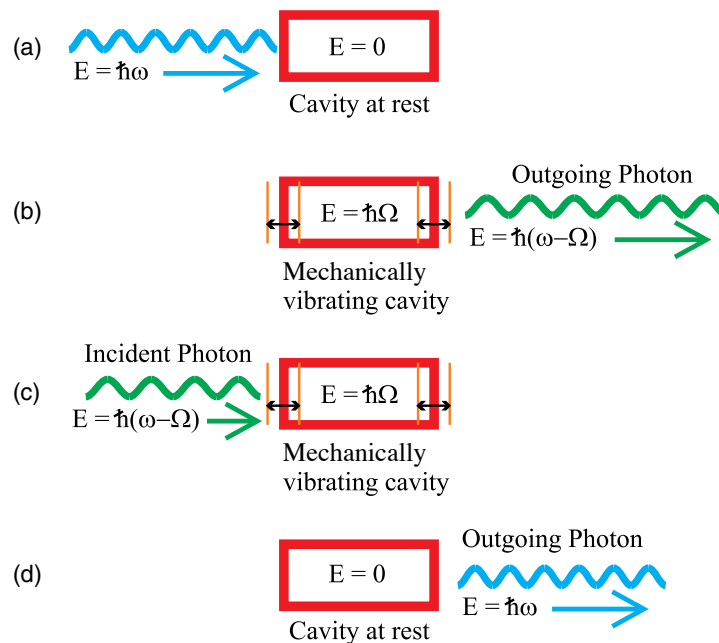
The conclusion here is that any “monochromatic” source can be used to excite a material resonance if the excitation frequency ω' is comparable to the linewidth Γ . If the linewidth is too narrow, then the intensity is not large enough at the wings to get a signal. So the ideal source is one with a broad linewidth.

2.4d. Mechanical Excitation in the Quantum Realm

For completeness, we note that at low-enough light intensities, a single photon can induce vibrations in a macroscopic cavity. The cavity is essentially a box with reflecting surfaces that allow the light to bounce to and fro inside. In the process, the photon loses energy as it imparts mechanical energy to the cavity, stretching its wavelength, which leads to a redshift. Figures 16(a) and 16(b) show a diagram of the process. As shown in Figs. 16(c) and 16(d), the reverse process leads to cooling when the photon gains energy from the cavity.

Law was the first to model the exchange of energy between a photon and a mechanical vibration [31]. Since both the photon and the vibrational modes are quantized, they are treated on an equal footing. A review of cavity optomechanics can be found in the literature [32]. While the field of cavity optomechanics is an important one, we will not discuss it further because the photomechanical effects that are central to this

Figure 16



(a) A photon incident on a cavity (b) makes it vibrate, losing energy to the mechanical mode as it leaves the system. (c) In the reverse process, an incident photon (d) gains energy from the cavity, thus cooling it.

review are all macroscopic processes. While all phenomena can be traced to microscopic origins, we will operate under the assumptions that photons are plentiful, and classical electromagnetic field theory applies.

3. MICROSCOPIC COMPARISON BETWEEN OPTICS AND MECHANICS

Section 2 describes how the optical path length combines the refractive index and the length in a symmetric way. As such, all photomechanical response mechanisms should have analogous optical ones. Here we show that this analogy holds down to microscopic scales and that the response time is approximately inversely proportional to the magnitude of the response.

Before delving into the details, we want to assure the reader that they should not be confused and frustrated by the many mechanisms that can lead to a photomechanical response or a light-induced refractive index change. This section provides an intuitive description of the ideas that carry forward to the specific mechanisms.

Each of the various processes responds on its own characteristic time scales, which are approximately inversely proportional to the magnitude of the response. Section 4 relates the microscopic origins of the photomechanical effect to the macroscopically observed phenomena while Section 6 describes the various mechanisms. This section uses a toy model of a material to show how the optical response is related to the photomechanical effect, and why the time scales of the various mechanisms are different. The rest of the paper fills in the details, with this section providing the physical intuition needed to understand it.

There are many possible toy models that predict the same behavior. The important ingredient is that the stimulus (an applied electric field or light) moves a charge—which leads to an optical response—or moves a mass—which leads to a mechanical response. In reversible processes, which are of interest in many applications, the system must return to the same state when the light or electric field is turned off. So there must be an opposing action by the material to the stimulus.

Examples of mechanisms that meet these criteria include thermal processes, where the stimulus moves objects against thermal agitation. The motion can be translational or rotational. Alternatively, the opposing process may be elastic in nature. Combinations of these processes might also be at play, such as elastic materials under thermal buffeting. Furthermore, the microscopic units might act independently or interact to respond collectively. Finally, the process might be treatable classically or quantum-mechanically. Understanding these processes becomes simple if we keep in mind that the origin of the response boils down to a stimulus that moves masses and/or charges in opposition to forces inside the material.

The simplest classical model of the basic element of a material is a mass m and charge q attached with a spring of force constant k to a massive object. This could be the electron in a molecule or a hole in a semiconductor. Under the action of a static electric field E , the displacement x of the mass is

$$x = qE/k. \quad (101)$$

Equation (101) shows how a displacement results from an applied electric field. Light will do the same, though through a slightly more complicated route, as we later show. The induced dipole moment $p = qx$ is then given with the help of Eq. (101) by

$$p = q^2 E/k. \quad (102)$$

For a material made of N such springs per unit volume, the polarization P is given by

$$P = q^2 E/k. \quad (103)$$

To determine the optical response, we use the constitutive equation between the electric displacement D and the polarization

$$D = E + 4\pi P = \epsilon E, \quad (104)$$

where the last equality defines the dielectric constant ϵ .

Substituting Eq. (103) into Eq. (104) and solving for ϵ yields

$$\epsilon = 1 + 4\pi Nq^2/k. \quad (105)$$

Since the refractive index n is related to the dielectric constant via $n = \sqrt{\epsilon}$, this calculation shows how a moving charge—a mechanical response—also leads to an optical response.

An increased response of a new material to a fixed stimulus leads to more efficient devices, so understanding the origins and using this knowledge to make better materials is an active area of research. However, the response time is also an important factor.

One can define a figure of merit that takes into account the needs of a particular device. If a fast device with a large photomechanical response is required, then the ratio of the magnitude of the response to the response time can serve as such a figure of merit. In the case of the intensity-dependent refractive index, which could be used in making an all-optical switch, such a figure of merit is appropriate. While the intensity-dependent refractive index and response times can vary by 12 orders of magnitude, the figure of merit for most materials varies by 2 orders of magnitude [30].

One can understand these large ranges in response time by considering the reorientation mechanism of a highly anisotropic molecule. A long and skinny molecule is highly birefringent, so even a small rotation in response to light leads to a large change in the bulk material's refractive index. However, the time it takes for the molecule to rotate fully is longer for larger molecules because of inertia. In summary, as the size of a molecule increases, the magnitude of the response and the response time both increase, resulting in a ratio that changes less than each.

A liquid crystal is an example of a material that operates based on the collective rotation of many molecules. In a sense, the system is equivalent to one huge molecule, but the individual molecules can rotate more easily. As a result, the response is large, but the response time is on the order of milliseconds compared with the femtosecond time scale to move an electron across a molecule.

4. RELATIONSHIP BETWEEN MICROSCOPIC AND BULK MECHANICAL PROPERTIES

The elasticity of a material ultimately originates in the statistical and quantum properties of the atoms and molecules from which the material is composed. Light can change these properties to induce a photomechanical effect. All mechanical and photomechanical behaviors of a material can be modeled by the collective action of interconnected microscopic springs whose equilibrium lengths and complex force constants change under light exposure [33]. The real part of the force constant describes the elastic properties and the imaginary part the viscosity. Changes in the

equilibrium length and spring constant due to light exposure lead to light-induced strain and stress in the bulk material—the focus of this paper. A spring model has the added advantage of being universally familiar to the physical sciences, giving an intuitive basis for understanding phenomena and providing a springboard for generalization.

A bulk material expands in response to a force and returns to its original equilibrium configuration after the force is turned off. One can visualize this process as originating in springs that when stretched oppose the force and return to their natural lengths when released. When there are no oscillations during release, the damping term (imaginary part) is larger than the elastic one (real part). If the material is stretched and held for an extended time, the spring deforms as would a real one, leading to a different natural length. Hysteresis in a material's Young's modulus can be modeled by a spring constant with hysteresis. Nonlinear terms that account for non-Hookean behavior in the underlying "springs" lead to corresponding nonlinear behavior in the mechanical properties and photomechanical response. In short, there is a one-to-one correspondence between the behavior of a network of springs and a viscoelastic material.

The properties of a bulk material are often modeled classically with phenomenological parameters. In a composite material, one can similarly model the component spring parameters for a particular material composition based on the mechanisms responsible in that material. Then, one can study how the bulk response changes when the component springs are changed or rearranged. The spring model provides a general framework that applies to all materials. As an example, the box below describes how an entropic spring behaves in every way as does a mechanical spring. Later we will see how atoms in molecules also behave as if connected with mechanical springs.

The continuum approach is an approximation when the object is much larger than the sizes of the underlying particles. It is instructive to consider the microscopic picture as an aid to developing an understanding of the quantum origin of the forces and how processes at the molecular level contribute to the strain.

Chemical bonds are the smallest units with an elasticity and can be understood in terms of simple quantum principles. Consider two positively charged nuclei in a sea of electrons as shown in Fig. 17. Figure 17(a) shows the nuclei when they are close together. The electrons repel each other, causing the electron cloud to occupy the outer periphery of the symmetry axis. As such, the nuclei experience a strong repulsive force.

Entropic model of a spring

Here we describe the entropic model of a polymer, which illustrates one special case as an example of how a particular mechanism can be modeled to calculate a spring constant [34]. Though the source of this force constant is nature's push toward keeping entropy at a maximum, the system behaves in a way that an observer lacking a powerful microscope to resolve individual polymer chains would call a spring.

The restoring force in an ideal mechanical spring is linear in its extension, so the spring potential energy is a quadratic function of the extension, or $V = \frac{1}{2}k(x - x_0)^2$, where k is the spring constant and x_0 the spring's resting length. Thus, the spring constant can be determined from the second derivative evaluated at the equilibrium length, or $k = \left. \frac{d^2V}{dx^2} \right|_{x=x_0}$. In the case of the entropic spring, the Helmholtz free energy is a function of the length of the polymer chain, and differentiation yields

$$k = \frac{3k_B T}{N b^2}, \quad (106)$$

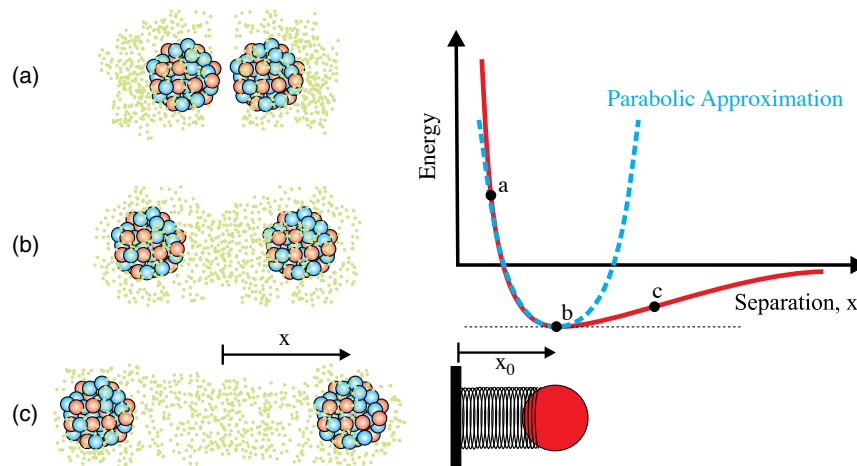
where T is the temperature, N is the number of links in the polymer chain, b is the length of a link, and k_B is Boltzmann's constant. So while the spring constant originates in the entropy, the polymer chain behaves as a spring with a temperature-dependent force constant $k(T)$. Polymer chains in series and in parallel from the entropic calculation give the same results as for springs in series and parallel. For example, if the number of units N is doubled to $2N$, the spring constant is a factor of 2 smaller. This result is trivially obtained from Eq. (106) and also follows from the classical mechanical law of the addition of two springs in series.

When the nuclei are further apart as shown in Fig. 17(b), part of the electron cloud fills the volume between them, thus partially screening the positive nuclei so that the repulsive force between them is balanced by the attraction of each nuclei to the nearby electron cloud. Under this condition, the nuclei are stationary. When the nuclei are even further apart as shown in Fig. 17(c), the attractive force decreases as the negatively charged electron cloud becomes more spread out. The electron cloud between the nuclei is classically viewed as a chemical bond that acts like a tiny spring. We will use this picture in future discussions.

The molecular energy as a function of the separation between the nuclei can be calculated, as follows. For fixed nuclear separation, x , the wave functions of the electrons are computed using the Schrödinger equation. The electron density is determined from the wave function, and the Coulomb energy of interaction between the nuclei and between the electrons and the nuclei are calculated. The total energy is then determined as a function of x . The red curve in Fig. 17 shows a plot of the total energy as a function of x that is obtained with this method. The three points labeled a , b , and c correspond to the three configurations shown to the left.

x_0 (point b) corresponds to the equilibrium separation. For small amplitude oscillations about this minimum, the potential is approximately parabolic and the linear

Figure 17



Two nuclei at three different separations, and the calculated energy as a function of separation. For small displacements from the minimum, the system is approximately a linear harmonic oscillator.

theory of elasticity applies, giving a linear restoring force $F = -k(x - x_0)$. For larger amplitude oscillations, the nonlinear terms contribute, and the force is given by a series expansion

$$F = -k(x - x_0) - \frac{1}{2}k^{(1)}(x - x_0)^2 - \frac{1}{6}k^{(2)}(x - x_0)^3 - \dots, \quad (107)$$

with a corresponding potential energy function

$$V(x) = \frac{1}{2}k(x - x_0)^2 + \frac{1}{6}k^{(1)}(x - x_0)^3 + \frac{1}{24}k^{(2)}(x - x_0)^4 + \dots. \quad (108)$$

The effective n^{th} -order spring constant can be determined from the potential energy function

$$k^{(n)} = \left. \frac{\partial^{(n+2)} V(x)}{\partial x^{(n+2)}} \right|_{x=x_0}. \quad (109)$$

The interaction of light with a material can be classically treated by considering an impulse to a spring that responds according to Eq. (108). The second approach is a quantum one in which the affect of the light on the electron cloud is modeled as a change in the spring constant and equilibrium position of the nuclei.

Classical spring models have been applied by Sekkat [35] to study the microscopic origins of the light-induced surface relief gratings [36–38] through a photoisomerization force along the gradient of the intensity [39–41]. Dramatic time-lapse photographs show the evolution of such gratings [42–44]. Such models can be used to determine the response function of a single molecule as a damped harmonic oscillator, which reacts to a delta function impulse with damped oscillations. We will not delve into the details of such models, but Subsection 4.1 will provide a general theory of light-induced body forces that uses such models.

The quantum picture, on the other hand, treats the electron clouds quantum-mechanically and the bonds between nuclei classically. Subsection 4.4 develops the quantum model as reported by Zhou *et al* [33].

4.1. Body Forces and the Linear Response Function

In this section, we start from the microscopic picture to develop a continuum model of a material in the presence of body forces in the spirit of Sekkat's treatment [35]. Consider first a one-dimensional piece of a material made of a series of masses connected with springs as shown in Fig. 18. The equilibrium positions have a period a , and the displacement at site i from equilibrium is η_i .

Assuming that the displacements are small so that only the first term in Eq. (108) is appreciable, the Lagrangian of the system is given by [45]

$$L = \frac{1}{2} \sum_i m_i \dot{\eta}_i^2 - \frac{1}{2} \sum_i k_i (\eta_{i+1} - \eta_i)^2, \quad (110)$$

where the potential energy is stored in the massless springs and the kinetic energy is carried by the motion of the atoms of mass m_i . The Euler–Lagrange equations in the presence of the body forces F_n yield

$$\frac{d}{dt} \left(\frac{\partial L}{\partial \dot{\eta}_n} \right) - \frac{\partial L}{\partial \eta_n} = F_n, \quad (111)$$

and when applied to Eq. (110) yield

$$m_n \ddot{\eta}_n - k_{n-1}(\eta_n - \eta_{n-1}) + k_n(\eta_{n+1} - \eta_n) = F_n, \quad (112)$$

where we have used $\partial \eta_i / \partial \eta_n = \delta_{in}$.

Equation (112) gives the coupled equations of motion for each site n in terms of the displacements of the two adjacent sites (at $n - 1$ and $n + 1$). In the limit when a is much smaller than the size of the chain, we can re-express Eq. (112) in the continuum limit, where $\eta_n \rightarrow \eta(x)$ and $\eta_{n\pm 1} \rightarrow \eta(x \pm a)$, with $\eta(x)$ representing the displacement of the mass $m(x)$ at position x . Eq. (112) then becomes

$$m(x) \ddot{\eta}(x) - k(x-a)(\eta(x) - \eta(x-a)) + k(x)(\eta(x+a) - \eta(x)) = F_b(x), \quad (113)$$

where $F_b(x)$ is the body force applied to mass $m(x)$, which is attached to a spring of average force constant $k(x)$.

For small a ,

$$k(x-a) \approx k(x) + a \frac{\partial k(x)}{\partial x}, \quad (114)$$

so Eq. (113) becomes

$$m(x) \ddot{\eta}(x) + k(x)[\eta(x+a) - 2\eta(x) + \eta(x-a)] - a \frac{\partial f(x)}{\partial x} [\eta(x) - \eta(x-a)] = F_b(x). \quad (115)$$

Next, using

$$\eta(x) - \eta(x-a) \approx a \frac{\partial \eta(x)}{\partial x} \quad \text{and} \quad \eta(x+a) - 2\eta(x) + \eta(x-a) \approx a^2 \frac{\partial^2 \eta(x)}{\partial x^2}, \quad (116)$$

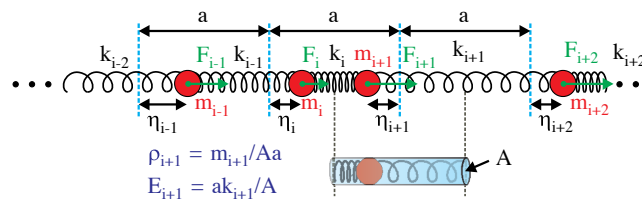
Equation (113) can be expressed as

$$m(x) \ddot{\eta}(x, t) - \frac{\partial}{\partial x} \left(k(x) \frac{\partial \eta(x, t)}{\partial x} \right) a^2 = F_b(x, t). \quad (117)$$

Up to this point, we have not explicitly labeled the time dependence of each parameter, but have added it here to remind the reader that the body force can depend on time, as do the displacements.

When a charged object oscillates, it can lose energy to radiation. An oscillating mass on a spring can lose energy to its environment predominantly in the form of heat. This

Figure 18



Elastic material can be viewed as a series of particles with masses m_i at sites i and massless springs with force constants k_i . In the continuum limit, a uniform elastic cylinder of volume aA , mass m_i , and Young's modulus $E_i = ak_i/A$ represents one of the masses and the two adjacent springs, as shown in light blue. The body forces, F_i , due to the photomechanical effect will in general depend on the position.

effect can be added to the equations of motion with a velocity-dependent drag term of the form $\gamma \dot{\eta}(x, t)$. We will add this term to the bulk equations that are derived below.

Imagine that space is filled with parallel lines of springs and masses such that N springs pierce an area element S that is perpendicular to the lines of springs. To keep the problem simple for now, we ignore interactions between the parallel chains of springs/masses—keeping only interactions within each line. Then, the cross-sectional area per spring is $A = S/N$, and the volume of one mass is $V = Aa$, as shown by the blue cylinder in Fig. 18. Dividing Eq. (117) by V , we get

$$\rho(x)\ddot{\eta}(x, t) - \Gamma\dot{\eta}(x, t) - \frac{\partial}{\partial x} \left(E(x) \frac{\partial \eta(x, t)}{\partial x} \right) = f_b(x, t), \quad (118)$$

where $\rho(x) = m(x)/V$ is the mass density, $E(x) = k(x)a/A$ is Young's modulus, $f_b(x)$ is the body force density, and the velocity-dependent damping term $-\Gamma\dot{\eta}(x, t)$ has been added to account for energy dissipation from the system.

Recall that $\eta(x, t)$ is the displacement. When the mass density is a constant, $\rho(x) = \rho_0$, it is more convenient to express the results in terms of the strain, $u = \partial\eta/\partial x$, and the body stress, $f_b = \partial\sigma_b/\partial x$. Differentiating both sides of Eq. (118) with respect to position, we get

$$\rho_0\ddot{u}(x, t) - \Gamma\dot{u}(x, t) - \frac{\partial^2 \sigma(x, t)}{\partial x^2} = \frac{\partial^2 \sigma_b(x, t)}{\partial x^2}, \quad (119)$$

where we have used the fact that $E(x)u(x, t) = \sigma(x, t)$. With this last approximation, the material response function is assumed to be instantaneous and local, conditions that can be relaxed when needed.

Equations (118) and (119) are two ways to express the wave equation in the presence of a spatially and temporally varying body force. These differential equations can be solved numerically, and some simple special cases have analytical solutions. Differential equations yield integration constants, which are determined from the boundary conditions. The following section gives simple examples with analytical solutions to which we apply two types of boundary conditions.

Equations (118) and (119) will apply to stretched rods along their symmetry axis and will be a good approximation to other geometries. A solution of the most general case must take into account the tensor nature of properties that we approximate here with scalar quantities.

4.2. Examples of Light-Induced Body Force

In this section, we consider three examples: (1) a uniform charged rod in a static electric field, (2) a uniform dielectric rod in a static uniform optical field, and (3) a uniform dielectric rod in a static optical field with Gaussian intensity profile. We will consider clamped ends and free ends as examples of boundary conditions. In all cases, we assume that effects of gravity are negligible as are interactions between charges within the material.

4.2a. Charged Rod in an Electric Field

Case #1 Clamped at Both Ends

Consider a uniformly charged elastic material with linear charge density λ and an electric field E that is applied to the region $a \leq x \leq b$. This yields a body force density $f_b = \lambda E/A$. Using Eq. (118) in static equilibrium, the region with the field applied gives the condition

$$-\frac{\partial \sigma(x)}{\partial x} = \frac{\lambda}{A} E, \quad (120)$$

which upon integration yields

$$\sigma(x) = -\frac{\lambda}{A} E x + c_1, \quad (121)$$

where c_1 is a constant. The stress in each field-free region is constant. If σ_0 is the stress in the region $0 \leq x \leq a$, continuity of stress leads to

$$\sigma(x) = \begin{cases} \sigma_0 & \text{for } 0 \leq x \leq a \\ -\frac{\lambda E}{A}(x-a) + \sigma_0 & \text{for } a \leq x \leq b \\ -\frac{\lambda E}{A}(b-a) + \sigma_0 & \text{for } b \leq x \leq L \end{cases}, \quad (122)$$

where L is the length of the rod.

σ_0 is determined from the clamped boundary condition that the length remains unchanged, or

$$\int_0^L u(x) dx = \int_0^L E \sigma(x) dx = 0, \quad (123)$$

where the integral is split into the three regions of stress as given by Eq. (122), which yields

$$\sigma_0 = \frac{\lambda E}{A} (b-a) \left[1 - \left(\frac{a+b}{2L} \right) \right], \quad (124)$$

and

$$\sigma(x) = \begin{cases} \frac{\lambda E}{A} (b-a) \left[1 - \left(\frac{a+b}{2L} \right) \right] & \text{for } 0 \leq x \leq a \\ -\frac{\lambda E}{A} \left(x - b + \frac{b^2 - a^2}{2L} \right) & \text{for } a \leq x \leq b \\ -\frac{\lambda E}{A} \left(\frac{b^2 - a^2}{2L} \right) & \text{for } b \leq x \leq L \end{cases}. \quad (125)$$

It is important to point out that the stress is positive in regions where the material is elongated relative to its free state and negative when it is compressed. When the electric field is applied upward, the material above the region of applied field will be compressed (negative stress), and the material below is stretched (positive stress). In this case $E > 0$, and since $b > a$ and $b + a < L$, Eq. (125) predicts a positive stress for $x < a$ and a negative stress when $x > b$, as we expect.

From the stress given in Eq. (125), the strain can be trivially calculated using $u = E_o^{-1} \sigma$. (Note that here E_o represents Young's modulus, to differentiate it from the electric field magnitude E .) Figure 19(a) shows the charged slab with no electric field applied, and the red lines drawn on the surface are equally spaced for the unstrained material. When the electric field is applied downward, as shown in Fig. 19(b), the material below is compressed (negative stress), and the material above is stretched (positive stress). In the region of the electric field, the strain is a linear function of distance, and changes smoothly from the value above to the value below, as described by Eq. (125) with $E < 0$ for the downward-pointing field. Because the electric field is localized in space, the red fiduciary lines are pulled through the region of the field. As a result, more lines are below the field region than above. Note that the force on the upper clamp need not be the same as on the bottom clamp.

Case #2 Clamped at One End

Consider the case where the rod is clamped at $x = 0$, while the end at $x = L$ is unconstrained as shown in Fig. 19(c). Recall that Eq. (122) is the general solution to which the boundary conditions need to be applied. Rather than using the fixed length condition given by Eq. (123), we demand that the stress vanishes on the free end, or $\sigma(x) = 0$ for $b \leq x \leq L$. This yields

$$\sigma_0 = \frac{\lambda E}{A}(b - a), \quad (126)$$

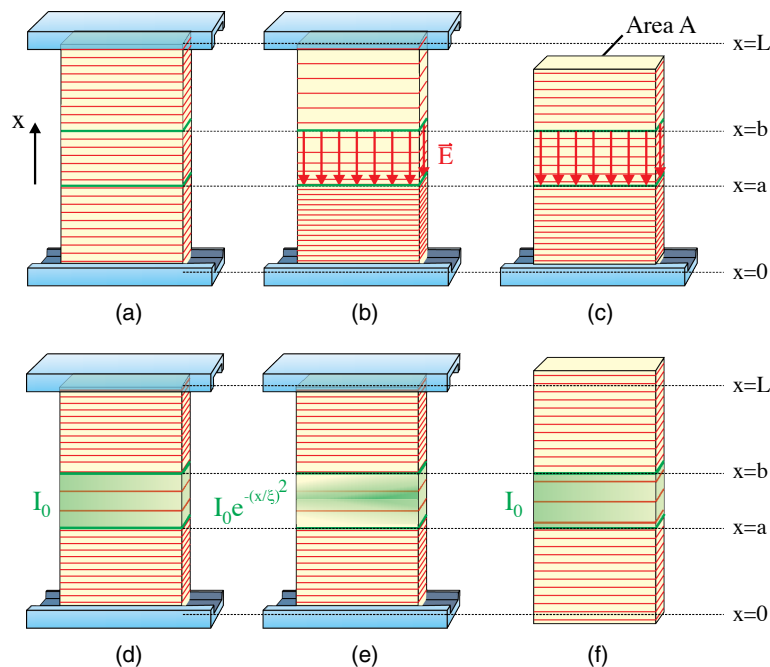
which gives the stress profile,

$$\sigma(x) = \begin{cases} \frac{\lambda E}{A}(b - a) & \text{for } 0 \leq x \leq a \\ \frac{\lambda E}{A}(b - x) & \text{for } a \leq x \leq b \\ 0 & \text{for } b \leq x \leq L \end{cases}, \quad (127)$$

Let us evaluate Eq. (127) for the special case when the whole rod is immersed in the electric field, so $a = 0$ and $b = L$. Then, $\sigma = \frac{\lambda L E}{A}(1 - \frac{x}{L})$, which is just Eq. (68), the result for the uniformly charged rod in Subsection 2.3b.

As shown in Fig. 19(c), the material above the field remains unstrained, and the material below is compressed, making a smooth transition between the two in the region of the electric field. Equation (127) shows this behavior for $E < 0$. As in the clamped

Figure 19



Rod with a rectangular cross section that is clamped or unclamped while immersed in an electric field or illuminated with light. (a) The equally spaced red lines are drawn on the unstressed rod as reference markers. (b) A uniformly charged rod clamped on both ends immersed in an electric field (red arrows) in the region $a \leq x \leq b$ and (c) a rod clamped only on one end. (d) A rod clamped at both ends and illuminated with uniform intensity light (green) in the region $a \leq x \leq b$ and (e) illuminated with a Gaussian beam. (f) A uniformly illuminated unclamped rod. Adapted from [46].

case, material passes through the electric field from above to the region below because the electric field is fixed in space.

4.2b. Optical Field in a Dielectric Rod—Instantaneous and Local Response

The electric field in a light wave oscillates with a period that is much shorter than mechanical oscillation times. As such, the effect of light on the mechanical response resides not in the electric field, which averages to zero over a mechanical period, but in the intensity. The mechanisms will be described in detail in Section 6. For the discussion at hand, the important property of all mechanisms is that no net force results. Instead, the light will induce stress, which is represented by a second rank tensor with a unique axis, but unlike the force, there is no unique direction.

As usual, we will treat the simple case of a rod and take advantage of the geometry, which allows all quantities to be represented by scalars. We will treat the special cases of an illuminated rod that is clamped and unclamped under both uniform illumination and a beam with a Gaussian intensity profile. In the calculations here, we assume that the photomechanical effect is fast compared with the turn-on time of the light, so that the response is instantaneous. Then, the induced bound stress is proportional to the intensity, so $\sigma_b(x) = -\kappa_\sigma I(x)$, where κ_σ is the photomechanical constant. If the material has a nonlinear response, then the induced stress is given by

$$\sigma_b(x) = - \sum_{n=1}^{\infty} \kappa_\sigma^{(n)} I^n(x), \quad (128)$$

where $\kappa_\sigma^{(n)}$ is the static n^{th} -order photomechanical constant. Since Eq. (128) assumes that the body stress at point x in the material is proportional to the intensity at point x , it implies that the photomechanical response is local. However, since a stress at point x can cause a disturbance that propagates along the material, this nonlocal behavior resides in the mechanical wave equation of the material.

In this work, we consider only a spatially local photomechanical response; however, in Section 6, we will take into account temporal nonlocality, where the response time of the material is incorporating through a temporal response function. So the reader should keep in mind that the body force due to the photomechanical response, σ_b , will always be spatially local, but the wave equation allows strain and stress waves, associated with σ , to propagate in the material.

Case #1a Clamped Rod—Uniform Intensity profile

Consider a rod of length L that is clamped on both ends and illuminated uniformly with light of intensity I in the region $a \leq x \leq b$ so that the stress in this region is given by Eq. (128), which leads to a Dirac delta body force density given by

$$f_b = \frac{\partial \sigma_b}{\partial x} = - \sum_{n=1}^{\infty} \kappa_\sigma^{(n)} I^n [\delta(x - a) - \delta(x - b)]. \quad (129)$$

We note that, with this definition, $\kappa_\sigma > 0$ corresponds to an elongational stress and $\kappa_\sigma < 0$ corresponds to a compressional stress. For now, we define $\kappa_\sigma \equiv \kappa_\sigma^{(1)}$ and consider only the linear term. Later, we will add nonlinearity. Substituting Eq. (129) into Eq. (118) with $\ddot{u} = 0$ and $\dot{u} = 0$ (static response) and integrating yields

$$\sigma(x) = \sigma_0 + \kappa_\sigma I \int_0^x dx [\delta(x - a) - \delta(x - b)], \quad (130)$$

where σ_0 is the integration constant. Because the integral vanishes when $x < a$ and $x > b$, σ_0 is the uniform stress on both sides of the illuminated region. In the illuminated region, the stress is $\sigma = \sigma_0 + \kappa_\sigma I$.

The clamped boundary condition requires the length of the rod to remain unchanged, or

$$\int_0^L dx \sigma(x) = \int_0^L dx \left(\sigma_0 + \kappa_\sigma I \int_0^x dx [\delta(x-a) - \delta(x-b)] \right) = 0, \quad (131)$$

which yields

$$\sigma_0[(L-b) + a] + (\sigma_0 + \kappa_\sigma I)(b-a) = 0. \quad (132)$$

Equation (132) can be used to solve for σ_0 , yielding

$$\sigma_0 = -\kappa_\sigma I \frac{(b-a)}{L}. \quad (133)$$

Inside the illuminated region,

$$\sigma = \sigma_0 + \kappa_\sigma I = \kappa_\sigma I \left(1 - \frac{(b-a)}{L} \right). \quad (134)$$

Thus, with $\kappa_\sigma > 0$, $\sigma > 0$ in the illuminated area, so the material is elongated, while in the dark region $\sigma_0 < 0$, the material is compressed.

Figure 19(d) shows the rod when the central portion is illuminated. Note that the stress in the dark region—given by σ_0 —is the fraction of the length of the rod that is illuminated $(b-a)/L$ multiplied by the photomechanical stress.

Case #1b Clamped Rod—Gaussian Intensity Profile

Finally, let us consider a beam that is focused to a rectangle that floods the rod from its side so that it is a Gaussian function along the rod and for fixed x it is uniform along its width so that the intensity profile is given by

$$I(x) = I_0 \exp[-((x-x_0)/\xi)^2]. \quad (135)$$

Recognizing that Eq. (118) for a static rod is simply given by

$$\frac{\partial \sigma}{\partial x} = -\frac{\partial \sigma_b}{\partial x}, \quad (136)$$

Eq. (136) can be integrated to yield

$$\sigma(x) = -\sigma_b(x) + \sigma_0. \quad (137)$$

Applying Eq. (137) to the Gaussian profile given by Eq. (135) yields

$$\sigma(x) = \sigma_0 + \kappa_\sigma I_0 \exp[-(x-x_0)/\xi]^2]. \quad (138)$$

Again, the clamped boundary condition requires that the length remain fixed, so

$$\int_0^L dx (\sigma_0 + \kappa_b I_0 \exp[-((x-x_0)/\xi)^2]) = 0. \quad (139)$$

Assuming that the Gaussian width is much smaller than the length of the rod, or $\xi \ll L$, and that the peak center is near the middle so that the intensity is low at the clamps, Eq. (139) becomes

$$\sigma_0 L + \kappa_\sigma I_0 \xi \sqrt{\pi} = 0. \quad (140)$$

Solving Eq. (140) for σ_0 yields

$$\sigma_0 = -\kappa_\sigma I_0 \frac{\xi}{L} \sqrt{\pi}. \quad (141)$$

It is instructive to compare Eqs. (133) and (141). In both cases, the magnitude of the stress at the clamps is given by the photomechanical stress ($\kappa_\sigma I$ or $\kappa_\sigma I_0$) times a geometrical factor that describes approximately the fraction of the rod's length that is illuminated. If we define the average intensity of the exposed region as

$$\bar{I} = \frac{\int_0^L I(x) dx}{\int_0^L dx}, \quad (142)$$

both Eqs. (133) and (141) can be written as

$$\sigma_0 = -\kappa_\sigma \bar{I}. \quad (143)$$

This result is general for the linear photomechanical effect, as can be verified by integrating Eq. (139) with an arbitrary function of intensity.

When the response function is nonlinear and expressed as a series expansion of the form

$$\sigma_b(x) = -\sum_{n=1}^{\infty} \kappa_\sigma^{(n)} I^n(x), \quad (144)$$

it is straightforward to show that

$$\sigma_0 = -\sum_{n=1}^{\infty} \kappa_\sigma^{(n)} \bar{I}^n, \quad (145)$$

where \bar{I}^n ($\neq \bar{I}^n$) is given by

$$\bar{I}^n = \frac{\int_0^L I^n(x) dx}{\int_0^L dx}. \quad (146)$$

Section 7 discusses how the linear and nonlinear terms can be measured.

Case #2 Unclamped Rod

In the case of the unclamped rod, the stress outside the illuminated region vanishes, so $\sigma_0 = 0$, and the stress inside is given simply by

$$\sigma(x) = -\sigma_b(x) = \sum_{n=1}^{\infty} \kappa_\sigma^{(n)} I^n(x). \quad (147)$$

Figure 19 summarizes all the cases described in this section.

4.3. Other Factors

The response functions can also depend on temperature as well as the thermal and mechanical history of the material. A myriad of other response functions can be defined. For example, the relationship between strain and stress, or stress and electric field, can be described by separate response functions. In all cases, they arise from the properties of the material, so are in principle calculable from the same fundamental properties and thus related to each other.

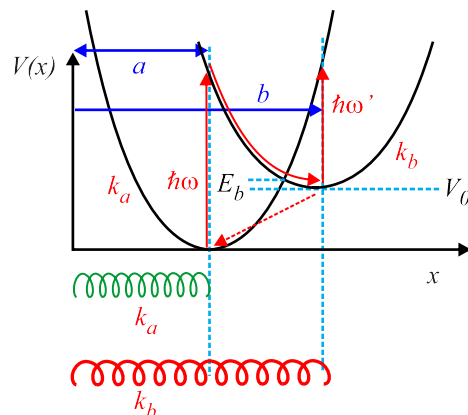
The more sophisticated reader may have noticed that all the calculations presented above are in a coordinate system whose axes align with the principle axes of the strain tensor. Appendixes B, C, and D describe the strain tensor, stress tensor, and Poisson's ratio. Whenever possible, we simplify the discussion by choosing stress and strain along one principal axis, such as the axis of a long and uniform thin rod, so that a scalar description is appropriate. It is straightforward to generalize our account of a photomechanical response to cases where the tensor properties are required, but these cases are just too messy when the focus is on understanding the principles underlying the theory.

4.4. Quantum Origins of the Photomechanical Response

The above section describes a fully classical model in which bonds are treated as springs and the light exerts a force on the masses that are connected with springs. This model ignores the fact that chemical bonds in an excited molecule can have a different equilibrium length and spring constant than in the ground state. In fact, all the various excited electronic states of the system will have different bond lengths. Below, we concentrate on a system with two electronic states, and show how the quantum picture leads to a classical interpretation that can be used to determine the efficiency of light conversion to mechanical work. The approach is the one developed by Zhou *et al* [33].

The classical model depicted in Fig. 17 shows the energy as a function of the distance between two nuclei. We call this the energy surface. The parabolic approximation near the origin makes it possible to treat the system as a classical spring. The left-hand parabola in Fig. 20 represents the same energy surface as in Fig. 17. The ground state spring constant of this energy surface we call k_a , and a is the separation between the nuclei.

Figure 20



Effective force constant k_a and resting length a of a molecule changes to spring constant k_b and new resting length b upon excitation with light. Reprinted from [33].

Upon excitation by light of energy $\hbar\omega$, the electron cloud changes shape leading to a new energy surface as shown on the right-hand part of Fig. 20. It has a different curvature and position of the energy minimum. This is modeled as a change in both the spring constant to k_b and the resting length of the spring to $x = b$. The massive nuclei respond slowly, so the length of the molecule just after it is excited is initially of length $x = a$, the resting length of the ground state spring. Subsequently, the length relaxes to b , doing work on the molecule's surroundings as it expands from length $x = a$ to $x = b$.

The spring would rest at $x = b$ in its excited state configuration if not for quantum or thermal tunneling that overcomes the barrier E_b , bringing the molecule back to the ground state parabola and doing no useful work due to the random nature of tunneling. To summarize, we model the full process classically as a change in spring constant and resting length upon photon absorption, and a relaxation back to the ground state energy surface with a phenomenological decay parameter. When the excitation rate greatly exceeds the tunneling rate, a large population of excited state molecules is generated. As we will show, the population ratio for a given excitation intensity can be determined from the ratio of the excitation and relaxation rates. The difference between this model and the previous one in Subsection 4.1 is the change in spring constant and equilibrium length upon excitation rather than a force applied to the masses due to the light.

The energy provided to the system by the absorbed photon is $\hbar\omega$, but V_0 of that energy does no work, so the net work provided is $\hbar\omega - V_0$. One might imagine that minimizing V_0 maximizes the efficiency; but, the parameters in this spring model cannot be varied arbitrarily because they are interrelated and constrained. The transition from length a to b provides energy,

$$\hbar\omega - V_0 = \frac{1}{2}k_b(a - b)^2, \quad (148)$$

which illustrates the relationship between the work provided and the spring's properties.

Figure 20 shows that a photon of energy $\hbar\omega'$ can force the transition to the ground state by exciting the molecule to the energy surface of curvature k , followed by relaxation back to its resting state. The photon thus accelerates decay, and because tunneling is avoided, the molecule can do additional work on its environment as it comes to rest while also increasing the speed of the process.

The first photon supplies energy $\hbar\omega - V_0$, and the second photon contributes $\hbar\omega' + V_0$, yielding total work

$$dV = (\hbar\omega - V_0) + (\hbar\omega' + V_0) = \hbar\omega + \hbar\omega', \quad (149)$$

making the cycle 100% efficient, converting the full energy of the light into work. Though possible, there would be great difficulty in taking advantage of the energy because the molecule first expands and then contracts, requiring the phases of the light pulses to be just right.

This analysis does not account for the small fraction of absorbed photons that lead to a length change, but rather considers only the efficiency assuming that a photon is absorbed. The requirement that two separate photons be absorbed is proportional to the joint probability, thus further lowering the efficiency. The design of an efficient photomechanical device requires that all such factors be taken into account.

The classical spring model of the photomechanical response of the quantum process is summarized in Fig. 21. The photomechanical response can take place on various size scales, so this model applies equally well to a molecule, a chunk of material, a liquid crystal domain, interconnected molecules/polymers, etc. The only important qualities are that it has a viscoelastic response and that light affects these properties.

We now consider a loop with four steps that starts with (1) stretching the spring, (2) applying light to change the spring's properties, (3) bringing the spring back to its original length with the light on, then (4) returning the spring to its original state when the light is extinguished.

When the sample is stretched by a force F , Hooke's law allows the potential energy to be expressed in several forms in terms of two of the three parameters F , k , and x ,

$$V(x) = \frac{1}{2}k(x - x_0)^2 = \frac{F^2}{2k} = \frac{1}{2}F(x - x_0), \quad (150)$$

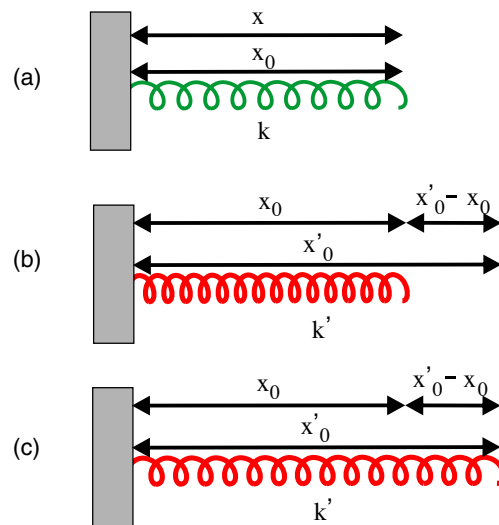
where x_0 is the resting length of the spring and k is its force constant. k is complex, and the imaginary part yields damping. Here for simplicity we assume that the imaginary part is negligible.

The light-induced change in spring constant and equilibrium position is schematically shown in Fig. 21. The spring's resting length is x_0 , and the spring constant is k . Immediately after excitation, the spring constant becomes k' , but its length remains x_0 due to inertia. The molecular bonds relax to the excited length x'_0 . To summarize, upon excitation, $x_0 \rightarrow x'_0$ and $k \rightarrow k'$, resulting in work on the environment. The energy increase is

$$dV = \frac{1}{2}k'(x'_0 - x_0)^2 \leq \hbar\omega. \quad (151)$$

For a reversible process, the energy imparted to the system cannot exceed the photon energy $\hbar\omega$. When the molecule deexcites to the state with spring constant k , its

Figure 21



(a) Resting spring of length x_0 . (b) Immediately after the spring is excited by light, its spring constant changes to k' , but its length remains unchanged due to inertia. The spring's length increases to x'_0 over nuclear vibrational time periods. (c) The spring after relaxing to its excited length x'_0 . Reprinted from [33].

length will relax back to x_0 . Equation (151) implies that 100% efficiency is possible. The parameters x_0 , x'_0 , k , and k' originate in the quantum state of the system, hence its wave function, making it difficult to determine which properties of a molecule lead to the optimal set of parameters for optimizing the efficiency of light energy to mechanical work.

k and x_0 can be determined from a measurement of Young's modulus of a sample and the sample's resting length. k' and x'_0 , on the other hand, can be determined from part of the cycle shown in Fig. 22, which starts with no applied force ($F = 0$) with equilibrium length x_0 . Then, the spring is stretched to a length x by an applied force $F_1 = k(x - x_0)$. Since the applied force is controllable and the length change is measured, the spring constant can be determined from these two measured properties according to

$$k = \frac{F_1}{x - x_0}. \quad (152)$$

This is how Young's modulus is measured in a bulk chunk of material.

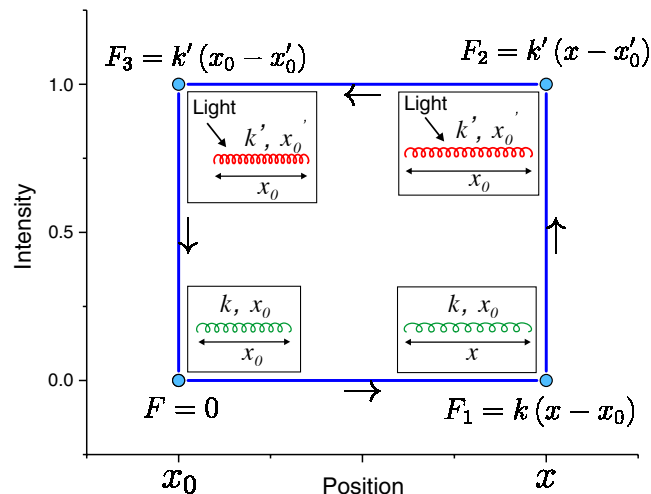
Next, light illuminates the spring, causing the equilibrium length to change to x'_0 and the spring constant to become k' . The applied force needed to keep the length fixed is

$$F_2 = k'(x - x'_0). \quad (153)$$

Since both x'_0 and k' are unknowns, this equation alone cannot be used to determine them individually. To do so, the spring is next compressed to its original length while the beam is on, which requires a force,

$$F_3 = k'(x_0 - x'_0). \quad (154)$$

Figure 22



Light engine. At rest, $x = x_0$, and $F = 0$. (1) The spring is stretched to x by the force F_1 ; then, (2) the intensity is turned on requiring a force F_2 to keep the spring's length fixed as its spring constant and equilibrium length changes. (3) A compressional force brings the spring back to its original length in the presence of the light and (4) relaxes to its resting state when the light is turned off and the compressional force released. Reprinted from [33].

Equations (153) and (154) can be used to solve for k' and x'_0 , yielding

$$k' = \frac{F_2 - F_3}{x - x_0}, \quad (155)$$

$$x'_0 = \frac{F_2 x_0 - F_3 x}{F_2 - F_3}. \quad (156)$$

Equations (155) and (156) can be substituted into Eq. (151) to determine the energy gained when exciting the spring in terms of the measured parameters during the cycle given by Fig. 22, yielding

$$dV = \frac{1}{2} \frac{F_3^2}{F_2 - F_3} (x - x_0). \quad (157)$$

Determining this energy does not require the properties of the initial spring because it was not stretched. If it had been, k would have been required, which is determined from Eq. (152).

The energy provided to the spring by the light is determined from Eq. (157) and is given in terms of the measured forces applied and displacements measured. A more special case is the one where the spring constant does not change appreciably ($k \approx k'$) and the photomechanical energy derives solely from a change in the resting length. In this case, the change in energy upon exciting the molecule is given by

$$dV = \frac{1}{2} k (x'_0 - x_0)^2 = \frac{1}{2} \frac{1}{k} (F_1 - F_2)^2, \quad (158)$$

where the second equality in Eq. (157) is derived by expressing $x_0 - x'_0$ in terms of the forces F_1 and F_2 and the spring constant k . Note that when the spring constants are the same, only forces F_1 and F_2 need to be measured provided that k is known from a measure of Young's modulus.

The cycle shown in Fig. 22 is an indication that the system can be used as a motor that operates with constant illumination. An example of such motors using photomechanical "belts" wrapped around wheels to make an engine [46] and a turbine configuration [47] has been reported by Knežević and Warner.

The spring model is a useful metaphor for imagining the photomechanical response of a material in an intuitive way [33]. In contrast to the equilibrium models such as heating, which requires the light to remain on to keep the material at higher temperature, the mechanical spring model as presented assumes that the molecule will quickly deexcite. Subsequently, another photon will need to be supplied to re-excite it. However, molecules with long-lived excited states can persist in the excited mechanical state over long time scales. Then, the molecule can be forced to deexcite using a second photon that is tuned to the appropriate wavelength. In this case, the molecule can be toggled between two states. Collections of molecules, on the other hand, must follow population models, which behave analogously to the thermal model, because they act incoherently.

Zhou's spring model is physically different from Sekkat's model [33,35]. The spring-like molecules in Sekkat's model undergo trans-cis-trans photoisomerization, which is purported to lead to a worm-like motion that induces mass diffusion in an electric field gradient [48]. In Zhou's model, the materials are uniformly illuminated, eliminating gradient forces—aside from residual field gradients at the sample's edges. The

volume of these regions is small, so mass diffusion effects under typical photomechanical characterization experiments as we describe here will be negligible in their contributions to the photomechanical constants.

4.5. Photomechanical Unit

A photomechanical unit (PM) unit is made with an active molecule of spring constant k_a and a passive part in parallel with it having spring constant k_e that represents the environment, both in their resting state of length a as shown in Fig. 23. Upon being excited by light, the active molecule's length changes to b , and the force constant becomes k_b . The passive environment counters the length change, leading to an equilibrium length x_b , where $a < x_b < b$. The equilibrium length is calculated from a balance between the two spring forces, or

$$k_b(b - x_b) = k_e(x_b - a). \quad (159)$$

The passive spring is stretched by $x_b - a$ from its equilibrium length and the active molecule by an amount $b - x_b$.

Solving Eq. (159) for x_b yields

$$x_b = \frac{bk_b + ak_e}{k_e + k_b}. \quad (160)$$

Using Eq. (160), the resting length of the parallel spring combination is

$$x_b - a = \frac{(b - a)k_b}{k_e + k_b}. \quad (161)$$

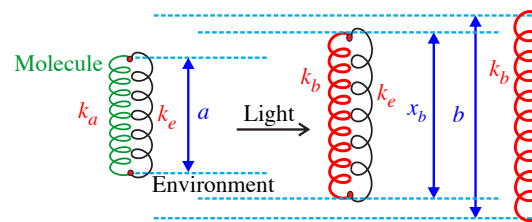
Also,

$$b - x_b = \frac{(b - a)k_e}{k_e + k_b}. \quad (162)$$

Using Eq. (161), the potential energy of the two-spring system upon excitation of the photomechanical molecule is given by

$$V(k_e) = \frac{1}{2}(k_b + k_e)(x_b - a)^2 = \frac{1}{2} \frac{k_b^2}{k_e + k_b} (b - a)^2, \quad (163)$$

Figure 23



Photoactive molecule of spring constant k_a in parallel with a passive element of spring constant k_e , both of length a , equilibrate to length x_b when excited from its equilibrium length. The passive element prevents the dye from fully expanding upon excitation to its excited resting length b . Reprinted from [33].

where we have used the fact that the spring constant of the PM unit in the excited state is given by

$$k_b^{\text{eff}} = k_b + k_e. \quad (164)$$

In the ground state, the PM unit's spring constant is

$$k_a^{\text{eff}} = k_a + k_e. \quad (165)$$

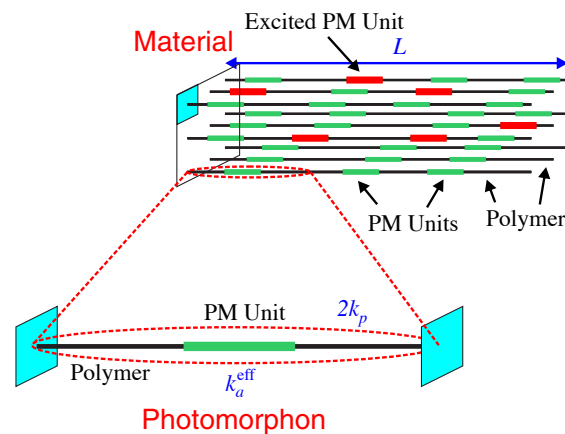
4.6. Photomorphon

A photomechanical material is made of a collection of smaller parts that when acting together yield the bulk photomechanical response. The smallest piece of the material that has the same intensive property as the bulk is called a photomorphon [33]. The concept of the photomorphon is fundamental in the way atoms are fundamental to materials.

We use the dye-doped polymer as a paradigm for describing a photomorphon to illustrate how the bulk response originates in the active microscopic part of the material. Consider a dye molecule that is dispersed into a host polymer. The section of the molecule that interacts with the polymer is called the PM unit. As we discuss later, the PM unit contains the active molecule that changes length in response to light, and the resistance to its length change due to the environment is modeled by placing a passive spring in parallel with it. The reason for defining it in this way will become more clear later.

For simplicity, picture the polymer as a one-dimensional chain as shown in Fig. 24. Figure 25(a) shows the average chain with one PM unit attached to a segment of length ℓ . This is the average unit in the sense that the spacing between PM units is random, and here we use the average length. This average chain is called the photomorphon, which acts as the unit cell of a photomechanical material. To summarize, the photomorphon is a passive spring in series with a PM unit, and the PM unit is made of the active photomechanical molecule in parallel with a passive spring.

Figure 24



Materials are made from smaller units that when acting together give the bulk response. The smallest photomechanical part of a material that retains the properties of the bulk material is called a photomorphon. This figure illustrates the concept with a polymer, where a section of a passive chain contains the light-actuated photomechanical unit. Reprinted from [33].

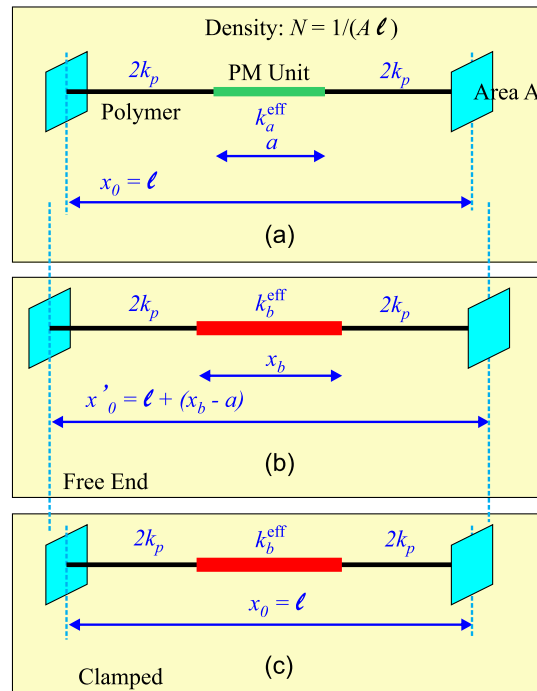
We can imagine a photomorphon being made of photoactive molecules embedded in a glassy polymer, as one has for a dye-doped polymer or a polymer with the photoactive molecules covalently attached. Even a more complex system such as a dye-doped LCE, as shown in Fig. 26, can be modeled as a photomorphon. The active molecule used in many photomechanical materials is the class of azobenzene dyes [49,50], which change from a trans to cis isomer upon excitation.

One dye molecule surrounded by a liquid crystal in its nematic phase is the PM unit, and the liquid crystal is the hindering environment in parallel with the photomechanical molecule. The photomorphon is then one PM unit in series with the polymer backbone, which connects the PM units in series.

The purported reorientational mechanism of the photomechanical response starts with a photon-induced shape change of the dye from the trans to the cis conformation, which interferes with the aligning forces in liquid crystal and causes a decrease in its orientational order. As a result, the PM unit deforms, and its spring constant changes. The photomorphon, which includes the elastomer chain, will then deform and lead to a bulk photomechanical response.

In a one-dimensional chain, $n = 1/\ell A$ is the number density of the active dye, the number density of the PM unit, and the number density of the photomorphon because there is one of each in a photomorphon. The fraction of the material occupied by the PM unit is a/ℓ . The average PM unit shown in Fig. 25(a) has an effective spring constant of k_a^{eff} and resting length a , which are determined from the composition and structure of the material. For example, the dye molecule might be in parallel with part of the polymer or might straddle two chains.

Figure 25



(a) “Average” photomorphon contains one photomechanical unit of length a with spring constant k_a^{eff} in series with a polymer chain of length ℓ and total polymer spring constant k_p . Two boundary conditions are possible: (b) the excited state photomorphon with free ends and (c) the clamped photomorphon. Reprinted from [33].

Taking the spring constant of the polymer on both sides of the PM unit to be $2k_p$ gives a series spring constant k_p . Then, the spring constant k of the resting photomorphon is given by

$$k = \frac{k_p k_a^{\text{eff}}}{k_p + k_a^{\text{eff}}}. \quad (166)$$

Similarly, the excited state spring constant of the photomorphon for an excited PM unit of spring constant k_b^{eff} is given by

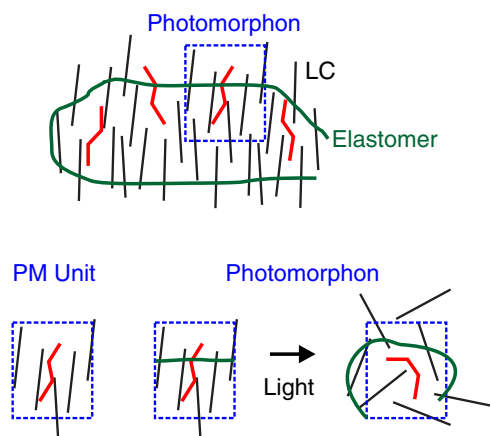
$$k' = \frac{k_p k_b^{\text{eff}}}{k_p + k_b^{\text{eff}}}. \quad (167)$$

The goal is to calculate the photomechanical response of the photomorphon upon excitation of the PM unit in terms of the spring parameters developed here, which in turn are related to the fundamental quantum properties of the molecules. Two extreme configurations are possible. The ends of the photomorphon can be free to move as in Fig. 25(b), or the ends can be clamped, as shown in Fig. 25(c). Thus, the clamped configuration yields uniform photomechanical stress with constant length while the unclamped length change of the photomorphon equals the length change of the PM unit. These will be treated later.

5. STATISTICAL MODEL

As described in the paper by Zhou [33], a material in its steady state is made of a collection of resting and excited photomorphons. The relative populations are determined from a balance between excitations from the light source and spontaneous and possibly stimulated deexcitation. In the absence of light, at high-enough temperatures,

Figure 26



Generality of the photomorphon is illustrated by applying it to the dye-doped liquid crystal elastomer, which is made with mesogens (molecules that interact with each other to form a liquid crystal phase) that are covalently attached to an elastomer chain. Molecules that change conformation are doped into the material and align themselves through steric interactions with the liquid crystal. A dye molecule with surrounding mesogens is the PM unit, and the PM unit with the attached elastomer is the photomorphon. Light changes the conformation of the molecule from trans to cis, interfering with the liquid crystalline ordering and deforming the elastomer, thus changing the material's properties. Reprinted from [33].

excited state populations might become significant. This section determines the bulk material properties from a weighted population average to determine various quantities such as Young's modulus and the photomechanical constants. The approach is to first determine the population-averaged properties of the photomorphon; then, relative populations of the species are determined from population dynamics models; and finally the population models are applied to determine the dynamics of the photomorphon. In particular, the length change and force in the unclamped and clamped configurations will be determined in terms of the populations and used to calculate their time evolution as a function of intensity.

5.1. Force and Length Change

For an excited state population fraction n_e , the ground state population fraction is $1 - n_e$, so the average photomorphon length in the unclamped configuration, $\bar{\ell}$, according to Fig. 27 is

$$\bar{\ell}(\ell) = \ell(1 - n_e) + (\ell + (x_b - a))n_e = \ell + n_e(x_b - a). \quad (168)$$

Recall that ℓ is the resting length of the photomorphon and $x_b - a$ is the length change of the photomorphon upon excitation. The population-weighted average force constant for photomorphons connected in series is

$$\frac{1}{K(n_e)} = \frac{n_e}{k'} + \frac{1 - n_e}{k} \rightarrow K(n_e) = \frac{k}{1 - n_e \left(1 - \frac{k}{k'}\right)}. \quad (169)$$

The change in the average resting length upon excitation from the ground state is

$$\delta\bar{\ell}(n_e) = n_e(x_b - a), \quad (170)$$

giving a strain

$$u(n_e) = \frac{\delta\bar{\ell}}{\bar{\ell}} = n_e \frac{(x_b - a)}{\bar{\ell}}, \quad (171)$$

and the force on the walls in the clamped configuration will be

$$F(n_e) = K(n_e)\delta\bar{\ell} = \frac{n_e k(x_b - a)}{1 - n_e \left(1 - \frac{k}{k'}\right)}, \quad (172)$$

where we have used Eqs. (169) and (170).

Figure 27



“Average” photomorphon’s properties will be the population-weighted average, where n_e is the fraction of excited photomorphons in the material. Reprinted from [33].

5.2. Population Dynamics

The temperature determines the equilibrium populations of excited and ground state molecules in the absence of light. The light drives excitations that change the populations, which decay back to equilibrium when the light is extinguished. The time evolution of the populations calculated below will later be applied to determining the time dependence of the forces and displacements using the results from Subsection 5.1.

Consider a collection of N photoactive molecules with N_e of them in their excited states. Light will convert the lower energy state to the higher energy one, and deexcitation from the excited state can be stimulated with light. The excited state population will also decay in the absence of light to its equilibrium population. The number densities of photoactive molecules and excited state molecules follow as $\rho = dN/dV$ and $\rho_e = dN_e/dV$ with V denoting the volume. Thus, the time evolution of the excited state population density is

$$\begin{aligned} \frac{d}{dt}\rho_e(\vec{r}, t) = & [\rho(\vec{r}, t) - \rho_e(\vec{r}, t)]\eta_0(\vec{r}, t)v_{\text{ph}}(\vec{r}, t) \\ & - \rho_e(\vec{r}, t)\eta_e(\vec{r}, t)v_{\text{ph}}(\vec{r}, t) - \beta(\vec{r}, t)\rho_e(\vec{r}, t), \end{aligned} \quad (173)$$

where η_0 is the probability that an incident photon converts a ground state molecule to its excited state, η_e is the probability of converting an excited state molecule to its ground state, β is the population decay rate in the absence of light, and v_{ph} is the number of photons per unit time at position \vec{r} and time t that can excite a photoactive molecule from the ground state. The number of photons per unit time is expressed in terms of the power by

$$v_{\text{ph}}(\vec{r}, t) = \frac{P(\vec{r}, t)}{\hbar\omega}, \quad (174)$$

where $\hbar\omega$ is the photon energy and P is the power at position \vec{r} and time t . Substituting Eq. (174) into Eq. (173) gives

$$\begin{aligned} \frac{d}{dt}\rho_e(\vec{r}, t) = & [\rho(\vec{r}, t) - \rho_e(\vec{r}, t)]\frac{\eta_0(\vec{r}, t)}{\hbar\omega}P(\vec{r}, t) \\ & - \rho_e(\vec{r}, t)\frac{\eta_e(\vec{r}, t)}{\hbar\omega}P(\vec{r}, t) - \beta(\vec{r}, t)\rho_e(\vec{r}, t). \end{aligned} \quad (175)$$

Clearly, the spatial and time dependencies in Eq. (175) can result in complex population dynamics. We have already made the approximation that Eq. (175) is linearly dependent on the power; however, local fields at the interface can also have an affect on the linear polarization and absorption characteristics of chromophores in dye-doped systems [51], which can affect the values of η_0 and η_e near interfaces. Likewise, the η_0 , η_e , and β parameters can depend on local environmental conditions such as temperature [52] and pH [53]. Thus, models pertaining to specific situations are often used to capture much of the relevant phenomena while neglecting some minor or secondary details, especially when the simplified models result in closed-form solutions. Many situations allow the parameters η_0 , η_e , and β to be approximated as constants, which greatly simplifies Eq. (175).

Many situations can warrant approximations to the intensity vector given in Eq. (175). For example, a Gaussian beam can be expanded beyond the area of the material. Then, the incident intensity can be approximated as uniform over the surface of the material. When light is incident on a macroscopic photomechanical material with a curved surface, such as light incident on a bent film [44,54], the light over the curved surface

will refract at different angles, and the transmitted intensity will also decrease with increasing angle of incidence over the surface. For samples with shallow bends and short penetration depths, models often neglect the dependence of the vector intensity on the incident angle and approximate the intensity as a function of depth [55,56].

There are a few common models for attenuation of the intensity as a function of depth. For low pump intensities, the Beer–Lambert law is typically used to approximate the intensity of light in the material; however, at high intensities, the absorbers are saturated with light, and an intensity-dependent absorption coefficient is required. Long-lived excited states can also result in time-dependent attenuation [57], where closed-form expressions of equations with mathematical forms similar to Eq. (175) can still be found, although they are usually complicated.

By assuming a photomechanical material that is much thinner than the thickness required to attenuate the light, a simple model can be assumed that captures the general features of photomorphon population dynamics without specific macroscopic system details such as optical hole burning. If the parameters η_0 , η_e , and β can be assumed constant, and if the sample is thin enough, then Eq. (175) can be written as

$$\frac{d}{dt}\rho_e(t) = [\rho(t) - \rho_e(t)]\frac{\eta_0}{\hbar\omega}P - \rho_e(t)\frac{\eta_e}{\hbar\omega}P - \beta\rho_e(t), \quad (176)$$

where P is a constant in the thin film approximation, and we have assumed that the parameters η_0 , η_e , and β are also constant. Integrating Eq. (176) over the volume results in a first-order rate equation for the number of molecules in the excited state,

$$\frac{dN_e}{dt} = (N - N_e)\left(\frac{\eta_0 P}{\hbar\omega}\right) - N_e\left(\frac{\eta_e P}{\hbar\omega}\right) - \beta N_e. \quad (177)$$

We note that the population dynamical equation given by Eq. (177) is used extensively in many areas of physics and chemistry, such as in self-healing systems [58], and was first applied to the photomechanical effect by Finkelmann *et al.* [59] and later used by Harvey to analyze the photomechanical stress response [60].

Defining the cross section $\sigma_i^{(\text{cs})} = A_b\eta_i$ for state i , where A_b is the area of the beam, and re-expressing Eq. (177) in terms of the intensity $I = P/A_b$, after some rearrangement of the terms, we get

$$\frac{dN_e}{dt} = NI\left(\frac{\sigma_0^{(\text{cs})}}{\hbar\omega}\right) - N_e I\left(\frac{\sigma_0^{(\text{cs})} + \sigma_e^{(\text{cs})}}{\hbar\omega}\right) - \beta N_e. \quad (178)$$

Equation (178) is of the form

$$\boxed{\frac{dn_e}{dt} = \alpha_0 I - n_e(\alpha I + \beta)} - \beta'(n_e - n_e^{(0)}(T)), \quad (179)$$

where the boxed term is Eq. (178) and the added term will be discussed shortly. We have divided Eq. (178) by N to get the fractional number density $n_e = N_e/N$, and

$$\alpha_0 \equiv \frac{\sigma_0^{(\text{cs})}}{\hbar\omega}, \quad \text{and} \quad \alpha \equiv \frac{\sigma_0^{(\text{cs})} + \sigma_e^{(\text{cs})}}{\hbar\omega}. \quad (180)$$

In the absence of photon-induced deexcitation, $\alpha = \alpha_0$.

The un-boxed term in Eq. (179) accounts for temperature-dependent population dynamics. $n_e^{(0)}(T)$ is the excited state population of the dark sample at temperature T , which is derived from the partition function and given by

$$n_e^{(0)}(T) = \frac{1}{1 + e^{V_0/k_B T}}, \quad (181)$$

where V_0 is the energy difference between the ground and excited states of molecules in a PM unit and k_B is the Boltzmann constant.

Subsection 6.5b describes real material systems where the spring is one isomer and what we call the excited spring is another one. Isomers are just different shapes of the same material as one would get when rotating two parts of a molecule around a bond. The class of stilbene molecules has two isomers with an energy difference $V_0 = 0.052$ eV [61]. At room temperature, where $k_B T \approx 1/40$ eV, the excited state population fraction given by Eq. (181) is $n_e^{(0)} = 0.11$. Thus, 11% of the molecules, a significant fraction, are in the excited state. For an azopolymer $V_0 = 0.29$ eV [62] yielding an excited state population of $n_e^{(0)} = 9.2 \times 10^{-6}$, which is negligible.

For a photomechanical material driven by molecular shape changes at two different energies, the ideal material would typically have isomerizable molecules with relatively large energy differences between the two isomer energies, which result in the vast majority of the equilibrium population being a single isomer that can be photoisomerized by an external light source. If the system is knocked out of equilibrium to a population n_e , it will relax back into equilibrium at a rate $\beta'(n_e - n_e^{(0)}(T))$.

Before proceeding, it is useful to check some of the limiting cases of Eq. (179). In steady state ($dn_e/dt = 0$) for an isolated molecule ($\beta' = 0$), we get the equilibrium population

$$n_e = \frac{\alpha_0 I}{\beta + \alpha I}, \quad (182)$$

giving vanishing excited state population when the system is not excited ($I = 0$) and a population $n_e = \alpha_0/\alpha$ when $I \rightarrow \infty$. With no stimulated deexcitation ($\alpha = \alpha_0$), the system will be fully excited. Otherwise, it reaches a steady state determined by the competition of stimulated excitation and deexcitation. When only thermal equilibrium dominates, the equilibrium excited state population is given by $n_e = n_e^{(0)}(T)$ and decays to equilibrium from non-equilibrium population $n_e(0)$ according to

$$n_e(t) = n_e^{(0)}(T) + (n_e(0) - n_e^{(0)}(T)) \exp[-\beta' t]. \quad (183)$$

All the limiting cases behave as expected.

Now consider Eq. (179) for the steady state ($dn_e/dt = 0$) with no light ($I = 0$), which yields a population

$$n_e = \frac{\beta' n_e^{(0)}(T)}{\beta + \beta'}. \quad (184)$$

When $\beta' = 0$, Eq. (184) correctly predicts that an isolated molecule will be in its ground state. When thermal agitation dominates, so $\beta' \gg \beta$, we get the correct thermal population $n_e = n_e^{(0)}(T)$. When both β and β' are comparable, however, the equilibrium population is between these two limits. This is at odds with the observation that a system in thermal equilibrium (in the absence of external pumping) should have an excited state population $n_e = n_e^{(0)}$.

Resolving these issues requires that we carefully take into account all the physical processes. Recall that β is the spontaneous decay rate of an isolated molecule while β' is the decay rate due to thermal processes, such a collisions between molecules. α and α_0 , on the other hand, describe the transition rates stimulated by the light. This description misses the important fact that the molecules are in thermal equilibrium with the light even in the absence of a pump beam, so the light intensity can never vanish, but rather will have a blackbody spectrum.

As such, the theory needs to be generalized to include both the incident light—which comes from the outside—and the blackbody light—which is emitted and absorbed by the molecules in the ensemble. A hand-waving way to include this effect is to add the blackbody intensity to the incident intensity, or

$$I \rightarrow I + \frac{32\pi^2\omega^2}{c^2} + \frac{1}{\exp[\hbar\omega/kT] - 1}, \quad (185)$$

where ω is the photon frequency and c is the speed of light. When photoisomerization requires a visible photon, a back of the envelop calculation shows that at room temperature the blackbody contribution is negligible compared with typical applied intensities. However, the intensity never vanishes except at zero temperature. When the blackbody spectrum is properly taken into account, the equilibrium population will always be given by $n_e^{(0)}$. The rigorous calculation is beyond the scope of this paper, so will not be formally treated here.

Now getting back to the problem at hand of calculating the population dynamics, integration of Eq. (179) gives

$$\frac{\ln(\alpha_0 I + \beta' n_e^{(0)}(T) - n_e(\alpha I + \beta + \beta'))}{-\beta - \beta' - \alpha I} = t + C, \quad (186)$$

where the integration constant C is determined from the condition $n_e(0) = n_e^{(0)}(T)$, yielding

$$C = \frac{\ln(\alpha_0 I + \beta' n_e^{(0)}(T) - n_e^{(0)}(T)(\alpha I + \beta + \beta'))}{-\beta - \beta' - \alpha I} = \frac{\ln(\alpha_0 I - n_e^{(0)}(T)(\alpha I + \beta))}{-\beta - \beta' - \alpha I}. \quad (187)$$

Substituting Eq. (187) into Eq. (186) and solving for $n_e(t)$, the time dependence of the excited state population of photomorphons after the light is turned on at $t = 0$ is

$$n_e(t) = \frac{\alpha_0 I + \beta' n_e^{(0)}(T) - (\alpha_0 I - n_e^{(0)}(T)(\beta + \alpha I))e^{-(\beta + \beta' + \alpha I)t}}{\beta + \beta' + \alpha I}. \quad (188)$$

When the light is turned off, a similar calculation leads to the decay of excited state population as

$$n_e(t) = n_e^{(0)}(T) + (n_e(t_0) - n_e^{(0)}(T))e^{-(\beta + \beta')(t - t_0)}. \quad (189)$$

$n_e(t_0)$ is the population of excited state photomorphons at the instant the light is turned off after it had acted for a time t_0 . Evidentially, the rise time constant with the light on depends on the power while the decay time constant depends only on $\beta + \beta'$.

This model is general and applies to a broad class of materials. For the special case of a LCE, the time constant is observed to be independent of power [60]. This implies that $\beta + \beta' \gg \alpha I$ for the power range used in those experiments. If this is so, Eq. (188) yields the long-time amplitude,

$$\begin{aligned}
n_e(t \rightarrow \infty) &= \frac{\alpha_0 I + \beta' n_e^{(0)}(T)}{\beta + \beta' + \alpha I} \approx \frac{\alpha_0 I + \beta' n_e^{(0)}(T)}{\beta + \beta'} - \frac{(\alpha_0 I + \beta' n_e^{(0)}(T))(\alpha I + \beta')}{(\beta + \beta')^2} \\
&= \frac{\beta' n_e^{(0)}(T)}{\beta + \beta'} + \frac{\alpha_0}{\beta + \beta'} \left(1 + \frac{\beta' n_e^{(0)}(T) \alpha}{(\beta + \beta') \alpha_0} \right) I + \frac{\alpha_0 \alpha}{(\beta + \beta')^2} I^2. \quad (190)
\end{aligned}$$

In the zero-intensity limit, Eq. (190) yields

$$n_e(t \rightarrow \infty) = \frac{\beta' n_e^{(0)}(T)}{\beta + \beta'}, \quad (191)$$

so if the thermal decay rate is large ($\beta' \gg \beta$), the system's excited state population is $n_e^{(0)}(T)$, as we would expect for a system in thermal equilibrium. If the natural decay rate is large ($\beta' \ll \beta$), then the system will be found in its ground state. If there is no thermal decay, i.e., $\beta' = 0$, then in the low-intensity limit,

$$n_e(t \rightarrow \infty) = I \alpha_0 / \beta, \quad (192)$$

and the excited population grows in proportion to the intensity with slope α_0/β . This makes sense; as the decay rate β decreases, excitation wins over decay. In this limit, the time constant is approximately given by

$$\tau = \frac{1}{\beta + \alpha I} \approx \frac{1}{\beta} - \frac{\alpha}{\beta^2} I. \quad (193)$$

In the high-intensity regime,

$$n_e(t \rightarrow \infty) \approx \frac{\alpha_0}{\alpha} \quad (194)$$

and

$$\tau \approx \frac{1}{\alpha I} \rightarrow 0. \quad (195)$$

The parameters α , α_0 , and β can be determined from measurements of the intensity dependence of equilibrium excited state populations and time in various combinations of the limiting cases.

Even when the average populations of the two species are fixed, the light continually induces conversion between them. When the light is extinguished, the system will decay into its state of thermal equilibrium, where again, thermal agitation causes the molecules in the ensemble to excite and deexcite, keeping the global populations constant.

5.3. Length Dynamics

Starting with populations given by Eqs. (188) and (189), and the thermal excited state population given by Eq. (181), the light-induced strain will be given by Eq. (171), yielding

$$u(I, T, t) = \frac{(x_b - a)}{\ell} \left[\frac{\alpha_0 I + \frac{\beta'}{1+e^{V_0/k_B T}} - \left(\alpha_0 I - \frac{\beta + \alpha I}{1+e^{V_0/k_B T}} \right) e^{-(\beta + \beta' + \alpha I)t}}{\beta + \beta' + \alpha I} \right] \quad (196)$$

after the pump light is turned on and

$$u(I, T, t) = \frac{(x_b - a)}{\ell} \left[\frac{1}{1 + e^{V_0/k_B T}} + \left(n_e(t_0) - \frac{1}{1 + e^{V_0/k_B T}} \right) e^{-(\beta + \beta')(t - t_0)} \right] \quad (197)$$

after the light is turned off. Equations (196) and (197) embody most of the physics of the material having to do with the PM unit within the photomorphon, as we describe below.

First consider thermal expansion, which corresponds to the temperature derivative of the strain with no illumination applied—given by Eq. (196) with $t = 0$ —where the system is in thermal equilibrium. In that case, we get

$$u(T) = \frac{(x_b - a)}{\ell} \left[\frac{1}{1 + e^{V_0/k_B T}} \right], \quad (198)$$

so the thermal expansion coefficient at temperature T_0 is given by

$$\left. \frac{\partial u(T)}{\partial T} \right|_{T=T_0} = \frac{(x_b - a)}{\ell} \left[\frac{\frac{V_0}{k_B T_0^2} e^{V_0/k_B T_0}}{(1 + e^{V_0/k_B T_0})^2} \right] + \left. \frac{1}{\ell} \frac{\partial \ell}{\partial T} \right|_{T=T_0}. \quad (199)$$

The first term in Eq. (199) is the length change of the photomorphon due to the length change of the “average” PM unit in the photomorphon, which depends on the temperature-dependent population of the excited unit. The second term is added *ad hoc* to account for the thermal expansion coefficient of the polymer, which is treated as a passive element and therefore not part of the theory. The second term is understood as the change in photomorphon length due solely to the polymer when the PM unit’s length is unchanged. If the PM unit is a small fraction of the length of the photomorphon, the second term is just the thermal expansion coefficient of the neat polymer, and will dominate thermal expansion.

The photomechanical strain amplitude can be determined as a function of intensity by setting $t \rightarrow \infty$ in Eq. (196), yielding

$$u(I) = \frac{(x_b - a)}{\ell} \left[\frac{\alpha_0 I + \beta' n_e^{(0)}(T)}{\beta + \beta' + \alpha I} \right]. \quad (200)$$

In analogy with Eq. (128), for small I we can define the n^{th} -order photomechanical strain coefficients $\kappa_u^{(n)}$ according to

$$\sigma_u = \sum_{n=1}^{\infty} \kappa_u^{(n)} I^n. \quad (201)$$

Expanding Eq. (200) in a Taylor series in the intensity yields

$$\kappa_u^{(0)} = \frac{(x_b - a)}{\ell} \cdot \frac{\beta' n_e^{(0)}(T)}{\beta + \beta'}, \quad (202)$$

and for $n > 0$ gives

$$\kappa_u^{(n)} = \frac{1}{(n-1)!} \cdot \frac{(x_b - a)}{\ell} \cdot \frac{1}{\beta + \beta'} \cdot \left(\alpha_0 - \frac{\beta' \alpha n_e^{(0)}(T)}{(\beta + \beta') n} \right) \left(-\frac{\alpha}{\beta + \beta'} \right)^{n-1}. \quad (203)$$

When the thermal decay rate is much longer than optical excitation and relaxation time scales, $\beta' = 0$, Eq. (203) gives

$$\kappa_u^{(n)} = \frac{1}{(n-1)!} \cdot \frac{(x_b - a)}{\ell} \cdot \frac{\alpha_0}{\beta} \left(-\frac{\alpha}{\beta} \right)^{n-1}. \quad (204)$$

For large I , we can define the n^{th} -order photomechanical strain coefficients $\kappa_u^{(-n)}$ according to

$$\sigma_u = \sum_{n=0}^{\infty} \kappa_u^{(-n)} I^{-n}. \quad (205)$$

Using Eq. (200) with $\beta' = 0$ yields

$$\kappa_u^{(-n)} = \frac{1}{n!} \cdot \frac{(x_b - a)}{\ell} \cdot \frac{\alpha_0}{\alpha} (-\beta)^n. \quad (206)$$

These expressions hold for $n \geq 1$ in the small intensity limit and $n \leq 0$ in the large intensity regime.

The above theory is limited specifically to the situation where light changes the population of excited photomorphons. However, the theory can be extended, albeit in an inelegant way, to account for other phenomena. For example, energy absorbed from a light beam will heat the material. This heating can result from the energy released during relaxation of the excited PM unit back to its ground state, or from other excitations of the material that do not result in a photomechanical response.

A simple way to include the heating mechanism is to separately model the temperature of the material with the light beam as the heat source, then substituting the temperature into Eqs. (196) and (197) to get the induced strain. Heating thus requires the intermediate steps of applying the heat equation to determine the temperature. Heating is modeled later in this paper as an individual mechanism in terms of the thermal expansion coefficient, independent of its source.

There are complications that arise when heating acts with other mechanisms. An approximate way to model the effect is to assume that photothermal heating and PM unit excitation act independently. This might be a good approximation when the heat leads to thermal expansion of the polymer but does not affect the PM unit. When both are acting, the mechanisms couple, leading to complex interactions, which we do not describe here.

The various model parameters can be determined from measurements of the length of a material as a function of time after it is illuminated. Since visual measurements are limited to frame rates of video capture systems, and the images stored in large data files need to be processed to get this information, length change measurements are not ideal. Force measurements, as described below, are more practical to implement, but the model equations are somewhat messy. Intuition may suffer as a result, but the additional clutter does not adversely affect data analysis.

5.4. Force Dynamics

Using the populations given by Eqs. (188) and (189), and the thermal excited state population given by Eq. (181), the force given by Eq. (172) immediately after the light is turned on can be expressed as

$$F(I, T, t) = \frac{k(x_b - a) \left[\alpha_0 I + \frac{\beta'}{1+e^{\beta_0/k_B T}} - \left(\alpha_0 I - \frac{\beta+\alpha I}{1+e^{\beta_0/k_B T}} \right) e^{-(\beta+\beta'+\alpha I)t} \right]}{\beta + \beta' + \alpha I - \left(1 - \frac{k}{k'} \right) \left[\alpha_0 I + \frac{\beta'}{1+e^{\beta_0/k_B T}} - \left(\alpha_0 I - \frac{\beta+\alpha I}{1+e^{\beta_0/k_B T}} \right) e^{-(\beta+\beta'+\alpha I)t} \right]}. \quad (207)$$

When the light is turned off, the force is given by

$$F(I, T, t) = \frac{k(x_b - a) \left[1 + (n_e(t_0) (1 + e^{V_0/k_B T}) - 1) e^{-(\beta+\beta')(t-t_0)} \right]}{(1 + e^{V_0/k_B T}) - \left(1 - \frac{k}{k'}\right) \left[1 + (n_e(t_0) (1 + e^{V_0/k_B T}) - 1) e^{-(\beta+\beta')(t-t_0)} \right]}, \quad (208)$$

where t_0 is the time the light is turned off and $n_e(t_0)$ is the excited population at t_0 .

In the limit $t = 0$, Eq. (207) becomes

$$F(I, T) = \frac{k(x_b - a)}{e^{V_0/k_B T} + \frac{k}{k'}}, \quad (209)$$

which is just the force due to the excited state population. The force vanishes at zero temperature, where there is no excited state thermal population. For infinite temperature, the force becomes

$$F(I, T) = \frac{kk'(x_b - a)}{k + k'}. \quad (210)$$

When $k = k'$, the force is that of a spring of force constant $k/2$, which makes physical sense since half the springs are in their excited states at infinite temperature. Note that the effect of the polymer can be added by taking into account its temperature dependence in the form of Eq. (199).

In the limit of infinite time, the amplitude of the PM effect given by Eq. (207) is

$$F(I, T) = \frac{k(x_b - a) \left[\alpha_0 I + \frac{\beta'}{1 + e^{V_0/k_B T}} \right]}{\beta + \beta' + \alpha I - \left(1 - \frac{k}{k'}\right) \left[\alpha_0 I + \frac{\beta'}{1 + e^{V_0/k_B T}} \right]}. \quad (211)$$

The stress response can be cast in terms of the photomechanical coefficients $\kappa_\sigma^{(n)}$ in the low- and high-intensity regimes as we have done for the strain response. This is left to the reader.

Using Eq. (181) to place Eqs. (207) and (208) into a more compact form yields

$$F(I, T, t) = \frac{A[\alpha_0 I + \beta' n_e^{(0)}(T) - (\alpha_0 I - (\beta + \alpha I) n_e^{(0)}(T)) e^{-(\beta+\beta'+\alpha I)t}]}{\beta + \beta' + \alpha I - B[\alpha_0 I + \beta' n_e^{(0)}(T) - (\alpha_0 I - (\beta + \alpha I) n_e^{(0)}(T)) e^{-(\beta+\beta'+\alpha I)t}]}, \quad (212)$$

where

$$A = k(x_b - a) \quad \text{and} \quad B = 1 - \frac{k}{k'}. \quad (213)$$

When the light is turned off, we have

$$F(I, T, t) = \frac{A[1 + (n_e(t_0)/n_e^{(0)}(T) - 1) e^{-(\beta+\beta')(t-t_0)}]}{1/n_e^{(0)}(T) - B[1 + (n_e(t_0)/n_e^{(0)}(T) - 1) e^{-(\beta+\beta')(t-t_0)}}. \quad (214)$$

We have cast the time evolution in this form because it is expressed in terms of the independent parameters A , B , $n_e^{(0)}(T)$, α , α_0 , β , and β' . Fits of Eq. (212) and (214) can be applied to understanding the contributing mechanisms and which processes are at work. For example, if light-induced deexcitation from the excited to ground state photomorphon is negligible compared with excitation rates from the ground state,

Eq. (180) predicts that $\alpha = \alpha_0$. Alternatively, if the excited state population is negligible at the measurement temperature, then we can set $n_e^{(0)} = 0$. We stress that given the fact that many types of samples, such as LCEs, are not highly uniform, the data might not be clean enough for a fit to give a set of parameters that definitively determined underlying mechanisms. It is sometimes better to fit the data with the parameters restricted in various ways (such as setting $\alpha = \alpha_0$) to see which fits are the best.

For illustration, if we assume that the initial excited state population is vanishingly small, which is the case when $V_0/k_B T \gg 1$, after the pump light is turned on at $t = 0$, the force given by Eq. (212) evolves according to

$$F(I, T, t) = \frac{A\alpha_0 I [1 - e^{-(\beta+\beta'+\alpha I)t}]}{\beta + \beta' + \alpha I - B\alpha_0 I [1 - e^{-(\beta+\beta'+\alpha I)t}]} \quad (215)$$

The time evolution of the decay process is given by Eq. (214) with $n_e^{(0)} = 0$, yielding

$$F(I, T, t) = \frac{An_e(t_0)e^{-(\beta+\beta')(t-t_0)}}{1 - Bn_e(t_0)e^{-(\beta+\beta')(t-t_0)}} \quad (216)$$

Photothermal heating not only changes the populations, thus leading to a photomechanical response, but the spring constant k also can depend on temperature. These are higher-order effects because they require a two-step process. First, the sample's temperature must increase due to absorption of light. Then, the temperature increase changes the populations or spring constants. At high-enough intensity, these processes might dominate, but should not be significant under typical laboratory conditions.

6. MECHANISMS

There are many microscopic mechanisms that can lead to photomechanical effects. Before considering specific examples, we revisit the response function, as introduced in Subsection 2.2 and applied to the wave equation in Subsection 2.3. In those examples, a body force was applied to excite a wave, but the response function was used to solve for the mechanical wave in regions without body forces.

The body stress can also be related to the applied optical field via a photomechanical response function. For now, we assume that this response is spatially local, so that the body stress at a point in the material is proportional to the field at that point—a condition we later relax. The temporal nonlocality leads to a stress that in general will depend on the electric field at all previous times.

Recall that the response function describes the stress as a function of time in response to an intensity whose time dependence is a delta function. The most common response for many materials is a decaying oscillation, as one would find in a bell after it is struck with a hammer. This ringing response is the solution of the damped harmonic oscillator. As such, we will use this differential equation as an example. The approach for any other type of response can be solved in the same way by starting with the appropriate differential equation. The differential equation for the harmonic oscillator can be generalized to include nonlinear forces simply by making the restoring force a polynomial, which yields

$$\ddot{x} + 2 \sum_{n=1}^{\infty} \gamma_n \dot{x}^n + \sum_{n=1}^{\infty} \omega_n^2 x^n = \frac{F(t)}{m}, \quad (217)$$

where $F(t)$ is the driving force, ω_1 is the frequency of the linear harmonic oscillator that is related to the spring constant k and mass m via $\omega_1^2 = k/m$, and γ_1 is the damping coefficient. The other terms in the series are the nonlinear ones.

To get the response to a delta function impulse, we start by solving Eq. (217) with $F(t) = 0$ using perturbation theory. Expressing the solution as

$$x(t) = \sum_{n=1}^{\infty} \lambda^n x^{(n)}(t), \quad (218)$$

and substituting it into Eq. (217) to first-order, in λ we get

$$\ddot{x}^{(1)} + 2\gamma_1 \dot{x}^{(1)} + \omega_1^2 x^{(1)} = \frac{F(t)}{m} \quad \text{or} \quad \hat{O}_t x^{(1)} = \frac{F(t)}{m}, \quad (219)$$

where

$$\hat{O}_t \equiv \frac{d^2}{dt^2} + 2\gamma_1 \frac{d}{dt} + \omega_1^2. \quad (220)$$

We have recast Eq. (219) in the more compact form by defining the operator \hat{O}_t using Eq. (220).

With no driving force, $F = 0$, the solution to Eq. (219) is of the form

$$x^{(1)} = x_{10} e^{-\gamma_1 t} \cos(\omega t + \phi). \quad (221)$$

Equation (221) is the homogeneous solution, which is the damped oscillator response after a delta function impulse.

To get the value of ω , we substitute Eq. (221) into Eq. (219) with $F(t) = 0$, which yields

$$\omega = \sqrt{\omega_1^2 - \gamma_1^2}. \quad (222)$$

Thus, the oscillating frequency becomes the natural frequency of oscillation when damping vanishes ($\gamma_1 \rightarrow 0$), and critical damping, with no oscillations, is observed when $\gamma_1 = \omega_1$.

Next we seek to determine the inhomogeneous solution for a general driving force $F(t)$, which we can view as being constructed by a sequence of impulses. We posit that this can be accomplished by finding a response function $R^{(1)}(t - \tau)$ such that

$$x^{(1)}(t) = \int_{-\infty}^{+\infty} d\tau R^{(1)}(t - \tau) \frac{F(\tau)}{m}. \quad (223)$$

To see how this approach works, we operate on both sides of Eq. (223) with \hat{O}_t , yielding

$$\hat{O}_t x^{(1)}(t) = \int_{-\infty}^{+\infty} d\tau \hat{O}_t R^{(1)}(t - \tau) \frac{F(\tau)}{m}. \quad (224)$$

Applying Eq. (219) to the left-hand side of Eq. (224) yields

$$\frac{F(t)}{m} = \int_{-\infty}^{+\infty} d\tau \hat{O}_t R^{(1)}(t - \tau) \frac{F(\tau)}{m}. \quad (225)$$

Equation (225) is clearly an identity when

$$\hat{O}_t R^{(1)}(t - \tau) = \delta(t - \tau). \quad (226)$$

Our task is to find a function $R^{(1)}(t - \tau)$ that satisfies Eq. (226). Clearly, any homogeneous solution of Eq. (219) (with $F(t) = 0$) satisfies Eq. (226) everywhere except for the point $t = \tau$. The strategy is thus to find a piecewise function made of the homogeneous solutions, which will obey Eq. (226) away from $t = \tau$ and that the point joining the two regions has the appropriate discontinuity at $t = \tau$ to yield the Dirac delta function.

Let us use the trial response function,

$$R^{(1)}(t - \tau) = A e^{-\gamma_1(t-\tau)} \cos[\omega(t - \tau) + \phi] \Theta(t - \tau), \quad (227)$$

where $\Theta(t - \tau)$ is the step function, which vanishes when its argument is negative and $\Theta(x) = 1$ otherwise. Clearly, Eq. (227) satisfies Eq. (226) away from $t = \tau$. Our goal is to determine the amplitude A which satisfies Eq. (226).

Equation (227) has built-in causality, so the response function vanishes when the response precedes the force, or $R^{(1)}(t - \tau) = 0$ for $\tau > t$. Continuity of the response function requires that it vanish at $\tau = t$, and therefore the phase must be either $\phi = -\pi/2$ or $\phi = +\pi/2$. Either choice will result in the same response function. The displacement as a function of time from a driving force $F(\tau)$ is then given by Eq. (221) to be

$$x^{(1)}(t) = \int_{-\infty}^t d\tau A e^{-\gamma_1(t-\tau)} \sin[\omega(t - \tau)] \frac{F(\tau)}{m}. \quad (228)$$

Assuming that the function in Eq. (227) is the appropriate one, it follows from Eq. (226) that

$$\begin{aligned} & \lim_{\epsilon \rightarrow 0} \int_{t+\epsilon}^{t-\epsilon} d\tau \delta(t - \tau) \\ &= A \lim_{\epsilon \rightarrow 0} \int_{t+\epsilon}^{t-\epsilon} d\tau \hat{O}_t e^{-\gamma_1(t-\tau)} \sin[\omega(t - \tau)] \Theta(t - \tau) \\ &= A \lim_{\epsilon \rightarrow 0} \int_{t+\epsilon}^{t-\epsilon} d\tau \left[\frac{d^2}{dt^2} + 2\gamma_1 \frac{d}{dt} + \omega_1^2 \right] e^{-\gamma_1(t-\tau)} \sin[\omega(t - \tau)] \Theta(t - \tau), \quad (229) \end{aligned}$$

where $\hat{O} R(t - \tau) = 0$ when $t \neq \tau$. Although continuous, the response function is not functionally smooth at $\tau = t$.

The amplitude A can be found by evaluating the integrals in Eq. (229). The left-hand side of Eq. (229) is unity by definition of the Dirac delta function if the limits of integration include $\tau = t$, which it does by construction. Thus, Eq. (229) becomes

$$1 = A \lim_{\epsilon \rightarrow 0} \int_{t-\epsilon}^{t+\epsilon} d\tau \left(\frac{d^2}{dt^2} + 2\gamma_1 \frac{d}{dt} + \omega_1^2 \right) e^{-\gamma_1(t-\tau)} \sin[\omega(t - \tau)] \Theta(t - \tau). \quad (230)$$

Of the three terms in parentheses on the right-hand side of Eq. (230), the integral of the first term is the only discontinuous one at $\tau = t$. To see why this is so, consider the response function that is shown in Fig. 28(a). It has a discontinuity of the time derivative as shown in Fig. 28(b). The other two terms, given by the response function

(second term) and the integral of the response function (third term), vanish because of continuity at $\tau = t$. Consequently, Eq. (230) becomes

$$1 = -A \lim_{\epsilon \rightarrow 0} \theta(t - \tau) \frac{d}{d\tau} e^{-\gamma_1(t-\tau)} \sin[\omega(t - \tau)] \Big|_{\tau=t-\epsilon}^{\tau=t+\epsilon}. \quad (231)$$

Evaluating the derivative in Eq. (231) yields

$$1 = -A \lim_{\epsilon \rightarrow 0} \theta(t - \tau) \left\{ \omega e^{-\gamma_1(t-\tau)} \cos[\omega(t - \tau)] - \gamma_1 e^{-\gamma_1(t-\tau)} \sin[\omega(t - \tau)] \right\} \Big|_{\tau=t-\epsilon}^{\tau=t+\epsilon}. \quad (232)$$

Equation (232) gives the amplitude $A = 1/\omega$, leading to the response function

$$R^{(1)}(t, \tau) = \frac{1}{\omega} e^{-\gamma_1(t-\tau)} \sin[\omega(t - \tau)]. \quad (233)$$

The response to any time-dependent force $F(\tau)$ can be determined using Eq. (228) with $A = 1/\omega$.

Next we consider the second-order correction, where we will directly work from the assumption of a harmonic solution that can be written in complex form. Substituting Eq. (218) into Eq. (217) and keeping terms to order λ^2 gives

$$\ddot{x}_2 + \Omega_2^2 x_2 = -\Omega_2^2 (x_1^2 + x_1 x_1^*). \quad (234)$$

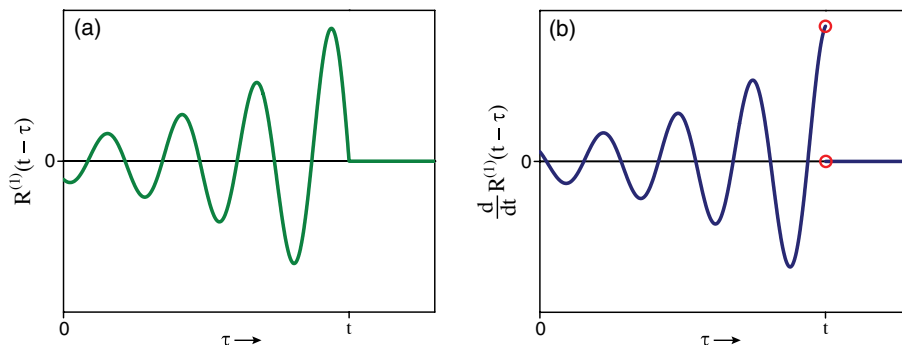
The complex first-order solution given by Eq. (237) acts as a time-dependent source term to the second-order equations. The general solution is intractable, but the special case of the harmonic driving force is solvable, and is an instructive example worth discussion.

Sinusoidal driving force

Here we illustrate the use of the response function for a damped harmonic oscillator driven by a sinusoidal force

$$F(t) = F_0 \cos(\omega' t). \quad (235)$$

Figure 28



(a) Functional form of the under-damped oscillator response function and (b) the time derivative of the response function, which shows the discontinuity at the circled end points.

Using the Euler formula, $\cos \theta = [\exp(i\theta) + \exp(-i\theta)]/2$, and taking either the first or second term, the complex halves of the driving force may be written as

$$F_{\pm}(t) = \frac{F_0}{2} e^{\pm i\omega' t}, \quad (236)$$

where F_0 is a constant. Substituting Eq. (236) into Eq. (228) with $A = 1/\omega$ from Eq. (233) gives

$$x_{\pm}^{(1)}(t) = \frac{F_0}{2m\omega} \int_{-\infty}^t d\tau e^{-\gamma_1(t-\tau)} \sin[\omega(t-\tau)] e^{\pm i\omega' t} = \frac{F_0}{2m} \cdot \frac{e^{\pm i\omega' t}}{\omega_1^2 - \omega'^2 \pm i\omega'\gamma_1}, \quad (237)$$

where we have used the relationship $\omega^2 = \omega_1^2 - \gamma_1^2$. Equation (237) has a resonance at $\omega_1 = \omega'$. Clearly, $x_-^{(1)} = (x_+^{(1)})^*$. After some mathematical trickery, the real response derived from Eq. (237) is

$$\begin{aligned} x^{(1)}(t) = x_+^{(1)}(t) + x_-^{(1)}(t) &= \frac{F_0}{2m} \left[\frac{e^{i\omega' t}}{\omega_1^2 - \omega'^2 + i\omega'\gamma_1} + \frac{e^{-i\omega' t}}{\omega_1^2 - \omega'^2 - i\omega'\gamma_1} \right] \\ &= \frac{F_0}{m\sqrt{(\omega_1^2 - \omega'^2)^2 + \omega'^2\gamma_1^2}} \cos(\omega' t + \vartheta), \end{aligned}$$

where

$$\vartheta = \tan^{-1} \left(\frac{\omega'\gamma_1}{\omega_1^2 - \omega'^2} \right). \quad (238)$$

Substituting Eq. (237) with $x_n = x^{(n)}(t)$ into Eq. (234) yields a differential equation of the form

$$\ddot{x}_2 + \Omega_1^2 x_2 = -\Omega_2^2 (A(\omega)^2 \exp(-2i\omega t) + |A(\omega)|^2), \quad (239)$$

where $A(\omega)$ is defined as the frequency-dependent amplitude of $x_+^{(1)}$ in Eq. (237).

The inhomogeneous solution to Eq. (239) is of the form

$$x_2(t) = a \exp[-i(2\omega t - \phi_a)] + b \exp[i\phi_b], \quad (240)$$

where a , b , ϕ_a , and ϕ_b are real constants. Substituting Eq. (240) into Eq. (239) and projecting out the static and 2ω Fourier components yields the amplitude of the 2ω part

$$a = -\frac{\Omega_2^2 A(\omega)^2 \exp[-i\phi_a]}{\Omega_1^2 - 4\omega^2} \quad (241)$$

and the static part

$$b = -\frac{\Omega_2^2 |A(\omega)|^2}{\Omega_1^2}. \quad (242)$$

The wavelength dependence of the second-order response thus has resonances at $\omega = \omega_1$ and $\omega = \omega_1/2$, where $\omega_i = \text{Re}[\Omega_i]$. For a pump beam with two frequencies, the nonlinear term will couple them, resulting in a sum and difference frequency

response. Resonance is observed when the sum or difference frequency matches the natural frequency of the material.

This derivation parallels the one used to determine the nonlinear-optical response of a classical anharmonic oscillator. Details can be found in textbooks [30].

6.1. Fast Responses

Here we postulate the photomechanical response mechanisms of the fastest possible response.

6.1a. *Electronic Cloud Deformation*

We can use the analogy with nonlinear optics to postulate that the electronic mechanism should lead to the fastest photomechanical response [30]. A beam of light deforms the electron cloud in a molecule, which leads to a change in its dipole moment. This deformation is observed to take about a femtosecond as probed by measurements of light-induced changes of the optical properties of the molecule.

In a bulk material, the net effect is a change in the refractive index. As far as nonlinear-optical mechanisms, the electronic response is the fastest but also the smallest—by far—in magnitude. More massive particles excited nonrelativistically with the same energy move more slowly than do electrons, and therefore have a reduced response function. From the standpoint of virtual states, low-mass particles such as electrons have large delocalized wave functions relative to systems of more massive particles at the same energy.

Because the shape of the electron cloud effectively changes the shape of the molecule, this change should manifest itself as a change in the bulk material. However, the photomechanical effect will be substantially slower than the nonlinear-optical one because the entire atom/molecule, including the nuclei, needs to move on the macroscopic scale in order for the physical shape of the material to change whereas the optical properties depend only on interactions with light and the electron cloud.

To date, the direct electronic effect has not been observed in a bulk material, though the change of electron clouds in molecules is measured routinely in the lab. The indirect effect, where a deformation in the electron cloud initiates slower mechanisms such as the photoisomerization, is commonly observed.

6.1b. *Molecular Reorientation*

Another nonlinear-optical response mechanism that is commonly observed is molecular reorientation [30,63]. This effect is especially pronounced in the liquid phase, where the long axis of many molecules tends to align with the light's polarization axis [64]. In soft solid materials with dye inclusions, the force of the light acting on the molecules should stress the material as they rotate. The reorientational contribution to the optical Kerr effect has a picosecond response time, and its magnitude can be much larger than the electronic one. This is another possible mechanism of the photomechanical response that has not been observed.

Molecular reorientation of the sort described here is distinct from processes in which alignment is lost due to heat or change in the conformation of a dopant molecule within a liquid crystal. In the former, the electric field of the light applies a torque to align a molecule along the light's polarization axis while in the latter case, a change in conformation changes the shape of the molecule and therefore the shape of the surrounding material, or the liquid crystalline order is decreased due to energy deposited by the light, which turns to heat and induces a phase change.

6.2. Electrostriction and Photostriction

6.2a. Electrostriction

A static electric field separates the charges in a dielectric, thus inducing a polarization. The net charge on the surfaces are then acted upon by the same electric field, pulling them apart, thus stretching the material.

For simplicity, we consider an isotropic material, so the polarization is in the direction of the applied electric field. The polarization \mathbf{P} induced by a uniform electric field along \hat{z} , $\mathbf{E} = E\hat{z}$, is given by

$$\mathbf{P} = \chi^{(1)} E \hat{z}, \quad (243)$$

where $\chi^{(1)}$ is the linear susceptibility. Nonlinear terms become important for large electric fields, which we ignore here.

The induced surface charge density σ' is given by

$$\sigma' = \hat{n} \cdot \mathbf{P}, \quad (244)$$

where \hat{n} is the surface normal that points away from the material. Note that because there are not enough symbols available to assign unique ones to all quantities, we must by necessity use the same symbol multiple times. For example, here σ' is the surface charge and otherwise is used to denote stress. We use the “prime” to make it unique, but we warn the reader that the symbols might be confusing, so beware!

In a rectangular solid geometry, such as a thin film, the unit normal—along which the electric field is applied—points in opposite directions on the film’s two surfaces, thus resulting in a different sign in the charge density on these two surfaces. The electric stress (force per unit of surface area in the presence of the electric field) is given by $\sigma = \sigma' E$, so with the help of Eqs. (243) and (244), we get

$$\sigma = \chi^{(1)} E^2. \quad (245)$$

Since the charge density on each surface is of opposite sign, a uniaxial stress results, but there is no net force on the material.

In addition to yielding a strain response

$$u = \frac{\sigma}{E'} = \frac{\chi^{(1)}}{E'} E^2, \quad (246)$$

where E' is Young’s modulus (not to be confused with the electric field E) and u the strain, the electric field compression of the material also leads to an electric field-induced change in the refractive index and optical loss [65]. Both the length change and refractive index change of the material contribute to the quadratic electro-optic and electro-absorption response [65]. Equation (246) defines the electrostrictive constant $\chi^{(1)}/E'$, which relates the square of the electric field to the induced strain.

6.2b. Photostriction

The electric field due to a plane electromagnetic wave can also result in a stress. Using Poynting’s theorem, the intensity of a plane wave, I , is related to the electric field amplitude E through [30]

$$I = \frac{c}{8\pi} n |E|^2, \quad (247)$$

where c is the speed of light and n is the refractive index of the material. Substituting Eq. (247) into Eq. (246) yields the optically induced strain,

$$u = \frac{\sigma}{E'} = \frac{8\pi\chi^{(1)}}{cnE'} I, \quad (248)$$

and optically induced stress,

$$\sigma = \frac{8\pi\chi^{(1)}}{cn} I. \quad (249)$$

The phenomenon represented by Eqs. (248) and (249) is photostriction, and the coefficients are just the stress and strain photostrictive contributions to the photomechanical response,

$$\kappa_{\sigma}^{(1)} = \frac{8\pi\chi^{(1)}}{cn} \quad (250)$$

and

$$\kappa_u^{(1)} = \frac{8\pi\chi^{(1)}}{cnE'}, \quad (251)$$

which corresponds to the first term in the series given in Eq. (128), which defines the general photomechanical response.

6.2c. Field Gradients

Above we calculated the force on the surface of a material due to the interaction of an electric field with a surface charge that is induced by that electric field. An electric field gradient will also result in a force that acts over the volume of the material by acting on the volume density.

For now, we assume without loss of generality that the electric field is applied along the \hat{z} direction and that field also varies as a function of z . The volume charge density ρ is then given by

$$\rho = -\frac{\partial P}{\partial z} = -\chi^{(1)} \frac{\partial E}{\partial z}, \quad (252)$$

where the second equality is evaluated with the help of Eq. (243). Then, the stress on a sheet of charge of thickness dz , which has charge density ρdz due to an applied electric field E , is given by

$$d\sigma = -\chi^{(1)} E \frac{\partial E}{\partial z} dz, \quad (253)$$

where we have used ρ from Eq. (251).

Integrating Eq. (253) over the thickness of the material from $z = 0$ to $z = d$ yields the total stress,

$$\sigma = -\frac{1}{2}\chi^{(1)} (E^2(d) - E^2(0)), \quad (254)$$

The electric fields here can be a static applied field or the amplitude of a propagating electromagnetic field, which leads to electrostriction and photostriction.

6.2d. Experimental Observations

In principle, the photostrictive response should be fast, following the light pulse then decaying after the pulse has passed. The first experiment aimed at measuring the fast

response in a polymer optical fiber was reported by Zhou *et al.* [66]. In these experiments, a mirror is suspended from a vertically mounted fiber, and the fiber's end is probed with a 5 ns duration laser pulse. A second 5 ns pulse is launched into the fiber to induce a length change.

Figure 29 shows the length change data deduced from the optical probe (points), and the curve shows the 5 ns laser pulse. The length change appears to follow the pulse, then decays over a 20 ns time constant, presumably from the relaxation of the polymer. These data were puzzling given the fact that the response time measured is faster than the transit time of sound through the mirror—on the order of microseconds. This issue was never resolved, but the data were reproducible, with the signal disappearing when the light entering the fiber is blocked. Shimamura *et al.* used nanosecond pulses to induce bending in azo-containing cross-linked liquid crystal polymers (LCPs), but observed only a sub-millisecond response, as one would expect [67].

6.3. Photothermal Heating

This section derives the theory of how a material changes shape to light through photothermal heating. Photothermal heating can be a highly efficient process that rapidly increases the temperature of an illuminated material, which responds by thermal expansion. One avenue of material design is to target the photothermal heating mechanism alone. Photothermal heating can also be one mechanism of many that contributes to the photomechanical response, such as photoisomerization and piezoelectricity. Even in materials that are designed to take advantage of the other mechanisms, imperfect energy conversion efficiency of light to these other mechanisms leads to heat, and a photothermal response. This section focuses on photothermal heating. We begin by discussing the basics of thermal flow both in and out of a system as well as its dispersion through a system. We then discuss the thermal-induced strain caused by photothermal heating and heat transport through a photomechanical material.

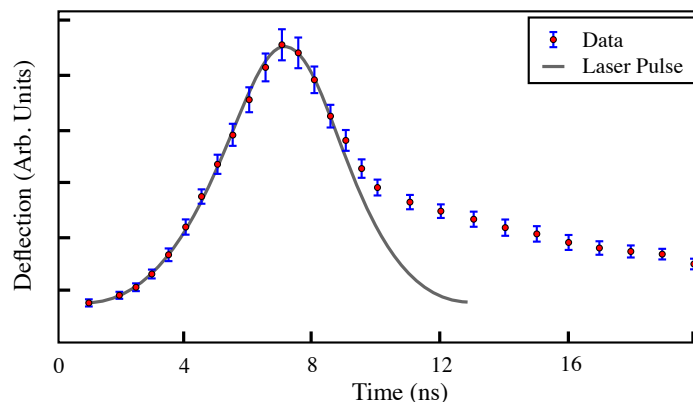
6.3a. Radiative Heat Transfer

All materials at nonzero temperature emit radiation. For simple bulk materials, the intensity radiated from the object's surface, I , is given by the Stefan–Boltzmann law,

$$I = \varepsilon \sigma T^4, \quad (255)$$

where σ is the Stefan–Boltzmann constant (which can be expressed in fundamental constants through a derivation via the Planck law), T is the absolute temperature at the

Figure 29



Measured deflection of the mirror (points) and the laser pulse (curve).

surface of the object, and ε is the material's emissivity. Similarly, the object's surface absorbs radiation from its surroundings via the same Stefan–Boltzmann law.

The emissivity of a material holds the same value for both emission and absorption of radiation when described by the classical thermodynamic Stefan–Boltzmann law. A highly emissive/absorptive material is called a “blackbody” with $\sigma \approx 1$, and a weakly emissive/absorptive material is called a “white body” in which $\sigma \approx 0$. Suppose an object's surface is at a temperature T_{obj} and placed in an environment with ambient temperature T_{amb} . The net intensity flowing from the object's surface to its surroundings is

$$I = \varepsilon\sigma(T_{\text{obj}}^4 - T_{\text{amb}}^4). \quad (256)$$

There are several assumptions underlying the Stefan–Boltzmann law. Specific material systems can be made to exchange radiative energy in several ways that can dominate the response relative to the weak radiative transfer mechanism assumed by the Stefan–Boltzmann law. Methods of radiative energy transfer such as those using directed energy beams will be later discussed.

6.3b. *Conductive and Convective Heat Transfer*

Heat transfer between an object's surface and its surroundings can be mediated by the transfer of microscopic kinetic energy from particles at the interface. This type of heat transfer is called “conduction” and requires particles of nonzero mass to be in contact with the object. The heat flow $\partial Q/\partial t$ into or out of a body enclosed by a surface S and surrounded by a medium that can transfer thermal energy is given by Fourier's law,

$$\frac{\partial Q}{\partial t} = - \oint_S k(\nabla T) \cdot d\vec{A}, \quad (257)$$

where k is the thermal conductivity, and dA is the contact area element with heat flowing in the direction normal to the interface at the closed surface. The minus sign signifies that the heat flows from a region of higher temperature to a region of lower temperature. Note that the thermal conductivity k depends on the physical properties of the object at its surface and the material/medium with which it is in contact. The thermal conductivity can also vary across the contact surface, and in general, this contribution will be added to all others when evaluating the heat flow in or out of a closed region of material.

Equation (257) can also be rewritten in terms of the heat flux density \vec{q} , where the heat flux density vector is oriented in the direction opposite to the local temperature gradient, $-\nabla T$. Thus, Fourier's law in differential form is given by

$$\vec{q} = -k(\nabla T). \quad (258)$$

The temperature of the masses that mediate conduction with the object can change over time. To simplify the treatment of the transient response, all masses in contact with the object are often assumed to have a static temperature. In practice, this assumption is typically implemented by adding a large heat sink made of a material with a large heat capacity and either a large mass or thermal diffusivity (explained later in detail) or by continuously replacing the contact masses with new masses at the same temperature. The latter process is called “convection.” Multistage convection processes are often found in automobiles with heat engines, where a mixture of water and ethylene glycol is cycled through the engine to remove heat from it; the mixture is then cycled through a radiator to transfer the heat to flowing air molecules.

If the diffusion of heat through the object is much faster than the rate at which heat flows through the object's surface, in the absence of material composition changes, and when heat is being generated within the material, then we may assume that the entire object is at a uniform temperature. If the object as a whole may be treated as a single entity, at a single temperature for a given time while interacting with its environment, then the object may be treated via a "lumped-sum analysis" (LSA).

When the dominant heat transfer mechanism at the surface of an object is conductive via an ideal heat sink or through ideal convection, the medium to which the heat is transferred is at constant and uniform temperature. If the macroscopic properties at the interface are also unchanged, then the rate at which heat is transferred to or from the object's surface is constant. Under such circumstances, an object characterized through a LSA with temperature T and surface area A will transfer heat through the surface as a function of time only, so

$$\frac{\partial Q}{\partial t} = -\kappa A(T - T_0), \quad (259)$$

where κ is the lumped heat transfer coefficient and T_0 is the temperature of the contact mass. Note that the minus sign implies "Newton cooling" when $T_0 < T$; under the same preliminary conditions, Eq. (259) gives heating when $T_0 > T$.

6.3c. Diffusion of Heat through a Material

We previously encountered cases that treat an entire object as having a single temperature. This LSA approach works well for small objects that internally conduct heat well while slowly exchanging heat at their boundaries. In practice, heat propagates through an object at a finite speed, and the transfer of heat from one location in a material to another occurs via the same mechanisms as the transfer of heat between objects.

Imagine an interface between two adjacent locations in a material. If these two locations are at different temperatures, then radiative heat transfer, conduction, and convection are all possible forms of heat flow. In a typical material, the mechanisms for heat flow are dominated by conduction between adjacent points. Thus, in the derivation of the heat equation that follows, we will assume that conduction is the only acting mechanism.

For any closed surface, the net heat flowing through it is given by

$$\oint_S \vec{q} \cdot d\vec{A} = \oint_S (-k\nabla T) \cdot d\vec{A} = \int_V [\nabla \cdot (-k\nabla T)] dV. \quad (260)$$

The first equality comes from the definitions of \vec{q} via Eqs. (257) and (258), and the final equality is the divergence theorem with a volume \mathcal{V} enclosed by the surface S . Because energy must be conserved, the change in the energy per unit time in the enclosed region $\partial Q_S/\partial t$ plus the amount of heat entering or leaving the system per unit time is zero when there are no sources of heat in the enclosed region, and following Eq. (260) is given by

$$\frac{\partial Q_S}{\partial t} + \int_V [\nabla \cdot (-k\nabla T)] dV = 0. \quad (261)$$

Next we seek to simplify Eq. (261). The heat capacity of a material is defined by

$$\delta Q_S = C\delta T. \quad (262)$$

The specific heat capacity c is the heat capacity of a material per unit mass, which can be used to get the heat capacity of an heterogeneous body via

$$C = \int_{\mathcal{V}} c(\vec{r})\rho(\vec{r})dV, \quad (263)$$

where the mass is calculated from the density $\rho(\vec{r})$ and volume element dV according to

$$m = \int_{\mathcal{V}} \rho dV. \quad (264)$$

Note that we assume that the material is in thermal equilibrium so the temperature is uniform. Then Eqs. (262–264) give

$$\delta T \int_{\mathcal{V}} c(\vec{r})\rho(\vec{r})dV = \delta Q_S \rightarrow \frac{\partial T}{\partial t} \int_{\mathcal{V}} c(\vec{r})\rho(\vec{r})dV = \frac{\partial Q_S}{\partial t}. \quad (265)$$

Substituting Eq. (265) into Eq. (261) yields

$$\frac{\partial T}{\partial t} \int_{\mathcal{V}} c(\vec{r})\rho(\vec{r})dV = \int_{\mathcal{V}} [\nabla \cdot (k\nabla T)]dV. \quad (266)$$

Equation (266) is the general heat equation, which assumes very little. To further simplify Eq. (266), we may assume that c and ρ are independent of position. Under such cases, Eq. (266) reduces to a partial differential equation, given by

$$\frac{\partial T}{\partial t} = \nabla \cdot (D\nabla T), \quad (267)$$

where the thermal diffusivity is defined as

$$D = \frac{k}{c\rho}. \quad (268)$$

Note that even when ρ and c are constants, the thermal diffusivity D is still a tensor quantity with position and time dependencies due to the nature of the thermal conductivity k . If we also assume that k is a scalar quantity that is independent of position and time, then Eq. (267) reduces to a simple partial differential equation that is first order in time and second order in space given by

$$\frac{\partial T}{\partial t} = D\nabla^2 T. \quad (269)$$

Note that we have only included heat conduction as a mechanism for heat transport. Convection currents will add an additional first-order spatial derivative term to Eq. (269), which results in an equation known as the advection-diffusion equation. We have also assumed that c , ρ , and k are constants in deriving Eq. (269), which is not always true due to temporal changes in the material (reversible and irreversible) as well as spatial inhomogeneities and anisotropy.

It was noted above that the thermal diffusivity is a tensor quantity due to the thermal conductivity for crystalline and semicrystalline materials. In Cartesian coordinates, the anisotropic heat equation, absent of any mass transport phenomena, may be stated with simplicity using the component form,

$$\frac{\partial T}{\partial t} = \sum_{i=1}^3 \frac{\partial}{\partial x_i} \sum_{j=1}^3 D_{ij} \frac{\partial}{\partial x_j} T, \quad (270)$$

where the components x_1 , x_2 , and x_3 are, respectively the x , y , and z components in Cartesian coordinates.

6.3d. Boundary and Initial Conditions

The boundary conditions at the surface of the object being described will specify, for example, the heat flowing into or out of the surface and the temperature at the boundaries. There are many possible boundary conditions that could be specified, but we will present only a few common ones.

Dirichlet boundary conditions specify the value of the function being evaluated at the boundary. For the heat equation, the temperature is explicitly stated at every position on a particular boundary as a function of time. Suppose we have a box with sides of lengths L_x , L_y , and L_z along the x , y , and z axes, respectively, as shown in Fig. 30. The Dirichlet boundary condition for the box's face in the $y-z$ plane at $x = 0$ is given by

$$T(x = 0, y, z, t) = f(y, z, t). \quad (271)$$

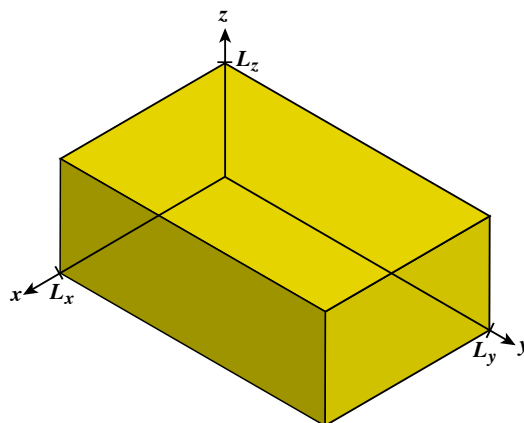
The function f specifies the temperature T over the $y-z$ plane at time t . The temperature at the other boundaries can be prescribed in the same manner.

Neumann boundary conditions specify the gradient of the function being evaluated at the boundary, which we may apply to the heat equation by specifying the temperature gradient at a boundary. Using the same box shown in Fig. 30, the Neumann boundary condition for the face in the $x-y$ plane at $z = L_z$ follows as

$$\left. \frac{\partial}{\partial z} T(x, y, z, t) \right|_{z=L_z} = f(x, y, t). \quad (272)$$

Here, the function f is used to describe the temperature gradient normal to the boundary interface (along the z axis in this example). Neumann boundary conditions are imposed when there is a known temperature gradient due to heat flowing into or out of the object at the boundary. When the gradient is set to zero with $f(x, y, t) = 0$, then

Figure 30



Box-like object in Cartesian coordinates in which heat flows.

this type of boundary condition represents a perfectly insulated surface with no heat flowing into or out of that boundary.

A third commonly used boundary condition is often referred to as the Robin boundary condition. This condition relates the gradient at the boundary to the function being evaluated at the boundary. The Robin boundary condition in the context of the heat equation for the face in the $x-z$ plane at $y = 0$ is given by

$$\left. \frac{\partial}{\partial y} T(x, y, z, t) \right|_{y=0} = f(x, z, t) T(x, y = 0, z, t) + g(x, z, t). \quad (273)$$

With an appropriate choice of functions and dimensions for the arbitrary functions f and g , where g is proportional to the temperature of the object in contact with the material, the Robin boundary condition can be used to describe conductive heat flow through the boundary.

Note that there are many other possible types of boundary conditions that can be relevant to the heat equation; for example, one can specify radiative heat transport between the surface of an object and its surroundings. Objects with lengthy dimensions can be approximated as infinite or semi-infinite, where boundary conditions can be constructed to maintain a convergent solution.

The heat equation is also first order in time. Thus, only one condition is required in time. The simplest, and by far the most commonly used condition, defines the temperature profile at some given time, and then one solves the heat equation forward in time from that moment. This temperature profile at a snapshot in time is called an “initial condition,” where the time is usually set to zero, and takes the form

$$T(x, y, z, t = 0) = f(x, y, z). \quad (274)$$

6.4. Heat Sources/Sinks and Photothermal Heating

Above, we have described how the temperature of an object can change through heat diffusion and the role of the surface in permitting heat to enter and exit the object according to the boundary conditions. Heat can also be generated or absorbed inside an object. A common example is a chemical reaction occurring in a localized region within a body. When the reaction is exothermic, it generates heat and is called a heat source. The region is called a heat sink when heat is absorbed by an endothermic reaction. Joule heating is another common mechanism that deposits heat inside a body, for example, by passing an electrical current through a conductor.

Light energy absorbed in a material typically excites it into a state of higher energy. This higher energy state can correspond to electrons being excited to higher energy eigenstates of the material or altogether being ejected from it when the photons are of high-enough energy such as with ultraviolet (UV), x rays, and gamma rays. Electrons that remain within the object can relax back into the ground state by re-emitting a photon, causing a change in the chemical potential through reactions or isomerization, or by transferring their energy to the surrounding material. The last process can result in either acoustic waves, or more commonly, disordered energy in the form of heat.

Because we are interested in photomechanical processes, we will focus on heat generation within a material due to light absorption. The heat equation is purely classical, and therefore, a classical electromagnetism approach is best suited to tackle the problem.

For light traveling in a region of space, the Poynting vector $\vec{S} = \vec{E} \times \vec{H}$ describes the flow of energy through an area. The intensity vector of each beam is defined by the time-averaged Poynting vector $\langle \vec{S} \rangle = \vec{I} = \langle \vec{S} \rangle$. The divergence of the Poynting vector $\nabla \cdot \vec{S}$ represents the instantaneous energy density flowing out of the enclosed region of space. For simplicity, let us assume a traveling electromagnetic wave in one dimension. Thus, dS/dx describes the instantaneous energy density flowing between two adjacent regions of space along the line of propagation. The spatial derivative of the time-averaged Poynting vector dI/dx , however, describes the change of average power per unit area, the intensity, of a beam between adjacent regions in space along the line of propagation. Thus, for a linear lossless dielectric medium $dI/dx = 0$ while dS/dx will be the instantaneous change of the propagating wave's energy density.

For a linear lossy material, the change in intensity is proportional to the intensity, $dI/dx \propto I$, which is referred to as Lambert's law, or sometimes the Beer–Lambert law. For a homogeneous and isotropic material, the heat equation with a heat source occurring from the absorption of a single beam of light traveling in the x direction can be written as

$$\frac{\partial T}{\partial t} = D\nabla^2 T - \alpha \frac{d}{dx} I(\vec{r}), \quad (275)$$

where α is the fraction of lost energy that generates heat. Equation (275) can be expressed in terms of the power $P(\vec{r}, t)$ by simply integrating over a cross-sectional area of constant phase passing through the point x .

For a monochromatic plane wave at low intensity, the amount of light absorbed in a cross-sectional area passing through x follows the Beer–Lambert law given by

$$\frac{d}{dx} P(x, y, z, t) = \zeta(x, y, z, t) P(x, y, z, t), \quad (276)$$

where we are using Cartesian coordinates and $\zeta(x, y, z, t)$ is the linear attenuation coefficient with dimensions of inverse distance. Note that ζ quantifies the light energy lost to all forms, not just heat.

Nonlinear effects are not included in the Beer–Lambert law, so the attenuation coefficient is assumed to be independent of the intensity. Thus, there is no intensity-dependent absorption. Such nonlinear effects, when added to Eq. (276), will result in a nonlinear differential equation that can be approximately solved [30], but such a derivation is beyond the scope of this section. Also note that more complex expressions for power attenuation are required when scattering is no longer negligible or when the material undergoes a phase change from photothermal heating. Scattering will be ignored here, but phase changes will be treated later. During processes that change the material, such as changes in the population of absorbers which result in optical hole burning, the attenuation coefficient will depend on time. Evidence of optical hole burning is often observed in photomechanical materials doped with azo-containing chromophores with long-lived cis states [55,56,68,69].

When the material is illuminated by a monochromatic beam, the coefficient can be written as

$$\zeta = A \sum_i \xi_i c_i, \quad (277)$$

where ξ_i represents the wavelength-dependent dimensionless coefficients that originate in the quantum constituents of the material and c_i represents the concentrations of the various types of absorbers. Note that when a specific type of absorber can be

excited to a long-lived state such as the case for trans-to-cis photoisomerization, then the local concentration of the trans isomer absorbers $c_t(x, y, z, t)$ changes as a function of time—the definition of optical hole burning. The long-lived excited state may also absorb light at the same wavelength and becomes a contributing absorber to $\zeta(x, y, z, t)$ in Eq. (276).

The simplest example of an intensity depth profile can be observed in photomechanical materials that are solely driven by the photothermal heating mechanism. For a uniform distribution of dopant chromophores that quickly relax back to the ground state after absorbing a photon, the concentration will be time-independent. Then, the solution to Eq. (276) for a beam traveling in the positive x direction follows as

$$P(x) = P_0 e^{-\xi c A x}, \quad (278)$$

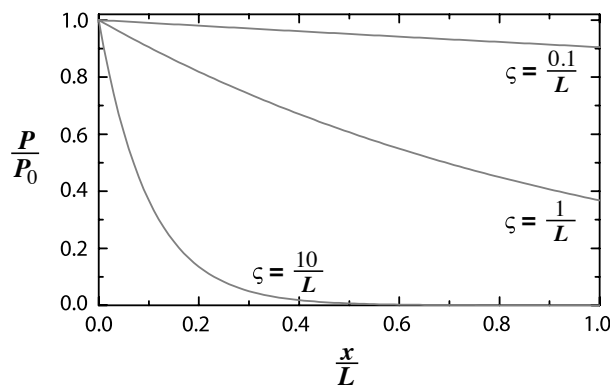
where P_0 is the light's power crossing the plane $x = 0$. Note that the solution shown in Eq. (278) based on many simplifying assumptions is also commonly referred to as the Beer–Lambert law, which was empirically determined by Beer. However, it should be emphasized that Eq. (278) is a special case of Eq. (276). The graph in Fig. 31 plots the power as a function of distance through a material of length L for three different constant values of ζ in Eq. (278). This power profile will be used as the source of heat in the material under the approximation that the mechanism is purely heating when the populations do not change over time.

It is worth noting that some disciplines and analysis tools quantify the absorbance of a material of thickness L as $\zeta' = -\frac{1}{L} \log_{10}(\frac{P}{P_0})$ as opposed to using $\zeta = -\frac{1}{L} \ln(\frac{P}{P_0})$. The two are related via $\zeta = \zeta' \ln 10$ or $\zeta = \zeta' \log_{10} e$. The conversion factor is $\log_{10} e = 1 / \ln 10 \approx 0.434$.

Equation (278) is a good approximation for the power when the sample is illuminated with a directed beam at the $x = 0$ boundary. The coefficient α is positive for beams directed in the positive x direction and negative for light propagating in the opposite direction. Long path lengths relative to the attenuation coefficient will result in a heat generation term with a decaying magnitude along the path of the beam through the material. A thin-enough material will uniformly generate heat throughout.

The Beer–Lambert law accurately describes the attenuation of light for short-lived excitations of absorbers when there are many more of them than potentially absorbed photons. Even with few absorbers per photon, the law is accurate for a short duration

Figure 31



Dissipation of power through a material of length L for different attenuation coefficients.

of time. Saturable absorption kicks in when the excited state lifetime exceeds the mean time between absorptions in a molecule.

When a material is saturated with light, the attenuation coefficient depends on the power and thus on the depth, which can be approximated by

$$\zeta = \frac{\zeta' P_0}{P_0 + P}. \quad (279)$$

In the steady-state approximation with constant ζ' , the profile of saturable absorption from a directed laser beam is determined by the expression

$$\frac{\partial P}{\partial x} = -\frac{\zeta' P_0}{P_0 + P} P. \quad (280)$$

Note that Eq. (280) assumes that the excited state lifetimes do not depend on the illumination intensity.

6.4a. Thermal Expansion

When matter is heated, the particles increase their kinetic energy. Although some materials can have either a thermally induced longitudinal expansion or contraction along a single direction, such as with nematic LCEs, there will be a net volumetric thermal expansion when the temperature change is too small to induce a phase change. Note that we are only considering reversible thermal expansion. In contrast, some materials can be engineered with internal stress that can shrink considerably upon heating for the first time [70]. At a uniform temperature T , the volume of a material is $V(T)$, where the volume can be expressed as a Taylor series expansion with respect to a reference volume and temperature $V(T_0)$,

$$V(T) = V(T_0) + \sum_{n=1}^{\infty} \frac{d}{dT} V(T) \Big|_{T=T_0} \frac{(T - T_0)^n}{n!}. \quad (281)$$

When the change in volume is sufficiently small, the expansion can be terminated to include only the linear term, yielding

$$V(T) \approx V(T_0) + \frac{d}{dT} V(T) \Big|_{T=T_0} (T - T_0). \quad (282)$$

For a small change in volume as $\Delta V = V(T) - V(T_0)$ and defining $V_0 = V(T_0)$, Eq. (282) may be re-expressed as

$$\frac{\Delta V}{V_0} \approx \beta_V (T - T_0), \quad (283)$$

where β_V is the coefficient of volumetric thermal expansion given by

$$\beta_V = \frac{1}{V_0} \frac{d}{dT} V(T) \Big|_{T=T_0}. \quad (284)$$

The expansion/contraction of a material of length $L(T)$ along a material axis can be formulated in the same way. The engineering strain from a change in temperature is given by

$$\frac{\Delta L}{L_0} \approx \beta_L (T - T_0), \quad (285)$$

where β_L is the coefficient of linear thermal expansion given by

$$\beta_L = \frac{1}{L_0} \left. \frac{dL(T)}{dT} \right|_{T=T_0}. \quad (286)$$

The strain approximation in Eq. (285) assumes a uniform temperature distribution; however, temperature gradients in an otherwise homogeneous material can cause shear stress in addition to normal stress.

Note that the relationship in Eq. (285) is independent of time, where we have derived such an approximation in the quasi-static regime. This approximation usually holds; however, one could expect a delayed response in the case of laser heating. The response time will have several factors associated with it where physical phenomena such as heat diffusion through the material, the rate at which heat enters or leaves the boundaries, and the time-dependent strain in response to changes in the stress may need to be addressed.

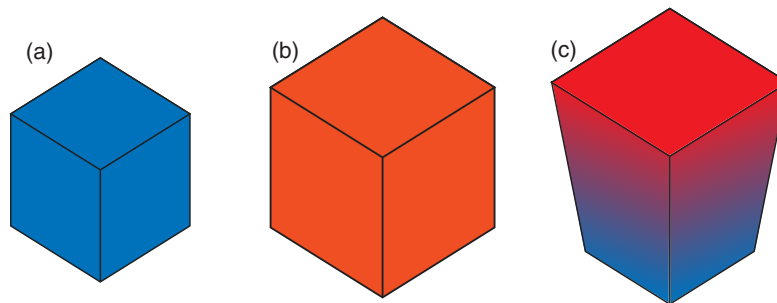
6.4b. Photomechanical Effect via Photothermal Heating

The photothermal mechanism of the photomechanical effect starts with light absorption, which increases the temperature of the material through photothermal heating. The increase in temperature induces a mechanical strain as the material expands and/or contracts along its axes. Here we give an example of a quasi one-dimensional system.

Suppose a box-like structure made of a homogeneous and isotropic material is heated with a laser. A plane wave of light is launched into the upper face of the material, so the face is uniformly illuminated. Both the illuminated face and the opposing face have equally conductive boundaries. The other four sides are assumed to be perfectly insulating. Thus, heat can flow through the box between the upper and bottom faces of the box, but not out the sides, making the problem one-dimensional.

Prior to illumination, the structure has a uniform temperature as shown in Fig. 32(a). When illuminated at a wavelength that is weakly absorbed through the material, the photothermal heat source is approximately uniformly distributed through the entire volume. Therefore, the bulk material is subject to the same local stress everywhere and expands to the larger volume shown in Fig. 32(b) when reaching steady state. When the laser light is at a wavelength that is strongly absorbed by the material,

Figure 32



Box made from a homogeneous and isotropic material that conducts heat at its upper and lower surface while being perfectly insulating on all other four sides. (a) A box in the dark in thermal equilibrium with the environment. The steady-state temperature distribution for a box illuminated through its upper surface for (b) small and (c) large optical absorbance. Red is hotter, and blue is cooler.

then most of the light is absorbed near the upper surface. The temperature in the steady state thus decreases as a function of depth into the material. As illustrated in Fig. 32(c), thermally induced strain is greatest at the illuminated face.

Next suppose that the material is formed into a thin flat disk, as shown in Fig. 33(a), and is made of the same isotropic material. The curved edge of the disk is an ideal insulator, and the flat surfaces are ideal heat conductors. The circular face is uniformly illuminated. When the disk weakly absorbs the laser light, heat is generated nearly uniformly through the material, and the disk expands as illustrated in Fig. 33(b). When the disk has a high coefficient of attenuation, then most of the heat is generated at the illuminated surface of the disk. The heating near the surface causes a temperature gradient, where the outside edge of the disk bends away from the laser source as shown in Fig. 33(c).

Note that in the case of the box, there will also be a small amount of bowing of this sort, but it will be negligible for a cube but will bow as the box gets thinner and becomes a sheet.

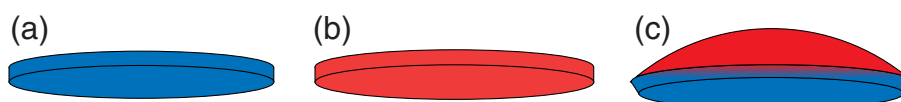
6.5. Photochemical Changes in Structure

This section describes the mechanisms of reversible and irreversible material deformations that originate from photochemical processes. There are several photochemical reactions that can cause irreversible changes in organic molecules [71], which lead to irreversible deformations in the bulk material. “Shape-memory” materials, for example, are designed to irreversibly change shape when illuminated [72–75]. The focus of this section is on processes that can result in reversible deformations, such as photoisomerization of molecules.

6.5a. Isomers

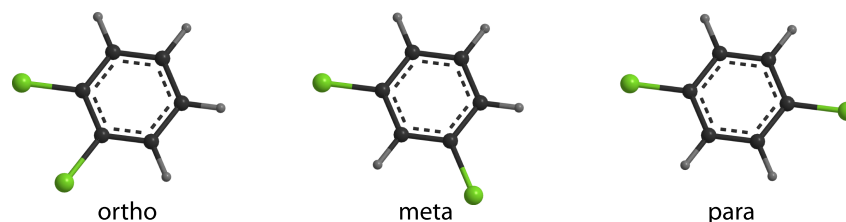
A molecule is an isomer of another molecule if it has the same number of atoms of each of its elements, but the types of bonds and general relative positions of some or all atoms are different [33,76]. Examples of isomers are given in Fig. 34, which shows

Figure 33



Thin disk made from a homogeneous and isotropic material that conducts heat equally through both flat surfaces but is insulating around its thin surface. (a) A disk in the dark and in thermal equilibrium with the environment. The steady-state temperature profile for a disk whose upper surface is illuminated when optical attenuation is (b) small and (c) large.

Figure 34



Structures of the ortho-, meta-, and para-dichlorobenzene isomers.

three different forms of dichlorobenzene. Isomers can have very different physical and optical properties relative to one another.

The simplest process for converting between isomers involves a proton that moves to a different site—a process called tautomerization. Tautomers can be formed by the transfer of a proton across a large molecule or by relocating it within a functional group.

Keto–enol tautomerization is an example of such proton motion. The two isomers acetaldehyde and vinyl alcohol are given in Fig. 35, where protons exchange thermally at room temperature. Acetaldehyde is much more stable in atmosphere than vinyl alcohol, so it dominates the population of molecules at room temperature [77]. Some tautomers can spontaneously convert between forms at room temperature while others need to first be excited by absorbing a photon through a process called phototautomerization. Such light-induced properties are thought to be responsible for some self-healing observations in dye-doped polymers [78–84].

6.5b. Photoisomerization

The process by which an illuminated molecule converts into another general isomeric form is called photoisomerization. Note that phototautomerization is a special case of photoisomerization. A simple four-state model catches the fundamental processes underpinning photoisomerization.

Figure 36 shows three views of the photoisomerization process. Figure 36(a) shows an energy surface diagram, Fig. 36(b) shows an energy level diagram, and Fig. 36(c) shows a picture of a molecule under various excitations where the red clouds represent the electrons and the black lines represent the bonds that connect the atoms in a molecule.

The energy surfaces, as shown in Fig. 36(a) by the parabolic curves, are plot of the energies as a function of nuclear coordinates. For a three-dimensional molecule made of N atoms, there are $3N$ nuclear coordinates. Figure 36(a) necessarily focuses on one generic coordinate. Note that these coordinates need not be the positions of nuclei but rather can be some more complicated function of coordinates that describe the shape, such a bond angle or length.

We begin by describing a few properties of energy surfaces, then we will move on to tracing a path on the surface to describe the sequence of events that changes the conformation of a molecule.

Electrons are much less massive than nucleons, so they respond to light instantaneously on time scales that nucleons react. A vertical excitation as represented by the arrow going from point 1 to point 2 results in the deformation of the electron cloud while the nuclei remain fixed, as shown in Fig. 36(c) corresponding to point 1 and point 2.

Figure 35



Structure of acetaldehyde and its tautomer vinyl alcohol.

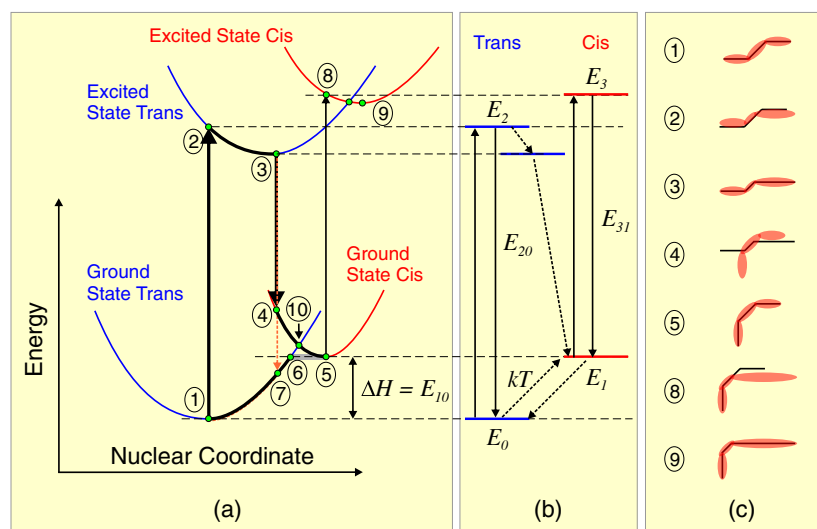
The lowest energy of the molecule in Fig. 36 is at point 1. Thermal excitations can cause a molecule to rotate or vibrate, which corresponds to motions of the nuclei, so follow the parabolic arc around point 1. In a sense, each isomer is a distinct molecule. Shown in Fig. 36 are the trans molecule (blue parabolas) and cis molecule (red parabola). The lowest energy state of the cis molecule corresponds to point 5. Light excitation of the cis isomer in its ground state will take it to point 8, resulting in a deformation of the electron cloud while the nuclei remain fixed as shown in Fig. 36(c). We thus refer to the parabola with the lowest minimum energy on the parabola as the ground electronic state manifold for that molecule, the next highest parabola as the first electronic excited state manifold, etc. The term manifold refers to the fact that for each electronic excitation, there are many possible energies depending on the positions of the nuclei.

Now we begin by describing the photoisomerization process by following the dark black loop starting and ending at point 1. The reader should study the corresponding points on Fig. 36(c) to understand how and where the shape changes.

The ultra-fast excitation from point 1 to point 2 upon the absorption of a photon deforms the electron cloud but leaves the nuclei fixed. The excited molecule can then either deexcite back to point 1 by emitting a photon or will slowly relax to point 3 as the nuclei adjust to the changed shape of the new electron cloud. The relative probability of the two choices is called the branching ratio. The path from point 2 to point 3 is called a non-radiative relaxation when heat is released instead of a photon. Note that the electron cloud will also continuously deform as the nuclei move, but we have kept the shape the same to avoid unnecessary complications that this would add to the discussion.

Once the system reaches point 3, it can deexcite to point 7 by emitting a photon, taking it to the ground state manifold of the trans isomer where the nuclei are oscillating along the parabola, or to the ground state manifold of the cis isomer at point 4. If the system transitions to point 4, the nuclei will remain unchanged, and the electron cloud will deform, emitting a photon in the process. This emitted photon is of lower energy

Figure 36



(a) Energy surface diagram, (b) energy level diagram (showing only key levels required for the discussion in the text), and (c) a highly schematic representation of the configuration of the nuclei (solid lines) and electron clouds (red areas) for the various stages of the photoisomerization process.

than the originally absorbed photon that excites the trans molecule. From there, the electrons will relax non-radiatively to point 5. From point 4, there is also a chance that the system will cross over back to trans ground state manifold when crossing point 10.

Point 5 is classically stable, so the molecule would live in that state indefinitely. However, thermal or quantum tunneling will eventually take the system from point 5, corresponding to the ground state of the cis isomer to point 6 from where it will relax back into the ground state of the trans monomer at point 1. The state at point 5 is long-lived enough for the population to persist for times scales exceeding seconds.

The path that goes through points 1, 2, 3, 7 and back to 1 is the common fluorescence cycle, where light is absorbed followed by a delayed emission of a lower energy photon without a change of isomer conformation.

Figure 36(b) represents the energy level diagram of a molecule that is initially in its ground state of energy E_0 . Such diagrams focus on the important energies and ignore the details of the non-radiative processes, which are shown as dashed lines. The excitation to the state with energy E_2 (vertical upward arrow) is mediated by the absorption of a photon. The molecule can then decay back into its ground state of energy E_0 (down arrow) or can non-radiatively decay into the lowest energy of the first excited state manifold of the trans isomer, then to the cis isomer at energy E_1 (diagonal dashed arrow) in which the nuclei have been rearranged. The state of energy E_1 is thus the ground state of a cis isomer, which is distinct from the trans isomer of ground state energy E_0 . This conversion between one isomer and another one is characteristic of photoisomerization.

A cis isomer of energy E_1 can relax back to the ground state of the trans isomer. Likewise, a trans molecule of energy E_0 can be thermally excited into the ground state of the cis isomer of energy E_1 . These isomerization routes are designated by the dashed arrows going into and out of the states with energy E_1 and E_0 as shown in Fig. 36(b). Note that thermal excitations to the states of energy E_2 and E_3 are improbable because of the large energy gap. Furthermore, an excitation from one isomer in its ground state to the excited state of the other isomer is even far less likely because both the electrons need to be excited and the nuclei need to be rearranged. Note that in the decay from the excited trans isomer to the ground state cis isomer, the intermediate state is often not shown. Thus, the four-level model captures the fact that there are two isomers of different structures, each having two electronic states; that is, the nuclear positions do not change for excitations from states of energy E_0 to E_2 or from E_1 to E_3 . Thus, an isomer in the E_1 energy state will have an absorption spectrum characterized by a peak at energy $E_3 - E_1$, and the isomer with ground state energy E_0 will have an absorption spectrum with a peak at energy $E_2 - E_0$.

In Fig. 36, we have chosen $E_3 > E_2$, but these energies can be reversed depending on the molecule. However, by definition, the predominant isomer population is the one with the lowest energy ground state, so $E_1 > E_0$. Only the dominant isomer, the one of lowest ground state energy, will be found at zero temperature, and the populations of the two isomers will become equal only at infinite temperature.

Molecules that photoisomerize are candidates for energy storage if the higher energy isomer has a long-enough lifetime [61,62]. Then, the energy difference $\Delta H = E_{10} = E_1 - E_0$ gives the storage capacity of a particular molecule.

Thus, there are three important energy scales. $E_{20} = E_2 - E_0$ is the energy difference between the electronic ground and excited state of the trans molecule, and $E_{31} = E_3 - E_1$ is the energy difference between the ground and electronic excited state. These energies correspond to the peaks observed when tracking absorption

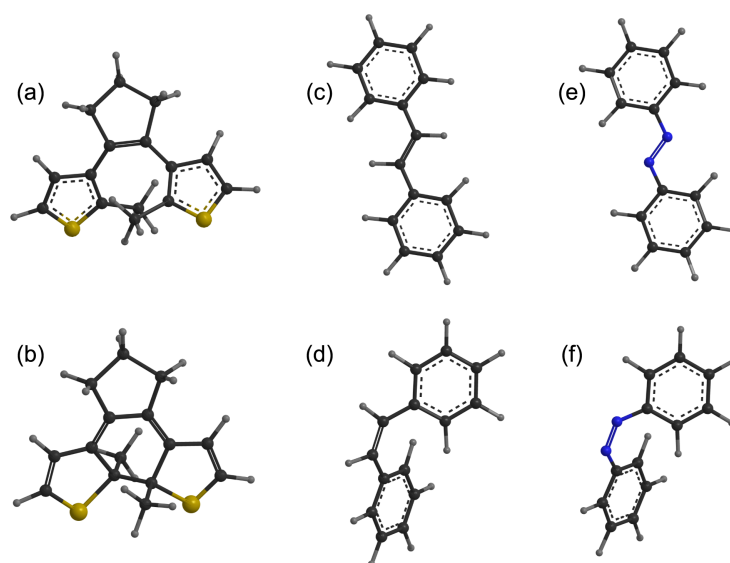
spectra, and typically fall in the visible to near UV part of the spectrum. The storage capacity defined by $\Delta H = E_{10} = E_1 = E_0$ is the energy difference between the ground state cis and ground state trans molecules. This storage capacity is typically much smaller than the electronic energy differences, falling into the near infrared range. The storage capacity is the energy used to determine the cis and trans populations using Boltzmann statistics, as we illustrated in Subsection 5.2 after Eq. (180).

To summarize, the left-hand parts of Figs. 36(a) and 36(b) represent the dominant isomer, which we call the trans state, while the right part shows the cis isomer. Each isomer is approximated to have two dominant states. Vertical arrows show electronic excitations/deexcitations of each isomer while diagonal arrows represent deexcitations that require a reconfiguration of the nuclei, which can lead to a conversion to the other isomer. The dashed arrows between the lowest energy states can exchange populations through thermally mediated transitions between isomers while solid arrows correspond to photon absorptions and emissions. In principle, non-radiative transitions are possible between the states of energy E_2 and E_3 , but these are usually not considered.

6.5c. Examples of Photochromic Molecules

Dithienylethene and its derivatives undergo photoisomerization from an open isomer shown in Fig. 37(a) to a closed isomer shown in Fig. 37(b). Both isomers are stable, where the reverse isomerization from closed to open is also induced by absorbing a photon. The molecular geometry is relatively unchanged with the largest relative position changes occurring at both methyl groups attached to the thiophenes [85]. Thus, dithienylethenes can only make a small direct photomechanical motion at the molecular scale; however, a macroscopic photomechanical motion can occur in crystals [86]. The changes in π conjugation between the two isomers also make dithienylethenes candidates for photoelectrical switches, which could be used to induce a mechanical motion in engineered systems. Other diarylethene-based switches have also been investigated for use as both chemical- and light-induced molecular switches [87].

Figure 37



Dithienylethene (a) open and (b) closed, stilbene (c) trans and (d) cis, and azobenzene (e) trans and (f) cis isomers.

Stilbene is a classic example of photoisomerization with a trans and cis form. The trans isomer as shown in Fig. 37(c) is of the lowest energy and therefore the dominant isomer. When the molecule absorbs a photon, the trans ethene bridge that connects the two benzene groups can be converted to the cis isomer form through out-of-plane rotation of the aromatic structures [88]. The cis isomer of stilbene is shown in Fig. 37(d). Back conversion through cis-to-trans photoisomerization can have competing processes, where the branching ratio of converting to dihydrophenanthrene can be upwards of 30% in alkane solvents at room temperature [89].

Another trans-cis photoisomerization process is observed in azobenzene. The trans isomer shown in Fig. 37(e) is the lowest energy state configuration. In addition to trans-cis photoisomerization, the cis isomer can thermally relax back to its trans configuration at room temperature. The cis isomer of azobenzene is illustrated in Fig. 37(f). Similar to stilbene, azo benzene is π conjugated across the bridge connecting the two benzene rings. Because the bridge is an azo instead of an alkene, the competing process that plagues cis-trans isomerization in stilbene is absent in azobenzene. Thus, azobenzene can be made to induce reversible deformations in photomechanical materials.

Functional groups can be introduced to the benzene positions to change its optical properties, which allows one to tailor the absorption characteristics of photoisomerizable derivatives. Most azobenzene derivatives photoisomerize from trans to cis, where the cis isomer is unstable and thermally relaxes back to the trans isomer. There are exceptions such as [0.0](3,3')-azobenzenophane, which is photoisomerized from cis to trans and thermally relaxes to the cis state [90].

6.6. Ordered Materials

Most of us begin learning about the properties of isotropic and homogeneous materials. Homogeneous materials have the same properties at all positions within the material. For measurements that have a directional component, isotropic materials will have the same measured property in any given direction. Sometimes a material is considered homogeneous in terms of its bulk properties, but the microscopic properties can vary within the material. For example, an amorphous polymer matrix is often considered homogeneous; however, the local electric fields can vary significantly within the material at the atomic scale and can cause inhomogeneous broadening in the absorption and emission spectra of dopant dye molecules. Similarly, isotropic materials can have short-range order, but no long-range order. The feathers of some birds are colored by locally ordered structures that do not have any long-range order [91,92].

6.6a. Anisotropic Materials

A homogeneous material that has no orientational order is called an isotropic material. When a material's properties are different depending on its orientation with respect to the direction of measurement, its physical and optical properties must be handled with more care. Many of the scalar parameters that describe isotropic materials such as stress and refractive index are expressed as tensors in anisotropic materials.

The simplest type of anisotropic material is one with uniaxial symmetry. When describing a uniaxial symmetric material, it is useful to imagine a cylinder with coordinates ρ , ϕ , and z . The material has the same properties in the ρ direction for all values of ϕ . The material properties along the z axis are different than those properties directed along the ρ direction in the cross-sectional plane.

Biaxial anisotropic materials have different properties along each of the three Cartesian axes. There are other types of anisotropy such as circular anisotropy,

where properties are different when traveling clockwise or counterclockwise within the material. The latter anisotropy is common in dielectric and magnetic materials.

6.6b. Crystals and Translational Symmetry

In contrast to anisotropic materials being made of oriented substituents that are themselves anisotropic, isotropic components can lead to anisotropy through spatial ordering. The simplest type of ordered material is a crystal with a cubic lattice structure. Each atom in the material is equally spaced along each of the three Cartesian axes. When the atoms are aligned in Cartesian directions, but the atomic spacings are not equal in each direction, then the material is anisotropic and belongs to the orthorhombic crystal class. There are seven crystal classes, including monoclinic, triclinic, tetragonal, hexagonal, and trigonal. Each crystal system can have multiple point groups with various symmetry properties.

6.6c. Polymers

Polymers are large molecules composed of repeating units of small molecules. Polymeric materials can be made of long single chains of small molecules such as polyurethane or poly(methyl methacrylate); chains can branch in some low-density polyethylenes, and polymer chains can be cross-linked to create a temperature stable material with excellent solvent resistance.

Many polymers are amorphous at room temperature, but local fields within can vary significantly leading to inhomogeneity that broadens absorption peaks of organic molecular dopants. However, when the wavelength of light is much longer than the scale of local field variations, the refractive index is homogeneous. Some polymers can be crystalline at room temperature. Opaque polymers tend to have medium crystallinity while transparent polymers have either a low or very high degree of crystallinity [93]. Some polymers that have low crystallinity (amorphous) can be made to align their chains by stretching or extrusion and thereby increase their crystallinity. Such an action will cause an isotropic polymeric medium to become anisotropic with long-range order.

6.6d. Liquid Crystals

A crystalline material can have both translational and orientational order while a liquid crystal generally has no translational order and has properties of both a liquid and a crystal. There are different classes of liquid crystals, each with varying types and degrees of order. They can have long-range order relative to many crystalline materials, which have a high degree of order over shorter distances. Dielectric single crystals on the macro scale at room temperature are difficult to grow, so materials with electronic or phononic conductivity are fabricated with imperfections or by fusing small crystals together with many grain boundaries. In contrast, liquid crystals have long-range order across the entire material such as those in the nematic phase, where the orientational order can also produce a large optical birefringence across the entire material.

The simplest liquid crystal is in the nematic mesophase. Much like a liquid, a nematic liquid crystal has no spatial order but has orientational order along a single axis called the *nematic director*, and the quantity describing average orientational order about the director is called the *orientational order parameter*. The uniaxial symmetry allows us to immediately define the order parameter as the mean of the second-order Legendre polynomial, $\langle P_2(\cos \theta) \rangle = (3\langle \cos^2 \theta \rangle - 1)/2$.

Other liquid crystal mesophases have an increased degree of order. For example, a biaxial nematic liquid crystal has two orientational order parameters in orthogonal

directions. The smectic mesophases of liquid crystals also have spatial order parameters. Some common mesophases are so called smectic A with layers molecules, each characterized by a director. The smectic B mesophase is made of layers of meogens with hexagonal translational order and uniaxial order in each layer, and the smectic C mesophase is made of layered molecules that are tilted along the same axis with respect to the uniaxial director. The columnar phases of discotic liquid crystal mesogens have spatial order as well as orientational order, most notably in either the hexagonal or rectangular orthogonal classes where the latter have a tilt (similar to the smectic C mesophase). Some disk-like mesogens can also exhibit the nematic phase, although the temperature range is often narrow. Many other liquid crystal mesophases have been identified such as the cholesteric and blue mesophases [94,95].

6.6e. Orientational Order Parameter of Nematic Liquid Crystals

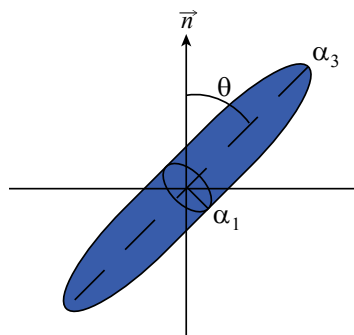
A single nematic mesogen (molecules that interact with each other to form a liquid crystal phase) with uniaxial anisotropic geometry as shown in Fig. 38 will form a nematic liquid crystal where the mesogens will on average align along a preferred axis called the director. The largest polarization is along the director. The largest polarizability, α_3 , of the molecule is along the $\hat{3}$ axis in the molecular frame.

There is a vast amount of experimental evidence to support the theoretical foundations that the uniaxial refractive index anisotropy in a nematic liquid crystal is due to anisotropic orientational order of the underlying molecules. Thus, the nematic phase's orientational order parameter tensor can be directly related to the linear refractive index tensor. There are many works that discuss the relationship between these two tensors in great detail [94–98]. For simplicity, we will simply define the scalar order parameter Q from which molecular theories of nematic liquid crystals can be understood, and it is defined as

$$Q = \left\langle \frac{3}{2} \cos^2 \theta - \frac{1}{2} \right\rangle, \quad (287)$$

which is the ensemble average of the second-order Legendre polynomial. The angle θ in Eq. (287) denotes the angle between the director (the direction of net molecular alignment) and the long axis of the liquid crystal molecule. The uniaxial scalar order parameter in Eq. (287) was first described by Tsetkov [99].

Figure 38



Liquid crystal with its long axis making an angle θ with respect to the director n . α_3 and α_1 are the molecular susceptibilities (also called polarizabilities) of the semi-major axis and the circularly symmetric semi-minor axis, respectively.

6.6f. Landau–De Gennes Theory

A way of treating the nematic-isotropic phase transition of a liquid crystal was proposed by De Gennes. This model of orientational order is based on a Landau-type theory of a phase transition [100]. The power of Landau–De Gennes theory is its ability to describe the short-range order of a nematic liquid crystal near the critical temperature of the nematic-isotropic phase transition. The long-range orientational order of uniaxial mesogens is completely disrupted while preserving local orientational order. The result is a hysteresis state in the order parameter as a function of temperature.

The free energy, F , of a liquid crystal in the nematic phase can be expanded in powers of the scalar order parameter, Q . Therefore, the free energy of a system comprising nematogens at constant pressure is

$$F(T, Q) = F_0(T) - f(T)Q + \frac{1}{2}A(T)Q^2 - \frac{1}{3}B(T)Q^3 + \frac{1}{4}C(T)Q^4 + \dots, \quad (288)$$

where F_0 is the temperature-dependent thermodynamic potential in the isotropic phase [94], and f is the term in the expansion representing the effects from an external field [97]. A , B , and C are all temperature-dependent coefficients.

The coefficients B and C are assumed to be weakly temperature-dependent such that they can be approximated as constants; we can assume them to be constant. The coefficient A is assumed to have the strongest dependence on temperature, where the function can be expanded as another power series. Assuming small changes in temperature, the coefficient A can be approximated as a linear function of temperature, $A = a(T - T_l)$, where a is a constant and T_l is the temperature just below the critical temperature T_{NI} of the nematic-isotropic phase transition.

Equilibrium is defined for stationary free energy, or

$$\frac{\partial F}{\partial Q} = 0. \quad (289)$$

Substituting Eq. (288) into Eq. (289), with powers of 4 and above neglected, we get

$$a(T - T_l) - BQ + CQ^2 = 0. \quad (290)$$

Solving Eq. (290) for Q yields the temperature-dependent order parameter,

$$Q = \frac{1}{2C} \left(B \pm \sqrt{B^2 - 4aC(T - T_l)} \right). \quad (291)$$

Figure 39 is a plot of Eq. (291), with the two roots corresponding to the two branches of the plot (red and blue dashed curves). This plot can be used to predict the behavior of Q as a function of temperature. For example, T_u can be calculated from Eq. (291) by finding the point at which the derivative tends to infinity. Using such an analysis, the nematic-isotropic phase transition temperature T_{NI} and the hysteresis upper limit temperature T_u can be rewritten in terms of T_l according to Eq. (291), yielding [97]

$$T_{NI} = T_l + \frac{2B^2}{9aC} \quad (292)$$

and

$$T_u = T_l + \frac{B^2}{4aC}. \quad (293)$$

6.6g. Maier–Saupe Theory

Examples of statistical theories of ordered fluids include those developed by Onsager [101], Zwanzig [102], Flory [103], Cotter [104–107], and Singh [108]. Maier–Saupe theory describes the long-range nematic order and the nematic-isotropic mesophase transition via local interactions between uniaxial mesogens. The theory predicts the alignment of rod-like mesogens with induced dipole moment interactions (London forces) with respect to a preferred direction of alignment called the director. The scalar order parameter given in Eq. (287) defines the axial orientational order parameter.

Maier–Saupe theory is a mean field theory. The interaction potential of the i th mesogen depends on its relative alignment to all other mesogens. The original Maier–Saupe theory assumed that the anisotropic interaction was predominantly due to anisotropic forces originating in the electric dipole interaction, which tends to align the molecular axes. Even in axial molecules, dipole moments can be induced in each molecule through the polarizability when they are brought into proximity. Then, the potential energy as a function of angle between them is minimum when their axes are aligned.

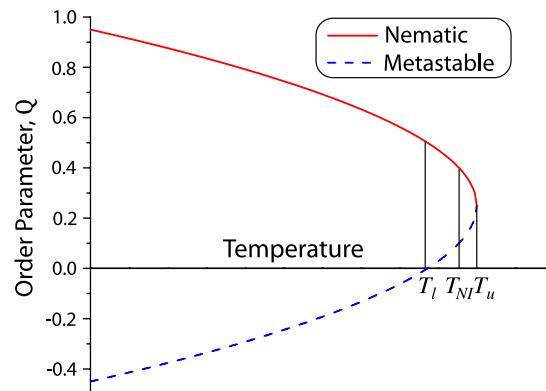
After the formulation of the theory, both attractive and repulsive forces were experimentally determined to significantly contribute to the nematic order [109,110]. Despite the initial assumption that only attractive forces contribute to the interaction potential, the Maier–Saupe theory provides the general features of the nematic order as a function of temperature. The assumption of attractive forces through induced dipole–induced dipole interactions requires the interaction potential to have an inverse volume squared dependence.

In the mean field approximation, the interaction potential of a mesogen with the “mean field” is given by

$$W = -\xi P_2(\cos \theta) \langle P_2(\cos \theta) \rangle = -\xi P_2(\cos \theta) Q, \quad (294)$$

where θ is the angle that a mesogen makes with the director, P_2 is the second-order Legendre polynomial, and ξ is the strength of the potential that couples the mesogen to the “mean field.” Note that the choice $\xi \propto V^{-2}$ well describes liquid crystals, where V is the mesogen volume and therefore $1/V$ is the mesogen number density. It makes

Figure 39



Landau–De Gennes theory with temperatures T_l , T_{NI} , and T_u . The Landau–De Gennes theoretical model predicts the hysteresis state of the second-order nematic-isotropic phase transition.

physical sense that interactions between molecules increase with number density. The constant of proportionality is the same for all mesogens because no correlations between individual molecules are treated in the mean field theory; the field simply strengthens when the average order $\langle P_2(\cos \theta) \rangle$ increases. Clearly W is minimum when $\theta = 0$ and the molecule is aligned along the director.

For N mesogens, the total energy U is given by $U = \frac{1}{2}N\langle W \rangle$, so using Eq. (294), we get

$$U = -\frac{1}{2}NQ^2. \quad (295)$$

The system's energy is minimized when $Q = 1$, the condition for fully aligned mesogens.

All thermodynamics are derived from the partition function Z . Using the orientational potential energy given by Eq. (294), the partition function can be expressed as

$$Z = \int_{-1}^1 d(\cos \theta) e^{-W/k_B T} = \int_{-1}^1 d(\cos \theta) e^{\xi P_2(\cos \theta) Q/k_B T}. \quad (296)$$

The internal energy U can also be calculated from the ensemble average using Eq. (296) [111], yielding

$$U = \frac{1}{2} \frac{N}{Z} \int_{-1}^1 d(\cos \theta) [-\xi Q P_2(\cos \theta)] e^{\xi P_2(\cos \theta) Q/k_B T} = -\frac{1}{2} N \xi Q^2, \quad (297)$$

where the last equality arises from Eq. (295).

The Helmholtz free energy is defined as

$$F = U - TS. \quad (298)$$

Because $\xi \propto V^{-2}$, the entropy follows from Eq. (296) as

$$S = -N \frac{\xi}{T} Q^2 + N k_B \ln Z. \quad (299)$$

Substituting Eqs. (297) and (299) into Eq. (298) yields

$$F = \frac{1}{2} N \xi Q^2 - N k_B T \ln Z. \quad (300)$$

Any extrema of the free energy can be obtained from Eq. (289), yielding

$$N \xi Q^2 - N k_B T \left(\frac{1}{Z} \frac{\partial Z}{\partial Q} \right) = 0, \quad (301)$$

where

$$\frac{\partial Z}{\partial Q} = \frac{\xi}{k_B T} \int_{-1}^1 d(\cos \theta) P_2(\cos \theta) e^{\xi P_2(\cos \theta) Q/k_B T}. \quad (302)$$

Substituting Eq. (302) into Eq. (301) yields

$$N \xi Q - N \xi \frac{1}{Z} \int_{-1}^1 d(\cos \theta) P_2(\cos \theta) e^{\xi P_2(\cos \theta) Q/k_B T} = 0. \quad (303)$$

Equation (303) can now be rewritten as a self-consistent equation,

$$Q = \frac{\int_0^1 d(\cos \theta) P_2(\cos \theta) e^{\xi P_2(\cos \theta) Q / k_B T}}{\int_0^1 d(\cos \theta) e^{\xi P_2(\cos \theta) Q / k_B T}}, \quad (304)$$

where the lower limits of integration have been changed because the functions of the angle θ are even; however, these changes in the lower limit of integration are not necessary.

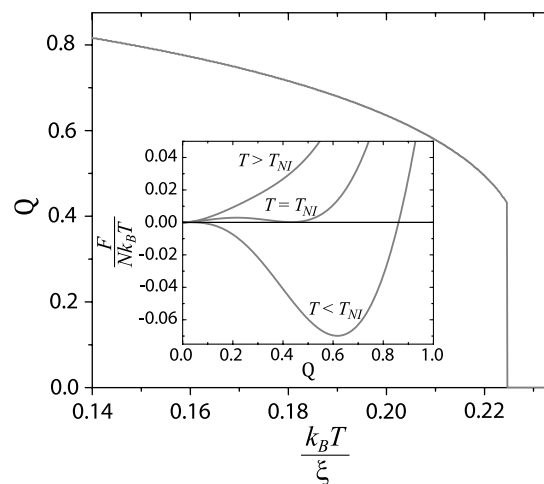
The order parameter as a function of the temperature can be determined via the self-consistent equation, Eq. (304). It can also be determined by first expressing the free energy as a function of Q and T , and then minimizing the function with respect to Q . The orientational order parameter is shown in Fig. 40, illustrating the nematic order parameter as a function of the Boltzmann energy in units of the mean interaction coefficient ξ . When only considering an orientational interaction, the free energy is always zero in the isotropic phase, i.e., when $Q = 0$. At the critical temperature, the free energy associated with the orientational interaction potential touches the horizontal axis at two locations, at $Q = 0$ and again at a local minimum for $Q > 0$. Therefore, a bistable point occurs at the nematic-isotropic mesophase transition.

6.6h. Maier–Saupe Model of Photochromic and Non-Photochromic Mesogens with Similar Interaction Potentials

Consider a liquid crystal made with two types of mesogens. In the nematic phase, assume that the mesogens are evenly dispersed and that neither mesogen forms aggregates. Since the mesogens in the uniaxial nematic phase are evenly distributed, the polar angle of a mesogen is the single parameter that fully describes it. The orientational distribution for a mesogen of type #1, characterized by the polar angle θ_0 , is given by

$$\rho(\theta_0) = \frac{N}{Z} \int_0^\pi e^{-[W_1(\theta_0, \theta_1, \dots, \theta_n) + W_2(\theta_{n+1}, \theta_{n+2}, \dots, \theta_N)] / k_B T} \prod_{i=1}^N d(\cos \theta_i), \quad (305)$$

Figure 40



Uniaxial, orientational order parameter of a nematic liquid crystal doped with trans-cis photochromic molecules graphed against the Boltzmann energy $k_B T$ divided by the mean interaction coefficient ξ . The inset shows the free energy as a function of the order parameter below, at, and above the nematic-isotropic mesophase transition temperature T_{NI} .

with the partition function defined as

$$Z = \int_0^\pi e^{-[W_1(\theta_0, \theta_1, \dots, \theta_n) + W_2(\theta_{n+1}, \theta_{n+2}, \dots, \theta_N)]/k_B T} \prod_{i=0}^N d(\cos \theta_i). \quad (306)$$

The potentials W_1 and W_2 are for mesogens of type #1 and type #2 with total number of particles n and $N - n$.

Let us consider two types of cylindrical mesogens: a photostable mesogen and a cylindrical photochromic mesogen (oriented trans azobenzene derivative) that interacts with light to form a sphere (thermally tumbling cis azobenzene derivative). Then, there are three potential energies in the single distribution function associated with the photostable mesogen, the trans azobenzene derivative, and the cis azobenzene derivative. For a spherical cis azobenzene, the orientational potential is independent of angle. Thus, the single particle distribution reduces to Eq. (304) for the mesogens, and only two orientational potential energies are needed to describe the single orientational distribution of the cylindrical mesogens. However, the trans molecules that have converted to the cis isomer are removed from the population.

The expectation value of the second-order Legendre polynomial of any mesogen is given by

$$\langle P_2(\cos \theta_0) \rangle = \int_0^\pi P_2(\cos \theta_0) \rho(\theta_0) d(\cos \theta_0). \quad (307)$$

There can be large differences between the two potential energies W_1 and W_2 in Eq. (305); however, for the *special case* when the two types of mesogens are similar such that $W_1 \approx W_2$, the single mesogen approach applies. For simplicity, we will only consider this special case in which the photostable mesogen is nearly indistinguishable from the photochromic mesogen in the trans state. Thus, we may write

$$W_1(\theta_0, \theta_1, \dots, \theta_n) + W_2(\theta_{n+1}, \theta_{n+2}, \dots, \theta_N) \approx W(\theta_0, \theta_1, \dots, \theta_N). \quad (308)$$

When Eq. (308) holds, Eq. (307) is equivalent to Eq. (304).

Let us set the total number of molecules N to be the sum of the number of photostable mesogens n_m , number of trans isomers n_t , and number of cis isomers n_c , so

$$N = n_m + n_t + n_c. \quad (309)$$

When all photochromic molecules are also all in their trans state, the potential energy is equivalent to Eq. (294) for the special case of $W_1 = W_2 = W$. The potential does, however, weaken when a population of photochromic molecules are in their cis state. The interaction coefficient may be written as an unknown function of the fraction of cis isomers, $\xi(N_c)$. Expanding the function as a power series gives

$$\xi(N_c) = \xi_0 - \xi_1 N_c - \xi_2 N_c^2 - \dots, \quad (310)$$

where N_c is the fraction of cis isomers in the system,

$$N_c = \frac{n_c}{n_m + n_t + n_c}. \quad (311)$$

Assuming that each term to the right of the linear term in Eq. (310) is much smaller in magnitude than $\xi_1 N_c$ for small N_c , then higher-order contributions may be neglected. Therefore, $\xi \approx \xi_0 - \xi_1 N_c$.

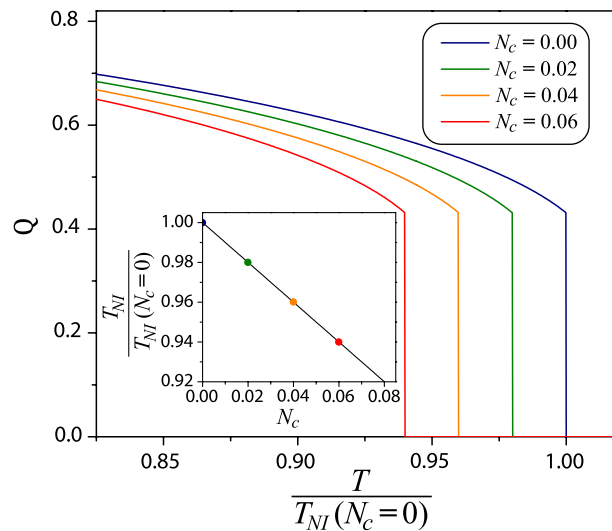
If we only consider the linear term in Eq. (310) ($N_c \ll 1$), then every trans isomer that becomes a cis isomer will no longer contribute to the local orientational aligning potential. When a single cis isomer takes the place of a mesogen, the surrounding mesogens have one less nearest-neighbor interaction. Imagine a planar grid with the plane's normal direction pointed in the same direction as the nematic director, then the four nearest molecules to the cis isomer interact with one less mesogen. Those mesogens each have four nearest-neighbors of which only three are other mesogens. There are also four second nearest-neighbors that are $\sqrt{2}$ further away on the grid. Each second nearest-neighbor associated with these positions relative to the cis isomer have one less mesogen at their second nearest-neighbor positions. Ignoring higher-order interactions (and mesogen-sphere steric interactions), we arrive at the approximation, $\xi_1 \approx \xi_0$.

Under the above set of approximations,

$$W \approx -\xi_0(1 - N_c)\langle P_2(\cos \theta) \rangle P_2(\cos \theta_i). \quad (312)$$

Figure 41 shows the order parameter as a function of temperature divided by the nematic-isotropic transition temperature for small fractions of cis isomers. The inset shows the nematic-isotropic transition temperature as a function of the fraction of cis isomers. Note again that the potential energy in the Maier–Saupe theory only considers the attractive term, where steric interactions can further reduce the orientational order. If the cis isomers can be approximated as spheres, then $\xi = \xi_0(1 - N_c)$ is the lower limit of order disruption due to the presence of cis isomers; steric interactions between the anisotropic mesogens and the cis isomers will further reduce the mean orientational order of the system.

Figure 41



Orientalional order parameter as a function of temperature for small fractions of cis isomers relative to the total number of molecules in the liquid crystal. The plotted functions assume a linear approximation where $T_{NI}(N_c > 0) = [1 - (\xi_1/\xi_0)N_c][T_{NI}(N_c = 0)]$ with $\xi_1/\xi_0 \approx 1$ as described in the inset. The transition temperature T_{NI} decreases as the cis population increases.

Note that we have presented a simple example of an extension to the Maier–Saupe theory for the special case of photochromic and non-photochromic mesogens that is only valid when the interaction potentials of the two types of molecules are similar. There are many other possible extensions to the Maier–Saupe theory. For example, smectic liquid crystals have both orientational and translational order; scalar orientational and translational order parameters can be used to describe different smectic liquid crystals. The McMillan model is an extension of the Maier–Saupe theory first used to describe the mean orientational and translational order of the smectic A mesophase [112]. The McMillan model has also been used to describe discotic mesophases [113].

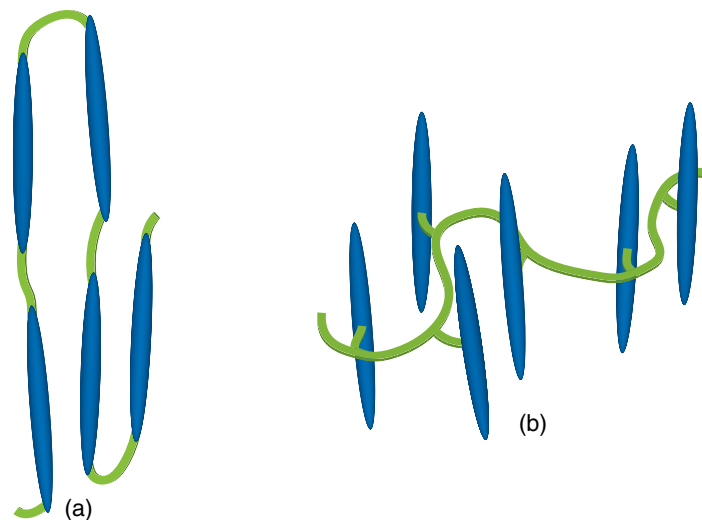
6.6i. Liquid Crystal Polymers and Elastomers

LCPs and LCEs are polymeric materials that have mesogenic moieties either built into the backbone of the polymer/elastomer or cross-linked to a side chain that attaches to the polymer backbone as illustrated in Fig. 42. A high degree of backbone alignment occurs when the mesogens are repeating within the backbone, while lower backbone alignment occurs for mesogens attached to the backbone using a short side chain [97]. Such materials combine the orientational order of liquid crystals with the amorphous properties of some polymeric materials. This allows for large induced strains via any process that changes the long-range order of mesogens.

Nematogens cross-linked to the backbone can collectively exhibit the nematic phase within a given temperature range. This type of orientational ordering leads to a uniaxial anisotropic index of refraction, and absorption cross section, of the bulk material in its nematic phase. Although a first-order phase transition from the nematic to the isotropic phase results in large strains, significant strains can still be achieved by simply reducing the long-range order over a small temperature range while near, but still below the nematic-isotropic phase transition temperature.

There are many types of LCPs and elastomers. Although the LCPs and elastomers reviewed in this paper are primarily based on cross-linked nematogens, many choices for the chemical structures of the backbone, cross-linker, and mesogen can be used to

Figure 42



Nematogens (blue prolate shapes) are attached to a polymeric material (green line) to form a liquid crystal polymer. The mesogens can either be (a) built into the backbone or (b) cross-linked to the backbone with a short side chain.

create an array of highly deformable materials. The matrices can also be doped with azobenzene dyes to add more functionality.

The coupling of the mesogens to the backbone in a LCE results in a mechanical deformations in the bulk polymer when the liquid crystals experience a phase change. Thus, in principle, light-induced changes in the liquid crystal cause commensurate changes in the bulk polymer. Thus, changes in the order parameter Q are also associated with changes in the shape of the material. Models of polydomain LCEs show this connection between the microscopic properties of the domains and the bulk response [114,115].

6.7. Leveraging Molecular Orientation

6.7a. Ordered Material

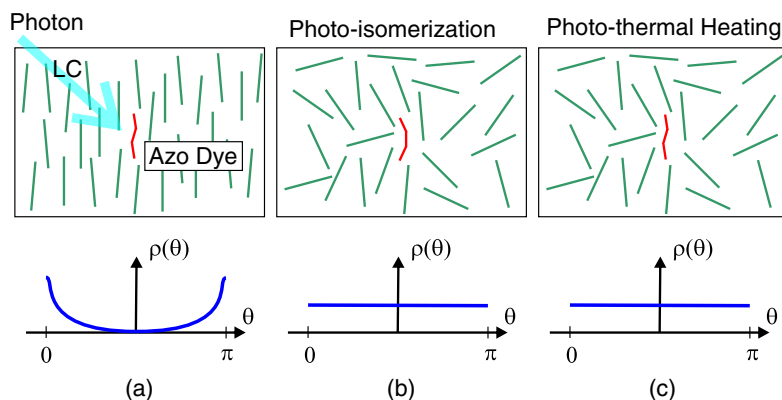
Subsection 6.6 describes how the photomechanical response can originate in a transition from an orientationally ordered material (such as a nematic liquid crystal) to a disordered one (such as the isotropic phase of a liquid crystal). Figure 43 summarizes the process.

Initially, the azo dye in its trans state fits into the liquid crystal domain and is orientated along the director. Upon absorbing a photon, the azo dye transitions to the cis isomer, causing the liquid crystalline domain to lose orientational order due to the mesogens and dopant molecules having incommensurate shapes. The orientational order of the domain can also be affected when the heat generated from the absorbed photon is deposited into the liquid crystalline domain.

The plots below the illustrations in Fig. 43 show the orientation distribution functions in the liquid crystal phase and the isotropic phase. In real systems, the domains will not be fully disordered, so the orientational distribution function will be peaked but with a broader width.

In most material, their lengths will decrease along the director, and their width will increase perpendicular to it when transitioning from the aligned to isotropic phase. Since molecules tend to absorb more light that is polarized along their longer axis, the photomechanical response should be much larger for light polarized along the

Figure 43



(a) Azo dye dopant in its trans state is aligned with the director of a liquid crystal domain. (b) After absorbing a photon, the azo dye converts to the cis state, which interferes with the ordering forces. (c) Photothermal heating mediated by the dopant also leads to a loss of orientational order even if the molecule does not change conformation. The bottom row of plots shows the orientational distribution function $\rho(\theta)$.

director than perpendicular to it. As a result, the polarization dependence of the photomechanical response should be highly anisotropic.

6.7b. Isotropic Material

Here we describe two processes in isotropic materials: angular hole burning and phase transitions.

In contrast to a liquid crystal, where the photomechanical effect originates in a light-induced change in orientational order or even a mesophase transition, orientational hole burning is the reverse process in which an isotropic material becomes anisotropic under the action of light.

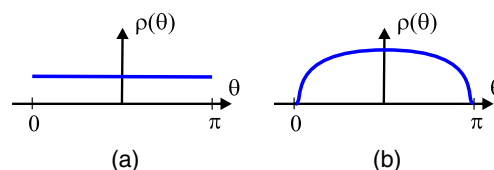
Consider a material that is initially in its isotropic state, such as a population of azo dyes in a glassy polymer matrix or incorporated into a polydomain LCE. Note that a polydomain LCE shows anisotropy in each microscopic domain, but the director in each microscopic domain is aligned in a different direction such that the bulk material is isotropic. Figure 44(a) shows the orientational distribution function of the isotropic material. Light penetrating this material will be more strongly absorbed by the molecules that are aligned with its polarization, forming the more compact cis state, which will more easily reorient through thermal diffusion. The net result is that the cis molecules will randomly reorient by the time they thermally relax into the trans state, leading to an isotropic trans population. Thus, molecules aligned along the light's polarization will be depleted, creating a "hole" in the orientational distribution function at the angle of light polarization. Figure 44(b) shows the orientational distribution function after light exposure.

Angular hole burning will be accompanied by a length decrease along the polarization of the light and an increase perpendicular to it. Similarly, the refractive index and optical absorbance will also decrease along the polarization direction and will increase perpendicular to it. As such, the angular hole burning mechanism can be characterized in materials by measuring the anisotropy of the photomechanical response, and, light-induced birefringence and dichroism.

There is a long history of angular hole burning being studied in dye-doped polymers [116–121], and the effect has been used to form surface relief gratings [36–41,48,122], to align molecules in a dye-doped polymer with photo-assisted electric field poling [123,124] to make electro-optic materials.

Alternatively, light can randomize a subset of aligned molecules in an otherwise isotropic material, leaving the material with net alignment. This effect can be permanent or reversible. Harvey and Terentjev [60] reported how measurements of the anisotropy in the stress response of a polydomain LCE originates from this kind of reversible population depletion. They used the polarization dependence of the photomechanical response to eliminate the heating contribution [60], as follows.

Figure 44



(a) Orientational distribution function of the population of azo benzene molecules in an isotropic sample. (b) The orientational distribution function after the isotropic material is exposed to light polarized along $\theta = 0$.

A polydomain material is made of microscopic domains of aligned mesogens; but, the domains are aligned randomly with respect to each other. When heated, the mesogens become disordered, and each domain shrinks along the director while expanding in the other two orthogonal directions, leaving the bulk material unchanged. Thus, they argued, if the only mechanism at work is heating from absorbed light, any observed volume changes will be isotropic.

The photoisomerization mechanism starts with the conversion of dopant molecules from the trans to cis isomer, where the shape change interferes with the steric interactions between mesogens, leading to a decrease of orientational order within a domain. When illuminated with polarized light, trans-cis photoisomerization induces a reduction of orientational order in those domains that have their directors predominantly aligned with the light's polarization—the orientation where light is most strongly absorbed. Thus, those domains will contract along the light's polarization while leaving the domains with the director aligned perpendicular to the polarization unchanged. As a result, the isotropic polydomain LCE will tend to shrink in the direction of the light's polarization due to photoisomerization. If the sample is constrained between clamps, then light polarized along the axis containing the force sensor will detect an increase in the stress. Light polarized perpendicular to the force sensor's detection axis will yield a small positive force. The sign conventions for the stress are described in Subsection 7.2.

If the effect were solely due to heating in an unstrained polydomain LCE, the material would show very little deformation in the bulk while exposure to polarized light would lead to contraction only in the direction of polarization. In the pre-strained or monodomain sample, heating would cause the sample to contract along the director with a small expansion in the perpendicular direction, thus not allowing this measurement to differentiate between photothermal heating and photoisomerization. Harvey and Terentjev found an anisotropy of the force, and so concluded that photoisomerization is dominant. Note that pre-straining the sample in a force experiment such as this one can align some of the domains, yielding an anisotropic response from heating.

Such elegant experiments in a dye-doped LCE provide strong evidence that a light-induced change in the conformation of a molecule interferes with the orientational order of the liquid crystal as shown in Fig. 43(b), resulting in the observed anisotropy of the force [60]. Harvey and Terentjev eliminate the heating mechanism based on the argument that if photothermal heating were responsible, the nearby randomly oriented domains would also shrink along their individual directors, and together would result in an isotropic force. This argument implicitly assumes that the temperature increase is uniform over many domains so that they act isotropically. Heat flowing in a way that leads to hot spots in those domains that are aligned with the polarization of the light can lead to an anisotropic response due to heating. Here we describe conditions where this might happen.

We start by considering the sequence of events that starts with the absorption of a single photon. The temperature change surrounding a single molecule that converts the photon's energy to heat is given by the specific heat of the surrounding material and its volume. Spin coating a thermoplastic polymer from a dye-doped solvent tends to yield the highest chromophore concentrations of molecules in bulk samples. For example, in DR1-doped PMMA [65], crystallites form when the number density exceeds about $N = 2 \times 10^{26} \text{ m}^{-3}$. LCEs are usually doped using diffusion; therefore, the number densities are typically much lower. We will use a density of $N \approx \times 10^{26} \text{ m}^{-3}$ as an upper limit for a dye-doped LCE, which yields a lower limit on the volume of polymer per molecule of $v = 10^{-26} \text{ m}^3$, and places a constraint on the upper limit of the temperature change.

With a specific heat capacity $C = 1.4 \times 10^3 \text{ J/kgK}$ and polymer density $\rho = 10^3 \text{ kg/m}^3$, the total mass of material heated is $M = 10^{-23} \text{ kg}$. Assuming that the heating is localized only to the volume surrounding one molecule, the temperature change due to the absorption of one photon of energy $\Delta H = 2 \times 10^{-19} \text{ J}$ is

$$\Delta T = \frac{\Delta H}{MC} = 10 \text{ K.} \quad (313)$$

This temperature change is not high enough to drive the nematic-to-isotropic transition in a typical LCE. For reference, the materials used by Harvey and Terentjev have a transition temperature of $T_{ni} = 76^\circ\text{C}$. However, the increased temperature will still lead to some decrease of the order parameter, which will result in a photomechanical response.

Polydomain samples such as the ones used in the experiments of Harvey and Terentjev [60] scatter visible light, so they have domain sizes on the order of a micrometer; thus, on the order of a billion azobenzene molecules can populate each domain.

To summarize, the sequence of events after a molecule absorbs a photon is as follows. The molecule transfers heat to the surroundings, which at early times is localized in the domain containing the molecule. At that time, the response is anisotropic but on a time scale that is much faster than the over-damped bulk response time. As the heat leaves the progenitor domain, the temperature of the domains in a spherical shell around it increases. Since the domains in the shell are randomly oriented, no net anisotropic response results except for the progenitor domain. The heat continues to expand into larger shells until the heat wave dissipates and the temperature returns to ambient. Because only one domain responds anisotropically to a single photon, the response is much smaller than if all the domains were aligned along a single direction.

Under constant illumination, photons will be absorbed by the other molecules in the domain. The temperature attained by a domain reaches steady state when the rate of energy absorption in a domain balances the energy flow leaving it. The steady-state temperature can be much higher than the temperature induced by a single photon on its volume of influence. All other domains are also being heated by photons. Initially, each domain will respond anisotropically, but on very fast time scales. For a three-dimensional material, the heat flows from each domain to the isotropic surroundings, and eventually the temperature becomes uniform throughout.

In a thin film, heat will flow away from the hot spot both within the plane of the film and perpendicular to its surface. To understand how this could lead to inhomogeneities, consider the two limiting cases for a sample that is thin compared with its other two dimensions so that it can be approximated as a thin infinite sheet. In the case where heat does not leave the sheet, it will diffuse through the material away from the “hot” domains until the temperature becomes uniform. Any inhomogeneity in the temperature will cause heat to flow, bringing the sample back to uniform temperature. Clearly, for a finite sheet, the temperature field must obey the boundary conditions, so in the steady state, the temperature smoothly varies from the interior temperature to the temperature of the environment at its surface.

In the other extreme, where the heat flows out of the sample perpendicular to its surface into the environment, which acts as a perfect heat sink that removes all heat, only the parts of the sample that are absorbing light will be hot. When both types of heat flow are in play, hot spots will be centered on domains that have absorbed a photon. The hot spots are spatially localized when heat flows out of the material and the spatial temperature profile is broadened when some of the heat diffuses through

the film. When the heat sink is strong but not perfect, then the heat will still dissipate long before reaching a clamped boundary; however, the illuminated region will still be hot, but the nearby regions surrounding the illuminated spot will be warm.

The orientations of the domains in polydomain materials are uniformly distributed. Since the probability of absorbing a photon is proportional to $\cos^2 \theta$, where θ is the angle between the light's polarization and the domain orientation, all domains will be heated to some degree, making it more likely that the material will reach a uniform temperature. In typical experiments, heat flows within the material at a higher rate than through the outer surface. That too acts to make the temperature homogenous. However, depending on the geometry and environment, heating might contribute to the anisotropy of the mechanical response of the material.

7. MEASURING PHOTOMECHANICAL RESPONSE FUNCTIONS

This section begins by introducing several experimental techniques used to determine the photomechanical response, followed with derivations that show how measurements are related to material parameters in several limiting cases. This section ends with examples of how these techniques can be used to study the mechanisms of the response.

7.1. Experimental Techniques

This subsection focuses on experimental techniques including the stress response for a clamped sample illuminated from its side, a clamped waveguide with light propagating within, determining the bending of a sample with a free end by video or with a probe light beam reflected from a mirror attached to its end, and using a partial reflector to determine the uniaxial photomechanical strain response.

7.1a. Clamped Sample–Side Illumination

This experimental configuration was first reported by Harvey and Terentjev [60], which can be built for a few hundred USD, and samples can be harvested from household items [125]. The upper clamp is placed in series with a load cell that measures the force, which is related to the strain in the material. We assume that the material is in the form of a slab of thickness t , width w , and length $\ell + 2a$ between the two clamps. The clamps are assumed rigid so that the sample's length cannot change. This will be a good approximation as long as the apparatus is much stiffer than the sample.

A beam of light is focused onto the middle section with a cylindrical lens to a line of width ℓ . For simplicity, we assume that the intensity is uniform within ℓ and dark outside. We will later relax this assumption. The length of the elastomer on either side of the illuminated area is of length a . We will also assume that the sample is thin enough so that the intensity inside is uniform throughout its thickness.

If the dominant mechanism is photothermal heating, the concentration of the light-absorbing dopants can be decreased so that the $1/e$ absorption length is longer than the sample thickness. Then the thin film approximation holds even for samples that might otherwise be considered thick.

Materials made from LCEs relying on the photoisomerization mechanisms might require higher chromophore concentrations to observe a photomechanical response. Then, the intensity rapidly attenuates as a function of the penetration depth through the material, making the intensity nonuniform. In such cases, the calculations that follow hold for each slice of material over which the intensity is approximately constant. Then, the total force at the load cell is a sum over the contributions from the individual

slices. In such cases, there are some subtleties that need to be taken into account with regards to how the samples are held in the clamps, but the problem is tractable.

The description here is a special case of the calculation presented in Subsection 4.2b. However, here we apply a graphical technique that circumvents the need to solve differential equations and aids with fortifying the intuition.

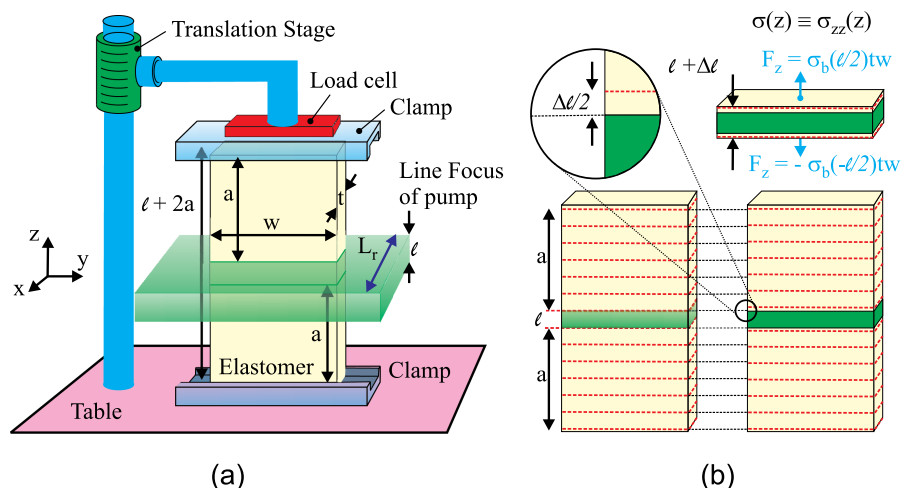
Static Intensity

We start with the simplest case where the intensity, I , is constant and determine the stress and strain profiles in response to a photomechanical stress after all time dependencies have settled to a steady state. Thus, the measurement is taken after a time that is long compared with the time it takes an acoustical wave to travel back and forth in the material, and much longer than the response time of the material.

Figure 45(b) shows the sample before and after the light is turned on. The green band marks the illuminated part. Some material leaves the illuminated area and reaches steady state in the dark region. Thus, the fiduciary markings at the edges of the illuminated region prior to light exposure will move a distance $\Delta\ell/2$ into the dark region after exposure. This leads to elongation in the exposed area and compression in the dark regions above and below, keeping the total length constant.

Assuming that $\sigma = 0$ in the dark state (even when the sample is pre-stressed, we can subtract the initial stress and formulate the problem in terms of the change in stress), in the illuminated state, the strain will be positive in the illuminated volume and negative in the dark region for a positive photomechanical coefficient. The opposite behavior is observed for a negative coefficient. The rectangular volume element $w \times \ell \times t$ is flooded with a constant intensity throughout [the intersection of the green slab with the yellow sample in Fig. 45(a)] by using a lens with a long-enough focal length such that the Rayleigh length is much longer than the sample thickness, $L_r \gg t$. Then, adapting Eq. (129) to the symmetric geometry of the apparatus, the photomechanical stress acts along the length given by coordinate z in proportion to

Figure 45



(a) Example of an experiment that measures the photomechanical properties of a material. The green rectangular volume represents the laser beam after it is focused with a cylindrical lens to a uniform rectangle of height ℓ at the sample. The sample can be stretched with a translation stage to pre-stress it. (b) The red dashed lines on the unstressed sample are equally spaced fiduciary markings. The illuminated area expands, causing a compression in the dark parts. Reprinted from [33].

the intensity $I(z)$, yielding

$$\sigma_b(z) = -\kappa_\sigma I(z) = -\kappa_\sigma I[\theta(z + \ell/2) - \theta(z - \ell/2)], \tag{314}$$

where κ_σ is the photomechanical coefficient (a property of the material), θ is the Heaviside step function, and I is the intensity in the illuminated region.

If the focal length of the beam is much longer than the sample thickness so that the variation of the intensity is negligible over the thickness even far away from the focal point, the lens can be moved to bring the beam in and out of focus to increase ℓ and at the same time decrease the intensity but keeping the power constant. Since the intensity is maximin at the focus, which we call I_{\max} , we can express Eq. (314) as

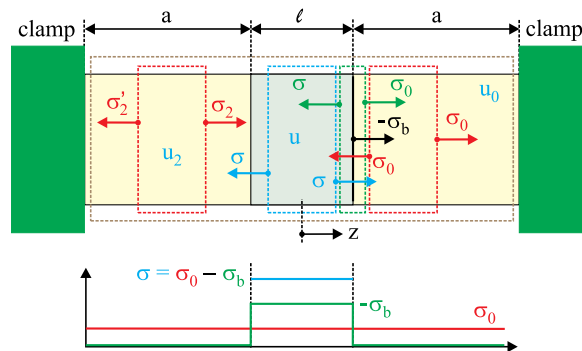
$$\sigma_b(z) = -\kappa_\sigma I_{\max} \frac{\ell_{\min}}{\ell} [\theta(z + \ell/2) - \theta(z - \ell/2)], \tag{315}$$

where ℓ_{\min} is minimum height of the illuminated area when the sample is at the focus, θ is the Heaviside step function, and $\ell \geq \ell_{\min}$. Equation (315) is used when the photomechanical force is measured with the load cell as a function of the position of the lens, and Eq. (314) is used when the intensity is varied when keeping the size of the focused spot fixed.

Figure 46 shows a front view of the material (turned on its side for convenience) in the clamp, where the light blue shaded region in the middle is the illuminated section, and so experiences a body force due to the light through the photomechanical effect given by Eq. (314) or Eq. (315). The five dashed rectangles are representative volume elements that we will consider below. Note that the only nonzero component of the stress is σ_{zz} , which we call σ .

We approach this problem by drawing volume elements in the material, as shown in Fig. 46 by the dashed lines, and determining the net force on the volume by adding the forces on the surface. We note that the volume element extends into the page and matches the thickness of the sample. The front, back, top, and bottom surfaces experience no net forces if the stress is along z , so we need only calculate the forces on the left and right faces of the volume element. If the volume element includes the interface between an illuminated section, the body force due to the photomechncal effect must be added to the forces on the two surfaces to get the net force.

Figure 46



Front view of a clamped material (turned on its side for convenience) that is uniformly illuminated in the region $|z| \leq \ell/2$ (light blue). The plot below shows the stress distribution over the length of the sample.

As described by Eq. (46), the i th component of the force, F_i , on a surface element, dA_j , due to a stress σ is given by $F_i = \sigma_{ij}dA_j$. First, consider the left region. The area element is by convention a vector that is perpendicular to the surface, and pointing outward from the volume. Thus, the force on the red rectangle is given by $tw(\sigma_2 - \sigma'_2)$, where we can see from Fig. 45 that the cross-sectional area perpendicular to \hat{z} is tw . When the material is in static equilibrium, the net force vanishes, so $\sigma_2 = \sigma'_2$. Since this rectangle can be drawn of arbitrary width (as long as the left and right sides are contained within the unilluminated section), the stress must be uniform, so the force read by the load cell (if one were placed on the left clamp) could be used to determine the stress in the unilluminated section.

The same argument can be applied to each of the other three regions, as shown with blue and red rectangles. Because the illumination is uniform, the stress in the middle section will also be uniform. Body forces only appear in parts of the material where the stress changes, as it does at the interface between the light and dark parts.

The green dashed rectangle straddles the interface between the illuminated volume and the right part of the sample. Because the system is in static equilibrium, the net force on the volume element vanishes, so the sum of the force inside the box due to the body force and the forces at the surface must add to zero. Before solving this problem, it is useful to first use our intuition to understand the effect of the light, which causes this slice to expand; because this expansion pushes against the material in the dark region, it will compress and act upon the interface as a reaction force. As such, it is natural to expect the stress to be different in these two regions.

With the photomechanical effect in play, it introduces a body stress, σ_b , which acts on the interface. The equilibrium condition then becomes

$$tw(-\sigma_b + \sigma_0 - \sigma) = 0 \quad \text{or} \quad \sigma = \sigma_0 - \sigma_b. \quad (316)$$

Note that the negative sign associated with σ_b arises from the minus sign in Eq. (118). Equation (316) holds in the limit when the rectangle becomes infinitesimally thin, as long as the volume element includes the interface; so, the body force originates at the interface. Formally, Eq. (316) is a consequence of Eq. (C3) in Appendix C applied to the step function in Eq. (314), which shows that a body force results from discontinuities in the stress. Finally, we note that the body forces at the two interfaces that define the illuminated section act in opposite directions, thus stretching the illuminated region. The equilibrium position is reached when all the forces balance. Finally, consider the large brown rectangle. The two body forces due to the two interfaces are in opposite directions, so they cancel. Since the net body force vanishes, $\sigma_2 = \sigma_0$, making the system fully symmetric, as we would expect.

To complete the analysis, we need to apply the boundary conditions, that is $\delta(\ell + 2a) = 0$, or $\delta\ell = -2\delta a$, which yields

$$u\ell = -2u_0a. \quad (317)$$

According to Eq. (4), the strain in each section is given by $u_i = \sigma_i/E$, which when substituted into Eq. (317) relates the stresses,

$$\sigma = -\sigma_0 \frac{2a}{\ell}. \quad (318)$$

Substituting Eq. (318) into Eq. (316) yields

$$\sigma_0 = \frac{\sigma_b}{1 + \frac{2a}{\ell}} = -\kappa_\sigma I \frac{\ell}{L}, \quad (319)$$

where in the last equality, we have used the sample length $L = \ell + 2a$ and the definition of the photomechanical stress, $\sigma_b = -\kappa_\sigma I$. Equation (319) is clearly identical to Eq. (133). Since the load cell measures the force,

$$f = \sigma_0 t w, \quad (320)$$

Eq. (318) relates what is measured by the load cell to the body force due to the light source.

The final step is to relate the measured force to the photomechanical coefficient, κ_σ , using Eqs. (315), (319) and (320), which yields

$$\kappa_\sigma = \frac{L}{t w} \cdot \frac{1}{\ell_{\min} I_{\max}} \cdot f = \frac{L}{t w} \cdot \frac{1}{\ell I} \cdot f. \quad (321)$$

Since L is the length of the material between the clamps, the term after the first equality shows that κ_σ is independent of the beam's width as long as the power illuminating the sample is fixed. We can use the fact ${}_{\min} W$ that is the area of the beam at the focus, so the power is, $P = I_{\min} W$ which when substituted into Eq. (321) yields

$$\kappa_\sigma = \frac{L}{t} \cdot \frac{1}{P} \cdot f. \quad (322)$$

Thus, *if the photomechanical response is linear, so that κ_σ is independent of the intensity*, then the photomechanical coefficient depends only on the power of the pump beam, and not on its width.

Equation (321) can be easily generalized for any intensity profile. Recall that Eq. (143) shows that $\sigma_0 = -\kappa_\sigma \bar{I}$, where \bar{I} is the average intensity over the material in the illuminated region. Then, Eq. (321) becomes

$$\kappa_\sigma = \frac{1}{t w} \cdot \frac{1}{\bar{I}} \cdot f, \quad (323)$$

where for the uniformly illuminated case, $\bar{I} = \ell I / L$, Eq. (321) results. Recognizing that $P = w L \bar{I}$, Eq. (323) gives

$$\kappa_\sigma = \frac{L}{t} \cdot \frac{1}{P} \cdot f. \quad (324)$$

As such, we see that the distribution of the power is unimportant in the determination of the photomechanical constant in the low-intensity regime where the response is linear, so Eq. (322) is fully general and does not require the shape of the beam profile to be known.

κ_σ has units of inverse velocity, so when expressed in units of the speed of light, it is a dimensionless quantity that is independent of the system of units used in getting the result.

At this point, we re-emphasize that Eq. (315) assumes a linear and local response function. If the response function was nonlinear, the next term in the series would be of the form

$$\sigma_b^{(2)}(z) = \kappa_\sigma^{(2)} \left(I_{\max} \frac{\ell_{\min}}{\ell} \right)^2 [\theta(z + \ell_{\min}/2) - \theta(z - \ell_{\min}/2)], \quad (325)$$

which would then lead to the second-order response function

$$\kappa_\sigma^{(2)} = \frac{L\ell}{tw} \cdot \frac{1}{\ell_{\min}^2 I_{\max}^2} \cdot f = \frac{L}{tw} \cdot \frac{1}{\ell I^2} \cdot f = \frac{wL\ell}{t} \cdot \frac{1}{P^2} \cdot f. \quad (326)$$

So if the second-order correction given by Eq. (326) was dominant, *in an experiment where the power is fixed*, a plot of the beam width ℓ as a function of the inverse force measured by the load cell, $1/f$, would have a slope in proportion to the second-order photomechanical coefficient, $\kappa_\sigma^{(2)}$.

Keeping the beam width constant, a measure of the force as a function of laser power would have a slope that is proportional to the linear coefficient, and the slope of the derivative would be proportional to the second-order coefficient. With a constant beam width, $\ell_{\min} I_{\max} = \ell I$, and Eqs. (315), (319), and (320) can be solved for the force on the load cell, f , yielding

$$f = \frac{tw\ell \sum_{n=1}^{\infty} \kappa_\sigma^{(n)} I^n}{L}, \quad (327)$$

where we assume that the body stress due to the photomechanical stress in the illuminated area is given by

$$\sigma_b = - \sum_{n=1}^{\infty} \kappa_\sigma^{(n)} I^n. \quad (328)$$

The reason for the negative sign will be discussed in Subsection 7.2.

Thus, Eq. (328) allows the load cell reading f as a function of the intensity I to be fit to the function

$$f = \sum_{n=1}^{\infty} b_n I^n, \quad (329)$$

and the fit parameters b_n will be related to the photomechanical stress constants according to

$$\kappa_\sigma^{(n)} = - \frac{L}{tw\ell} b_n. \quad (330)$$

In a highly nonlinear system, the power series expansion may not hold. One example is a power law force of the form

$$\sigma_b = E \left(\frac{I}{I_c} \right)^n, \quad (331)$$

where E is Young's modulus of the material given by

$$E = \frac{\partial \sigma}{\partial u}. \quad (332)$$

The coefficient E in Eq. (331) ensures that the right-hand side has units of stress; I_c is the critical intensity parameter—defined as the intensity at which the light-induced strain is unity; and the exponent n need not be a rational number.

Using Eq. (331), the load cell reading as a function of the intensity is given by

$$f = \frac{t w \ell E}{L} \left(\frac{I}{I_c} \right)^n, \quad (333)$$

so a plot of f versus I fit to $f = bI^n$ will yield the exponent n , and the critical intensity can be computed from the measured quantities according to

$$I_c = \left(\frac{t w \ell E}{b L} \right)^{1/n}. \quad (334)$$

Note that the exponential behavior given by Eq. (331) is usually a low-intensity approximation to a saturation model, which is of the form

$$\sigma_b = \frac{E}{1 + \left(\frac{I}{I_c} \right)^n}. \quad (335)$$

In the high-intensity regime, Eq. (335) asymptotically approaches E , having the value $\sigma_b = E/2$ when $I = I_c$.

Finally, we can rewrite Eq. (328) in the form

$$\sigma_b = E \sum_{n=1}^{\infty} \left(\frac{I}{I_c^{(n)}} \right)^n, \quad (336)$$

where E is Young's modulus and $I_c^{(n)}$ defines the critical intensity for the n^{th} -order term, which defines the intensity at which the photomechanical stress equals Young's modulus. The critical intensities are related to $\kappa_{\sigma}^{(n)}$ according to

$$\kappa_{\sigma}^{(n)} = \frac{E}{(I_c^{(n)})^n}. \quad (337)$$

The strength of the nonlinearity can be quantified by the intensity at which the linear and the quadratic terms become equal, which we call the crossover intensity I_{cr} , which is given by

$$I_{cr} = \frac{(I_c^{(2)})^2}{I_c^{(1)}}. \quad (338)$$

In a real material, light is lost due to absorption and scattering as it travels through the material. This effect needs to be taken into account when determining the photomechanical constants. If the absorbance is independent of intensity, as it will be in most cases when two-photon absorption can be ignored, the intensity will decay exponentially into the material according to

$$I(x, y, z) = I_0(0, y, z) \exp[-x/x_0], \quad (339)$$

where x_0 is the length over which $1/e$ of the light is lost to scattering and absorption, and $I_0(0, y, z)$ is the light intensity at the surface of the material. We have already considered the case where the light intensity varies as a function of z along the length

of the sample, but we had assumed that the intensity is constant along the sample's width.

If we view the sample as being made of infinitesimally thin slabs of width dx , each slab will behave as we have calculated above, but with an intensity given by Eq. (339). The total force on the load cell will then be a sum over all the slabs, yielding

$$f = -w\kappa_\sigma \bar{I} \int_0^t dx \exp[-x/x_0] = x_0 w \kappa_\sigma \bar{I} (1 - \exp[-t/x_0]), \quad (340)$$

where \bar{I} is the average intensity incident on the surface of the sample.

Solving Eq. (340) for κ_σ yields

$$\kappa_\sigma = \frac{1}{x_0(1 - \exp[-t/x_0])w} \cdot \frac{1}{\bar{I}} \cdot f. \quad (341)$$

Expressing Eq. (341) in terms of the power over the surface yields

$$\kappa_\sigma = \frac{L}{x_0(1 - \exp[-t/x_0])} \cdot \frac{1}{P} \cdot f. \quad (342)$$

When the absorption length x_0 is long compared with the sample thickness t , then $x_0(1 - \exp[-t/x_0]) \approx t$, so Eqs. (341) and (342) reduce to Eqs. (323) and (322), respectively. Equation (342) is the most general expression for the linear photometrical response, and the most simple to apply.

Step Function Intensity

The most general description of a material is through its response function, as given by Eq. (89). One possible experimental protocol is to pulse the pump light with a duration that is fast compared with the response time. Assuming a delta function $I = I_0\delta(t)$ intensity, Eq. (89) for the stress response becomes

$$\sigma^{(1)}(t) = \int_{-\infty}^{+\infty} d\tau R_\sigma^{(1)}(t - \tau) I_0\delta(\tau) = R^{(1)}(t) I_0. \quad (343)$$

The measured stress given by Eq. (343) directly gives the response function.

Alternatively, the light intensity can be turned on instantaneously to I_0 , giving the step function at $t = 0$ with $I(t) = I_0\theta(t)$, so that Eq. (89) becomes

$$\sigma^{(1)}(t) = I_0 \int_0^{+\infty} d\tau R_\sigma^{(1)}(t - \tau). \quad (344)$$

Differentiating Eq. (344) with respect to time and solving for the response function yields

$$R_\sigma^{(1)}(t) = \frac{1}{I_0} \frac{d}{dt} \sigma^{(1)}(t). \quad (345)$$

The same can be applied to the time after the light is turned off.

Typically, the stress response can be approximated by a sum of exponentials of the form

$$\sigma^{(1)}(t) = \sum_i \sigma_i (1 - \exp[-t/t_i]), \quad (346)$$

and this is a good way to analyze data when the underlying mechanisms are unknown. In special cases where the mechanisms are known, such as photoisomerization-induced stress, the stress response can be more complex as given by Eq. (212).

A summation of the linear responses given by Eq. (346) may not be well-suited to describe the step function response of complex systems with large nonlocal and nonlinear responses. However, if the linear response function is much faster than the transient response to nonlocal and nonlinear behavior, then an on/off square wave input intensity will wash out the slow transient response after several periods. Then, the summed exponential response function $R(t - \tau) = \sum_i A_i \exp[b_i(t - \tau)]$ is a good approximation after a few cycles when the other transients have subsided, as shown by Dawson *et al.* [126,127].

Figure 47 shows a typical experimental protocol using step functions of increasing intensities. This allows for the intensity dependence to be determined. The linear response function is a good approximation when the stress response is linear in the intensity, whereas a higher-order response is required in the nonlinear regime. Also shown is an exponential stress response as read by a force in the clamped configuration. Note that such an experiment can be repeated for a range of pre-strains and temperatures to determine the response function for different phases of the material.

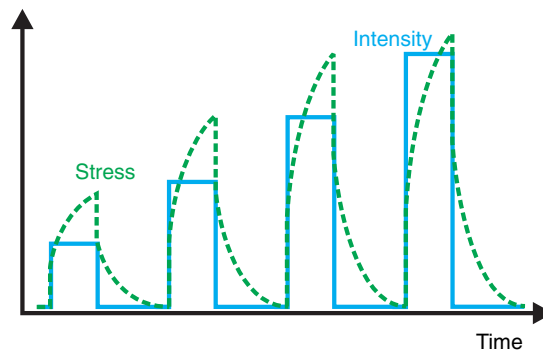
Figure 48 shows sample data at one intensity for a DO1-doped LCE of 600 μm thickness [33]. The error bars are determined from sampling statistics, and the fit is to a simple exponential during pumping and relaxation.

7.1b. Clamped Material–Waveguide Geometry

The clamped photomechanical stress response as measured with the apparatus shown in Fig. 45 uses pump light that illuminates the sample from the side. An alternate geometry corresponds to light that propagates in the sample, as it would in a waveguide. This guiding geometry is most appropriate for thin cylindrical samples that act as optical fibers. Such a geometry would be appropriate for characterizing polymer optical fibers [128].

For such measurements, the sample would be mounted with collets so that light can be launched into one end. In one configuration of the experiment, the light fully illuminates the cross-sectional area, as shown in Fig. 49. All the mechanisms would then contribute, such as photothermal heating and photoisomerization. Also, photostriction would act on the surface of the fiber where the electric field gradient is the largest.

Figure 47



Stress is measured as a function of time for a series of step function intensities of increasing amplitude. Reprinted from [33].

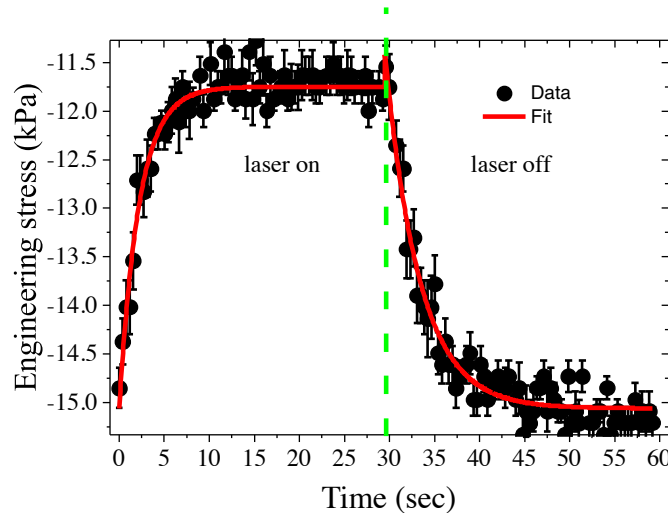
Assuming that the intensity is Gaussian through the surface, as shown in the bottom part of the figure, the gradient peaks at the $1/e$ width. If a short pulse is launched into the fiber, the inward force would only act at the location of the pulse, and would propagate at the group velocity. The neck-down region shown in Fig. 49 would be the shape of the fiber for an instantaneous response. Otherwise, the shape of the fiber would be more complex, with a shock wave at its front due to the fact that the light pulse travels much faster than the speed of sounds, with oscillations in its wake. The expected behavior is far too complex to describe here.

The simplest case is for a static beam or a pulse duration that greatly exceeds the transit time over the length of the fiber. In the steady-state case, the fiber cross section will reach an equilibrium shape, and the Poisson ratio (see Appendix D) will determine the axial extension in terms of the degree of radial compression. In the clamped geometry, the force of the ends on the collets is measured, and the Poisson ratio is used to determine the transverse force.

7.1c. Bending

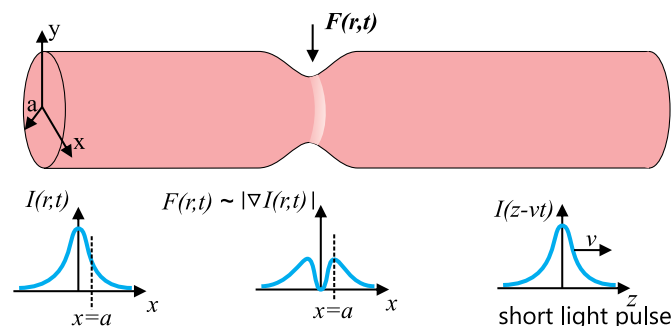
The unclamped geometry typically consists of a material that is held by one end while the other end is free to bend or elongate. Figure 50 shows an experiment designed by Bian and coworkers to measure the degree of bending in response to light [42].

Figure 48



Typical time dependence of the photomechanical stress for DO1 (Disperse Orange 1) Azo dye-doped liquid crystal elastomer of 600 μm thickness. Reprinted from [33].

Figure 49



Deformation of a fiber in response to a pulse that is traveling along its axis.

A tiny piece of a microscope coverslip is metalized with silver to make a mirror and glued onto the free end of a fiber while the other end is anchored to a transparent glass slide. Light is launched through the glass slide to actuate the fiber, and the degree of bending is probed with another laser that reflects from the mirror and passes through a lens/pinhole then onto a detector. Note that the mass is small enough to add negligible inertia.

The experiment relies on the Gaussian shape of the probe beam to associate the intensity read by the detector with a bend angle of the fiber end, as follows. The pinhole is placed at the $1/e$ intensity point of the probe beam for a fiber in its dark state. Thus, small changes in the angle of the mirror due to fiber bending results in a large change of the amount of light passing to the detector.

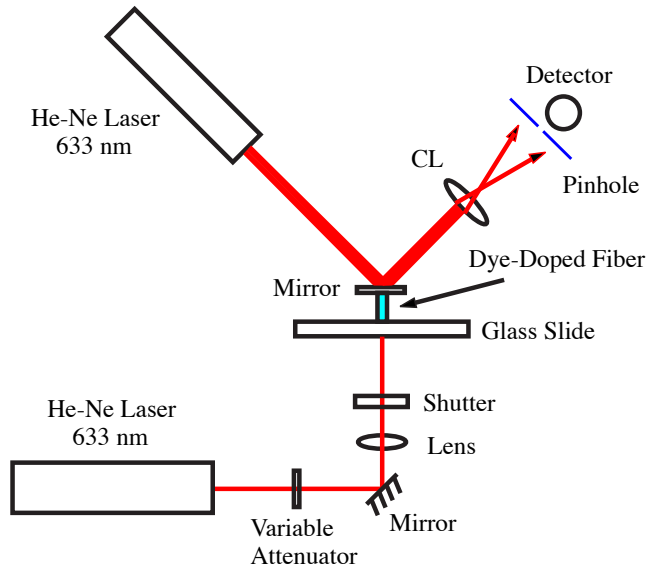
Figure 51(a) shows a dark fiber, and Fig. 51(b) shows an illuminated one with a beam parallel to its axis and shifted by a distance x . The fiber is observed to both bend and elongate. Note that this is a fiber without a mirror attached to its end.

Figure 52 shows the change in the transmitted intensity through the pinhole as a function of the distance of the pump beam from the fiber axis. The relationship between the transmitted intensity and the deflection angle is determined by placing the fiber-with-mirror on a rotation stage and measuring the transmitted power through the pinhole as a function of angle.

Figure 53 shows a plot of the deflection angle as a function of the detector voltage that measures the power transmitted through the pinhole. A fit of the data to a polynomial yields the calibration curve used to determine the deflection angle as a function of time when the fiber is pumped. The advantage of optical probing is that the response time of the experiment is limited only by the speed of the analog to digital converter.

The time dependence of the photomechanical response required a bi-exponential fit, yielding a slow process with a response time constant of about 3 s associated with molecular reorientation and a fast time constant of 120 ms associated with photothermal heating. Figure 54 shows a plot of the amplitude of the slow process as a function

Figure 50



Experiment used to measure the degree of fiber bending in response to light. The light transmitted through the pinhole is a measure of the degree of bending of the fiber. Reprinted from [42].

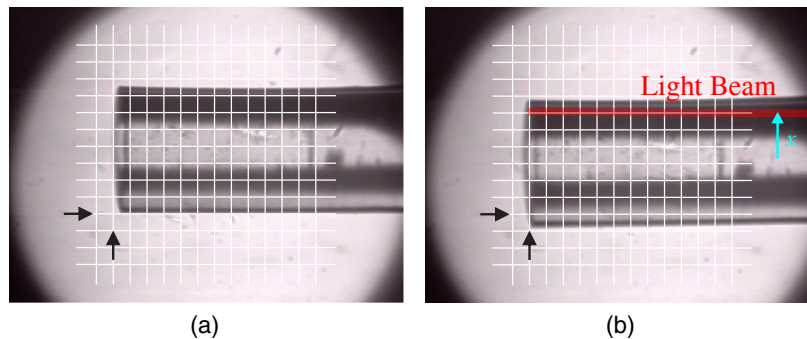
of pump power. The fiber is found to first bend in one direction, and then at a critical power it bends dramatically in the opposite direction. Bian and coworkers argued that this observation is due to a collective buildup in stress that is released at high intensity. This mechanism is yet to be understood and illustrates the riches of phenomena underlying the photomechanical response.

Other researchers have used observations of the degree of photomechanical bending in response to side illumination to characterize the material's response, and theories needed to analyze the response have been developed [43,129,130].

7.1d. Uniaxial Strain

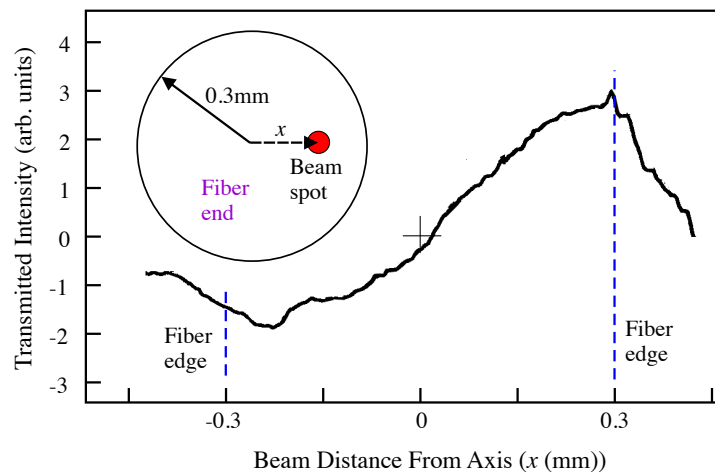
Uniaxial strain can be measured by taking a video of the movements of the free end of a sample to determine the change in the length of the material induced by light. The time response of such measurements is limited by the frame rate of the apparatus, and the many frames collected can tax the memory, as well as requiring postprocessing to determine the length from the images. An alternative method is to use a probe beam that directly measures the change in the material's thickness.

Figure 51



(a) Dark fiber and (b) a fiber illuminated with a beam that is launched parallel to the fiber a distance x from its axis. The arrows show a fixed point in space, and the reticules are for reference. Reprinted from [42].

Figure 52



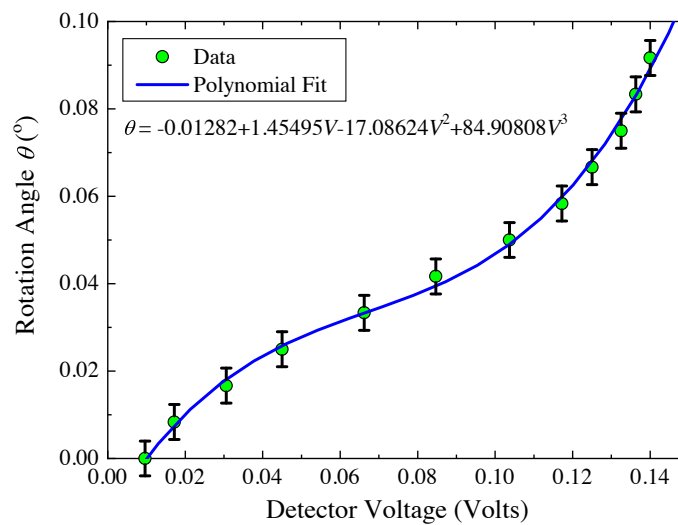
Intensity transmitted through the pinhole as a function of the distance of the pump beam from the fiber axis. Reprinted from [42].

Dawson devised a sensitive apparatus for measuring the length change of a sample using a mechanically balanced microscope slide whose weight is mostly born by the fulcrum [131]. The sample then needs only to overcome the inertia of the thin coverslip that is in contact with the free end.

Figure 54(a) shows a schematic diagram of the setup. The bottom plate is thick and massive to provide a stable support for the sample. The upper microscope slide is balanced on adjustable posts to minimally stress the material. Incident light that changes the sample thickness changes the position of the upper plate. Because the sample's thickness changes are small, the upper and lower plates remain approximately parallel.

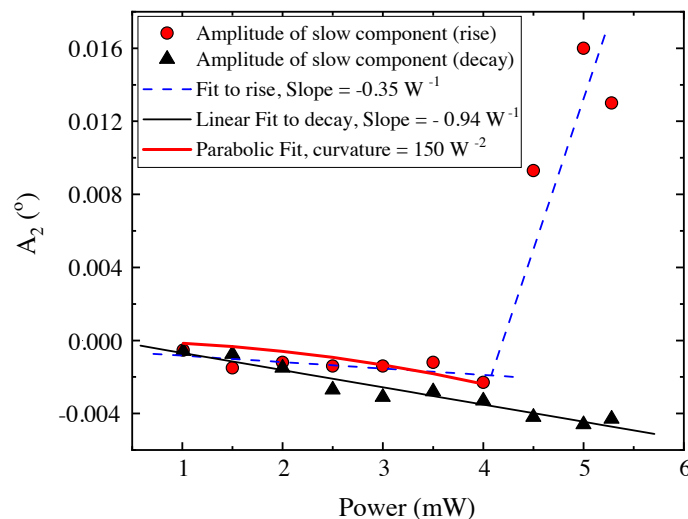
A probe beam passes through the parallel plates away from the sample. These regions can be partially silvered so that the parallel plates form a Fabry–Perot interferometer of high finesse. The Fresnel reflections from the plates can be used without silvering

Figure 53



Rotation angle as a function of the detector voltage (points) is used to get the calibration curve (fit). Reprinted from [42].

Figure 54



Amplitude of the slow process as a function of pump power. Reprinted from [42].

the surfaces to make a low-finesse interferometer. The change of the intensity of the transmitted probe beam determines the change in length. Figure 55(b) shows the transmitted power as a function of time, measured with a photo-detector and recorded with an oscilloscope after the pump beam is turned on then off, as shown with the solid red and dashed blue curves. The time resolution is limited by the rise time of the detector and the bandwidth of the oscilloscope. In principle, the time resolution can be as short as a nanosecond.

The transmitted probe power is converted to a length change using the fact that the distance between peaks corresponds to a change in sample thickness of one wavelength of the probe beam. The temperature change of the sample can be measured with a thermistor that is inserted into the sample. Since the thermistor damages the sample, the light-induced temperature change of the sample is measured after all the photomechanical experiments are complete. The close correlation between temperature change and sample thickness change in dye-doped LCEs was one of several observations that established the photothermal heating mechanism as the dominant one.

7.2. Sign Conventions

The sign conventions can be confusing. Here we discuss the signs of various material parameters using the standard definitions. We begin with the definition of Young's modulus.

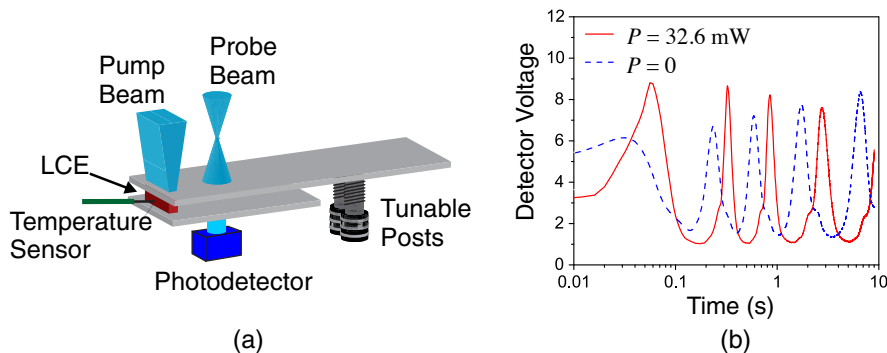
Recall that Eq. (4) holds if the system is linear, so that the displacement is always linearly proportional to the stress while Eq. (332) is required in the nonlinear regime. In the linear regime,

$$\sigma = E \frac{\Delta L}{L}, \quad (347)$$

so for a positive Young's modulus, the material's length increases in the direction of the applied stress. Young's modulus is negative if the sample's length decreases when the force acts to increase it—a very rare feat. Thus, because most materials expand in the direction of the applied force, a positive Young's modulus is the most common.

Analogous to the static stress response given by Eq. (328), the static strain response is given by

Figure 55



(a) Thin glass coverslip is balanced onto the top of the sample using tunable posts. (b) The transmitted power through the glass plates of the probe beam as a function of time. Adapted from [131,132].

$$\frac{\Delta L}{L} = u = \sum_{n=1}^{\infty} \kappa_u^{(n)} I^n. \quad (348)$$

Because the intensity is always positive, it stands to reason that the photomechanical constants are positive if the induced strain is positive. One can view the strain response as a change in the equilibrium length, so under light illumination, the length changes by ΔL when the sample is physically unconstrained.

The stress response in the clamped configuration is a more complex matter. Consider a sample initially at its resting length while clamped on both ends to prevent its length from changing. Under light illumination, the equilibrium length changes by ΔL , so the sample's length between the clamps is $-\Delta L$ from its equilibrium length. Thus, a sample whose length increases under light exposure will be compressed between the clamps.

For the discussions that follow, we consider only the linear terms in Eqs. (328) and (348) and view the process in steps where, first, the free sample is illuminated and the length increases according to Eq. (348). Then, we imagine clamps applied, which squeeze the sample to bring it back to length L requiring the length to decrease in length by an amount $-\Delta L$. Substituting Eq. (348) into Eq. (347) for the squeezed situation yields

$$\sigma = -E\kappa_u^{(1)} I. \quad (349)$$

Therefore, a sample that elongates yields a negative stress.

Equation (349) quantifies the fact that a material whose length increases when exposed to light will induce a negative stress provided that Young's modulus is positive. Intuition is best served when the stress response is of the same sign as the strain response; hence, the minus sign in Eq. (348). Comparing Eqs. (348) and (349) gives the relationship

$$\kappa_\sigma^{(1)} = E\kappa_u^{(1)}, \quad (350)$$

making the stress and strain response of the same sign.

7.3. Applications to Studies of Materials

This section describes how the various experimental techniques have been applied to measuring the photomechanical response of key materials to study the underlying mechanisms.

7.3a. Bending

Qualitative studies of bending during illumination can be used to glean information about the underlying mechanisms [133]. For example, consider the mechanisms of heating versus light-induced changes in isomer population in a thin film where mostly trans molecules are aligned in the plane of the film. A freely hanging film that is heated from one side with a heat gun induces a temperature gradient. The film will bend toward the heat source if the heating effect leads to a contraction of the material. There are two possible sources of heat-induced stress: (1) the cis population can increase on the heated side more than on the back side through thermal excitation, and (2) the heat can lead to thermal expansion/contraction of the host material. In a liquid crystal host, heating brings the material closer to transitioning to the isotropic phase, thus causing the material to shrink as the order parameter decreases. In a glassy polymer, heating leads to thermal expansion. The first process is more likely to take

place in a stilbene while most azo dyes should have a negligible heat-induced change in isomer populations. We will loosely refer to both mechanisms that contribute together to the heat gun experiment as the heating mechanism. Note that these two contributions to the heating mechanisms can be separated by comparing doped and un-doped hosts after taking into account the transition temperatures.

With light applied to one side, the *cis* population can increase from both heating and photoinduced isomerization. So, both effects will result in bending toward the light source. If one adjusts the light source to heat the material at the same rate as the heat gun, the mechanisms will be purely heating if the magnitude of the effect is the same in both experiments. Thus, if the photoisomerization mechanism is substantial compared with heating, a difference will be observed.

Light can also induce a transition from the *cis* to *trans* state. Often, the wavelength at which photoisomerization acts to produce *cis* isomers from *trans* is different than the wavelength of the reverse process. In this case, light of a different wavelength can be applied to the previously excited material. If the film bends away from the light, then photoisomerization is responsible when heat alone cannot drive such a process.

Lahikainen *et al.* determined the wavelengths for these distinct processes, as well as the role of heating in a liquid crystal network (LCN) [133]. This is in contrast to the more [42] quantitative work by Bian described in Subsection 7.1c, which used the response time and time dependence of the magnitude of the bending angle to separate the heating mechanisms from photoisomerization.

7.3b. Uniaxial Photomechanical Stress

In the clamped configuration described in Subsection 7.1a, light is applied to the side of a vertically mounted sample, and the stress in the vertical direction is measured through the upper clamp as a function of time. Typical data are shown in Fig. 48. To ensure that the photomechanical response is uniform throughout the sample, the light illuminates the whole side, and the dopant chromophore concentration is adjusted so that the $1/e$ optical absorption length is much greater than the sample thickness. For these data, the DR1 and DO11 concentrations were 0.01% and 0.28% by weight, respectively.

As an example of how the angular hole burning mechanism can be separated from heating, we draw on Subsection 6.7, which describes how for an isotropic material, polarized light will lead to an increase of the length (and stress) of the material perpendicular to the polarization of the light and a decrease perpendicular to it. Since the material is isotropic, the degree of sample heating should be independent of the pump light's polarization angle, leading to uniaxial stress that is also polarization independent. Note that Subsection 7.3d derives a more quantitative analysis of how the mechanisms can be separated.

In addition to polarization-dependent measurements, one can use a molecule that has only one configuration—so does not photoisomerize—as a control. Such molecules have a greatly suppressed probability of reorientational diffusion. (Some diffusion is possible from the thermal excitation of molecules along the light's polarization.) The photothermal heating contribution should be the same in both samples as long as Young's modulus, the thermal expansion coefficients, and the amount of light absorbed by the two samples are the same.

Figure 56 shows the intensity dependence of the stress for light of two polarizations (parallel and perpendicular to the vertical axis) for DR1-doped PMMA polymer fiber, which photoisomerizes, and D011-doped PMMA fiber, which does not [33]. The photomechanical stress for D011 is independent of polarization, as we would expect

for a purely thermal mechanism. The data are fit to a quadratic function, as shown by the curves. We note that all fibers were made to have a rectangular cross section.

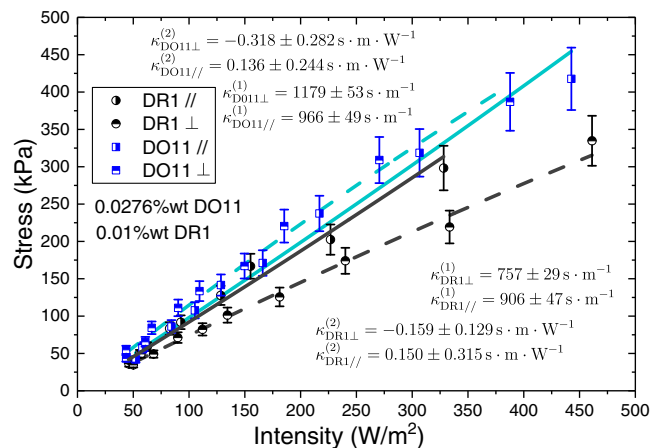
The photomechanical stress measured in DR1 when excited by light parallel to the vertical axis is found to be the same as for DO11—also consistent with photothermal heating. In addition, these runs show an increase in the stress so the fiber length is increasing. The perpendicular component is just outside the uncertainty range for being a purely heating effect. However, the length perpendicular to the long axis appears to be decreasing, opposite to what is predicted for angular hole burning.

Polymers are known to have different properties based on their stress-temperature history. For example if they are pulled into fibers under slightly different conditions of humidity, stress, and variations in composition, their rheological properties can be different [134]. Thus, the fact that the transverse length change is slightly outside the measurement uncertainty range is far short of definitive proof that angular hole burning contributes, leading the researchers to conclude that the dominant mechanism is photothermal heating [33].

Another piece of evidence is the time constant of the process. Figure 57 shows the time constants as a function of intensity for parallel and perpendicular pump polarizations in DR1 and DO11 samples [33]. Within experimental uncertainty, the linear response function time constants are all the same (the small box to the right shows the average time constant for each sample for each polarization). This result is consistent with the same mechanisms being at work for both samples and that photothermal heating dominates.

Changes in the isomer populations can also lead to a photomechanical stress in addition to thermal expansion of the polymer. Because the cis isomer is more compact in the direction of the original trans isomer, the length will decrease with an increased population of cis isomers, which counteracts the increased length of the polymer caused by photothermal heating. Thus, the photomechanical stress is smaller for DR1. The data agree with this model and show, on average, the DR1 sample has a smaller photomechanical force.

Figure 56



Intensity dependence of photomechanical stress of DR1-doped PMMA and DO11-doped PMMA for excitation polarization along and perpendicular to the fiber of 200 μm thickness. Note that by convention, the stress is negative, but is plotted as positive for convenience. Reprinted from [33].

The data suggest the tentative conclusion that angular hole burning contributes little to the photomechanical response, but that the dominant heating mechanism is accompanied with a photoinduced change in the isomer population, leading to a slightly smaller photomechanical response than for a material with dopants that have only one conformation. Finally, the extra degree of freedom from an isomerizable dye might increase the heat capacity of the material, thus decreasing the temperature change and the stress induced by the photothermal length change. The reader must be cautioned that some of these effects may be smaller than material variations, sample history, and measurement uncertainty.

7.3c. Uniaxial Length Change

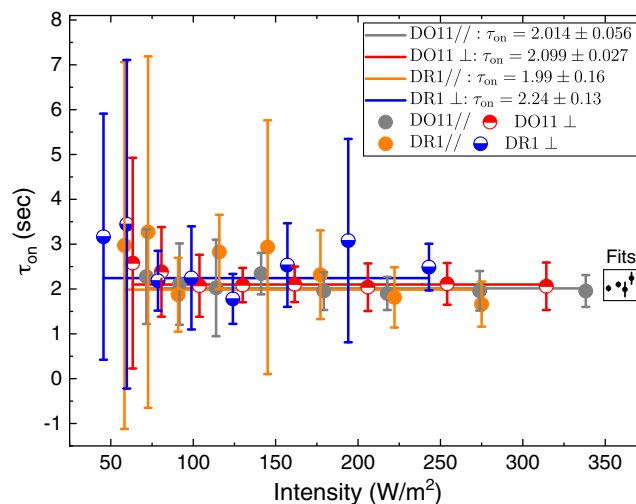
Here we review how Dawson *et al.* applied the balanced glass plate technique described in Subsection 7.1d to measure the length change of a dye-doped cross-linked LCE, and how this was used to deduce the underlying mechanism [131].

Figure 58(a) shows the data, and the inset shows the structures of the two dopant dyes measured; the azo dye DO3, which changes conformation when exposed to light, and DO11, which does not. The host elastomer is poly(methylhydrosiloxane) (PMHS). The concentrations were chosen so that both samples absorb the same amount of light. The host material is a cross-linked siloxane polymer with pendent side chain mesogenic units as shown in Fig. 58(b). The sample is 400 μm thick, 2 mm long, and 400 μm wide.

The measured change in length as a function of time after the pump laser is turned on is measured for both samples, and found to be the same for almost three decades of time. This suggests that the same mechanism is at work. Given that DO11 has no contribution from photoisomerization, the data strongly suggest that photoisomerization plays no role.

After characterizing the length change, the temperature change was measured as a function of time, and the amount of heating in both samples is found to be the same. Note that the strain observed gives a thermal expansion coefficient of about

Figure 57



Time constants of the turn on of stress upon illumination for DR1/PMMA and DO11/PMMA for both polarizations. The tiny inset on the right plots the average time constant for each sample and polarization as well as the error bars derived from the fits. Reprinted from [33].

$\delta L/L \approx 10^{-3} \text{ K}^{-1}$, which is in the correct ballpark for PMHS. More rigorous calculations by Dawson showed that the time evolution of the length change and temperature is consistent with thermal diffusion through the sample and into the substrates [132].

Finally, Dawson painted the inner face of the top plate black to absorb all of the light so that the sample remained dark, but heat generated by absorbed light was able to diffuse into the sample. The temperature dependence as a function of time and for several intensities was again found to be the same in both DO11 and DO3 [131]. These sets of consistent results show that the photothermal heating mechanism dominates and that photoisomerization does not contribute from either the direct effect of a conformational change in the dopant changing the liquid crystalline order or the indirect effect from heating changing the population of trans isomers. Rather, the light is absorbed by the dopant chromophore, which heats the liquid crystal and changes its order parameter. This is the same result reported in dye-doped PMMA polymer fibers described in Subsection 7.3b, but here, changes in the liquid crystal lead to strain rather than thermal expansion of the polymer.

7.3d. Mixed Orientational Hole Burning and Photothermal Heating

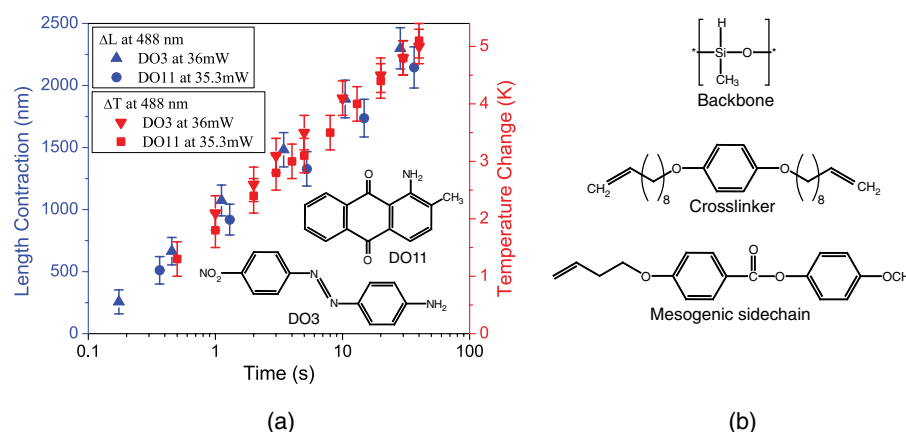
Since heating is a common mechanism that dominates the photomechanical response in many materials, it is instructive to describe how a mixture of these two mechanisms can be studied using polarized light. The derivation will apply equally well to an isotropic dye-doped polymer or polydomain LCE.

We consider the clamped experiment that measures stress along the long axis of the sample. With σ_{\parallel} the measured stress response to light polarized along the long axis and σ_{\perp} the stress response measured for the perpendicular polarization, the ratio is

$$\frac{\sigma_{\parallel}}{\sigma_{\perp}} = \frac{\sigma_{\parallel}^{(\text{heat})} + \sigma_{\parallel}^{(\text{hole})}}{\sigma_{\perp}^{(\text{heat})} + \sigma_{\perp}^{(\text{hole})}}, \quad (351)$$

where the superscript refers to the mechanism. Note that heating and orientational hole burning are generally coupled, as given by Eq. (211)—where the temperature depends on the intensity—so will not be additive. For low intensities, additivity is a good approximation as shown in the box that follows.

Figure 58



(a) Measured length (blue symbols) and temperature change (red symbols) for DO3 (triangles) and DO11 dye (circles). (b) The poly(methylhydrosiloxane) backbone, cross-linker, and mesogenic sidechain. Adapted with permission from [130].

Here we show how in the limit of low intensity, additivity of the mechanisms is a good approximation. Consider the temperature-dependent term in Eq. (211), which under a small temperature change ΔT with $\Delta T/T \ll 1$ can be generalized by making the substitution $T \rightarrow T + \Delta T$. After some algebraic calisthenics, to first order in the temperature change, we get

$$\frac{\beta'}{1 + e^{V_0/k_B(T+\Delta T)}} \approx \frac{\beta'}{1 + e^{V_0/k_B T}} + \frac{1}{2} \frac{1}{\cosh(V_0/k_B T) + 1} \frac{\Delta T}{T}. \quad (352)$$

If the temperature change is proportional to the applied intensity $\Delta T = \xi I$, then using Eq. (352), the photomechanical force given by Eq. (211) becomes

$$F(I, T) = \frac{k(x_b - a) \left[\alpha_0 I + \frac{\beta'}{1 + e^{V_0/k_B T}} + \frac{\xi}{2T} \frac{1}{\cosh(V_0/k_B T) + 1} I \right]}{\beta + \beta' + \alpha I - \left(1 - \frac{k}{k'}\right) \left[\alpha_0 I + \frac{\beta'}{1 + e^{V_0/k_B T}} + \frac{\xi}{2T} \frac{1}{\cosh(V_0/k_B T) + 1} I \right]}. \quad (353)$$

Equation (352) shows that the added term is linear in the intensity and can be combined with the $\alpha_0 I$ term, so additivity holds. We note that as the temperature is increased, Eq. (352) shows that the photothermal contribution decreases as long as the temperature is low compared with the cis-trans energy difference, or $V_0/k_B T \ll 1$.

For the isotropic sample being considered here, the heating contribution is polarization independent, yielding

$$\sigma_{\parallel}^{(\text{heat})} = \sigma_{\perp}^{(\text{heat})} \equiv \sigma^{(\text{heat})}(I), \quad (354)$$

where we assume that the light-induced stress depends on intensity and, according to convention as described in Subsection 7.2, $\sigma^{(\text{heat})}(I)$ is defined to be negative when the stress acts to make the sample expand upon heating and positive when it acts to make it contract. The stress can also depend on temperature, but for this illustration, we assume that the experiments are performed at room temperature.

It is useful here to emphasize the definition of the sign of the stress to avoid confusion. If a sample is stretched between two clamps so that its length is fixed, the light-induced stress is defined to be positive when it acts to make the sample shrink and negative when it acts to make it expand.

For a material made mostly of trans isomers, orientational hole burning leads to a decrease in length along the direction of polarization and an increase perpendicular to it, or

$$\sigma_{\parallel}^{(\text{hole})} = -2\sigma_{\perp}^{(\text{hole})} \equiv \sigma^{(\text{hole})}(I), \quad (355)$$

with $\sigma^{(\text{hole})}(I) > 0$. For a sample made of mostly cis isomers, one can devise a scenario where the sample would expand in the direction of light polarization. The factor of 2 comes from the fact that half of the molecules that reorient away from the pump beam's polarization become aligned with the long axis of the sample and, hence, are measured by the stress sensor, and the other half aligns with the beam's propagation direction. The formal derivation that leads to this factor of 2 requires the use of the orientational distribution function [65, 135], which is beyond the scope of this paper.

Substituting Eqs. (354) and (355) into Eq. (351) yields

$$\frac{\sigma_{\parallel}}{\sigma_{\perp}} = \frac{\sigma^{(\text{heat})}(I) + \sigma^{(\text{hole})}(I)}{\sigma^{(\text{heat})}(I) - \frac{1}{2}\sigma^{(\text{hole})}(I)} = \frac{1 + \sigma^{(\text{hole})}(I)/\sigma^{(\text{heat})}(I)}{1 - \frac{1}{2}\sigma^{(\text{hole})}(I)/\sigma^{(\text{heat})}(I)}. \quad (356)$$

Recall that $\frac{\sigma_{\parallel}}{\sigma_{\perp}}$ is the measured stress ratio and $\frac{\sigma^{(\text{hole})}(I)}{\sigma^{(\text{heat})}(I)}$ is the ratio of the contributions of the two mechanisms. Using Eq. (356), we can solve for the ratio of the underlying contributions, yielding

$$R \equiv \frac{\sigma^{(\text{hole})}(I)}{\sigma^{(\text{heat})}(I)} = \frac{\frac{\sigma_{\parallel}}{\sigma_{\perp}} - 1}{1 + \frac{1}{2}\frac{\sigma_{\parallel}}{\sigma_{\perp}}}. \quad (357)$$

R is positive for a material that shrinks when heated, such as an elastomer, and is negative for a material that expands when heated, such as a dye-doped polymer.

Finally, we can use the ratio R determined from Eq. (357) to get the individual contributions using Eqs. (354) and (355), as follows. Equation (357) can be used to eliminate $\sigma^{(\text{hole})}$ in all the equations using

$$\sigma^{(\text{hole})}(I) = R\sigma^{(\text{heat})}(I), \quad (358)$$

which applied to Eq. (355) yields

$$\sigma_{\parallel}^{(\text{hole})} = R\sigma^{(\text{heat})}(I). \quad (359)$$

Using Eqs. (354) and (359), the measured parallel stress [numerator of Eq. (351)] is

$$\sigma_{\parallel} = \sigma_{\parallel}^{(\text{heat})} + \sigma_{\parallel}^{(\text{hole})} = (R + 1)\sigma^{(\text{heat})}(I), \quad (360)$$

which yields the heating mechanism alone in terms of the measured quantities given by

$$\sigma^{(\text{heat})}(I) = \frac{\sigma_{\parallel}}{R + 1}, \quad (361)$$

and the orientational hole burning mechanism is calculated with the help of Eq. (358), yielding

$$\sigma^{(\text{hole})}(I) = \frac{R\sigma_{\parallel}}{R + 1}. \quad (362)$$

Now we are ready to get the individual contributions from heating and orientational hole burning using Eqs. (354) and (355), or

$$\sigma_{\parallel}^{(\text{heat})} = \sigma_{\perp}^{(\text{heat})} = \frac{\sigma_{\parallel}}{R + 1}, \quad (363)$$

$$\sigma_{\parallel}^{(\text{hole})} = \frac{R\sigma_{\parallel}}{R + 1}, \quad (364)$$

and

$$\sigma_{\perp}^{(\text{hole})} = -\frac{1}{2}\frac{R\sigma_{\parallel}}{R + 1}. \quad (365)$$

Equations (363), (364), and (365) give all of the individual mechanisms that contributed to each polarization.

We can apply the above analysis to the dye-doped PMMA data shown in Fig. 56. In the low-intensity regime, the photomechanical stress is linear in the intensity, so that

$$\frac{\sigma_{\parallel}}{\sigma_{\perp}} \approx \frac{-\kappa_{\parallel}^{(1)} I}{-\kappa_{\perp}^{(1)} I} = \frac{\kappa_{\parallel}^{(1)}}{\kappa_{\perp}^{(1)}}, \quad (366)$$

where the negative signs come from Eq. (328). Table 1 shows this ratio for DO11- and DR1-doped PMMA polymer fibers using the parameters in Fig. 56.

Since DO11 does not isomerize, we expect there to be no angular hole burning, yet the data show a slight nonzero amount that appears to be statistically significant. The uncertainties were prorogated from the value of $\kappa_{\sigma}^{(1)}$ determined from the plot. Since the variations in the material can be larger than statistical uncertainty, and variations observed in the same sample can exceed 15%, the result is consistent with no angular hole burning.

The angular hole burning fraction in DR1 is about the same as in DO11, but the positive sign implies that angular hole burning aligns the molecules along the light's polarization. This runs counter to the model; however, the ratio is smaller than the typically observed sample-to-sample variations, so angular hole burning is likely not responsible in both materials.

Thermal expansion of a thermoplastic is caused by photothermal heating. Conversion of the trans isomer to the more compact cis form upon heating leads to contraction, which opposes thermal expansion. Table 1 shows the contributions from photothermal heating and hole burning. Though the amount of energy absorbed by DO11 and DR1 is the same, thermal expansion appears to be greater in DO11. Since DO11 has only one conformation, one explanation is that it does not have a contribution from an increased population of cis isomers as does DR1. An alternate explanation is that the DR1 thermal isomerization in DR1 leads to an added degree of freedom that increases the material's heat capacity, thus lowering the temperature increase and thus the thermal photomechanical response.

The above analysis assumes that the material is isotropic. If not, the model can be tweaked. For example, if the dye molecules are isotropically distributed but the polymer chains are aligned due to stresses imparted to the material when being fabricated, an increase in temperature can cause the material to shrink in the alignment direction. Depending on this alignment direction, this can lead to an increase or decrease of the force relative to the isotropic response.

Finally, the molecules might be slightly aligned in an otherwise isotropic polymer, so more light can be absorbed for one polarization than the other one. All of these effects can explain the peculiarities of the DR1 data. For example, if the DR1 molecules are aligned with the long axis, the photomechanical response would be larger for the parallel polarization, resulting in what appears to be an angular hole burning response that adds to the thermal response. A more thorough analysis of the data is required to determine these other contributions, such as dichroism measurements, which are sensitive to chromophore alignment, and birefringence, which can be used to determine polymer alignment. Such measurements during optical pumping would give a real-time picture of which underlying mechanisms are at play.

Table 1. Fractional Contribution from Angular Hole Burning Calculated from the Polarization-Dependent Stress and the Individual Contributions to Each Mechanism in Dye-Doped PMMA

Dye	$\frac{\sigma_{\parallel}}{\sigma_{\perp}}$	$R = \frac{\sigma_{\text{(hole)}}}{\sigma_{\text{(heat)}}}$	$\kappa_{\parallel}^{(\text{heat})}$ (s · m ⁻¹)	$\kappa_{\parallel}^{(\text{hole})}$ (s · m ⁻¹)	$\kappa_{\perp}^{(\text{hole})}$ (s · m ⁻¹)
DO11	0.819(±0.056)	-0.128(±0.039)	1108(±75)	-142(±11)	71(±6)
DR1	1.197(±0.077)	+0.123(±0.048)	807(±54)	99(±35)	-49(±17)

8. EFFICIENCY AND FIGURE OF MERIT

One of the motivations for developing a technology based on photomechanical materials is their potential high efficiency for converting light energy directly into mechanical work without the need for intermediary devices such as solar cells, wires, and motors. This section focuses on the efficiency of the photomechanical effect due to various parts of the material. The penultimate goal here is to determine the overall efficiency taking into account all contributions, as proposed by Zhou and coworkers [33]. From this we develop a figure of merit for a photomechanical material.

8.1. PM Unit Efficiency

The efficiency of the PM unit is governed by Eq. (163), which expresses the potential energy available for doing work. In the absence of the spring environment of force constant k_e , the full energy of the photomechanical potential $V_0 \equiv V(0)$ from the molecule is available. With an elastic environment, the PM unit efficiency is given by

$$\xi_{\text{PM}} = \frac{V(k_e)}{V_0} = \frac{k_b}{k_e + k_b}. \quad (367)$$

The efficiency of the PM unit given by Eq. (367) is unity when $k_e = 0$ and gets smaller as k_e increases and energy is lost to the parasitic environment. Thus, the best photomechanical material is one made of a dense network of interconnected photoactive molecules in the absence of a passive environment.

8.2. Photomorphon Efficiency

The fundamental photomechanical efficiency is determined by the fraction of a photon's energy that is delivered to the bulk response per unit of volume, v . For simplicity, we assume that the material's Young's modulus is unchanged by light, so Eq. (158) with $k = k'$ yields

$$v = \frac{dV}{Al} = \frac{1}{2} \frac{1}{k} (F_1 - F_2)^2 / \ell A = \frac{1}{2} \frac{1}{EA/\ell} (A\sigma_1 - A\sigma_2)^2 / \ell A, \quad (368)$$

where we have converted all the microscopic values to bulk ones and expressed the results in terms of strain in lieu of force. Multiplying out all the lengths and areas, and using the photomechanical stress definition to first-order in the field converts Eq. (368) to the form

$$v = \frac{1}{2} \frac{1}{E} (\kappa_\sigma^{(1)})^2 I^2. \quad (369)$$

Equation (369) is derived from the microscopic picture. The macroscopic equivalent is the mechanical energy density stored in a strained linear material ϵ with $\sigma = Eu$, yielding

$$\epsilon = \int_0^u du' \sigma(u') = \int_0^u du' E u' = \frac{1}{2} E u^2. \quad (370)$$

For a linear photomechanical response with $u = \kappa_u^{(1)} I$, Eq. (370) becomes

$$\epsilon = \frac{1}{2} E (\kappa_u^{(1)})^2 I^2 = \frac{1}{2} \frac{1}{E} (\kappa_\sigma^{(1)})^2 I^2, \quad (371)$$

which is the same as Eq. (369).

Equations (369) and (371) suggest an efficiency figure of merit for a material of the form

$$\text{FOM} = \frac{1}{E} (\kappa_{\sigma}^{(1)})^2 = E (\kappa_u^{(1)})^2, \quad (372)$$

where the last equality uses the relationship $\kappa_{\sigma}^{(1)} = E \kappa_u^{(1)}$ to express the efficiency in terms of the strain response. Thus, a measure of the clamped stress-photomechanical coefficient and Young's modulus together uniquely defines the figure of merit.

9. OVERVIEW OF PHOTOMECHANICAL MATERIALS

The observations of photoinduced deformations in materials is extensive. In this section, we focus on hallmark discoveries of photomechanical behavior in solid-state systems and summarize the materials' response. Some of the materials described here have been mentioned in previous sections in the context of device designs, illustrations of mechanisms, or material characterization examples. This section reviews all the materials in one place with an emphasis on how they respond to light. Tables 3 and 4 in Appendix A tabulate the properties of many materials and structures.

We begin by tabulating the figure of merit defined by Eq. (372) for some representative materials for which quantitative data are available [33]. Table 2 shows both the stress and strain response as well as the figure of merit.

The best figures of merit are for DO11- and DR1-doped PMMA, which are dominated by photothermal heating as discussed in Subsection 7.3b. The figure of merit for a monodomain LCE is an order of magnitude larger than for a polydomain material, which is expected based on the fact that the domains are all aligned so act together coherently. The stress induced by polarized light in one domain is along the domain's director, and the strength of the stress is a function of the component of the light's electric field along the director. As a result, domains aligned with the light's polarization axis provide the largest stress while those that are perpendicular to the light's polarization contribute nothing, with those in between contributing sub-optimally. Since the domains are randomly oriented in a polydomain sample, the stress is reduced by the orientational average over the domains, leading to the order-of-magnitude drop.

9.1. "Photophone"

As described in Section 1, Alexander Graham Bell is credited with the discovery and application of the photomechanical effect as a key component of the photophone. The photophone converts voice to modulated light, which travels to the receiver where it is converted back to sound. A critical part of the receiver is the battery-powered selenium detector, which converts the modulated light to electricity that drives a speaker

Table 2. Summary of the Measured Photomechanical Response, Young's Modulus, and Figure of Merit for All Measured Materials^{a,b}

Material	$\kappa_{\sigma}^{(1)}$ (s/m)	E (Mpa)	$\kappa_u^{(1)}$ (s · m/N)	τ_{on} (s)	FOM (10^{-4} s ² /N)
Monodomain LCE	-23.4 ± 1.2	2.99 ± 0.02	7.8 ± 0.4		1.83 ± 0.13
Polydomain LCE	-4.5 ± 1.9	1.26 ± 0.01	3.6 ± 1.5	$5s, I \rightarrow 0$	0.16 ± 0.10
CNT LCE	-0.98 ± 0.07	0.457 ± 0.0002	2.1 ± 0.2		0.020 ± 0.002
DR1-PMMA;	906 ± 47	2240 ± 200	0.37 ± 0.04	1.99 ± 0.16	3.66 ± 0.42
DR1-PMMA; ⊥	757 ± 29	2240 ± 200	0.44 ± 0.04	2.24 ± 0.13	2.56 ± 0.30
DO11-PMMA;	966 ± 49	2240 ± 200	0.17 ± 0.02	2.014 ± 0.056	4.16 ± 0.48
DO11-PMMA; ⊥	1179 ± 53	2240 ± 200	0.18 ± 0.02	2.099 ± 0.027	6.20 ± 0.72

^aCNT LCE is a liquid crystal elastomer doped with carbon nanotubes.

^bAdapted from [33].

[2]. The selenium material was prepared by heating the selenium over a stove until its appearance dimmed. According to Alexander Graham Bell, the best photophone results were obtained when the gas was shut off immediately after the first sign of localized melting, where the melted portions immediately recrystallize. The selenium was reported to have small crystal domains with many smaller crystalline grains appearing upon further cooling. Overheating resulted in a smooth surface as imaged through an optical microscope.

A rubber diaphragm was the first reported photomechanical material [136]. This motivated the first search for materials that more effectively convert light directly to sound. This search waned over the years as the photophone was found to be impractical given the line-of-site requirement between transmitter and receiver. Over a century later, however, new applications for photomechanical materials led to a renewed interest in designing novel composites with increased efficiency. Here we review some of that literature.

9.2. Bilayer Materials

Crystals and ceramics composed of molecules/unit cells with asymmetric charge distributions can often exhibit piezoelectricity. Piezoelectricity is the induced displacement of electric charges as a result of a strain/stress applied to a material. The reverse phenomenon also occurs in the same type of material, where stress can be induced as a result of an applied electric field. The latter can be used to make electromechanical actuators from piezoelectric materials.

Piezoelectric materials can also be made into photomechanical actuators. For example, doping lead lanthanum zirconium titanate (PLZT) ceramics with small amounts of niobium and tungsten creates a material that undergoes a mechanical deformation when exposed to light [13]. A bilayer can be made by layering two thin sheets of PLZT ceramics with differing polarization directions. When the photostrictive sheet is illuminated with UV light, there is a photovoltaic effect generated, which induces reverse piezoelectricity, and thereby results in a photostrictive strain [12]. The strain in a single layer causes the bilayer to bend. After the light is turned off, the bilayer returns to its original shape illustrating reversible photomechanical actuation.

The “Uchino Walker” was created to show how simple circuitless devices can be made from photomechanical actuators. Here, the bilayer actuators previously discussed were used as a leg in the walker. The two-legged walker had a set of bilayers that were attached to a plastic slab as illustrated in Fig. 3. The legs were alternately illuminated with light, which resulted in a walking motion. It is important to note that the photomechanical bilayer used in the walker is a truly reversible photomechanical transducer, where the power to drive Uchino’s walker was carried in the optical signals. Recently, the photothermal effect coupled with the adsorption and desorption of water has been used as a mechanism for a different type of walker [137]. A biomorph was also shown to mimic the circadian rhythms of some plant leaves [138].

Many other types of photoresponsive compatible monoliths have been used to create photomechanical bilayers, where photothermal heating is the dominant mechanism in most of the recently reported photomechanical bilayers [139]. Adhering a thin strip of material under lateral stress to a thin flexible substrate can cause the newly formed bilayer to undergo a bending motion. Such bending motion is commonly observed in thin bilayers that are made of two materials with large differences in their coefficients of thermal expansion (or contraction), where bending occurs when heat is applied. Many photomechanical materials made of amorphous bilayers are simply the result of photothermal heating, most of which utilize the large photoconversion efficiency of graphene [140–143]. In fact, two substrates of the same material can be made into

a photothermally driven photomechanical cantilever by simply doping one layer to give it strong light-absorbing and high photothermal conversion efficiency properties [144–146]. Composite materials such as carbon nanopowder-PDMS can coat a one-way, shape-memory Ni–Ti alloy, where the large photothermal temperatures from the coating can cause a phase change in the Ni–Ti to create a two-way, reversible photomechanical material [147].

In addition to bilayers, the photothermal effect can cause a bending motion in highly absorbing monoliths by side-pumping the monolith to create the same large temperature gradient observed in bilayer cantilevers actuated by light absorption in the surface layer [148]. Other interesting photomechanical phenomena occur in multilayers. Microribbon layers were shown to laterally expand upon light irradiation and contract when irradiated by an electron beam [149]. The photomechanical behavior of a multilayer structure of MoS nanoscale sheets layered between PDMS slabs is described via a straintronic-photothermic effect [150].

9.3. Crystals of Small Molecules

Crystallized small molecules have been well-investigated for their photomechanical capabilities [151]. Photoisomerization and photochemical reactions within the densely packed crystals can cause macroscopic mechanical motions with fast response times [152]. Both reversible and irreversible photomechanical effects have been observed; crystalline materials that undergo irreversible photomechanical changes at large scales can be reversibly photo-deformed when one or more dimensions are small.

9.3a. Irreversible Photomechanical Effects in Molecular Crystals

The photophone is an example of a reversible photomechanical system powered by a local energy source (battery). When the photomechanical behavior is a single material and a local energy source is required to drive the mechanical motion, then the material itself must also store the energy to be released. Such a process is irreversible and often results in bursts analogous to the release of mechanical stresses in heated popcorn.

Organic crystals can form in a state of quasi-equilibrium where internal stresses compete with attractive forces. When a mechanical force is applied to such a crystal, the barrier energy can sometimes be overcome, and mechanical energy is released from localized stress relaxation. This release of mechanical energy can propagate through the crystal and release more energy by severing additional stressed bonds. Some induced fracture lines will result in a net release of mechanical energy. In rare cases, crystals can release mechanical energy upon illumination by a UV light source [153]. When the absorption of light causes a phase change in the crystal, the system is momentarily out of thermal equilibrium. The internal stresses that result from this phase change can result in a forcible explosion of mechanical energy [154,155].

The explosion of a crystal upon illumination is an extreme case of what is known as the photosalient effect, first observed by Etter *et al.* [156] with the effect being named decades later [157]. Not all single crystals explode when photochemical reactions take place, such as the photodimerization reaction to light. Many of the known photosalient effects in crystals result in hopping or leaping of the material immediately after illumination. Investigations have reported various photosalient effects in organic crystals [158–162].

9.3b. Reversible Photomechanical Effects in Molecular Crystals

Some small-molecule organic crystals have been shown to exhibit reversible or partially reversible photomechanical behavior. For a perfectly reversible system, the

internal energy of the system after one full cycle is equal to the energy of the initial state. Both photochromic and photothermal effects can play a role in the reversible photomechanics of organic crystals.

Due to the photochromic nature of the azo functional group and the propensity for azobenzene compounds to crystallize, photomechanical effects have been observed in thin crystalline films of azobenzene derivatives. The films were shown to exhibit a moderate macroscopic bend when side-pumped with a continuous wave laser. The maximum deflection angle was observed at intensities of between 1.2 W/cm^2 to 1.6 W/cm^2 in disperse red 13, para red, and 4-diethylamino-4'-nitroazobenzene [163]. Salicylideneanilines form another class of photochromic molecules that also crystallize, where reversible photomechanical switching was observed. Such molecules have photochromic responses to different wavelengths of light, which result in stable macroscopic bends in the crystals upon UV illumination and straight crystalline films being recovered when illuminated with lower-energy light in the visible spectrum [164].

Films and fibers of photochromic organic crystals have been identified as photomechanical cantilevers [44,165–170]. Photodimerization-induced bending of molecular crystals of non-photoisomerizable structures have also been reported [171,172]. Some large photosolvent crystals that crack under illumination have been shown to self-heal [173], which results in a reversible process.

9.4. Amorphous Photochromic Polymers

Photochromic polymers are typically rigid backbone polymers with repeating photochromic moieties. The photomechanical materials made from photochromic azo polymers reviewed in this section have relatively large energy differences between the two isomer states. The temperature changes in the material upon illumination are assumed to result in negligible changes in the isomer populations, where thermal expansion from a temperature change was found to be negligible in the surface inscription process of azobenzene polymers [174]. Polymer backbones containing azo functional groups were adopted early on in amorphous photochromic polymers [175] due to the trans-cis photoisomerization and the cis-trans isomerization back reaction. The cis-trans back reaction is key to the reversibility of azo-containing photomechanical materials. Stilbenes were expected to undergo permanent macroscopic deformations due to irreversible back reactions of the cis isomer; however, Liao *et al.* showed that the macroscopic bending of α -cyanostilbene-containing polymers can be re-straightened via an external mechanical force [176]. Trans-cis isomerization of the azo groups causes rigid backbone segments to bend and contort resulting in macroscopic deformations [177]. The use of azo-containing polymers as photomechanical materials is now widespread [178]. Other photochromic moieties can cause physical deformations in polymeric materials such as the photoinduced changes in the thickness of diarylethene-based polymer thin films [179].

Polyimides are commonly used in the backbone of photochromic polymers. Although azo-containing polyimides [8] have relatively high backbone rigidity, their crystallinity can reduce the resultant photomechanical strain [178]. Cross-linking the polyimide polymer can decrease the crystallinity and, in turn, increase the resultant photoinduced strain [180]. Reducing the backbone rigidity of azo-containing polyimides also increases the photomechanical strain and reversibility [181]. Photochromic polymer backbones based on polyvinyl pyridine [176], polyamide [182], and polyamide acid [183] have also been used to create photomechanical materials.

Some photochromic polymers do not deform through direct bending of the backbone. Small photomechanical effects have been observed when the photoisomerizable group is on the side chain of polyimides without cross-links [184]. Large photoinduced deformations have been observed in the soft amorphous polymer siloxane with azo groups only in its side chain [185]. The photoinduced deformation of an interpenetrating network of azobenzene-cross-linked poly(vinyl ether) occurs from the severing of trans-trans cross-links through trans-cis photoisomerization [186]. Norborene with an organometallic ruthenium-pyridine-sulfoxide side chain has been shown to photomechanically bend, where hardening of the illuminated side upon photoisomerization is the hypothesized mechanism [187].

The photo-driven cantilever is the most common application of azo-containing photomechanical polymers. Other phenomena have also been observed such as thin strips of azo-polymers that produce photomechanical-driven waves when pumped at a large incident angle [188]. The UV sensitivity and localized photoinduced stress of photochromic polymers has been used to create surface relief gratings [122,189].

9.5. Polymers

Many amorphous polymeric materials have excellent optical properties in the visible spectrum and stretch into the UV part of the spectrum. The optical quality of amorphous polymers makes them well-suited in architectures with multiple geometries and pumping methods beyond the side-pumping technique used to illuminate the majority of photomechanical materials. The elasticity of polymers ranges from very flexible to rigid, which allows for broad tunability of the photomechanical-induced stresses and strains. Some polymers can irreversibly deform from radiation while under mechanical stress, where a redistribution of stresses during illumination can result in a permanent deformation [190].

Efficient energy transfer from an optical beam to a photomechanical device requires materials with properties that are tailored to optimize light-matter interactions. The availability of numerous small molecular dyes makes it possible to fabricate a wide variety of photomechanical materials by doping them into amorphous polymers. The constituent dyes can be chosen for their absorption spectra to design devices that respond in a specific wavelength range. The peak absorption wavelength, photothermal conversion efficiency, and photochromic effect are the most common properties that need to be provided by the dopant molecule. The functional groups of the azobenzene molecules in an azobenzene-doped polymer thin film affect the elastic modulus upon UV/visible light illumination [191]. Thus, the end groups can be changed to attain the desired properties. A mechanism attributed to the photomechanical effect of some polymeric materials is due to photochromic effects; for example, a photomechanical walker was constructed from a thin strip of 1,2-Bis[(anthracen-9-ylmethylene) amino]ethane doped PVDF [192]. For polymers doped with azobenzene derivatives, the immediate trans-cis photoisomerization can be negligible; however, it has been hypothesized that the thermal tumbling of the cis isomer and relaxation into a trans isomer of orientation along the light propagation axis in an optical fiber geometry results in a sustained enhancement of a photomechanical bend in an end-pumped polymer optical fiber [42,193].

All-polymer optical fibers are a specific subset of photomechanical architectures that have been well-investigated due to their end-pumped geometry [21,22,194–196]. The fibers have been shown to far exceed the requirements for length changes in interferometer feedback setups from optical length changes [22]. Cascaded photomechanical devices in an optical-driven series circuit can be constructed due to the end-pumped geometry [193].

Multiple doped-polymer materials with different wavelength responses have been fused together in various ways to create a side-pumped deformable network [197]. The network can take on multiple physical configurations depending on the wavelength(s) of light used to pump the photomechanical network. A single polymeric material has been shown to either bend or lengthen depending upon the mechanism of action; UV light causes photoisomerization of azobenzene molecules at the surface to bend the material, and near infrared light absorbed by graphene oxide (GO) causes thermal expansion [198]. The narrow absorption lines of rare-Earth elements have been used to fine tune the wavelength selection of photothermal-responsive hydrogel actuators [199].

9.6. Liquid Crystal Elastomers/Polymers

The photomechanical properties of LCNs gained scientific attention at the beginning of the century [54,200–202]. Polymeric LCNs such as LCPs [203] (linear or branched) and LCEs [204] (cross-linked) transduce light into macroscopic mechanical work through a change in the long-range order of the anisotropically oriented constituents.

There are a few mechanisms responsible for the change in the long-range order that leads to macroscopic deformations in the orientation of such photomechanical materials. Photothermal heating causes the temperature to rise, where both isomerizable and non-isomerizable dyes increase the temperature, which can decrease the order parameter(s) [131]. Trans-cis photoisomerization of the side chain, backbone, or distributed dyes can disrupt the orientational order through both attractive Van der Waals and repulsive steric forces [97]. The functional groups on an azobenzene derivative affect the photomechanical response [205].

Shape persistence has been shown in LCP networks containing fluorinated azobenzene, where the deformation can persist for many days [206]. Photochromic mesogens other than azobenzenes have also been investigated such as diarylethene-based LCPs [207]. Photoreorientation via trans-cis isomerization followed by a cis-trans back reaction was also found to contribute to macroscopic deformations in certain microscopic geometries [208]. The macroscopic changes from the molecular reorientation mechanism are much greater in ordered materials than in dye-doped polymers due to the cumulative effect from long-range ordering of mesogens. More complex LCNs with dopant dyes and in-chain azo dyes have been demonstrated, which can be patterned with light then induced to make complex shape changes upon heating [133].

Linear strains [201] and bends [54] are the two most common motions observed in an ordered material radiated by a light source. A bending phenomenon occurs when the material is side-pumped at a wavelength that is largely absorbed by photochromic molecules such that the penetration depth is shorter than the material's thickness [209]. Bending can also be achieved from near-surface absorption of molecules with high photothermal conversion efficiencies due to the nonlocal heating via thermal diffusion. For the case of a LCE with a thin width of 0.5 mm relative to a 4 mm length, it was shown that thermal diffusion of heat from surface absorption of light induces a bending motion [128]. Bending from an induced temperature gradient has also been shown in a LCE by placing a soldering iron near one side of the material [210]. Photoisomerization can also induce bending in a LCE [211]. A detailed analysis of the bending kinetics was given by Corbett *et al.*, which includes effects from saturable absorption and molecular hole burning [55].

Linear strains are observed in side-pumped configurations when the penetration depth is much greater than the thickness of the material or when diffusion/conductance conditions allow for lumped-sum approximations [212,213], where a negligible intensity gradient causes the material to uniformly reduce its order through the illuminated

plane oriented with the director. Such linear strains also occur for short penetration depths in uniaxial LCEs when pumped with a propagation direction parallel to the director [131]; photothermal heating in azobenzene-containing LCEs is the dominant mechanism of action under highly absorbing conditions that result in a short penetration depth relative to the length of the film along the director [132]. Beam profile shape and heterogeneous materials can be used to create other deformations such as twists, kinks, curls, and periodic waves [214–216]. Because the systems have orientational order, the degree of deformation depends on the polarization of the pump beam [60].

Some LCPs can convert light energy into mechanical motion quickly, which has been exploited to create photomechanical light harvesters that operate at relatively high frequencies [129]. A LCE film was used to mimic the action of a flytrap plant when exposed to light [217]. LCE/PEDOT:PSS bilayers have been used to make photomechanical conductive films that can be used in soft robotic devices such as relays [218], or they can be used as passive systems in organic photovoltaics to capture more light.

9.7. Biological Photomechanical Materials

Photomechanics is ubiquitous in nature. The most common photomechanical responses are based on interactions within complex systems rather than from a single material. For example, the pupillary light reflex is triggered by an increase in light intensity received by photoreceptors in the eye that transmit signals to the midbrain via the optic nerve, where in turn, the midbrain processes the incoming signal and sends an outgoing signal back through the ciliary nerve which controls the pupillary muscle [219,220]. Another common mechanical response to light in humans is called the photic sneeze reflex where a change from low light levels to relatively high-intensity light, such as the light from the midday sun showing after a cloud passes over, causes some individuals to sneeze [221].

As an example of a less complex system, the eyes of a *drosophila* (two-winged fly) respond via photoisomerization of rhodopsin to meta-rhodopsin, which catalyzes the release of a guanine nucleotide protein subunit to activate phospholipase C followed by hydrolysis of the minor membrane and activation of the transient receptor potential [222]. Some *Melanophila* and *Aradus* sensillum were also discovered to convert infrared light into micromechanical work [223].

Biobased photomechanical materials have recently gained interest. The modification of peptides with azobenzene derivatives allows reversible microscopic shape conversion from nanoribbons to nanospheres [224]. An azobenzene-containing peptide was observed to have a reduced rigidity upon illumination due to trans-cis photoisomerization, which resulted in β -hairpin assemblies to be formed [225]. Poly(ethylene glycol) hydrogels were cross-linked with azobenzene-containing peptides to create a biobased gel that could reversibly change its gel modulus [226].

10. DEVICES

Photomechanical materials offer the potential for all sorts of novel devices. As extensively described above, Bell used photomechanical materials to convert light to sound and the Uchino Walker converted light to work in the form of a walking motion. Other applications include the control of a mirror. As described in Subsection 7.1c, Bian *et al.* connected a small mirror to the end of a cylindrical photomechanical DR1-doped PMMA optical fiber, and found that a beam of light launched into the fiber end off-axis but parallel to it at cylindrical coordinate ρ could be used to induce bending in the

$\hat{\rho}$ direction at an angle in proportion to ρ [42]. This geometry could be used for an all-optical beam steering device.

Ye *et al.* took this concept one step further by building a tilt mount, where a photomechanical fiber replaces a mechanical actuator. As a result, a mirrored glass slide could be tilted with fine precision to the desired angle [194]. Both Bian and Ye used these device configurations to study the photomechanical response of the material. Bian reflected a beam of light from the mirror and passed it through a pinhole, using the transmittance as a measure of the angle [42]. Ye used a similar concept but replaced the pinhole with a quad photo-detector to measure the deflection angle [194]. In both cases, the mechanisms of the response were studied through the time response of the deflection angle. Bian found what appears to be a collective response that is yet to be fully understood [42].

Both of these optically controlled beam steering devices could be easily reconfigured for optical feedback by deflecting the light that is reflected from the mirror into the photomechanical material. Multistability should result, as described below for a different geometry; but, the principles are the same: the angle of the mirror is controlled with light, and the light is controlled by the angle of the mirror.

10.1. Bulk Photomechanical Optical Device

The basis of the next revolution will be all-optical devices that perform optical logic in response to sensory information and respond by changing shape and encoding information on a beam of light. In contrast to electronic devices, in which logic operations are the domain of the CPU, with sensory input and displays being separate devices, the fundamental photomechanical device provides all functionality in a single POD.

The light intensity in a POD (and emitted from it), as well as its mechanical state (length, shape, stiffness, etc.), depends on the intensity of light entering it and other stimuli acting on it (such as force, temperature, and chemical environment). A POD was first demonstrated as a bulk polymer-optical fiber inside an interferometer [21,193,227,228] and was later miniaturized to a mesoscale waveguide device that can be easily integrated with many other devices [22].

Figure 59 shows the first POD, made of a freely hanging polymer optical fiber that supports a mirror, which forms one arm of an interferometer. The interferometer is highlighted by the dashed box. The light leaving the interferometer is reflected right, up, and left before encountering a lens, which focuses the beam onto the end of the multi-mode DR1-doped polymer-optical fiber with appropriate spot size so that the light uniformly illuminates the fiber end to couple the light into a propagating optical mode. The light that reaches the bottom end of the fiber is absorbed by the mount that attached the fiber to the mirror, so no light from the fiber leaks into the interferometer.

The light leaving the interferometer encounters a thin glass plate that reflects a small portion of the light onto a photo-detector so that its power can be recorded. A shutter is placed in front of the photomechanical fiber so that the beam can be blocked and unblocked.

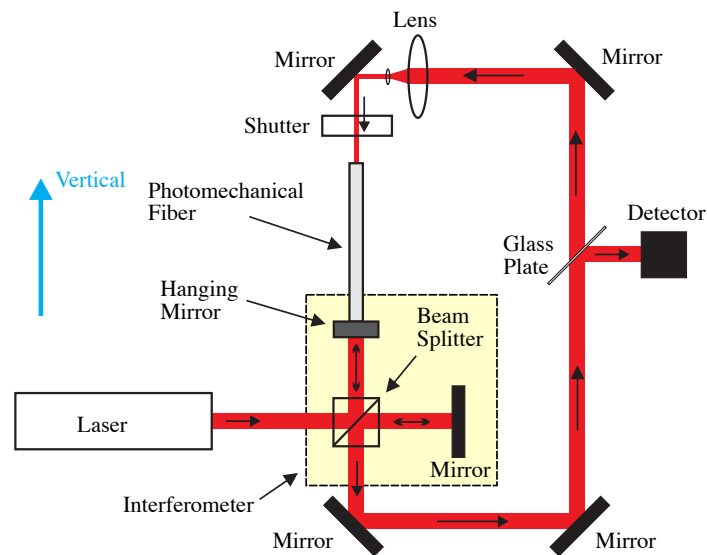
As we show below, the system will reach a steady state that finds the light intensity exiting the interferometer a constant in time as is the fiber's length. A force applied to the hanging fiber that moves the mirror will change the intensity of light leaving the interferometer. This intensity change in the fiber leads to a photomechanical force that resists the change in the movement of the mirror, bringing the mirror back to its steady-state position. The photomechanical force and the elastic response of the fiber act together to stabilize the mirror.

Figure 60 shows the data. The experiment starts with the shutter closed, so the fiber is dark. Over a time span of about 270 s, the fiber's 30 cm changes by about 600 nm, the wavelength of the light in the interferometer. This length change might be due to creep of the polymer or small temperature changes. With a thermal expansion coefficient of about 10^{-4} , a 1°C change in temperature would lead to a length change of about 30,000 nm. The observed length change of 600 nm corresponds to a temperature change of about 0.02°C , a reasonable amount of temperature fluctuations.

The shutter is opened at 270 s, forcing the length of the fiber to change, which leads to the sharp drop in the intensity leaving the interferometer (point x to y in Fig. 60). The fiber length remains stable as expected for about a minute, then jumps to another length (point p). At this point, the length and the intensity leaving the interferometer stay constant indefinitely. The stability of the length over long times is as expected (analysis given later).

To further study the response of the system to external forces, the optical table that holds the experiment is pounded by fist. The arrows in Fig. 60 label the times at which the table is struck. Each time, the system hops to a new stable configuration. Without mechanical shocks, the system remains in each of those states indefinitely. However, the highest intensity state (point q in Fig. 60) is unique in that the mass's position remains stable even under intense mechanical shocking; the intensity fluctuations while being shocked correspond to root mean square length changes of the fiber of about 3 nm. Thus, the hanging mirror is stable to within 3 nm, which is being stabilized by a fiber of 30 cm length. As such, the level of stability is one part in 10^8 , meaning that vibrations can be actively suppressed to a strain level of 10^{-8} .

Figure 59



Demonstration of a photomechanical optical device (POD) in a polymer optical fiber with external interferometer (inside dashed box). A freely hanging mirror that is part of an interferometer is suspended from a photomechanical polymer optical fiber that is flooded with light from the output of the interferometer. If the fiber changes length, the interferometer output changes and applies a force through a photomechanical effect in the fiber to the mirror that counters the length change through active feedback. Adapted from [21].

When the feedback shutter is closed, the intensity oscillates and then settles back to a gentle meandering. The number of oscillations is equal to the number of intensity steps observed when the shutter was in its opened state and jarred with a fist to the table.

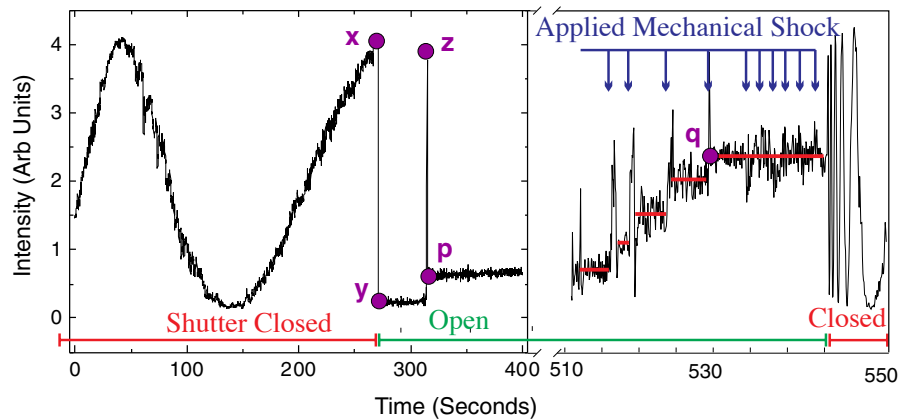
A simple graphical solution to the operation of the POD shown in Fig. 59 can be used to understand the observations. The two components of the device are the interferometer and the photomechanical fiber. The light output of the interferometer depends sinusoidally on the fiber length, and for small intensity, the length of the fiber is a linear function of the intensity within. Figure 61 shows the sinusoidal interferogram as the black curve and the linear photomechanical response as the dashed blue curve. The intersections between the two yield the steady-state solutions, but only the intersections in the unshaded regions are stable, labeled by green dots.

Next we interpret the data in Fig. 60 using Fig. 61. The reader should refer to both graphs when reading the narrative below. With no photomechanical response when the shutter is closed, the intensity meanders through one cycle, indicating that the fiber's length has changed by about the wavelength of the light, λ , or about 600 nm.

When the shutter is opened at point x , the photomechanical force brings the fiber to point y , the nearest stable point. Ambient vibrations cause the fiber length to oscillate about point y . If these vibrations increase the length into the red region, where the slope of the interferogram changes sign, the photomechanical force also changes direction, acting to bring the fiber length to point p at the higher intensity. Note that in getting to point p , the system passes through the peak intensity corresponding to point z , through the path labeled by the dashed yellow part of the interferogram in Fig. 61.

Each mechanical impulse that takes the system into the unstable region (shaded red) of longer fiber length results in a photomechanical forcing that further increases the

Figure 60



Light leaving the interferometer as measured with the photo-detector as a function of time. For the first 270 s, the shutter is closed, so the fiber is dark. At 270 s (point x), the shutter is open, illuminating the fiber and inducing a photomechanical force that decreases the intensity (point y) and stabilizes the length of the fiber. The intensity spontaneously jumps to a new intensity (point p) at about 320 s. After 500 s, mechanical impulses are applied to the table by way of a banging fist at the times shown by the arrows, knocking the system through several quasi-stable states. The state of highest intensity (point q) corresponds to the mirror position being stable to within 3nm in a 30 cm fiber, or one part in 10^8 stability. Adapted from [21].

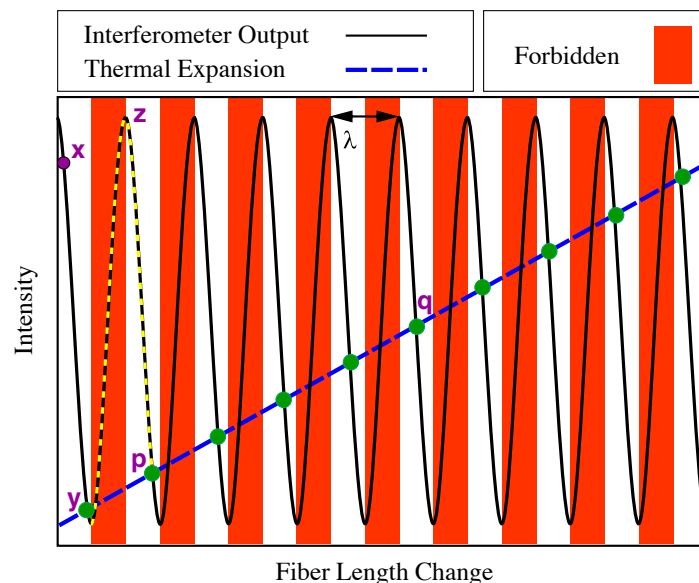
fiber length and lowers the mirror into the next stable state. During this elongation, the power in the fiber increases until it hits the peak fringe power, then falls as it settles into the next stable state. This explains the spikes at each step. The system jumps to ever higher power levels and longer length when struck due to the fact that the nearest unstable region is to the right, where the distance to the minimum is smaller than for displacements to the left.

The photomechanical force is largest at point q , the midpoint intensity where the slope of the interferogram is the largest and, therefore, the photomechanical restoring force is the strongest. Also, to reach a stable minimum, the fiber's length must increase into the next shaded region, which from point q requires the largest displacement to reach. These two factors acting together make the midpoint ultra-stable, keeping the fiber strain below 10^{-8} even under intense mechanical agitation.

Since each step corresponds to an additional peak being traversed, the five observed steps corresponds to a total displacement of about 3000 nm. When the shutter is closed, the observed intensity oscillates through these five peaks as the system relaxes back to point x . The graphical solution thus explains all the observations. Numerical simulations can be used to get quantitative data.

This demonstration of a POD is significant because it includes all five device classes. The device is (1) powered solely with light; (2) information is transmitted on a beam of light, (3) which senses and encodes information about the position of the mirror; (4) optical logic is built into the interferometer, whose output intensity changes in a way that keeps the mirror position fixed; and (5) light-driven actuation adjusts the position of the mirror.

Figure 61



Intensity leaving the interferometer as a function of fiber length change (solid black curve) and the fiber length change as a function of intensity inside the fiber due to the photomechanical effect (dashed blue line). The stable equilibria are given by the intersections between the two plots as shown by the green dots. The shaded red areas correspond to unstable solutions. The points x , y , z , and p labeled here correspond to the points on Figure 60. Adapted from [21].

10.2. Miniaturized POD

Device elements must be small and integrable so that they can act in concert to do more complex computations in response to external inputs, and to respond with a change in shape or light output that provides useful functionality. A miniaturized POD in a waveguide is shown in Fig. 62.

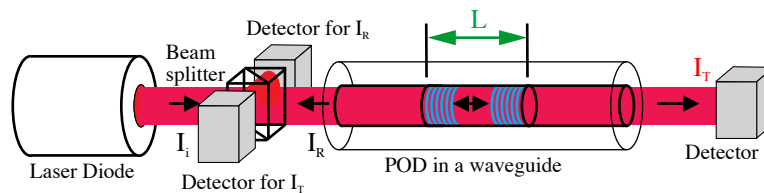
The light enters the POD from the left, and the power inside the POD depends on the separation between the mirrors. Through the photomechanical effect, the mirror separation depends on the power, so optical feedback is built into a POD of this design, which acts as the bulk device in Fig. 59. The POD has a reflected output to the left and a transmitted output to the right. The incident, reflected, and transmitted intensities can be measured with the beam splitter and detectors as shown in the figure.

This miniaturized waveguide POD device is a sensor, actuator, and logic element, all operating with light. As such, it acts as an all-optical transistor in that it can be used to control the flow of one beam of light with another. However, it is much more computationally powerful because it can act as an optical or mechanical memory, storing information in the intensity or its length, and its response depends on the stress or light applied to it.

Another important feature of a POD is its multistable response, where many output intensities are possible for one input intensity, as shown by the input-output response of the system in Fig. 63. This response is calculated from the inverse of the single-valued function shown in the inset. The branches with positive slopes are the stable ones, so as the light power is tuned up, the output follows the arrows that point to the right, hopping to the next branch when reaching a critical point as for example points b to c . As the intensity is decreasing, the output intensity does not trace the same curve as when increasing, taking the upper branch as shown by the left-pointing arrows, hopping downward at the critical points as shown by the dashed lines. Bistability, i.e., two stable output intensities for one input intensity, is illustrated by points a and d . As the intensity is increases, multistability is observed; for example, there are at least two stable points above point g .

Figure 64 shows the output intensity as a function of input intensity of a POD made of a DR1-doped PMMA optical fiber [22]. The ends are of the retroreflector type shown in the inset. Note that other reflector types can be used, such as bare ends themselves, which have low reflectivities, thus making low-finesse cavities to Bragg reflectors, which are highly reflecting at one specific wavelength, thus providing high finesse and high wavelength sensitivity. Each POD in a collection of Bragg grating PODs in series can be designed to act on different wavelengths, thus allowing individual PODs to be accessed by using the appropriate wavelength of light.

Figure 62

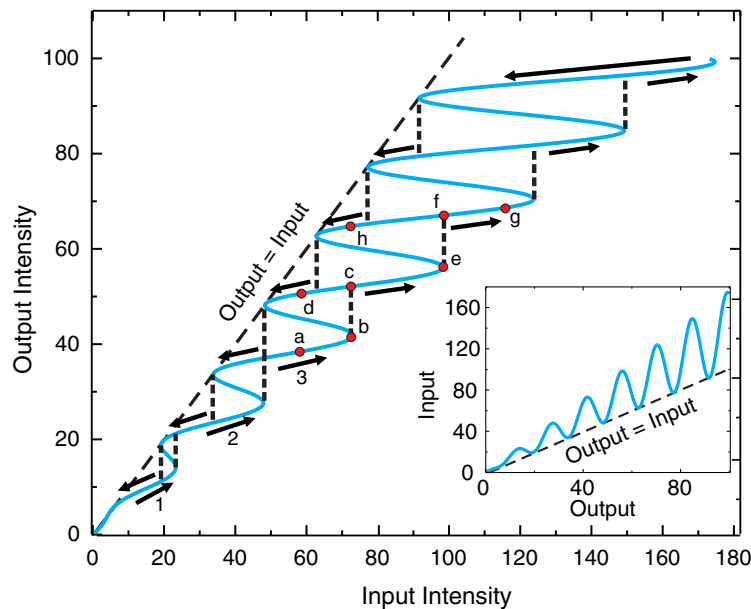


POD in a waveguide. The light power between the Bragg reflectors depends on the spacing between the Bragg mirrors, and the spacing depends on the power, so that feedback is built into the system. The input comes from the left. The outputs are to the left and to the right, which can be detected to characterize the device.

The power of the POD is in its inherent integrability and multi-functionality. Since each POD has two outputs, it can transmit information to its two nearest-neighbors. Its nearest-neighbors can also send information to a POD from its left or right inputs. Figure 65 shows an example of a multi-waveguide device that incorporates many PODs, which serves to illustrate its versatility. If the waveguiding cores are placed close together, light will jump between waveguides, adding yet another degree of design flexibility.

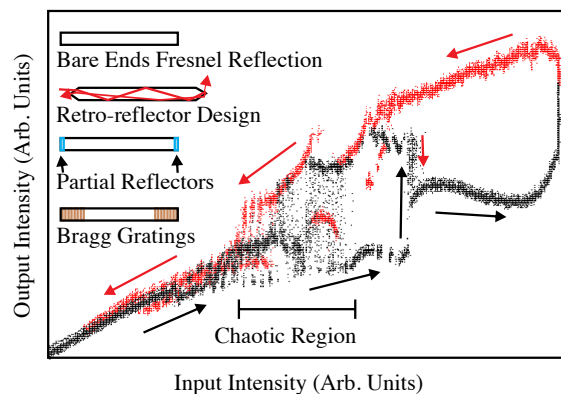
To understand how such a complex fiber can be made starts with a description of how a core is placed into a fiber, as follows. Polymer optical fibers with cores begin as “preforms,” which are made by drilling holes in an approximately 1 cm diameter polymer rod and filling them with a polymeric material of higher refractive index [230]. Alternatively, the preform can start as a half-cylinder in which grooves with semicircular cross sections are machined into the flat sections. When the two halves are pressed together, they make a cylinder with a hole, in which a cylinder of the solid core material is placed [231], as shown in Fig. 66(a). This approach is preferable when

Figure 63



Observed multistability in a POD. Adapted from [229].

Figure 64

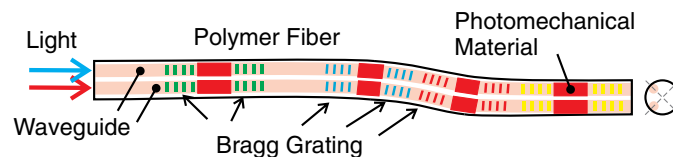


Observed bistability in a POD.

the preform is long because it is simple to machine a long groove into a planar surface but the drill depth is limited by the length of the drill bit—longer bits are less rigid, making it impossible to drill a straight hole. Figure 66(b) shows a rectangular cross section preform that can be made with the same process.

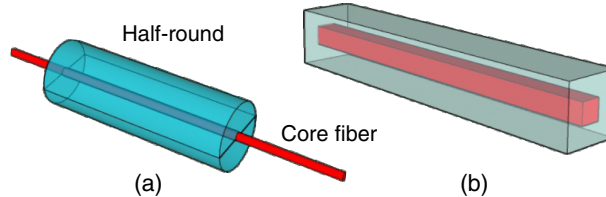
The process starts by first making a mixture of liquid monomer (the precursor of a polymer) with chromophore solute. The mixture is then polymerized in a test tube, the cylindrical preform is removed by breaking the glass, and the preform is pulled into a thick fiber [shown in red in Fig. 67(a)] using a drawing tower where an oven softens the preform. Figure 67(b) shows the starting pieces, and Fig. 67(c) shows the two half-rounds being pressed around this core fiber at elevated temperature to fuse the pieces together [231]. This preform can then be pulled into a fiber as shown in Fig. 67(d). The drawing process preserves the ratio of the core to cladding diameter, making the drawn fiber a miniature version of the preform in cross section.

Figure 65



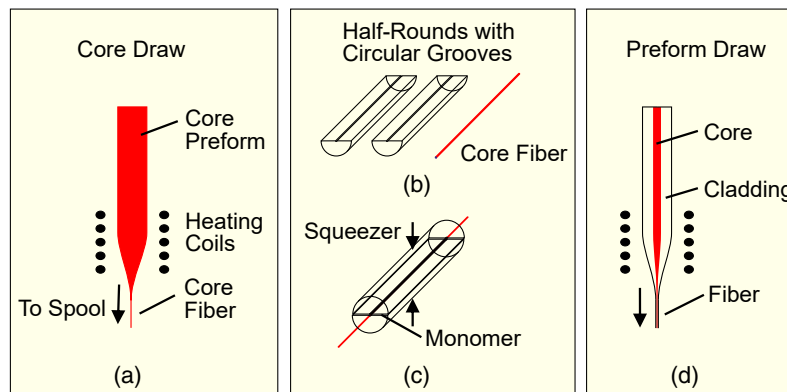
Polymer optical fiber with multiple waveguiding cores that each incorporates many PODs in series.

Figure 66



(a) Dye-doped core fiber is pressed between two half-rounds at elevated temperature to make a preform. (b) A rectangular preform can be made in the same way.

Figure 67



(a) Solid preform being pulled into a core fiber, (b) which fits into the grooves of two half-rounds, (c) is pressed at elevated temperature to make a preform with a core, (d) which is pulled into a fiber. Adapted from [231].

Fabricating a fiber with multiple cores follows the same procedure, where parallel cores can be placed in grooves of a half-round. Figure 68(a) show two cores on a plan made with two half-rounds. Non-planar structures can be also be made. Figure 68(b) shows how three sections can be combined to make a three-core fiber, and Fig. 68(c) shows a four-core fiber. Arbitrary patterns can be made by bringing together pieces in this way.

In the three-core structure shown in Fig. 68(b), the fiber can be made to bend in the direction of each of the three cores by illuminating one of them. Illuminating pairs of cores with unequal intensities will induce bending in any direction that falls within the 120° arc defined by the two cores and the fiber's central axis. Illuminating all three with the same intensity will cause the fiber length to change without bending, and illumination of the three cores with arbitrary intensities can yield elongation and bending in any direction. Thus, a three-core fiber can be used to position an object in three-dimensional space.

10.3. Integrating Photomechanical Devices

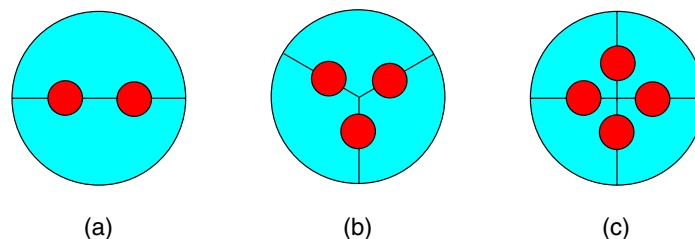
The true power of photomechanical devices is leveraged when they are combined. Here we describe a demonstration of how photomechanical devices can be cascaded and methods for integrating fiber-based PODs.

10.3a. Cascading Devices

In a cascaded system, the output of one device serves as the input of another one. The POD geometry requires transparent materials so that a high-enough light level leaves the first device to actuate the next one. In cases where the material absorbs or scatters light, a two-beam configuration can be used to make each device using the same geometry as shown in Fig. 55. Unlike a POD, which is multistable, these devices are simpler in that the transmitted probe beam is a single-valued function of the pump intensity illuminating the first POD. Multistable operation is possible if two such devices are configured as described later in this section.

LCEs in a pump/probe interferometer device, as shown in Fig. 69(c), have been cascaded in an optical series circuit to create a proof-of-concept network of photomechanical devices [126]. The transmitted probe intensity that passes through the glass plates of the top device (called the output) is controlled by the pump intensity launched into the LCE (called the input). This probe (output) then acts as the pump (input) for the next stage. Thus, a change in the intensity of the input to the first device changes the distance between its plates, which changes the output intensity. This changes the spacing between the plates of the second device, thus changing its output.

Figure 68



Multiple dye-doped cores are made in a fiber by pressing multiple sections at elevated temperature to make a preform.

The operation of the cascaded device can be tuned by adjusting the initial spacing between the glass plates to make the transmitted probe intensity increase or decrease when the material is pumped. In the configuration shown in Fig. 69(c), the initial tuning is such that the upper device output is complimentary to the bottom device, as shown in Fig. 69(a). After re-tuning the device, the two stages act in sync, as shown in Fig. 69(b).

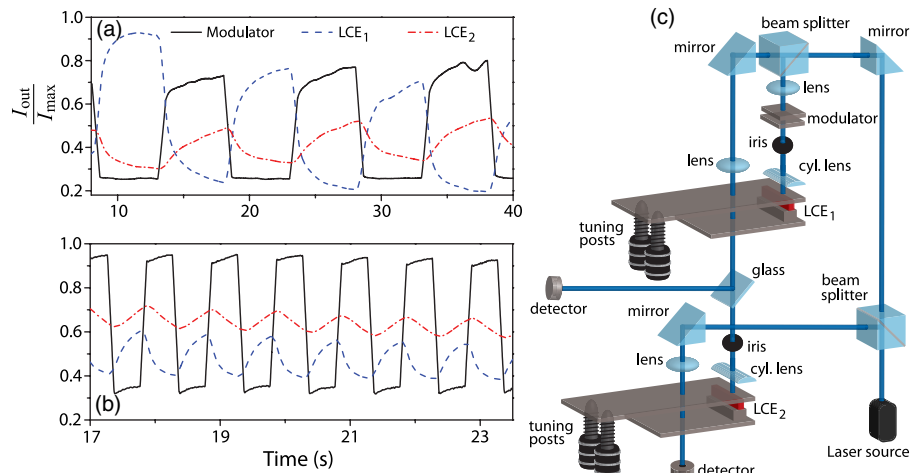
Note that the probe beams at each stage can be of different colors, but in the example here, they are supplied by the same laser. This simple device can also be reconfigured into a feedback geometry, where the output of the second device is the input to the first one. These two devices acting together will then behave like a POD. As such, while not easily miniaturizable into a waveguide geometry as in a polymer fiber POD, the same kinds of functionality can be demonstrated in such two-beam devices.

Two-beam devices potentially have many applications, and the simplicity of the series configuration makes it easy to test new architectures and materials. Dye-doped LCEs have been used in educational laboratory settings to teach students about photoinduced stress [125], and such cascaded devices could be the next step in an undergraduate laboratory on photomechanical materials.

10.3b. Integrating PODs

A fiber with PODs as shown in Fig. 65 is made by writing Bragg gratings in the waveguiding cores. Figure 70 shows how a refractive index pattern is burnt into a material from the intensity modulation due to interference between the two writing beams [232]. White light probes the grating, yielding a characteristic notch in the spectrum at wavelength $\lambda = 2n_0\Lambda$, which is reflected by the grating. Here n_0 is the refractive index of the material and Λ the wavelength of the grating. With this method, gratings can be written along the length of the fiber at will, so POD devices of the sort shown in Figs. 62 and 65 can be fabricated.

Figure 69



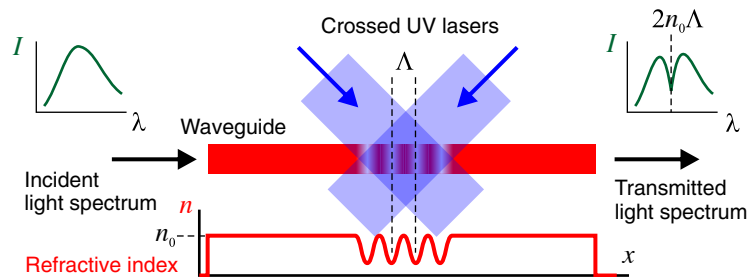
Two LCEs inside tunable Fabry–Perot interferometers cascaded in series. (a) The pump beam entering the first device, which we call the input, is shown as the solid curve and is a step function at 0.1 Hz. The output of the first device is used as the pump, or input, to the second device. The transmitted probe through each device, which we call the output, is also plotted. (b) The output of the first device is phase shifted by tuning the devices' initial position along the Airy functions, thus changing the phase relationship between the output of each device. (c) A diagram of the experimental setup for the series optical circuit. Adapted from [126,127].

Figure 65 is an example of integrated PODs, where each one acts as a sensor, actuator, and logic element. Furthermore, each POD can communicate with the other ones through light. For example, stress applied to one POD changes the intensity that it reflects and transmits. This will change the state of nearby PODs, leading to a cascade that flows through the system and feeds back on the originally stressed POD. As a result, the fiber will deform, and the intensity pattern within will change dramatically. These changes need not be static, and in general will result in complex time-dependent motion even for a continuous laser input. As such, this sort of fiber will act like a smart system, and if densely packed, can be viewed as a smart material that morphs in response to the environment.

Owing to the multistable nature of each POD, the fiber will have countless shape and intensity states. As such, it can adaptively learn or be programmed by exposing it to light from the outside and within the waveguide.

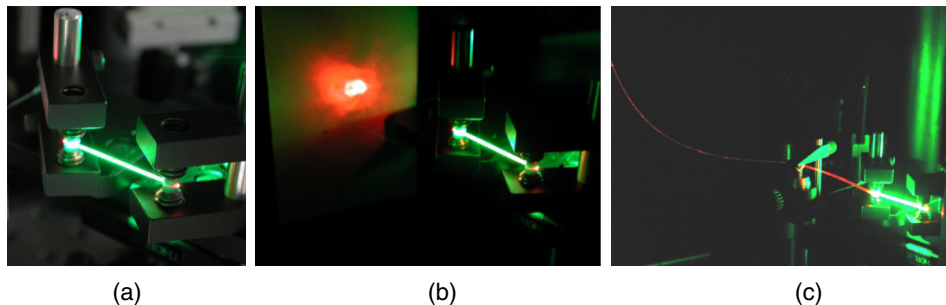
This fiber architecture can include embedded light sources in addition to those that power such a thread from the outside. Many organic molecules act as a gain medium. For example, Howell demonstrated that the dye known as Disperse Orange 11 (DO11) doped into a PMMA fiber can produce amplified spontaneous emission (ASE) light that propagates in the fiber when excited from its side [79]. Figure 71(a) shows a piece of such fiber that is illuminated with green light from its side [78]. Figure 71(b) shows a wide-angle view of the emitted red ASE light. Figure 71(c) shows the emitted light

Figure 70



Writing a Bragg grating using the interference pattern between two ultraviolet lasers. The sinusoidal refractive index profile reflects light at wavelength $\lambda = 2n_0\Delta$. The formation of the grating can be probed with a white light source, where the notch in the transmitted spectrum gives the Bragg condition. n_0 is the refractive index of the material, and Δ is the wavelength of the grating.

Figure 71



Piece of DO11-doped PMMA polymer optical fiber is excited with green light from its side. (b) Red ASE light is emitted from the fiber ends, as seen on the screen. (c) The ASE light is coupled into a polymer optical fiber.

being coupled into another polymer optical fiber. The DO11 dye was also shown to be capable of lasing [79].

These demonstrations of polymer optical fibers made of a gain medium illustrate the possibilities of making integrated devices that includes coherent sources built into the waveguide. In addition, these materials have been shown to selfheal after photodegradation. Figure 72 shows an inline distributed feedback Bragg (DFB) laser made by writing a grating into a fiber, with or without a cladding.

It is useful to pause and ponder the immense computing power and functionality of an integrated device made of PODs by comparing it with a neural network such as a brain, which is made of neurons that are interconnected through synapses. A neuron fires based on how many of its neighbors fire. Combining billions of neurons, each interconnected with thousands of others leads to sentience. How this happens is a mystery, but it comes down to electrical impulses emanating from neurons based on impulses that they sense.

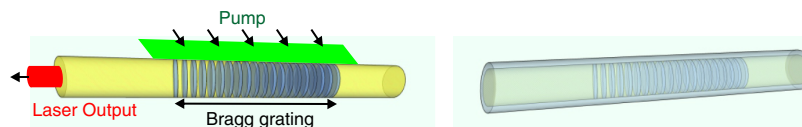
Replacing neurons with PODs and synapses with optical waveguides leads to huge improvements. First, the optical interconnections act much faster than electrical pulses, and more PODs can be interconnected both through light that travels through the device and is transmitted/reflected, but also through interactions between nearby devices though evanescent waves. Whereas the neuron fires based on surrounding inputs, the POD has built-in memory of the past through its multistability, and so will respond in a complex way to both stimuli from its surroundings as well as its history-dependent state.

A brain needs to be connected to sensors (eyes, ears, skin, nose) and actuators (muscles) to gather information and act on it. In contrast, each POD acts as a sensor, actuator, logic element, and light source, integrating together not only the logic elements, but all other functionality. Thus, the richer logic functions of the POD coupled with its multi-functionality opens up vast possibilities for applications that are at present unimaginable.

10.4. Photomechanical Energy Harvesters

When measuring the photomechanical motion of a cantilever, most researchers use optical techniques such as imaging and interferometry. The mechanical behavior caused by a transient light signal in a photomechanical material can be transduced to an electrical signal. A LCE layer and a graphene-PDMS layer was made into a photomechanical cantilever device that generated electrical energy upon bending [233]. A pyroelectric signal was obtained by periodically illuminating the material so that it would cycle between the bent and relaxed states. Similar electrical generation devices also based on photomechanical motion of a bilayer driven by a transient light signal have been reported, where the piezoelectric effect caused by the photomechanical deformation is the mechanism responsible for the generation of electrical energy [234,235].

Figure 72



DFB laser can be made in a gain medium by adding Bragg gratings.

Some photomechanical devices can be made to undergo a periodic mechanical motion while under constant illumination [236]. A photomechanical pendulum constructed from a bilayer actuator was shown to produce electric current in a coil wrapped around its end when allowed to oscillate in a static magnetic field [237]. A similar oscillating photomechanical device was used to harvest solar energy [238], where the piezoelectric effect generated the electrical energy as opposed to a coil and magnet.

11. CONCLUSION

The mechanisms of the photomechanical effect originate in diverse phenomena, yielding a rich and fertile playground for scientists who seek to build a deeper understanding of how microscopic light–matter interactions lead to the conversion of light to mechanical energy. This understanding guides materials scientists who synthesize new compounds and process materials to make composites with optimized response. These new materials are being built into demonstration devices that leverage key properties, which are being integrated into systems that have the potential for making ultra-smart materials that have immense computational power with built-in sensing and actuation throughout the continuum of the material. Such materials could adapt to the environment to function as any type of device, making obsolete the quaint notion that one needs a separate device for each application when one material can do it all.

We started with a history of the photomechanical effect and motivated the importance of the photomechanical response as the last device class that needs to be developed to enable the POD, whose computational power exceeds that of a transistor, but also shows optical and mechanical multistability, acts as a sensor, provides actuation, and transmits information to neighboring PODs, all using light.

An overarching theme of this review was to provide a unified view of a light-activated material unit, called a photomorphon, which applies over all size ranges from a molecule to a bulk material. This approach allows the material to be modeled in a general way. The interaction of light with matter is developed using the response function, which has built-in causality, and accounts for the full history of the influence of the light on the material on the present response. Nonlinear effects are also taken into account.

A large part of our review focused on the mechanisms of the photomechanical response, which are interesting in their own right. An understanding of the mechanisms also provides new ideas for making better materials. To this end, a significant portion of our work has focused on models of the mechanisms and measurements that provide insights into the mechanisms that are at work in specific systems.

Methods for measuring the photomechanical response were presented with a description of how these measurements can be used to determine the various mechanism that are at play, and a figure of merit was introduced that quantifies the efficiency of a material in its ability to convert light energy into mechanical work. Then, measurements on a sampling of materials were presented, and some key properties were tabulated followed by ideas for device designs. We then gave examples of device demonstrations and speculated on how such devices can be integrated to make highly intelligent materials and systems.

This review focused mostly on polymeric materials, whose photomechanical response falls far short of the needs of applications. New materials will undoubtedly need to be developed including crystals, which may have a superior photomechanical response

due to their high density of active molecules, high modulus, and absence of parasitic passive components [152,153,155,239,240]. Even so, major breakthroughs are required to make photomechanical materials efficient enough for applications. This review provides the multidisciplinary view that will be required for future innovations.

APPENDIX A: MATERIAL TABULATIONS

Abbreviations for Tabulated Materials

- LCPM – Liquid crystal polymer microparticles
- PDMS – Polydimethylsiloxane
- SWNT – Single-walled carbon nanotube
- MWNT – Multi-walled carbon nanotube
- HOPG – Highly ordered pyrolytic graphite
- PE – Polyethylene
- LDPE – Low-density polyethylene
- GO – Graphene oxide
- rGO – Reduced graphene oxide
- PVDF – Polyvinylidene fluoride
- PTFE – Polytetrafluoroethylene
- PBHPS – Poly(4,4'-bis(6-hydroxyhexyloxy)azobenzene phenylsuccinate)
- GNP – Graphene nanoplatelet
- PVOH – Polyvinyl alcohol
- LCE – Liquid crystal elastomer
- TEM – Thermally expanding microspheres
- LCN – Liquid crystal network
- EVA – Poly(ethylene-co-vinyl acetate)
- NP – Nanoparticle
- PDA – Polydopamine
- PMAz6Ac – 6-(4-methoxyphenylazo)phenoxyhexyl acrylate
- TAPB – 1,3,5-tris(4-aminophenyl)benzene
- TAPM – Tetra(4-aminophenyl)methane
- PMMA – Poly(methyl methacrylate)
- PC – Polycarbonate
- DR1 – Disperse red 1
- PI – Polyimide
- PA – Polyamide
- PAA – Poly(amide acid)
- DAA – 4,4'-Diaminoazobenzene
- 6FDA – 4,4'-(hexafluoroisopropylidene)diphthalic anhydride
- IPN – Interpenetrating polymer network
- NBA – N-benzylideneaniline

Table 3. Layered Photomechanical Materials

Bilayer materials	Reported mechanism	step resp. (s)	Thicknesses	Measurement	Amplitude	I (mW/cm ²)	λ (nm)	Ref.
GNP-PDMS/PDMS	Photothermal	1.7 (0.0001) ^a	80 μ m/50 μ m	Deflection/length	0.15	2950	808	[144]
Diarylethene deriv./Au	Photoisomerization	–	14 μ m/7 nm	Curvature change	0.396 mm ⁻¹	55	365	[241]
PVDF/Au	Photothermal	–	(28–110) μ m/80 nm	Force	10 ⁻⁴ N	7.6	633	[242]
Azobenzene-PHMS/polyimide	Photoisomerization	5	(8–30) μ m/25 μ m	Stress	1.4 MPa	225	442	[243]
Azobenzene cryst./LDPE	Photoisomerization	1.3	10 μ m/28 μ m	Bending angle	90°	20	365	[244]
PTFE-CNT/parraffin wax/Polyimide	Photothermal	0.4	100 μ m/20 μ m/10 μ m	Deflection/length	0.47	27	400–650	[245]
Graphene-PDMS/Cr	Photothermal	1	75 μ m/35 nm	Bending angle	90°	552	IR lamp	[141]
Azobenzene-LCP/LDPE	Photoisomerization	0.3	20 μ m/20 μ m	Stress	2.4 MPa	13.2	365	[237]
rGO/PDMS	Photothermal	0.5	4 μ m/40 μ m	Bending angle	156°	1500	808	[236]
PBHPS/methylcellulose	Photoisomerization	2.4	47 μ m/(26–81) μ m	Bending angle	45°	15	365	[246]
PLAZ derivative/LDPE	Photoisomerization	0.8	(5–10) μ m/(15–20) μ m	Stress	2.7 MPa	270	365	[247]
PDMS-GNP/Cr/Au	Photothermal	2.5	55 μ m/10 nm/100 nm	Stress	20.6 kPa	1106	IR lamp	[143]
SWNT/polycarbonate	Photothermal	0.5	1 μ m/10 μ m	Bending angle	90°	100	solar spectrum	[248]
rGO/polyimide	Photothermal	3	(150–200) μ m	Curvature change	0.45 cm ⁻¹	300	–	[249]
rGO-TEM-PDMS/PDMS	Photothermal	9	700 μ m/700 μ m	Curvature change	0.35 mm ⁻¹	–	IR lamp	[250]
GO/poly(N-isopropylacrylamide)-GO	Photothermal	17	–/–	Curvature change/stress	0.27 mm ⁻¹ /3 MPa	–	IR lamp	[251]
rGO/GO-PDA	Photothermal	0.5	1.2 μ m/0.9 μ m	Bending angle	180°	200	NIR lamp	[137]
Azo-polymer/silk	Photoisomerization	0.3	2 μ m/12 μ m	Bending angle	110°	70	365	[185]
nb-W-PLZT/nb-W-PLZT	Photovoltaic	1	200 μ m/200 μ m	Deflection/length	0.0075	17	366	[13,252]
MoS ₂ /PDMS multilayer	Photothermal	10	160 μ m layer-by-layer	Stress	24 kPa	50	405,532,640,808	[253]
LCE/graphene-PDMS/(Al/PVDF/Al)	Photothermal	12	26 μ m/35 μ m/25 μ m	Change in angle	46°	160	980	[233]
PMAz6Ac/PVOH multilayer	Photoisomerization	10	90 nm/220 nm	Bending angle	130°	14	365,375	[254]
Azo-LCE/PE	Photoisomerization	130	15 μ m/50 μ m	Stress	65 kPa	60	366	[255]

^aBacklash response.

Table 4. Monolith Photomechanical Materials

Material	Reported mechanism	step resp. (s)	Thickness	Measurement	Amplitude	I (mW/cm ²)	λ (nm)	Ref.
Molecular crystal								
Salicylideneaniline deriv.	Photoisomerization	8.7	(1.2 – 2.1) μm	Disp. angle	25°	40	365	[164]
Diarylethene deriv.	Photoisomerization	3.9	(3.8 – 16.7) μm	Curvature change	3.2 mm ⁻¹	200	365	[86]
Anthrylmethylene indanone	Photodimerization	780	(0.5 – 360) μm	Bending angle	180°	40	365	[256]
Photochromic polymer								
Azobenzene PVE:PC	Photoisomerization	2	11 μm	Strain	0.001 (0.0004) ^a	50 (30) ^a	365	[257]
Azobenzene LCN	Photoisomer./reorientation	1	20 μm	Bending angle	82°	250	442,457,488,514	[258]
PAA-TAPB	Photoisomerization	8.2	200 μm	Strain	-0.16	34	405	[259]
PAA-TAPM	Photoisomerization	4.5	200 μm	Strain	-0.19	34	405	[259]
Azobenzene LCP	Photoisomerization	10	(20–24) μm	Stress	1.35 Pa	150	365	[260]
Azobenzene PI	Photoisomerization	10	20 μm	Bending angle	84°	120	445	[183]
Azobenzene PA	Photoisomer./tautomerization	20	20 μm	Bending angle	78°	120	445	[182]
6FDA-DAA (DMF solution)	Photoisomerization	5	200 μm	Deflection/illum. length	1.4	20	442	[183]
crosslinked NBA	Photoisomerization	-	20 μm	Canilever force	150 μN	40	365	[261]
Azo-PVE-PCL	Photoisomerization	2	20 μm	Strain	0.00055	10	250–450	[262]
Guest-host polymer								
MWNT-PDMS	Photothermal	3.5	60 μm	Stress	58 kPa	500	808	[263]
GNP-PDMS	Photothermal	1.7	60 μm	Stress	19 kPa	500	808	[263,264]
HOPG-PDMS	Photothermal	1.5	60 μm	Stress	8 kPa	500	808	[264]
GO-PDMS	Photothermal	9	100 μm	Stress	47 kPa	16	IR lamp	[265]
DR1-PMMA	Photothermal/isomer./reorient.	0.3	550 μm	Bending angle	0.22°	40	633	[42]
DR1-PMMA	Photothermal	0.1	475 μm	strain	0.001	10	355	[194]
LCP/LCE								
LCPM-PVOH	Photoisomerization	10	80 μm	Bending angle	90°	60	360	[266]
GO-PDLC	Photothermal	4	50 μm	Bending degree	0.9	54	450	[267]
Azobenzene-LCN	Photoisomerization	1.5	(5–10) μm	Deflection/length	0.106	45	365	[268]
lazo-LCN	Photoisomer./reorientation	800	15 μm	Bending angle	43°	100	405	[205]
lazo-f-LCN	Photoisomer./reorientation	800	15 μm	Bending angle	20°	100	405	[205]
DO3-LCE	Photothermal/Photoisomer.	4	400 μm	Strain	-0.01	78	488	[131]
A9BZ9(DA9AB)-LCP	Photoisomerization	4	10 μm	Bending angle	88°	10	365	[269]

^aRef. [186].

APPENDIX B: STRAIN TENSOR

The deformation of a body is quantified by the strain tensor, which describes how nearby points are displaced from each other. Figure 73(a) shows a point at position \vec{x} and a nearby point at $\vec{x} + d\vec{x}$. Figure 73(b) shows the body when stressed, where the two points are displaced to coordinates \vec{x}' and $\vec{x}' + d\vec{x}'$. Figure 73(c) shows all the vectors on one plot.

The deformation displaces the point originally at \vec{x} by

$$\vec{u} = \vec{x}' - \vec{x}, \quad (\text{B1})$$

where \vec{u} is called the *displacement vector* and is a function of \vec{x} . As such, $\vec{u}(\vec{x})$ relates the displacement from any point \vec{x} in the unstressed material to its new coordinate when stressed. Equation (B1) can be differentiated to determine the change in the distance between two nearby points, yielding

$$d\vec{u} = d\vec{x}' - d\vec{x}. \quad (\text{B2})$$

Using Eq. (B2),

$$d\ell'^2 \equiv |d\vec{x}'|^2 = |d\vec{x} + d\vec{u}|^2 = \left| d\vec{x} + \sum_i \frac{\partial \vec{u}}{\partial x_i} dx_i \right|^2, \quad (\text{B3})$$

where use has been made of the fact that \vec{u} is a function of \vec{x} , and all sums are over the three cartesian components. With

$$d\ell^2 \equiv |d\vec{x}|^2, \quad (\text{B4})$$

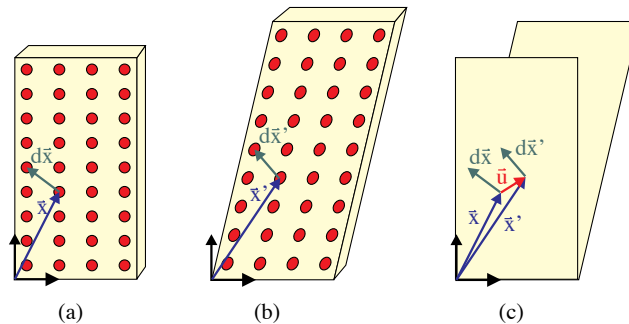
Eq. (B3) can be written in component form

$$d\ell'^2 = d\ell^2 + 2 \sum_{i,j} \frac{\partial u_j}{\partial x_i} dx_i dx_j + \sum_{i,j,k} \frac{\partial u_k}{\partial x_i} \frac{\partial u_k}{\partial x_j} dx_i dx_j. \quad (\text{B5})$$

Expressing Eq. (B5) in the form

$$d\ell'^2 = d\ell^2 + 2 \sum_{i,j} u_{ij} dx_i dx_j \quad (\text{B6})$$

Figure 73



(a) Unstressed body where \vec{x} labels a point in the material and $\vec{x} + d\vec{x}$ labels a nearby point. (b) The body is stressed, and the same points are labeled, but their coordinates are \vec{x}' and $\vec{x}' + d\vec{x}'$ after the deformation. (c) Just the vectors.

yields

$$u_{ij} = \frac{1}{2} \left(\frac{\partial u_i}{\partial x_j} + \frac{\partial u_j}{\partial x_i} + \sum_k \frac{\partial u_k}{\partial x_i} \frac{\partial u_k}{\partial x_j} \right), \quad (\text{B7})$$

where we have used the fact that the indices i and j are dummy indices so that

$$\sum_{i,j} \frac{\partial u_j}{\partial x_i} dx_i dx_j = \sum_{i,j} \frac{\partial u_i}{\partial x_j} dx_i dx_j. \quad (\text{B8})$$

u_{ij} is called the strain tensor.

The strain tensor defined by Eq. (B7) is symmetric, so it can be diagonalized. As such, there exists a coordinate frame in which the strain tensor has diagonal elements $u^{(1)}$, $u^{(2)}$, and $u^{(3)}$. In that case, Eq. (B6) becomes

$$d\ell'^2 = d\ell^2 + 2 \sum_i u^{(i)} dx_i^2. \quad (\text{B9})$$

The axes labeled i that make the strain tensor diagonal are called the principle axes of the tensor. It is important to understand that the principle coordinate frame can vary from point to point in the material.

Using Eqs. (B3) and (B4), Eq. (B9) can be written as

$$\sum_i (dx_i'^2 - dx_i^2 - 2u^{(i)} dx_i^2) = 0. \quad (\text{B10})$$

Since the three Cartesian components are independent, Eq. (B10) must hold for each one, so

$$\frac{dx_i'}{dx_i} = \sqrt{1 - 2u^{(i)}} \approx 1 - u^{(i)}, \quad (\text{B11})$$

or

$$u^{(i)} = \frac{dx_i - dx_i'}{dx_i}. \quad (\text{B12})$$

Recall that $d\vec{x}$ represents the distance between two nearby points in an unstressed material and dx_i' is the distance between the same two points when the material is deformed. $u^{(i)}$ defined in Eq. (B12) is the change in length per unit length of the i^{th} cartesian component at point \vec{x} in the material, which we call the strain along i .

In this paper, the i^{th} diagonal component of the strain will be denoted by u_i .

APPENDIX C: STRESS

Stress, σ , is also a tensor, where σ_{ij} is the force per unit area on surface j in the i direction. The force on a piece of the material enclosed within surface S is thus given by the vector sum of the forces over the surface, or

$$F_i = \sum_j \oint_S \sigma_{ij}(\vec{r}) d\vec{A}_j, \quad (\text{C1})$$

where F_i is the i^{th} component of the force and \vec{A} is the area vector, which is normal to the surface pointing outward. Using the divergence theorem, Eq. (C1) becomes an integral over the volume, given by

$$F_i = \sum_j \int_V \frac{\partial \sigma_{ij}(\vec{r})}{\partial x_j} dV. \tag{C2}$$

As an example, consider Fig. 74, which shows the contributions to the force on a cube from three of its surfaces. In this case, the total force on the volume element in the z direction is given by

$$F_z = [\sigma_{zz}(z + dz) - \sigma_{zz}(z)] dx dy + [\sigma_{zx}(x + dx) - \sigma_{zx}(x)] dy dz + [\sigma_{zy}(y + dy) - \sigma_{zy}(y)] dx dz. \tag{C3}$$

When the stress is expressed in a frame parallel to the principle axes, the stress tensor is diagonal, and $\sigma^{(i)} \equiv \sigma_{ii}$. In this case, Eq. (C3) becomes

$$F_z = [\sigma^{(z)}(z + dz) - \sigma^{(z)}(z)] dx dy. \tag{C4}$$

In this paper, the i^{th} diagonal component of the stress will be called σ_i .

APPENDIX D: POISSON’S RATIO

When a rod is stretched or compressed in the z direction, as shown in Fig. 75, its cross-sectional area can change. Poisson’s ratio is defined as the ratio of the strain in the direction of the applied stress and the strain perpendicular to it, or

$$\underline{\sigma} = -\frac{u_{zz}}{u_{xx}}. \tag{D1}$$

Consider the red spheres in Fig. 75, which “paint” a part of the material so that the deformation can be visualized. Poisson’s ratio is then given by

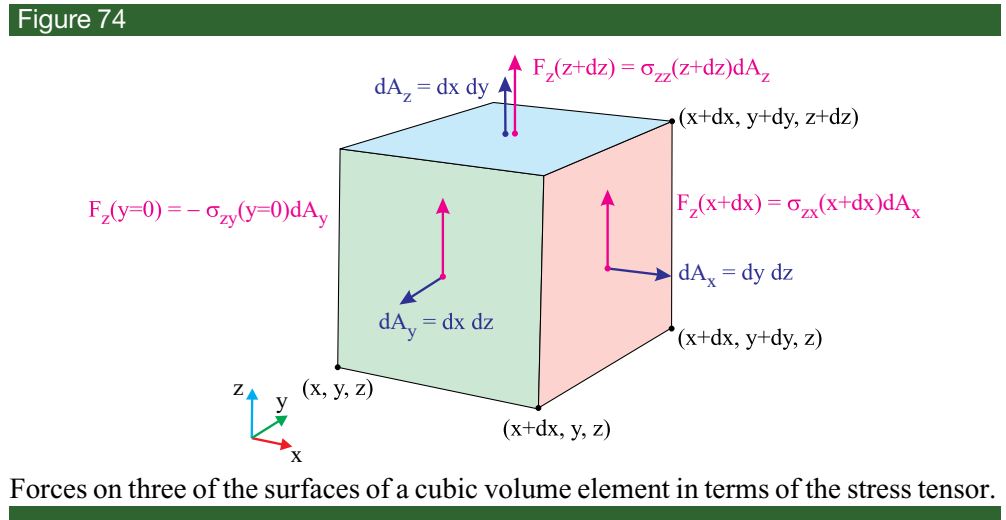
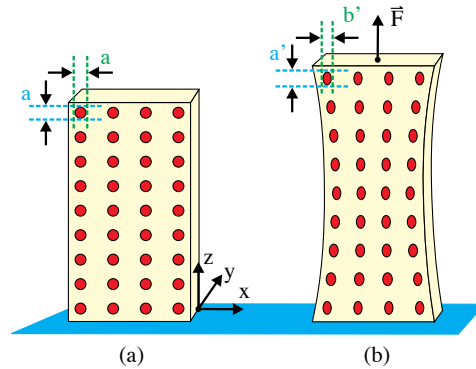


Figure 75



Poisson's ratio is given by the $\sigma = -u_{zz}/u_{xx}$.

$$\underline{\sigma} = -\frac{a' - a}{b' - b}. \quad (\text{D2})$$

If the deformation conserves volume, $\delta V = 0$, so $\delta(a^2b) = 2ab \cdot \delta a + a^2 \cdot \delta b = 0$. Then,

$$\frac{\delta a}{a} = -\frac{1}{2} \frac{\delta b}{b}, \quad (\text{D3})$$

and Poisson's ratio is $\underline{\sigma} = 2$. If the cross-sectional area remains unchanged, $a = a'$, and Poisson's ratio vanishes. Lakes reported a foam structure with negative Poisson's ratio, a material whose lateral dimension increases when the material is stretched [270].

A more nuanced treatment of the theory of elasticity can be found in the well-known volume by Landau and Lifshitz [271].

FUNDING

National Science Foundation, Directorate for Engineering (EFRI-ODISSEI:1332271).

DISCLOSURES

The authors declare no conflicts of interest.

REFERENCES AND NOTE

1. A. G. Bell, "On the production and reproduction of sound by light," Proceedings of the American Association for the Advancement of Science **29**, 115–136 (1881).
2. M. L. Kuzyk, "Tutorial on using photo-mechanical effects to make smart materials," <https://www.nlosource.com>.
3. J. Moser, "The microphonic action of selenium cells," *Philos. Mag.* **12**, 212–223 (1881).
4. J. Curie and P. Curie, "Development, via compression, of electric polarization in hemihedral crystals with inclined faces," *Bull. de la Société minéralogique de France* **3**, 90–93 (1880).
5. G. Lippmann, "Principe de la conservation de l'électricité," *Ann. Chim. Phys.* **24**(4), 145–178 (1881).

6. J. Curie and P. Curie, "Contractions and expansions produced by voltages in hemihedral crystals with inclined faces," *Comptes Rendus* **93**, 1137–1140 (1881).
7. J. Lagowski and H. C. Gatos, "Photomechanical effect in noncentrosymmetric semiconductors cds," *Appl. Phys. Lett.* **20**, 14–16 (1972).
8. F. Agolini and F. P. Gay, "Synthesis and properties of azoaromatic polymers," *Macromolecules* **3**, 349–351 (1970).
9. C. D. Eisenbach, "Isomerization of aromatic azo chromophores in poly(ethyl acrylate) networks and photomechanical effect," *Polymer* **21**, 1175–1179 (1980).
10. A. R. Hutson, "Piezoelectric Scattering and Phonon Drag in ZnO and CdS," *J. Appl. Phys.* **32**, 2287–2292 (1961).
11. K. Uchino and E. L. Cross, "Electrostriction and its interrelation with other anharmonic properties of materials," *Jpn. J. Appl. Phys.* **19**, L171–L173 (1980).
12. K. Uchino, "Photostrictive Actuator," in *Ultrasonics Symposium* (1990), pp. 721–723.
13. K. Uchino, "Ceramic actuators: principles and applications," *MRS Bull.* **18**(4), 42–48 (1993).
14. K. S. Kim, L. Kollar, and G. S. Pringer, "A model of embedded fiber optic Fabry-Perot temperature and strain sensors," *J. Composite Mater.* **27**, 1618–1677 (1993).
15. J. S. Sirkis, "Unified approach to phase-strain-temperature models for smart structure interferometric optical fiber sensors: part 1, development," *Opt. Eng.* **32**, 752–7773 (1993).
16. J. S. Sirkis and C. T. Mathews, "Experimental investigation of phase-strain-temperature models for structurally embedded interferometric fiber-optic sensors," *Experim. Mech.* **33**, 26–31 (1993).
17. E. D. L. Rosa, L. A. Zenteno, A. N. Starodumov, and D. Monzon, "All-fiber absolute temperature sensor using an unbalanced high-birefringence sagnac loop," *Opt. Lett.* **22**, 481–483 (1997).
18. M. Jinno and T. Matsumoto, "Ultrafast, low power, and highly stable all-optical switching in an all polarization maintaining fiber sagnac interferometer," *IEEE Photon. Technol. Lett.* **2**, 349 (1990).
19. H. Avramopoulos, P. M. W. French, M. C. Gabriel, H. H. Houh, J. N. A. Whitaker, and T. Morse, "Complete switching in a three-terminal sagnac switch," *IEEE Photon. Technol. Lett.* **3**, 235–237 (1991).
20. M. Camacho-Lopez, H. Finkelmann, P. Palffy-Muhoray, and M. Shelley, "Fast liquid-crystal elastomer swims into the dark," *Nat. Mater.* **3**, 307–310 (2004).
21. D. J. Welker and M. G. Kuzyk, "Photomechanical stabilization in a polymer fiber-based all-optical circuit," *Appl. Phys. Lett.* **64**, 809–811 (1994).
22. D. J. Welker and M. G. Kuzyk, "Optical and mechanical multistability in a dye-doped polymer fiber Fabry-Perot waveguide," *Appl. Phys. Lett.* **66**, 2792–2794 (1995).
23. H. Okamura, "Light-driven motor," *Opt. Eng.* **50**, 020503 (2011).
24. A. Schuster, *An Introduction to the Theory of Optics* (Edward Arnold, 1904).
25. J. H. Andrews, M. Aviles, M. Crescimanno, N. J. Dawson, A. Mazzocco, J. B. Petrus, K. D. Singer, E. Baer, and H. Song, "Thermo-spectral study of all-polymer multilayer lasers," *Opt. Mater. Express* **3**, 1152–1160 (2013).
26. N. J. Dawson, M. Aviles, J. H. Andrews, M. Crescimanno, J. B. Petrus, A. Mazzocco, K. D. Singer, E. Baer, and H. Song, "Thermo-spectral properties of plastic lasers," *Proc. SPIE* **8876**, 123–131 (2013).

27. D. Brewster, "Experiments on the depolarization of light as exhibited by various mineral, animal and vegetable bodies with a reference of the phenomena to the general principle of polarization," *Philos. Trans.* **105**, 29–53 (1815).
28. D. Brewster, "On the communication of the structure of doubly-refracting crystals to glass, murite of soda, flour spar, and other substances by mechanical compression and dilation," *Philos. Trans.* **106**, 156–178 (1816).
29. "This image is the work of a United States Department of Agriculture Employee and Freely available in the public domain."
30. M. G. Kuzyk, *Nonlinear Optics: A Student's Perspective* (CreateSpace, 2017).
31. C. K. Law, "Interaction between a moving mirror and radiation pressure: a Hamiltonian formulation," *Phys. Rev. A* **51**, 2537–2541 (1995).
32. M. Aspelmeyer, T. J. Kippenberg, and F. Marquardt, "Cavity optomechanics," *Rev. Mod. Phys.* **86**, 1391–1452 (2014).
33. B. Zhou, E. Bernhardt, A. Bhuyan, Z. Ghorbanishiadeh, N. Rasmussen, J. Lanska, and M. G. Kuzyk, "Theoretical and experimental studies of photomechanical materials," *J. Opt. Soc. Am. B* **36**, 1492–1517 (2019).
34. L. R. G. Treloar, *Physics of Rubber Elasticity* (Oxford University, 1975).
35. Z. Sekkat, "Optical tweezing by photomigration," *Appl. Opt.* **55**, 259–268 (2016).
36. N. Viswanathan, D. Kim, S. Bian, J. Williams, W. Liu, L. Li, L. Samuelson, J. Kumar, and S. Tripathy, "Surface relief structures on azo polymer films," *J. Mater. Chem.* **9**, 1941–1955 (1999).
37. S. Bian, J. Williams, D. Kim, L. Li, S. Balasubramanian, J. Kumar, and S. Tripathy, "Photoinduced surface deformations on azobenzene polymer films," *J. Appl. Phys.* **86**, 4498–4508 (1999).
38. J. He, S. Bian, L. Li, J. Kumar, S. Tripathy, and L. Samuelson, "Photochemical behavior and formation of surface relief grating on self-assembled polyion/dye composite film," *J. Phys. Chem. B* **104**, 10513–10521 (2000).
39. M. Saphiannikova and D. Neher, "Thermodynamic theory of light-induced material transport in amorphous azobenzene polymer films," *J. Phys. Chem. B* **109**, 19428–19436 (2005).
40. V. Toshchevikov, M. Saphiannikova, and G. Heinrich, "Microscopic theory of light-induced deformation in amorphous side-chain azobenzene polymers," *J. Phys. Chem. B* **113**, 5032–5045 (2009).
41. S. Moujdi, A. Rahmouni, T. Mahfoud, D. V. Nesterenko, M. Halim, and Z. Sekkat, "Surface relief gratings in azo-polymers revisited," *J. Appl. Phys.* **124**, 213103 (2018).
42. S. Bian, D. Robinson, and M. G. Kuzyk, "Optically activated cantilever using photomechanical effects in dye-doped polymer fibers," *J. Opt. Soc. Am. B* **23**, 697–708 (2006).
43. S. Serak, N. Tabiryanyan, R. Vergara, T. White, R. Vaia, and T. Bunning, "Liquid crystalline polymer cantilever oscillators fueled by light," *Soft Matter* **6**, 779–783 (2009).
44. H. Nakano, "Direction control of photomechanical bending of a photochromic molecular fiber," *J. Mater. Chem.* **20**, 2071–2074 (2010).
45. A. L. Fetter and J. D. Walecka, *Theoretical Mechanics of Particles and Continua*, Dover Books on Physics (Dover, 2003).
46. M. Knežević and M. Warner, "Optomechanical elastomeric engine," *Phys. Rev. E* **88**, 040501 (2013).
47. M. Knežević and M. Warner, "Optomechanical conversion by mechanical turbines," *Phys. Rev. Appl.* **2**, 044017 (2014).
48. Z. Sekkat, "Vectorial motion of matter induced by light fueled molecular machines," *OSA Continuum* **1**, 668–681 (2018).

49. Z. Mahimwalla, K. G. Yager, J.-I. Mamiya, A. Shishido, A. Priimagi, and C. J. Barrett, "Azobenzene photomechanics: prospects and potential applications," *Polym. Bull.* **69**, 967–1006 (2012).
50. A. Goulet-Hanssens, T. C. Corkery, A. Priimagi, and C. J. Barrett, "Effect of head group size on the photoswitching applications of azobenzene disperse red 1 analogues," *J. Mater. Chem. C* **2**, 7505–7512 (2014).
51. N. J. Dawson, J. H. Andrews, and M. Crescimanno, "Modeling off-resonant nonlinear-optical cascading in mesoscopic thin films and guest-host molecular systems," *Phys. Rev. A* **88**, 063831 (2013).
52. E. Fischer, "Temperature dependence of photoisomerization equilibria. Part I. Azobenzene and the azonaphthalenes," *J. Am. Chem. Soc.* **82**, 3249–3252 (1960).
53. N. J. Dunn, W. H. Humphries, A. R. Offenbacher, T. L. King, and J. A. Gray, "pH-dependent cis → trans isomerization rates for azobenzene dyes in aqueous solution," *J. Phys. Chem. A* **113**, 13144–13151 (2009).
54. Y. Yu, M. Nakano, and T. Ikeda, "Directed bending of a polymer film by light," *Nature* **425**, 145 (2003).
55. D. Corbett and M. Warner, "Linear and nonlinear photoinduced deformations of cantilevers," *Phys. Rev. Lett.* **99**, 174302 (2007).
56. D. Corbett, C. Xuan, and M. Warner, "Deep optical penetration dynamics in photobending," *Phys. Rev. E* **92**, 013206 (2015).
57. M. Knežević, M. Warner, M. Čopič, and A. Sánchez-Ferrer, "Photodynamics of stress in clamped nematic elastomers," *Phys. Rev. E* **87**, 062503 (2013).
58. Y. Zhu, J. Zhou, and M. G. Kuzyk, "Two-photon fluorescence measurements of reversible photodegradation in a dye-doped polymer," *Opt. Lett.* **32**, 958–960 (2007).
59. H. Finkelmann, E. Nishikawa, G. G. Pereira, and M. Warner, "A new opto-mechanical effect in solids," *Phys. Rev. Lett.* **87**, 015501 (2001).
60. C. L. M. Harvey and E. M. Terentjev, "Role of polarization and alignment in photoactuation of nematic elastomers," *Eur. Phys. J. E* **23**, 185–189 (2007).
61. L. Dong, Y. Feng, L. Wang, and W. Feng, "Azobenzene-based solar thermal fuels: design, properties, and applications," *Chem. Soc. Rev.* **47**, 7339–7368 (2018).
62. E. N. Cho, D. Zhitomirsky, G. G. D. Han, Y. Liu, and J. C. Grossman, "Molecularly engineered azobenzene derivatives for high energy density solid-state solar thermal fuels," *ACS Appl. Mater. Interfaces* **9**, 8679–8687 (2017).
63. R. W. Boyd, *Nonlinear Optics*, 3rd ed. (Academic, 2009).
64. P. P. Ho and R. R. Alfano, "Optical Kerr effect in liquids," *Phys. Rev. A* **20**, 2170–2187 (1979).
65. M. G. Kuzyk, C. W. Dirk, and J. E. Sohn, "Mechanisms of quadratic electrooptic modulation of dye-doped polymer systems," *J. Opt. Soc. Am. B* **7**, 842–858 (1990).
66. S. Zhou and M. G. Kuzyk, "Observation of fast photomechanical effects in a polymer optical fiber," in *Second International Conference on Intelligent Materials* (Technomic, 1994), pp. 1375–1380.
67. A. Shimamura, A. Priimagi, J.-I. Mamiya, M. Kinoshita, T. Ikeda, and A. Shishido, "Photoinduced bending upon pulsed irradiation in azobenzene-containing crosslinked liquid-crystalline polymers," *J. Nonlinear Opt. Phys. Mater.* **20**, 405–413 (2011).
68. D. Corbett, C. L. van Oosten, and M. Warner, "Nonlinear dynamics of optical absorption of intense beams," *Phys. Rev. A* **78**, 013823 (2008).

69. D. Corbett and M. Warner, "Bleaching and stimulated recovery of dyes and of photocantilevers," *Phys. Rev. E* **77**, 051710 (2008).
70. M. Trznadel and M. Kryszewski, "Thermal shrinkage of oriented polymers," *J. Macromol. Sci. C* **32**, 259–300 (1992).
71. J. Kagan, *Organic Photochemistry: Principles and Applications* (Academic, 1993).
72. E. Havens, E. A. Snyder, and T. H. Tong, "Light-activated shape memory polymers and associated applications," *Proc. SPIE* **5762**, 5762–5768 (2005).
73. J. S. Sodhi and I. J. Rao, "Modeling the mechanics of light activated shape memory polymers," *Int. J. Eng. Sci.* **48**, 1576–1589 (2010).
74. D. Habault, H. Zhang, and Y. Zhao, "Light-triggered self-healing and shape-memory polymers," *Chem. Soc. Rev.* **42**, 7244–7256 (2013).
75. J. Zhang, M. Huo, M. Li, T. Li, N. Li, J. Zhou, and J. Jiang, "Shape memory and self-healing materials from supramolecular block polymers," *Polymer* **134**, 35–43 (2018).
76. R. H. Petrucci, W. S. Harwood, and F. G. Herring, *General Chemistry: Principles and Modern Applications*, 8th ed. (Prentice Hall, 2002).
77. J. Peeters, V. S. Nguyen, and J.-F. Müller, "Atmospheric vinyl alcohol to acetaldehyde tautomerization revisited," *J. Phys. Chem. Lett.* **6**, 4005–4011 (2015).
78. B. Howell and M. G. Kuzyk, "Lasing action and photodegradation of disperse orange 11 dye in liquid solution," *Appl. Phys. Lett.* **85**, 1901–1903 (2004).
79. B. Howell and M. G. Kuzyk, "Amplified spontaneous emission and recoverable photodegradation in disperse-orange-11-doped-polymer," *J. Opt. Soc. Am. B* **19**, 1790–1793 (2002).
80. S. K. Ramini, B. Anderson, S. T. Hung, and M. G. Kuzyk, "Experimental tests of a new correlated chromophore domain model of self-healing in a dye-doped polymer," *Polymer Chem.* **4**, 4948–4954 (2013).
81. S. Ramini and M. Kuzyk, "A self healing model based on polymer-mediated chromophore correlations," *J. Chem. Phys.* **137**, 054705 (2012).
82. S. Ramini, N. Dawson, and M. Kuzyk, "Testing the diffusion hypothesis as a mechanism of self-healing in disperse orange 11 doped in poly(methyl methacrylate)," *J. Opt. Soc. Am. B* **28**, 2408–2412 (2011).
83. B. Anderson and M. G. Kuzyk, "Generalizing the correlated chromophore domain model of reversible photodegradation to include the effects of an applied electric field," *Phys. Rev. E* **89**, 032601 (2014).
84. S.-T. Hung, A. Bhuyan, K. Schademan, J. Steverlynck, M. D. McCluskey, G. Koeckelberghs, K. Clays, and M. G. Kuzyk, "Spectroscopic studies of the mechanism of reversible photodegradation of 1-substituted aminoanthraquinone-doped polymers," *J. Chem. Phys.* **144**, 114902 (2016).
85. N. Katsonis, M. Lubomska, M. M. Pollard, B. L. Feringa, and P. Rudolf, "Synthetic light-activated molecular switches and motors on surfaces," *Prog. Surf. Sci.* **82**, 407–434 (2007).
86. D. Kitagawa and S. Kobatake, "Crystal thickness dependence of photoinduced crystal bending of 1,2-Bis(2-methyl-5-(4-(1-naphthoyloxymethyl)phenyl)-3-thienyl)perfluorocyclopentene," *J. Phys. Chem. C* **117**, 20887–20892 (2013).
87. S.-Z. Pu, Q. Sun, C.-B. Fan, R.-J. Wang, and G. Liu, "Recent advances in diarylethene-based multi-responsive molecular switches," *J. Mater. Chem. C* **4**, 3075–3093 (2016).
88. L. Gutiérrez-Arzaluz, T. Rocha-Rinza, and F. Cortés-Guzmán, "Stilbene photoisomerization driving force as revealed by the topology of the electron density and QTAIM properties," *Comput. Theor. Chem.* **1053**, 214–219 (2015).

89. D. C. Todd and G. R. Fleming, "Cis-stilbene isomerization: temperature dependence and the role of mechanical friction," *J. Chem. Phys.* **98**, 269–279 (1993).
90. Y. Norikane, R. Katoh, and N. Tamaoki, "Unconventional thermodynamically stable cis isomer and trans to cis thermal isomerization in reversibly photoreversible [0.0](3,3')-azobenzenophane," *Chem. Commun.* **2008**, 1898–1900 (2008).
91. H. Noh, S. F. Liew, V. Saranathan, R. O. Prum, S. G. J. Mochrie, E. R. Dufresne, and H. Cao, "How non-iridescent colors are generated by quasi-ordered structures of bird feathers," *Adv. Mater.* **22**, 2871–2880 (2010).
92. S. F. Liew, J. Forster, H. Noh, C. F. Schreck, V. Saranathan, X. Lu, L. Yang, R. O. Prum, C. S. O'Hern, E. R. Dufresne, and H. Cao, "Short-range order and near-field effects on optical scattering and structural coloration," *Opt. Express* **19**, 8208–8217 (2011).
93. C. Maier and T. Calafut, "Design principles," in *Polypropylene*, T. Calafut, ed. (William Andrew, 1998), Chap. 12, pp. 109–144.
94. S. Singh, *Liquid Crystal Fundamentals* (World Scientific, 2002).
95. I.-C. Khoo, *Liquid Crystals*, 2nd ed. (Wiley, 2007).
96. M. J. Stephen and J. P. Straley, "Physics of liquid crystals," *Rev. Mod. Phys.* **46**, 617–704 (1974).
97. M. Warner and E. M. Terentjev, *Liquid Crystal Elastomers* (Oxford University, 2005).
98. D. Demus, J. Goodby, G. W. Gray, H.-W. Spiess, and V. Vill, "Theory of the liquid crystalline state," in *Physical Properties of Liquid Crystals* (Wiley-VCH, 2007), pp. 25–86.
99. V. Tsvetkov, "On molecular order in the anisotropic liquid phase," *Acta Physicochim.(U.S.S.R.)* **16**, 132–147 (1942).
100. P.-G. de Gennes, *The Physics of Liquid Crystals*, 2nd ed. (Oxford University, 1993).
101. L. Onsager, "The effects of shape on the interaction of colloidal particles," *Ann. N. Y. Acad. Sci.* **51**, 627–659 (1949).
102. R. Zwanzig, "First-order phase transition in a gas of long thin rods," *J. Chem. Phys.* **39**, 1714–1721 (1963).
103. P. J. Flory, "Phase equilibria in solutions of rod-like particles," *Proc. R. Soc. A* **234**, 73–89 (1956).
104. H. T. Peterson, D. E. Martire, and M. A. Cotter, "Lattice model for a binary mixture of hard rods of different lengths. Application to solute induced nematic→isotropic transitions," *J. Chem. Phys.* **61**, 3547–3555 (1974).
105. M. A. Cotter, "Hard spherocylinders in an anisotropic mean field: a simple model for a nematic liquid crystal," *J. Chem. Phys.* **66**, 1098–1106 (1977).
106. M. A. Cotter, "Generalized van der Waals theory of nematic liquid crystals: an alternate formulation," *J. Chem. Phys.* **66**, 4710–4711 (1977).
107. M. A. Cotter, "Generalized van der Waals theory of nematic liquid crystals: requirements for self-consistency," *J. Chem. Phys.* **67**, 4268–4270 (1977).
108. Y. Singh, "Density-functional theory of freezing and properties of the ordered phase," *Phys. Rep.* **207**, 351–444 (1991).
109. J. R. McColl, "Effect of pressure on order in the nematic liquid crystal p-azoxyanisole," *Phys. Lett. A* **38**, 55–57 (1972).
110. J. R. McColl and C. S. Shih, "Temperature dependence of orientational order in a nematic liquid crystal at constant molar volume," *Phys. Rev. Lett.* **29**, 85–87 (1972).
111. S. Chandrasekhar, *Liquid Crystals*, Cambridge Monographs on Physics (Cambridge University, 1977).

112. W. L. McMillan, "Simple molecular model for the smectic a phase of liquid crystals," *Phys. Rev. A* **4**, 1238–1246 (1971).
113. G. E. Feldkamp, M. A. Handschy, and N. A. Clark, "Mean field theory of liquid crystalline phases of disc-shaped molecules," *Phys. Lett. A* **85**, 359–362 (1981).
114. G. Skačej and C. Zannoni, "Molecular simulations shed light on supersoft elasticity in polydomain liquid crystal elastomers," *Macromol.* **47**, 8824–8832 (2014).
115. G. Skačej and C. Zannoni, "Molecular simulations elucidate electric field actuation in swollen liquid crystal elastomers," *Proc. Natl. Acad. Sci. USA* **109**, 10193–10198 (2012).
116. M. Dumont, S. Hosotte, G. Froc, and Z. Sekkat, "Orientational manipulation of chromophores through photoisomerization," *Proc. SPIE* **2042**, 1–12 (1993).
117. M. Dumont and Z. Sekkat, "Dynamic study of photoinduced anisotropy and orientation relaxation of azo dyes in polymeric films. Poling at room temperature," *Proc. SPIE* **1774**, 1–12 (1992).
118. M. Dumont, Z. Sekkat, R. Loucif-Saibi, K. Nakatani, and J. A. Delaire, "Photoisomerization, photoinduced orientation and orientational relaxation of azo dyes in polymeric films," *Nonlinear Optics* **5**, 395–406 (1992).
119. Z. Sekkat and M. Dumont, "Polarization effects in photoisomerization of azo dyes in polymeric films," *Appl. Phys. B* **53**, 121–123 (1991).
120. Z. Sekkat, D. Morichere, M. Dumont, R. Loucif-Saibi, and J. A. Delaire, "Photoisomerization of azobenzene derivatives in polymeric thin films," *J. Appl. Phys.* **71**, 1543–1544 (1992).
121. Z. Sekkat, J. Wood, and W. Knoll, "Reorientation mechanism of azobenzenes within the trans-to-cis photoisomerization," *J. Phys. Chem.* **99**, 17226–17234 (1995).
122. C. B. Kim, J. C. Wistrom, H. Ha, S. X. Zhou, R. Katsumata, A. R. Jones, D. W. Janes, K. M. Miller, and C. J. Ellison, "Marangoni instability driven surface relief grating in an azobenzene-containing polymer film," *Macromolecules* **49**, 7069–7076 (2016).
123. Z. Sekkat and W. Knoll, "Creation of second-order nonlinear optical effects by photoisomerization of polar azo dyes in polymeric films: theoretical study of steady-state and transient properties," *J. Opt. Soc. Am. B.* **12**, 1855–1867 (1995).
124. Z. Sekkat and M. Dumont, "Photoassisted poling of azo dye doped polymeric films at room temperature," *Appl. Phys. B* **54**, 486–489 (1992).
125. E. A. Bernhardt, C. M. Garrison, N. F. Rasmussen, J. T. Lanska, and M. G. Kuzyk, "An apparatus for measuring a material's photomechanical response," *Am. J. Phys.* **86**, 943–952 (2018).
126. N. J. Dawson, M. G. Kuzyk, J. Neal, P. Luchette, and P. Palffy-Muhoray, "Cascading of liquid crystal elastomer photomechanical optical devices," *Opt. Commun.* **284**, 991–993 (2011).
127. N. J. Dawson, M. G. Kuzyk, J. Neal, P. Luchette, and P. Palffy-Muhoray, "Integration of liquid crystal elastomer photomechanical optical devices," *Proc. SPIE* **8475**, 41–48 (2012).
128. M. G. Kuzyk, *Polymer Fiber Optics: Materials, Physics, and Applications*, Vol. **117** of Optical Science and Engineering (CRC Press, 2006).
129. M. Li, S. Lv, and J. Zhou, "Photo-thermo-mechanically actuated bending and snapping kinetics of liquid crystal elastomer cantilever," *Smart Mater. Struct.* **23**, 125012 (2014).
130. S. V. Serak, N. V. Tabiryan, T. J. White, and T. J. Bunning, "Azobenzene liquid crystal polymer-based membrane and cantilever optical systems," *Opt. Express* **17**, 15736–15746 (2009).

131. N. J. Dawson, M. G. Kuzyk, J. Neal, P. Luchette, and P. Palffy-Muhoray, "Experimental studies of the mechanisms of photomechanical effects in a nematic liquid crystal elastomer," *J. Opt. Soc. Am. B* **28**, 1916–1921 (2011).
132. N. J. Dawson, M. G. Kuzyk, J. Neal, P. Luchette, and P. Palffy-Muhoray, "Modeling the mechanisms of the photomechanical response of a nematic liquid crystal elastomer," *J. Opt. Soc. Am. B* **28**, 2134–2141 (2011).
133. M. Lahikainen, H. Zeng, and A. Priimagi, "Reconfigurable photoactuator through synergistic use of photochemical and photothermal effects," *Nat. Commun.* **9**, 4148 (2018).
134. C. H. Jiang, M. G. Kuzyk, J. L. Ding, W. E. Johns, and D. J. Welker, "Fabrication and mechanical behavior of dye-doped polymer optical fiber," *J. Appl. Phys.* **92**, 4–12 (2002).
135. M. G. Kuzyk and C. W. Dirk, *Characterization Techniques and Tabulations for Organic Nonlinear Optical Materials* (Marcel Dekker, 1998).
136. A. G. Bell, "Selenium and the photophone," *Nature* **22**, 500–503 (1880).
137. J. Mu, C. Hou, H. Wang, Y. Li, Q. Zhang, and M. Zhu, "Origami-inspired active graphene-based paper for programmable instant self-folding walking devices," *Sci. Adv.* **1**, e1500533 (2015).
138. X. Li, S. Ma, J. Hu, Y. Ni, Z. Lin, and H. Yu, "Photo-activated bimorph composites of Kapton and liquid-crystalline polymer towards biomimetic circadian rhythms of *Albizia julibrissin* leaves," *J. Mater. Chem. C* **7**, 622–629 (2019).
139. Y. Shi and Z. Chen, "Function-driven design of stimuli-responsive polymer composites: recent progress and challenges," *J. Mater. Chem. C* **6**, 11817–11834 (2018).
140. J. Loomis, B. King, and B. Panchapakesan, "Layer dependent mechanical responses of graphene composites to near-infrared light," *Appl. Phys. Lett.* **100**, 073108 (2012).
141. Leeladhar, P. Raturi, A. Kumar, and J. P. Singh, "Graphene-polydimethylsiloxane/chromium bilayer-based flexible, reversible, and large bendable photomechanical actuators," *Smart Mater. Struct.* **26**, 095030 (2017).
142. Leeladhar, P. Raturi, and J. P. Singh, "Sunlight-driven eco-friendly smart curtain based on infrared responsive graphene oxide-polymer photoactuators," *Sci. Rep.* **8**, 3687 (2018).
143. Leeladhar and J. P. Singh, "Photomechanical and chemomechanical actuation behavior of graphene-poly(dimethylsiloxane)/gold bilayer tube for multimode soft grippers and volatile organic compounds detection applications," *ACS Appl. Mater. Interfaces* **10**, 33956–33965 (2018).
144. D. Niu, W. Jiang, H. Liu, T. Zhao, B. Lei, Y. Li, L. Yin, Y. Shi, B. Chen, and B. Lu, "Reversible bending behaviors of photomechanical soft actuators based on graphene nanocomposites," *Sci. Rep.* **6**, 27366 (2016).
145. H. Liu, D. Niu, W. Jiang, T. Zhao, B. Lei, L. Yin, Y. Shi, B. Chen, and B. Lu, "Illumination-oriented and thickness-dependent photomechanical bilayer actuators realized by graphene-nanoplatelets," *Sens. Actuators A* **239**, 45–53 (2016).
146. W. Jiang, D. Niu, L. Wei, G. Ye, L. Wang, H. Liu, P. Chen, F. Luo, and B. Lu, "Controllable actuation of photomechanical bilayer nanocomposites for in vitro cell manipulation," *Carbon* **139**, 1048–1056 (2018).
147. M. G. Perez-Zúñiga, F. M. Sánchez-Arévalo, and J. Hernández-Cordero, "Enhanced photomechanical response of a Ni–Ti shape memory alloy coated with polymer-based photothermal composites," *Smart Mater. Struct.* **26**, 105012 (2017).
148. E. Wang, M. S. Desai, and S.-W. Lee, "Light-controlled graphene-elastin composite hydrogel actuators," *Nano Lett.* **13**, 2826–2830 (2013).

149. Y. Zhang, C. Peng, Z. Zhou, R. Duan, H. Ji, Y. Che, and J. Zhao, "Giant morphological change in layered microribbons featuring reversible sliding of stacking layers," *Adv. Mater.* **27**, 320–325 (2014).
150. V. Rahneshin, D. A. Ziolkowska, A. McClelland, J. Cromwell, J. B. Jasinski, and B. Panchapakesan, "The coupled straintronic-photothermal effect," *Sci. Rep.* **8**, 64 (2018).
151. P. Naumov, S. Chizhik, M. K. Panda, N. K. Nath, and E. Boldyreva, "Mechanically responsive molecular crystals," *Chem. Rev.* **115**, 12440–12490 (2015).
152. N. K. Nath, M. K. Panda, S. C. Sahoo, and P. Naumov, "Thermally induced and photoinduced mechanical effects in molecular single crystals—a revival," *CrystEngComm* **16**, 1850–1858 (2014).
153. M. K. Mishra, A. Mukherjee, U. Ramamurty, and G. R. Desiraju, "Crystal chemistry and photomechanical behavior of 3,4-dimethoxycinnamic acid: correlation between maximum yield in the solid-state topochemical reaction and cooperative molecular motion," *IUCrJ* **2**, 653–660 (2015).
154. R. Medishetty, A. Husain, Z. Bai, T. Runcevski, R. E. Dinnebier, P. Naumov, and J. J. Vittal, "Single crystals popping under UV light: a photosalient effect triggered by a [2+2] cycloaddition reaction," *Angew. Chem. (Int. Ed.)* **53**, 5907–5911 (2014).
155. A. Ravi and K. M. Sureshan, "Tunable mechanical response from a crystal undergoing topochemical dimerization: instant explosion at a faster rate and chemical storage of a harvestable explosion at a slower rate," *Angew. Chem. (Int. Ed.)* **57**, 9362–9366 (2018).
156. M. C. Etter and A. R. Siedle, "Solid-state rearrangement of (phenylazophenyl)palladium hexafluoroacetylacetonate," *J. Am. Chem. Soc.* **105**, 641–643 (1983).
157. P. Naumov, S. C. Sahoo, B. A. Zakharov, and E. V. Boldyreva, "Dynamic single crystals: kinematic analysis of photoinduced crystal jumping (the photosalient effect)," *Angew. Chem. (Int. Ed.)* **52**, 9990–9995 (2013).
158. L. Zhu, A. Agarwal, J. Lai, R. O. Al-Kaysi, F. S. Tham, T. Ghaddar, L. Mueller, and C. J. Bardeen, "Solid-state photochemical and photomechanical properties of molecular crystal nanorods composed of anthracene ester derivatives," *J. Mater. Chem.* **21**, 6258–6268 (2011).
159. R. Medishetty, S. C. Sahoo, C. E. Mulijanto, P. Naumov, and J. J. Vittal, "Photosalient behavior of photoreactive crystals," *Chem. Mater.* **27**, 1821–1829 (2015).
160. N. K. Nath, T. Runcevski, C.-Y. Lai, M. Chiesa, R. E. Dinnebier, and P. Naumov, "Surface and bulk effects in photochemical reactions and photomechanical effects in dynamic molecular crystals," *J. Am. Chem. Soc.* **137**, 13866–13875 (2015).
161. F. Tong, W. Xu, M. Al-Haidar, D. Kitagawa, R. O. Al-Kaysi, and C. J. Bardeen, "Photomechanically induced magnetic field response by controlling molecular orientation in 9-methylanthracene microcrystals," *Angew. Chem. (Int. Ed.)* **57**, 7080–7084 (2018).
162. Q. Yu, B. Aguila, J. Gao, P. Xu, Q. Chen, J. Yan, D. Xing, Y. Chen, P. Cheng, Z. Zhang, and S. Ma, "Photomechanical organic crystals as smart materials for advanced applications," *Chem. Eur. J.* **25**, 5611–5622 (2019).
163. O. S. Bushuyev, T. A. Singleton, and C. J. Barrett, "Fast, reversible, and general photomechanical motion in single crystals of various azo compounds using visible light," *Adv. Mater.* **25**, 1796–1800 (2013).

164. H. Koshima, K. Takechi, H. Uchimoto, M. Shiro, and D. Hashizume, "Photomechanical bending of salicylideneaniline crystals," *Chem. Commun.* **47**, 11423–11425 (2011).
165. S. Kobatake, S. Takami, H. Muto, T. Ishikawa, and M. Irie, "Rapid and reversible shape changes of molecular crystals on photoirradiation," *Nature* **446**, 778–781 (2007).
166. P. Naumov, J. Kowalik, K. M. Solntsev, A. Baldrige, J.-S. Moon, C. Kranz, and L. M. Tolbert, "Topochemistry and photomechanical effects in crystals of green fluorescent protein-like chromophores: effects of hydrogen bonding and crystal packing," *J. Am. Chem. Soc.* **132**, 5845–5857 (2010).
167. J. Lee, S. Oh, J. Pyo, J.-M. Kim, and J. H. Je, "A light-driven supramolecular nanowire actuator," *Nanoscale* **7**, 6457–6461 (2015).
168. D. Kitagawa, R. Tanaka, and S. Kobatake, "Dependence of photoinduced bending behavior of diarylethene crystals on irradiation wavelength of ultraviolet light," *Phys. Chem. Chem. Phys.* **17**, 27300–27305 (2015).
169. F. Tong, M. Liu, R. O. Al-Kaysi, and C. J. Bardeen, "Surfactant-enhanced photoisomerization and photomechanical response in molecular crystal nanowires," *Langmuir* **34**, 1627–1634 (2018).
170. Y. Hao, S. Huang, Y. Guo, L. Zhou, H. Hao, C. J. Barrett, and H. Yu, "Photoinduced multi-directional deformation of azobenzene molecular crystals," *J. Mater. Chem. C* **7**, 503–508 (2019).
171. L. Zhu, F. Tong, C. Salinas, M. K. Al-Muhanna, F. S. Tham, D. Kisailus, R. O. Al-Kaysi, and C. J. Bardeen, "Improved solid-state photomechanical materials by fluorine substitution of 9-anthracene carboxylic acid," *Chem. Mater.* **26**, 6007–6015 (2014).
172. R. O. Al-Kaysi, F. Tong, M. Al-Haidar, L. Zhu, and C. J. Bardeen, "Highly branched photomechanical crystals," *Chem. Commun.* **53**, 2622–2625 (2017).
173. D. P. Karothu, J. Weston, I. T. Desta, and P. Naumov, "Shape-memory and self-healing effects in mechanosensitive molecular crystals," *J. Am. Chem. Soc.* **138**, 13298–13306 (2016).
174. K. G. Yager and C. J. Barrett, "Temperature modeling of laser-irradiated azo-polymer thin films," *J. Chem. Phys.* **120**, 1089–1096 (2004).
175. K. G. Yager and C. J. Barrett, "Photomechanical surface patterning in azo-polymer materials," *Macromolecules* **39**, 9320–9326 (2006).
176. J. Liao, M. Yang, Z. Liu, and H. Zhang, "Fast photoinduced deformation of hydrogen-bonded supramolecular polymers containing a-cyanostilbene derivative," *J. Mater. Chem. A* **7**, 2002–2008 (2019).
177. D. H. Wang, K. M. Lee, Z. Yu, H. Koerner, R. A. Vaia, T. J. White, and L.-S. Tan, "Photomechanical response of glassy azobenzene polyimide networks," *Macromolecules* **44**, 3840–3846 (2011).
178. J. J. Wie, *Photomechanical Effects in Amorphous and Semicrystalline Polymers* (Wiley, 2017), Chap. 4, pp. 117–152.
179. C. Toccafondi, L. Occhi, O. Cavalleri, A. Penco, R. Castagna, A. Bianco, C. Bertarelli, D. Comoretto, and M. Canepa, "Photochromic and photomechanical responses of an amorphous diarylethene-based polymer: a spectroscopic ellipsometry investigation of ultrathin films," *J. Mater. Chem. C* **2**, 4692–4698 (2014).
180. D. H. Wang, K. M. Lee, H. Koerner, Z. Yu, R. A. Vaia, T. J. White, and L.-S. Tan, "Flexural-torsional photomechanical responses in azobenzene-containing crosslinked polyimides," *Macromol. Mater. Eng.* **297**, 1167–1174 (2012).
181. D. H. Wang, J. J. Wie, K. M. Lee, T. J. White, and L.-S. Tan, "Impact of backbone rigidity on the photomechanical response of glassy, azobenzene-functionalized polyimides," *Macromolecules* **47**, 659–667 (2014).

182. J. J. Wie, D. H. Wang, K. M. Lee, T. J. White, and L.-S. Tan, "The contribution of hydrogen bonding to the photomechanical response of azobenzene-functionalized polyamides," *J. Mater. Chem. C* **6**, 5964–5974 (2018).
183. N. Hosono, M. Yoshikawa, H. Furukawa, K. Totani, K. Yamada, T. Watanabe, and K. Horie, "Photoinduced deformation of rigid azobenzene-containing polymer networks," *Macromolecules* **46**, 1017–1026 (2013).
184. L.-H. He, "Deformation of amorphous azobenzene-containing polymer films induced by polarized light," *Acta Mech. Sin.* **28**, 1203–1208 (2012).
185. H. Wen, W. Zhang, Y. Weng, and Z. Hu, "Photomechanical bending of linear azobenzene polymer," *RSC Adv.* **4**, 11776–11781 (2014).
186. H.-K. Kim, X.-S. Wang, Y. Fujita, A. Sudo, H. Nishida, M. Fujii, and T. Endo, "Photomechanical switching behavior of semi-interpenetrating polymer network consisting of azobenzene-carrying crosslinked poly(vinyl ether) and polycarbonate," *Macromol. Rapid Commun.* **26**, 1032–1036 (2005).
187. Y. Jin, D. Harrington, A. A. Rachford, and J. J. Rack, "Stimulating changes in the elastic modulus of polymer materials by molecular photochromism," *RSC Adv.* **4**, 62920–62925 (2014).
188. A. H. Gelebart, D. Jan Mulder, M. Varga, A. Konya, G. Vantomme, E. W. Meijer, R. L. B. Selinger, and D. J. Broer, "Making waves in a photoactive polymer film," *Nature* **546**, 632–636 (2017).
189. C. Schuh, N. Lomadze, J. Rühle, A. Kopyshchev, and S. Santer, "Photomechanical degrafting of azo-functionalized poly(methacrylic acid) (PMAA) brushes," *J. Phys. Chem. B* **115**, 10431–10438 (2011).
190. K. N. Long, T. F. Scott, M. L. Dunn, and H. J. Qi, "Photo-induced deformation of active polymer films: single spot irradiation," *Int. J. Sol. Struct.* **48**, 2089–2101 (2011).
191. M. Moniruzzaman, P. Zioupos, and G. F. Fernando, "Investigation of reversible photo-mechanical properties of azobenzene-based polymer films by nanoindentation," *Scripta Materialia* **54**, 257–261 (2006).
192. Q. Yu, X. Yang, Y. Chen, K. Yu, J. Gao, Z. Liu, P. Cheng, Z. Zhang, B. Aguila, and S. Ma, "Fabrication of light-triggered soft artificial muscles via a mixed-matrix membrane strategy," *Angew. Chem. (Int. Ed.)* **57**, 10192–10196 (2018).
193. M. G. Kuzyk, D. W. Garvey, S. R. Vigil, and D. J. Welker, "All-optical devices in polymer optical fiber," *Chem. Phys.* **245**, 533–544 (1999).
194. X. Ye and M. G. Kuzyk, "Photomechanical response of disperse red 1 azobenzene dye-doped PMMA polymer fiber," *Opt. Commun.* **312**, 210–215 (2014).
195. D. J. Welker and M. G. Kuzyk, "Suppressing vibrations in a sheet with a Fabry–Perot photomechanical device," *Opt. Lett.* **22**, 417–418 (1997).
196. D. J. Welker and M. G. Kuzyk, "All-optical switching in a dye-doped polymer fiber Fabry–Perot waveguide," *Appl. Phys. Lett.* **69**, 1835–1836 (1996).
197. T. Fang, L. Cao, S. Chen, J. Fang, J. Zhou, L. Fang, C. Lu, and Z. Xu, "Preparation and assembly of five photoresponsive polymers to achieve complex light-induced shape deformations," *Mater. Design* **144**, 129–139 (2018).
198. S. Zhou, X. Tao, and Y. Gu, "Thickness-dependent thermal conductivity of suspended two-dimensional single-crystal In₂Se₃ layers grown by chemical vapor deposition," *J. Phys. Chem. C* **120**, 4753–4758 (2016).
199. S. Watanabe, H. Era, and M. Kunitake, "Two-wavelength infrared responsive hydrogel actuators containing rare-earth photothermal conversion particles," *Sci. Rep.* **8**, 13528 (2018).

200. P. M. Hogan, A. R. Tajbakhsh, and E. M. Terentjev, "UV manipulation of order and macroscopic shape in nematic elastomers," *Phys. Rev. E* **65**, 041720 (2002).
201. M. H. Li, P. Keller, B. Li, X. G. Wang, and M. Bruner, "Light-driven side-on nematic elastomer actuators," *Adv. Mater.* **15**, 569–572 (2003).
202. Y. Yu, M. Nakano, T. Maeda, M. Kondo, and T. Ikeda, "Precisely direction-controllable bending of cross-linked liquid-crystalline polymer films by light," *Mol. Cryst. Liq. Cryst.* **436**, [1235-1244], 281–290 (2005).
203. N. A. Platé and S. L. Schnur, *Liquid-Crystal Polymers* (Plenum, 1993).
204. J. Küpfer and H. Finkelmann, "Nematic liquid single crystal elastomers," *Makromol. Chem. Rap. Commun.* **12**, 717–726 (1991).
205. K. Min Lee, B. M. Lynch, P. Luchette, and T. J. White, "Photomechanical effects in liquid crystal polymer networks prepared with m-fluoroazobenzene," *J. Polym. Sci. A Polym. Chem.* **52**, 876–882 (2014).
206. S. Iamsaard, E. Anger, S. J. Aßhoff, A. Depauw, S. P. Fletcher, and N. Katsonis, "Fluorinated azobenzenes for shape-persistent liquid crystal polymer networks," *Angew. Chem. (Int. Ed.)* **55**, 9908–9912 (2016).
207. J.-I. Mamiya, A. Kuriyama, N. Yokota, M. Yamada, and T. Ikeda, "Photomobile polymer materials: photoresponsive behavior of cross-linked liquid-crystalline polymers with mesomorphic diarylethenes," *Chem. Eur. J.* **21**, 3174–3177 (2015).
208. T. Petrova, V. Toshchevikov, and M. Saphiannikova, "Light-induced deformation of polymer networks containing azobenzene chromophores and liquid crystalline mesogens," *Soft Matter* **11**, 3412–3423 (2015).
209. C. L. van Oosten, K. D. Harris, C. W. M. Bastiaansen, and D. J. Broer, "Glassy photomechanical liquid-crystal network actuators for microscale devices," *Eur. Phys. J. E* **23**, 329–336 (2007).
210. K. K. Hon, D. Corbett, and E. M. Terentjeva, "Thermal diffusion and bending kinetics in nematic elastomercantilever," *Eur. Phys. J. E* **25**, 83–89 (2008).
211. C. L. van Oosten, D. Corbett, D. Davies, M. Warner, C. W. M. Bastiaansen, and D. J. Broer, "Bending dynamics and directionality reversal in liquid crystal network photoactuators," *Macromolecules* **41**, 8592–8596 (2008).
212. C. Li, Y. Liu, C.-W. Lo, and H. Jiang, "Reversible white-light actuation of carbon nanotube incorporated liquid crystalline elastomer nanocomposites," *Soft Matter* **7**, 7511–7516 (2011).
213. H. Tian, Z. Wang, Y. Chen, J. Shao, T. Gao, and S. Cai, "Polydopamine-coated main-chain liquid crystal elastomer as optically driven artificial muscle," *ACS Appl. Mater. Interfaces* **10**, 8307–8316 (2018).
214. S.-K. Ahn, T. H. Ware, K. M. Lee, V. P. Tondiglia, and T. J. White, "Photoinduced topographical feature development in blueprinted azobenzene-functionalized liquid crystalline elastomers," *Adv. Funct. Mater.* **26**, 5819–5826 (2016).
215. S. J. Aßhoff, F. Lancia, S. Iamsaard, B. Matt, T. Kudernac, S. P. Fletcher, and N. Katsonis, "High-power actuation from molecular photoswitches in enantiomerically paired soft springs," *Angew. Chem. (Int. Ed.)* **56**, 3261–3265 (2017).
216. A. S. Kuenstler, H. Kim, and R. C. Hayward, "Liquid crystal elastomer waveguide actuators," *Adv. Mater.* **31**, 1901216 (2019).
217. O. M. Wani, H. Zeng, and A. Priimagi, "A light-driven artificial flytrap," *Nat. Commun.* **8**, 15546 (2017).
218. F. Greco, V. Domenici, A. Desii, E. Sinibaldi, B. Zupancic, B. Zalar, B. Mazzolai, and V. Mattoli, "Liquid single crystal elastomer/conducting polymer bilayer composite actuator: modelling and experiments," *Soft Matter* **9**, 11405–11416 (2013).

219. S. W. Ranson and H. W. Magoun, "The central path of the pupilloconstrictor reflex in response to light," *Arch. Neur. Psych.* **30**, 1193–1204 (1933).
220. H. W. Magoun, D. Atlas, W. K. Hare, and S. W. Ranson, "The afferent path of the pupillary light reflex in the monkey," *Brain* **59**, 234–249 (1936).
221. B. W. Whitman and R. J. Packer, "The photic sneeze reflex: literature review and discussion," *Neurology* **43**, 868–871 (1993).
222. R. C. Hardie and K. Franze, "Photomechanical responses in drosophila photoreceptors," *Science* **338**, 260–263 (2012).
223. D. Klocke and H. Schmitz, "Material properties of photomechanical infrared receptors in pyrophilous melanophila beetles and aradus bugs," *Acta Biomater.* **8**, 3392–3399 (2012).
224. C.-S. Chen, X.-D. Xu, S.-Y. Li, R.-X. Zhuo, and X.-Z. Zhang, "Photo-switched self-assembly of a gemini α -helical peptide into supramolecular architectures," *Nanoscale* **5**, 6270–6274 (2013).
225. T. M. Doran, D. M. Ryan, and B. L. Nilsson, "Reversible photocontrol of self-assembled peptide hydrogel viscoelasticity," *Polym. Chem.* **5**, 241–248 (2014).
226. A. M. Rosales, K. M. Mabry, E. M. Nehls, and K. S. Anseth, "Photoresponsive elastic properties of azobenzene-containing poly(ethylene-glycol)-based hydrogels," *Biomacromolecules* **16**, 798–806 (2015).
227. M. G. Kuzyk, D. J. Welker, and S. Zhou, "Photomechanical effects in polymer optical fibers," *Nonlinear Opt.* **10**, 409–419 (1995).
228. D. J. Welker and M. G. Kuzyk, "All-optical devices in polymer optical fiber," *Nonlin. Opt.* **15**, 435–442 (1996).
229. M. G. Kuzyk, *Nonlinear Optics: a Student's Perspective* (Create Space, 2017).
230. M. G. Kuzyk, U. C. Paek, and C. W. Dirk, "Guest-host fibers for nonlinear optics," *Appl. Phys. Lett.* **59**, 902 (1991).
231. D. W. Garvey, K. Zimmerman, P. Young, J. Tostenrude, J. S. Townsend, Z. Zhou, M. Lobel, M. Dayton, R. Wittorf, and M. G. Kuzyk, "Single-mode nonlinear-optical polymer fibers," *J. Opt. Soc. Am. B* **13**, 2017–2023 (1996).
232. P. L. Chu, "Polymer optical fiber Bragg gratings," *Opt. Photon. News* **16**, 52–56 (2005).
233. W. Wei, J. Gao, J. Yang, J. Wei, and J. Guo, "A NIR light-triggered pyroelectric-dominated generator based on a liquid crystal elastomer composite actuator for photoelectric conversion and self-powered sensing," *RSC Adv.* **8**, 40856–40865 (2018).
234. G. Uğur, J. Chang, S. Xiang, L. Lin, and J. Lu, "A near-infrared mechano responsive polymer system," *Adv. Mater.* **24**, 2685–2690 (2012).
235. J. J. Wie, D. H. Wang, V. P. Tondiglia, N. V. Tabiryan, R. O. Vergara-Toloza, L.-S. Tan, and T. J. White, "Photopiezoelectric composites of azobenzene-functionalized polyimides and polyvinylidene fluoride," *Macromol. Rapid Commun.* **35**, 2050–2056 (2014).
236. R. Tang, W. Sang, Y. Wu, C. Zhu, and J. Liu, "Multi-wavelength light drivable oscillatory actuator on graphene-based bilayer film," *Macromol. Mater. Eng.* **302**, 1600384 (2017).
237. R. Tang, Z. Liu, D. Xu, J. Liu, L. Yu, and H. Yu, "Optical pendulum generator based on photomechanical liquid-crystalline actuators," *ACS Appl. Mater. Interfaces* **7**, 8393–8397 (2015).
238. Y. Xiong, L. Zhang, P. Weis, P. Naumov, and S. Wu, "A solar actuator based on hydrogen-bonded azopolymers for electricity generation," *J. Mater. Chem. A* **6**, 3361–3366 (2018).

239. N. K. Nath, L. Pejov, S. M. Nichols, C. Hu, N. Saleh, B. Kahr, and P. Naumov, "Model for photoinduced bending of slender molecular crystals," *J. Am. Chem. Soc.* **136**, 2757–2766 (2014).
240. P. Naumov, S. C. Sahoo, B. A. Zakharov, and E. V. Boldyreva, "Dynamic single crystals: kinematic analysis of photoinduced crystal jumping (the photosalient effect)," *Angew. Chem. (Int. Ed.)* **52**, 9990–9995 (2013).
241. D. Kitagawa and S. Kobatake, "Photoreversible current ON/OFF switching by the photoinduced bending of gold-coated diarylethene crystals," *Chem. Commun.* **51**, 4421–4424 (2015).
242. S. S. Sarkisov, M. J. Curley, A. Fields, S. S. Sarkisov, and G. Adamovsky, "Photomechanical effect in films of polyvinylidene fluoride," *Appl. Phys. Lett.* **85**, 2747–2749 (2004).
243. D. E. Hagaman, S. Leist, J. Zhou, and H.-F. Ji, "Photoactivated polymeric bilayer actuators fabricated via 3D printing," *ACS Appl. Mater. Interfaces* **10**, 27308–27315 (2018).
244. Z. Liu, R. Tang, D. Xu, J. Liu, and H. Yu, "Precise actuation of bilayer photomechanical films coated with molecular azobenzene chromophores," *Macromol. Rapid Commun.* **36**, 1171–1176 (2015).
245. X. Yu, J. Pan, J. Deng, J. Zhou, X. Sun, and H. Peng, "A novel photoelectric conversion yarn by integrating photomechanical actuation and the electrostatic effect," *Adv. Mater.* **28**, 10744–10749 (2016).
246. H.-Y. Zhong, L. Chen, R. Yang, Z.-Y. Meng, X.-M. Ding, X.-F. Liu, and Y.-Z. Wang, "Azobenzene-containing liquid crystalline polyester with π - π interactions: diverse thermo- and photo-responsive behaviours," *J. Mater. Chem. C* **5**, 3306–3314 (2017).
247. J. Hu, X. Li, Y. Ni, S. Ma, and H. Yu, "A programmable and biomimetic photo-actuator: a composite of a photo-liquefiable azobenzene derivative and commercial plastic film," *J. Mater. Chem. C* **6**, 10815–10821 (2018).
248. X. Zhang, Z. Yu, C. Wang, D. Zarrouk, J.-W. T. Seo, J. C. Cheng, A. D. Buchan, K. Takei, Y. Zhao, J. W. Ager, J. Zhang, M. Hettick, M. C. Hersam, A. P. Pisano, R. S. Fearing, and A. Javey, "Photoactuators and motors based on carbon nanotubes with selective chirality distributions," *Nat. Commun.* **5**, 2983 (2014).
249. L. Yang, K. Qi, L. Chang, A. Xu, Y. Hu, H. Zhai, and P. Lu, "A powerful dual-responsive soft actuator and photo-to-electric generator based on graphene micro-gasbags for bioinspired applications," *J. Mater. Chem. B* **6**, 5031–5038 (2018).
250. Z. Tang, Z. Gao, S. Jia, F. Wang, and Y. Wang, "Graphene-based polymer bilayers with superior light-driven properties for remote construction of 3D structures," *Adv. Sci.* **4**, 1600437 (2017).
251. Z. Chen, R. Cao, S. Ye, Y. Ge, Y. Tu, and X. Yang, "Graphene oxide/poly (N-isopropylacrylamide) hybrid film-based near-infrared light-driven bilayer actuators with shape memory effect," *Sens. Actuators B* **255**, 2971–2978 (2018).
252. K. Uchino and M. Aizawa, "Photostrictive actuator using PLZT ceramics," *Jpn. J. Appl. Phys.* **24**, 139–141 (1985).
253. V. Rahmehin, F. Khosravi, D. A. Ziolkowska, J. B. Jasinski, and B. Panchapakesan, "Chromatic mechanical response in 2-D layered transition metal dichalcogenide (TMDs) based nanocomposites," *Sci. Rep.* **6**, 34831 (2016).
254. Y. Kuwahara, M. Kaji, J. Okada, S. Kim, T. Ogata, and S. Kurihara, "Self-alignment and photomechanical properties of alternative multi-layered films containing azobenzene polymer liquid crystal and polyvinyl alcohol layers," *Mater. Lett.* **113**, 202–205 (2013).

255. M. Yamada, M. Kondo, J.-I. Mamiya, Y. Yu, M. Kinoshita, C. J. Barrett, and T. Ikeda, "Photomobile polymer materials: towards light-driven plastic motors," *Angew. Chem. (Int. Ed.)* **47**, 4986–4988 (2008).
256. H. Koshima, H. Uchimoto, T. Taniguchi, J. Nakamura, T. Asahi, and T. Asahi, "Mechanical motion of molecular crystals induced by [4 + 4] photodimerisation," *CrystEngComm* **18**, 7305–7310 (2016).
257. H.-K. Kim, X.-S. Wang, Y. Fujita, A. Sudo, H. Nishida, M. Fujii, and T. Endo, "A rapid photomechanical switching polymer blend system composed of azobenzene-carrying poly(vinylether) and poly(carbonate)," *Polymer* **46**, 5879–5883 (2005).
258. L. Cheng, Y. Torres, K. Min Lee, A. J. McClung, J. Baur, T. J. White, and W. S. Oates, "Photomechanical bending mechanics of polydomain azobenzene liquid crystal polymer network films," *J. Appl. Phys.* **112**, 013513 (2012).
259. D. Kusano, R. Ohshima, N. Hosono, K. Totani, and T. Watanabe, "Photochemical reaction in azobenzene-containing rigid poly(amide acid) networks," *Polymer* **55**, 5648–5655 (2014).
260. L. Fang, H. Zhang, Z. Li, Y. Zhang, Y. Zhang, and H. Zhang, "Synthesis of reactive azobenzene main-chain liquid crystalline polymers via michael addition polymerization and photomechanical effects of their supramolecular hydrogen-bonded fibers," *Macromolecules* **46**, 7650–7660 (2013).
261. M. Kondo, K. Makino, K. Miyake, Y. Matsuo, R. Fukae, and N. Kawatsuki, "Coatable photomobile polymer films using spring-like photochromic compounds," *Macromol. Chem. Phys.* **219**, 1700602 (2018).
262. S. Tanaka, H.-K. Kim, A. Sudo, H. Nishida, and T. Endo, "Anisotropic photomechanical response of stretched blend film made of polycaprolactone-polyvinyl ether with azobenzene group as side chain," *Macromol. Chem. Phys.* **209**, 2071–2077 (2008).
263. J. Loomis and B. Panchapakesan, "Nanotechnology paper dimensional dependence of photomechanical response in carbon nanostructure composites: a case for carbon-based mixed-dimensional systems," *Nanotechnology* **23**, 215501 (2012).
264. J. Loomis, B. King, T. Burkhead, P. Xu, N. Bessler, E. Terentjev, and B. Panchapakesan, "Graphene-nanoplatelet-based photomechanical actuators," *Nanotechnology* **23**, 045501 (2012).
265. S. Ansari, C. Rahima, and M. N. Muralidharan, "Photomechanical characteristics of thermally reduced graphene oxide–polydimethylsiloxane nanocomposites," *Polym. Plast. Technol. Eng.* **52**, 1604–1610 (2013).
266. H. Yu, C. Dong, W. Zhou, T. Kobayashi, and H. Yang, "Wrinkled liquid-crystalline microparticle-enhanced photoresponse of PDLC-like films by coupling with mechanical stretching," *Small* **7**, 3039–3045 (2011).
267. L. Yu, Z. Cheng, Z. Dong, Y. Zhang, and H. Yu, "Photomechanical response of polymer-dispersed liquid crystals/graphene oxide nanocomposites," *J. Mater. Chem. C* **2**, 8501–8506 (2014).
268. Y. Yue, Y. Norikane, R. Azumi, and E. Koyama, "Light-induced mechanical response in crosslinked liquid-crystalline polymers with photoswitchable glass transition temperatures," *Nature Commun.* **9**, 3234 (2018).
269. A. Shimamura, A. Priimagi, J.-I. Mamiya, T. Ikeda, Y. Yu, C. J. Barrett, and A. Shishido, "Simultaneous analysis of optical and mechanical properties of cross-linked azobenzene-containing liquid-crystalline polymer films," *ACS Appl. Mater. Interfaces* **3**, 4190–4196 (2011).
270. R. Lakes, "Foam structures with a negative Poisson's ratio," *Science* **235**, 1038–1040 (1987).
271. L. D. Landau and E. M. Lifshitz, *Theory of Elasticity* (Pergamon, 1975).



Mark G. Kuzyk received his B.A. (1979), M.S. (1981), and Ph.D. (1985) degrees in physics from the University of Pennsylvania. He was a Member of Technical Staff at AT&T Bell Laboratories until 1990, then became a faculty member at Washington State University, Pullman, where he was also the Boeing Distinguished Professor of Physics and Materials Science and the Meyer Distinguished Professor of the Sciences, and is now Regents Professor. He is a Fellow of The Optical Society, the American Physical Society, and SPIE; was an Associate Chair of Physics and the Chair of the Materials Science Program; and presented the 2005 WSU Distinguished Faculty Address. Most recently, he was awarded the Eminent Faculty Award. He served as topical editor for JOSA B and is one of the founders of the ICONO conferences on organic nonlinear optics and the Foundations of Nonlinear Optics. In his spare time, he plays ice hockey in Moscow, Idaho.



Nathan J. Dawson received his B.S. (2004) from the University of Idaho and his Ph.D. (2011) from Washington State University. He began his first post-doc at Youngstown State University in 2011 and his second post-doc at Case Western Reserve University in 2013. He became an Assistant Professor of Physics at the University of The Bahamas in 2015 then an Assistant Professor of Physics and of Engineering at Hawaii Pacific University in 2017, where he is also an Adjunct Assistant Professor in the Department of Physics and Astronomy at Washington State University. He is a Senior Member of the International Society for Optics and Photonics (SPIE) and a fishing enthusiast.